A methodology for integrated thermofluid modelling of radiant superheaters in steady state and transient operations

Department of Mechanical Engineering
Faculty of Engineering and the Built Environment
University of Cape Town

Student Name: Mr Excellent Zibhekele Gwebu
Student Number: GWBEXC001

Supervisor: Professor Pieter G. Rousseau
Co-Supervisor: Professor Arnaud G. Malan
Co-Supervisor: Professor Louis M. Jestin

February 2019

Submitted to the University of Cape Town in fulfilment of the academic requirements for a doctoral degree in Mechanical Engineering.

KEY WORDS: SUPERHEATER, GAS RADIATION, DIRECT RADIATION, STEADY STATE, TRANSIENT

Eskom Specialisation Centre in Energy Efficiency

ABSTRACT

Critical components in coal-fired power plants such as final superheater heat exchangers experience severe conditions associated with high metal temperatures and high temperature gradients during base load and transient operations. Such adverse conditions could significantly reduce the life span of the components, especially due to the requirement of greater plant flexibility that is an essential part of the global power system transformation. Integrated thermofluid process models can be employed to obtain a better understanding of the relationship between the operational conditions and the metal temperatures. Thus, a methodology was developed to model radiant superheater heat exchangers in steady state and transient operations.

The methodology is based on a network approach which entails solving the transient one-dimensional forms of the conservation equations for mass, energy and momentum. The model building blocks account for the convective thermal resistance on the steam side, the conductive thermal resistances of the tube wall and scaling or fouling on the tube walls, as well as the convective and radiative thermal resistances and direct radiation on the flue gas side. The model captures the physical layout of the tube passes in a tubesheet via the arrangement of the network building blocks. It is also possible to connect tubesheets together across the width of the boiler as per the arrangement in a real plant.

The modelling methodology was first used to develop a process model of a convective cross-flow primary superheater heat exchanger with complex flow arrangement. The dual-tube 12-pass superheater was discretized along the flue gas flow path as well as along the steam flow path. The model was qualitatively validated using real plant data from literature and for reference purposes also systematically compared to conventional lumped parameter models. The ability of the model to analyse the effect of ramp rate during load changes on the tube metal temperature was demonstrated, as well as the ability to determine the maldistribution of flow and temperature on the steam and flue gas sides.

The methodology was also applied to model a U-shaped radiant superheater heat exchanger. Due to the challenges associated with obtaining comprehensive real plant data in an industrial setting, a validation methodology was proposed that is based on a combination of plant design C-schedules and a boiler mass and energy balance, as well as limited plant measurements. The consistent comparisons with C-schedule data provide evidence of the validity of the model, which was further demonstrated via the comparisons with real plant data. The model allows prediction of the steam mass flow and temperature distribution going into the outlet stub headers as well as the main outlet headers for different inlet flow and temperature distributions on the steam and flue gas sides. These results were compared to detail real-plant measurements of the outlet header temperatures. The model also allows prediction of the metal temperatures along the length of the tubes which cannot readily be measured in the plant. The model was applied to demonstrate the impact of different operational conditions on the tube metal temperatures.

Such integrated process models can be employed to study complex thermofluid process phenomena that may occur during intermittent, transient and low load operation of power plants. In addition, such models could be useful for predictive and preventative maintenance as well as online condition monitoring.

PLAGIARISM DECLARATION

I, ***Excellent Zibhekele Gwebu***, hereby declare the work contained in this dissertation to be my own. All information which has been gained from various journal articles, text books or other sources has been referenced accordingly. I have not allowed, and will not allow, anyone to copy my work with the intention of passing it off as their own work or part thereof.

Signed by candidate

Signature

11 February 2019

Date

DECLARATION: INCLUSION OF PUBLICATIONS

I confirm that I have been granted permission by the University of Cape Town's Doctoral Degrees Board to include the following publications in my PhD thesis, and where co-authorships are involved, my co-authors have agreed that I may include the publications:

1. E. Z. Gwebu and P. G. Rousseau, "A network Approach Applied in Modelling the Heat Transfer and Fluid Flow in a Superheater Heat Exchanger," in Modelling, Simulation and Identification, Calgary, Canada, 19 - 20 July 2017 [1].
2. P. G. Rousseau and E. Z. Gwebu, "Modelling of a Superheater Heat Exchanger with Complex Flow Arrangement Including Flow and Temperature Maldistribution," Heat Transfer Engineering, vol. 0, no. 0, pp. 1-17, 2018 [2].
3. E. Z. Gwebu and P. G. Rousseau, "Development and Validation of a Process Model for a Superheater Heat Exchanger in a Coal-Fired Power Plant Boiler," in 16th International Heat Transfer Conference, IHTC-16, Beijing, China, 10 - 15 August 2018 [3].

Signed by candidate

Signature

11 February 2019

Date

ACKNOWLEDGEMENTS

Firstly, I would like to thank and appreciate my supervisor professor Pieter Rousseau for his guidance throughout this PhD journey. He supported me, encouraged me and believed in me from the beginning until the very end. I will always be grateful for this.

Secondly, I would like to thank my co-supervisor professor Louis Jestin for his overall support and guidance throughout this research. Most importantly, I appreciate him for lending me his wealth of technical knowhow in coal-fired boilers. In addition, I would like to thank my second co-supervisor professor Arnaud Malan for his guidance in this research, especially in the field of computational fluid dynamics.

Furthermore, I would like to send my sincere gratitude to the rest of the management team in EPPEI's specialization centre in Energy Efficiency for their support throughout the research. This team include associate professor Wim Fuls, Dr Ryno Laubscher, Mr Priyesh Gosai and Mr Shane Ferguson.

This research wouldn't have been possible without the funding from Eskom through EPPEI as well as the funding from UCT through the postgraduate funding office. I am grateful for the financial support. Also, I would like to acknowledge Eskom RT&D and Dr Mark Newby for funding the installation of thermocouples on the final superheater studied in this research. I would also like to acknowledge M-Tech industrial allowing me to use the Flownex software. I would also like to appreciate all the staff members at the UCT interlibrary loan for their tireless efforts in finding me all the research material in needed from all over the world.

I would like to thank my colleagues and now friends; Whitney, Nikki, Lethu, Rushavya, Cheriska, Rendi, Patrick, Geoff, Willie, John, Gerto, Pieter, Rob, Colin and Jean-Piere, for their assistance, the vibrant discussions we had and the fun activities we did together during my time in the research unit. Moreover, I appreciate the EPPEI CMT, BISRU colleagues and friends and Lumka for ensuring a conducive environment for work and socializing in our offices. I would also like to appreciate the unwavering support I got from my friends, especially Mxolisi Myeza, Siphamandla Shabangu, Buhle Manana, Zethu Dlamini, Sive Nyanda and Nokwanda Hlophe.

I dedicate this dissertation to all my family members, more importantly to my mother for the unwavering support, patience and believing in me. May this work serve as a motivation for more people in my family and my village to further their studies. The sky is the limit. I will end with my favourite quote by Anthony Robbins which says, "It is in your moments of decision that your destiny is shaped".

TABLE OF CONTENTS

LIST OF FIGURES

LIST OF TABLES

NOMENCLATURE

General symbols

A	Area (m^2)	F	View factor
a	Emissivity weighting factor/ relative transverse pitch/ fraction of absorbed radiation energy	f	Friction factor/ function of/ fraction
ATT	Attemperator	FE	Furnace exit
AH	Airheater	FEM	Finite element method
b	Emissivity gas temperature polynomial coefficient/ width (m)/ relative longitudinal pitch (m)	FET	Furnace exit temperature
C	Capacity rate	FGR	Flue gas ratio
c	Specific heat capacity (kJ/(kgK))	FM	Flownex Model
CFD	Computational fluid dynamics	FNX	Flownex
CHONS	Carbon, Hydrogen, Oxygen, Nitrogen and Sulphur	FR	Mass flow ratios of specific streams
Cp	Mean overall heat capacity (kJ/(kgK))	FVM	Finite volume method
CV	Calorific value (kJ/kg)	FW	Feedwater
d	Diameter (m)	G	Flue gas mass excluding fly ash
DAR	Dry Air Required	g	Gravitational acceleration (m/s^2)
DCS	Distributed Control System	h	Specific static enthalpy (kJ/kg) / heat transfer coefficient ($W/(m^2K)$)/ height (m)
DR	Distributed resistance	HAR	Humid Air Required
e	Inside wall surface roughness (μm)	HHV	Higher heating value (kJ/kg)
EC	Economizer	IAPWS	International Association for the Properties of Water and Steam
Eu	Euler number	ID	Inner diameter (m)

K	Loss coefficient/ Overall extinction coefficient	Re	Reynolds number
k	Thermal conductivity (W/(mK))/ gas coefficient	RH	Reheater
L	Length (m)	S	Source term/ pitch/ control volume
l	Length (m)	s	Mean beam length (m)
LHV	Lower heating value (kJ/kg)	SDR	Simplified distributed resistance
LM	Lumped Model	SH	Superheater
LMTD	Logarithmic Mean Temperature Difference	St	Stoichiometric coeffiecient
M	Molar mass (kg/mol)/ flame centre modification factor	T	Temperature (°C or K)
$\dot{m}$	Mass flow rate (kg/s)	t	Time (s)
MCR	Maximum Continuous Rating	TAR	Theoretical Air Required
MEB	Mass and Energy Balance	TM	Taler et al. [4] Model
NTU	Number of Transfer Units	UA	Overall heat transfer coefficient (kW/K)
Nu	Nusselt number	V	Volume (m^3)
OD	Outer diameter (m)	*v*	Velocity (m/s)
OFL	Outer Fouling Layer (m)	$\dot{W}$	Power output (kW)
p	Static pressure (kPa)	*w*	Water vapour percentage in air/ intermediate momentum term
Pr	Prandtl number	WSGG	Weighted Sum of Gray Gases
Q	Thermal load of radiation	x	Horizontal position (Cartesian coordinates system)
$\dot{Q}$	Heat transfer rate (kW)	y	Vertical position (Cartesian coordinates system)/ mole fraction
q'	Direct radiation from the furnace	z	Elevation (m)/ number of tube rows
r	Volume fraction		

Greek symbols

ρ	Density (kg/m^3)	E	Ash deposition coefficient (m^2°C/W)
β	Coefficient accounting for reradiation/ Distributed resistance	λ	Thermal conductivity (W/mK)
Δ	Change in a property	φ	Angle of attack/ heat preservation coefficient/ configuration factor
σ	Stefan-Boltzmann constant (W/m^{2}K^4)	ψ	Average thermal efficiency coeficient
α	Absorptivity coefficient	x	Ash content/ mass fractions
κ	i-th gas absorptivity coefficient	μ	Dynamic viscosity/ fly ash concentration
ε	Emissivity/ effectiveness/ correction factor for angle of attack/ local porosity	ζ	Correction factor of the fuel

Subscripts

ash	Ash layer	e	Outlet/ exit/ energy
ave	Average	EA	Excess air
b	Burner	eq	Equivalent
BA	Bottom ash	F	Furnace center
bulk	total	fa	Fly ash
c	Mass/ convection and gas radiation	fg	Flue gas
co	Coke	flame	Flame in the furnace
conv	Convection	flow	Flow stream
cor	corrected	FSH	Final superheater
coal	Coal	g	Gas
credits	Auxiliary power (MW)	ha	Humid air
d	Tube diameter	i	Inlet / inner
direct	Direct radiation	in	Inlet

L	Losses/ longitudinal	rad	Radiation
l	Streamed length	ro	Radiation outside tube
lam	Laminar	roof	Roof of the boiler
LMTD	Logarithmic Mean Temperature Difference	s	Steam
m	Momentum	st	Steam
max	Maximum	scale	Scaling layer
mb	Mean beam length	T	Transverse
min	Minimum	t	Tube
o	Total or outer	tot	total
oft	Outer fouled tube	turb	Turbulent
out	Outlet	VDI	VDI heat atlas
p	Pipe wall	w	Tube wall/ work/ flue gas composition and temperature
plat	Platen superheater	ww	Waterwall
r	Radiation	z	Tube rows
rl	Platen superheater matrix	s	Geometric arrangement

Superscripts

^{0}	Old time values
^{n}	Current time step
$^{n+1}$	Next time step

1. INTRODUCTION

Boiler tube failures are a leading cause of unplanned capacity losses in South African coal fired power plants, as illustrated in Figure 1-1. These boiler tube failures are predominantly on the components that operate under high pressures and temperatures, i.e. the superheater and reheater heat exchangers. The high pressure and temperature steam escaping from a failed tube can cut the tubes around it hence increasing the maintenance and replacement costs. In addition to component replacement costs, the down time of a plant leads to revenue losses for the utility. In many cases operational anomalies are major contributors to these tube failures.

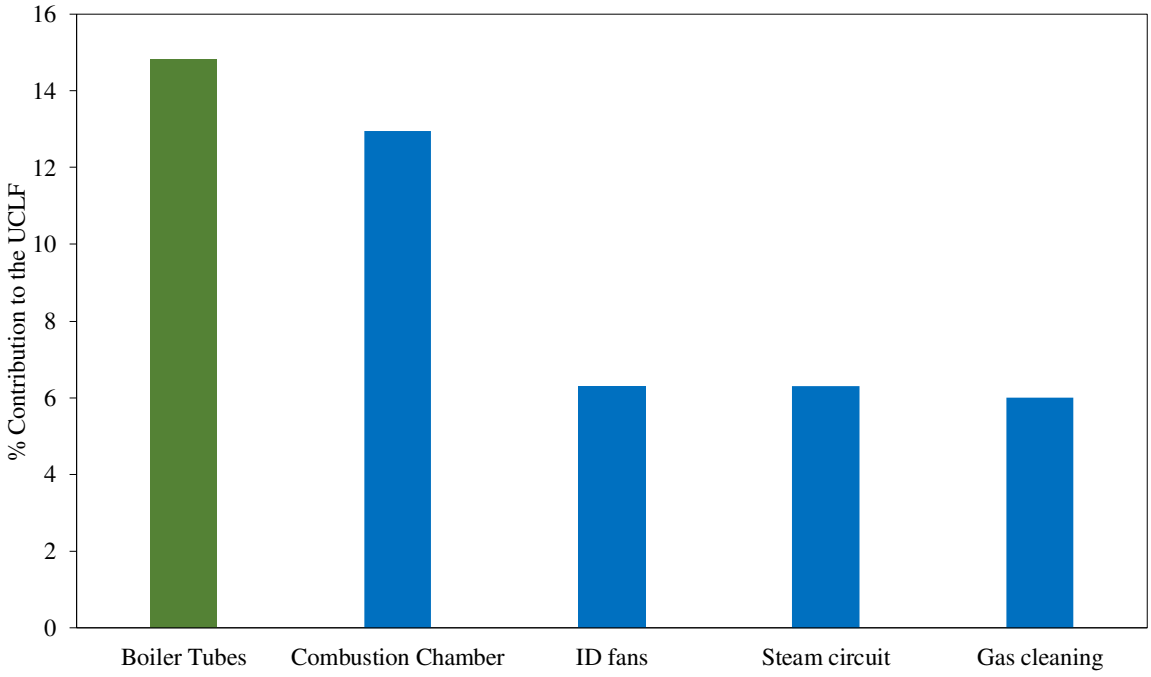

Figure 1-1: A breakdown of the top five contributions of boiler subsystems or components to the Unplanned Capacity Loss Factor (UCLF) in Eskom Coal fired fleet, Year to Date January 2015 [5].

According to Babcock & Wilcox, for coal-fired boilers it is possible to repair a tube leak and put the boiler back online, only to be forced offline within a short time by another tube leak. This emphasizes the need to identify and correct the root cause of the problem because a tube failure may be a symptom of other problems. Some knowledge of the different kinds of tube failures (their visual characteristics) and their causes does assist in the root cause analyses of the problem. These failures include the following: caustic attack, oxygen pitting, hydrogen damage, acid attack, stress corrosion cracking, waterside corrosion fatigue, superheater fireside ash corrosion, high-temperature oxidation, water

fireside corrosion, fireside corrosion fatigue, graphitization, dissimilar metal weld failure, tube erosion, short-term overheat, long-term overheat and thermal fatigue [6].

Short-term overheating is the ductile rupture of tube metal due to elevated temperatures. These high temperatures may be caused by lack of cooling from water or steam flow, especially during boiler start-ups. For example, if the condensate in boiler superheater tubes is not evaporated, this condensate will act as a blockage, hence starving certain sections of the tubes from cooling by steam [6]. This type of failure is characterised by a thin lipped "fish mouth" opening along the length of the tube as shown in Figure 1-2.

Figure 1-2: Thin lipped "fish mouth" opening characterizing short-term overheating.

Long-term overheating in tube metals, also known as creep failure, occurs after months or years of operation in elevated temperatures. This occurs especially in water walls, superheater and reheater tubes where during normal operation the metal temperature will degrade due to the high temperatures and pressures over the life of the component. Typical operation hours of such tube materials are about 200 000 hours. After such a time, the tube experiences creep rupture which is characterized by a thick-lipped opening as shown in Figure 1-3.

Heat exchangers in the convective pass of a coal-fired power plant boiler are made up of tubes which form the elements or tube sheets. The steam flowing in these tubes are either collected directly in a set of main headers, or in so-called stub headers from where it is fed to the main headers, as illustrated in Figure 1-4.

Figure 1-3: Thick lipped creep rupture characterizing long-term overheating [6].

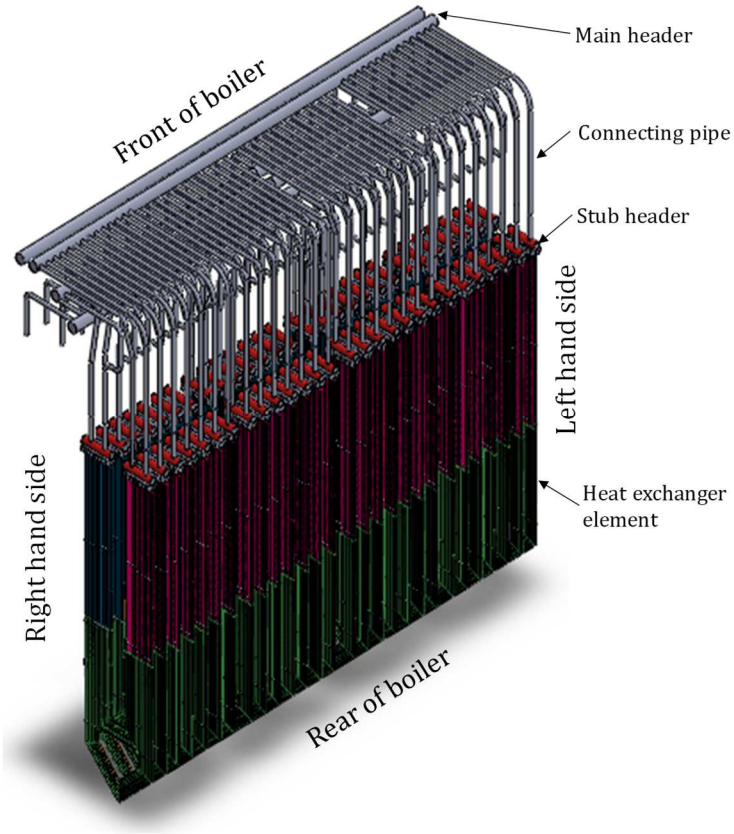

Figure 1-4: A three-dimensional CAD drawing of a superheater heat exchanger with sub headers.

Final superheater outlet headers are susceptible to failure because they operate under high pressures and temperatures. Some headers operate at temperatures close to 600 °C. These headers are typically made of P11 and P22 materials [7]. Even though these headers are designed to operate below the temperature limit and by taking creep failure into account, over time the material degrades, creep

damage accumulates, and material failure is inevitable. Damage is aggravated when the boiler undergoes cyclic operations such as start-ups, shut-down and load changes, because the time to failure due to creep can be accelerated. This is due to the fact that the cyclic operation introduces additional damage mechanisms, namely thermal fatigue and oxide notching [7].

During cyclic operations, the variation of the steam temperature induces a temperature gradient along the thickness of the header wall. Such a temperature gradient in turn introduces thermal stresses. When there is continuous variation of the temperatures it results in cycling thermal stresses which then induce thermal fatigue in the radial direction. The introduction of more intermittent renewable energy sources on the electricity supply grid means that coal-fired plants are forced to change its mode of operation from base load to two-shifting or low load variable operation [8, 9]. This is also the case in South Africa where times of intermittent surplus capacity amid weaker demand are becoming more prevalent.

Since subsystems like superheaters have elements connected along the length of the header, if the temperatures in these elements are different such that certain sections of the header expand more than others, bending stresses can be introduced. If these bending stresses are cycled, then thermal stresses in the axial direction can be introduced leading to tube-to-header weld cracks as well as failure on the header itself, as shown in Figure 1-5.

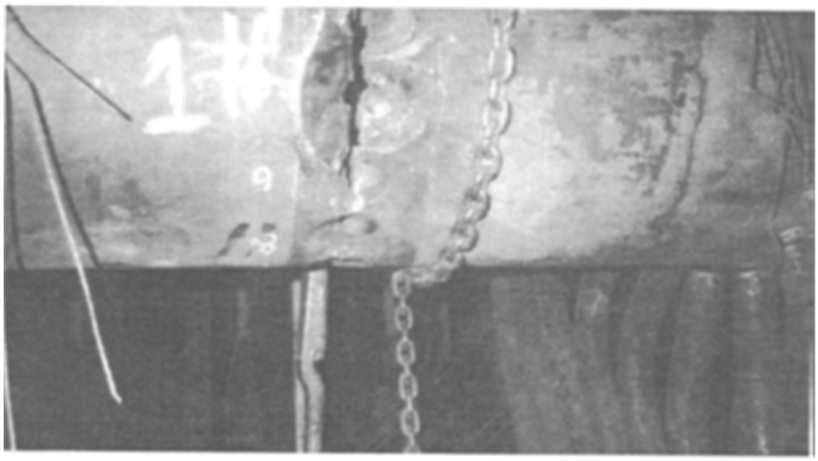

Figure 1-5: Failed header due to bending stresses [10].

According to Nakoneczny & Schultz [7] cracking in high temperature superheater headers has been found to occur in almost every weld position, as well as the ligament area between tube stub bore holes. Figure 1-6 shows some of the locations on a header that are susceptible to cracking. In general, header damage can be classified as repairable or non-repairable. Repairable damage mainly consists

of cracks or any failure that can be repaired through welding. Non-repairable damage consists of ligament (or bore hole) cracks which will require a replacement of the header.

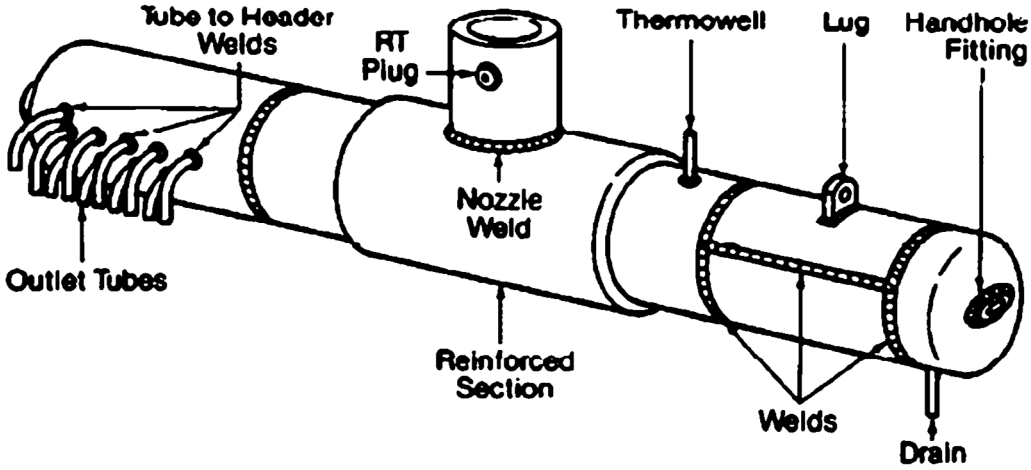

Figure 1-6: Locations on the header that are susceptible to cracking [7].

Combustion characteristics, steam flow and boiler load variations are three factors related to boiler operations that influence ligament damage in headers [7]. In terms of the influence from combustion, the arrangements of the burners on the furnace walls has an influence on the flue gas flow and temperature leaving the furnace to the convective pass. There are two configurations of burners, namely wall-fired and tangentially fired. For wall-fired boilers, the burners are on the front wall and/or the rear wall depending on the size of the unit. For tangentially fired boiler the burners are situated at the corners of the furnace. For each configuration there is an associated Furnace Exit Gas Temperature (FEGT) and flow profile which have an effect on the heat absorption of the downstream heat exchangers in the convective pass. An example of a typical FEGT profile for a wall fired boiler is shown in Figure 1-7c.

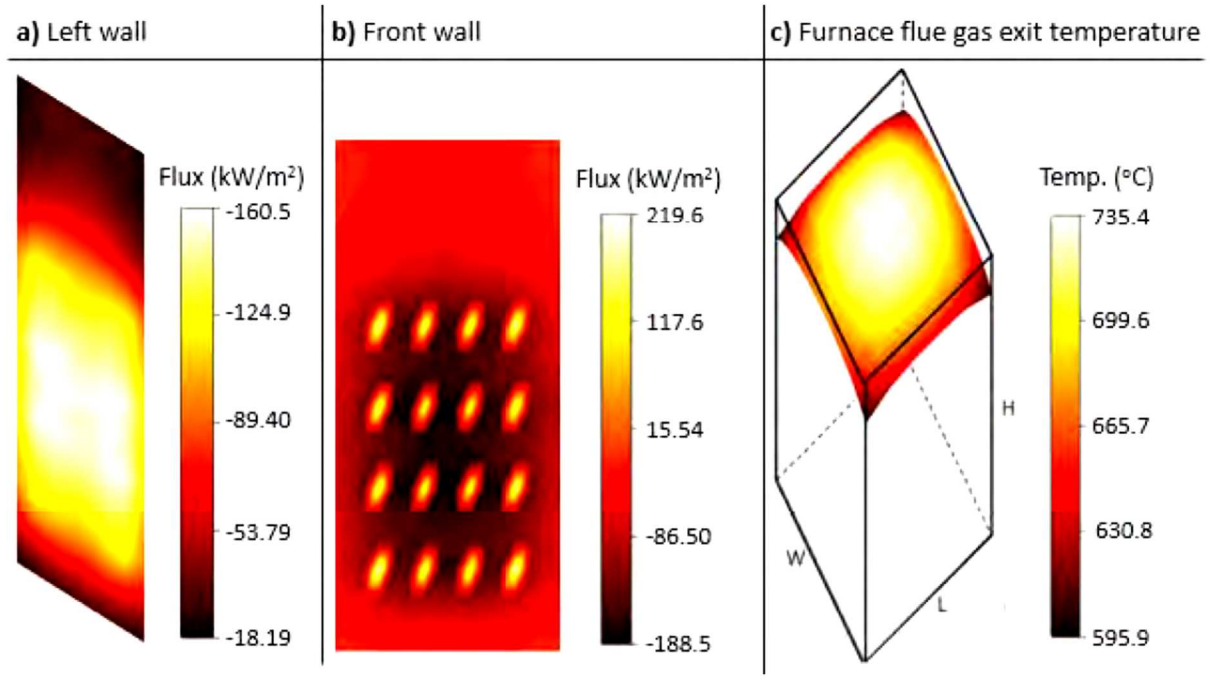

Figure 1-7: An example of a furnace exit gas temperature profile resulting from a wall-fired boiler. a) left wall flux, b) front wall flux and c) furnace exit gas temperature [11].

Since some of the heat exchangers in the convective pass are enclosed by the water walls and heat is also absorbed on these water-cooled walls, the temperature of the tubesheets near the side of the heat exchangers is lower than that of the inner tubesheets. Slagging on the furnace water walls and fouling on the heat exchangers in the convective pass also affect the temperature and flow distribution on the superheaters and reheaters. Fouling on the superheaters or reheaters is mostly experienced by the tube sheets in the middle of the heat exchanger, thus contributing to the creation of an M-type steam temperature profile on the outlet header. An example of such an M-type steam temperature profile is given in Figure 1-8.

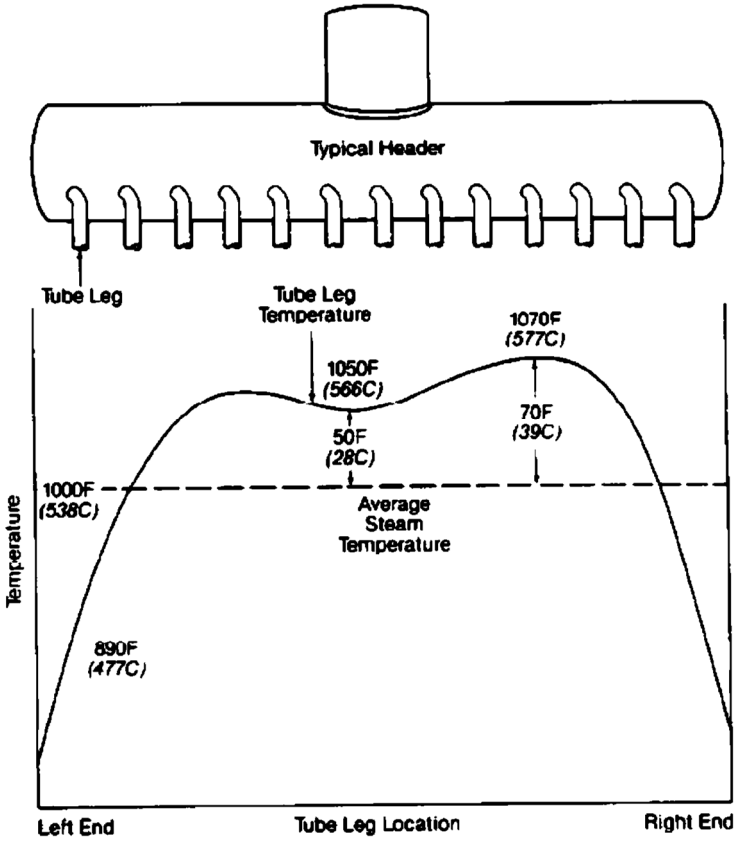

Figure 1-8: Steam temperature variation in a header [7].

In terms of the effect of boiler loads, Figure 1-9 demonstrates typical variations of tube leg temperature and average header temperature corresponding to load changes. For example, in the case of a load ramp up (from 0 to A) the boiler firing rate must increase to maintain the boiler pressure. In this period the boiler is temporarily over-fired to compensate for the effect of increased steam mass flow and boiler pressure drop. Therefore, during this period the boiler tube leg temperature will be higher than the average header temperature. This temperature difference on the header results in localized stresses which are much greater than those related to the steam pressure. The temperature differences also occur during ramp down. These stresses contribute to header crack initiation, especially along the bore hole penetration, which eventually lead to premature header failure [7].

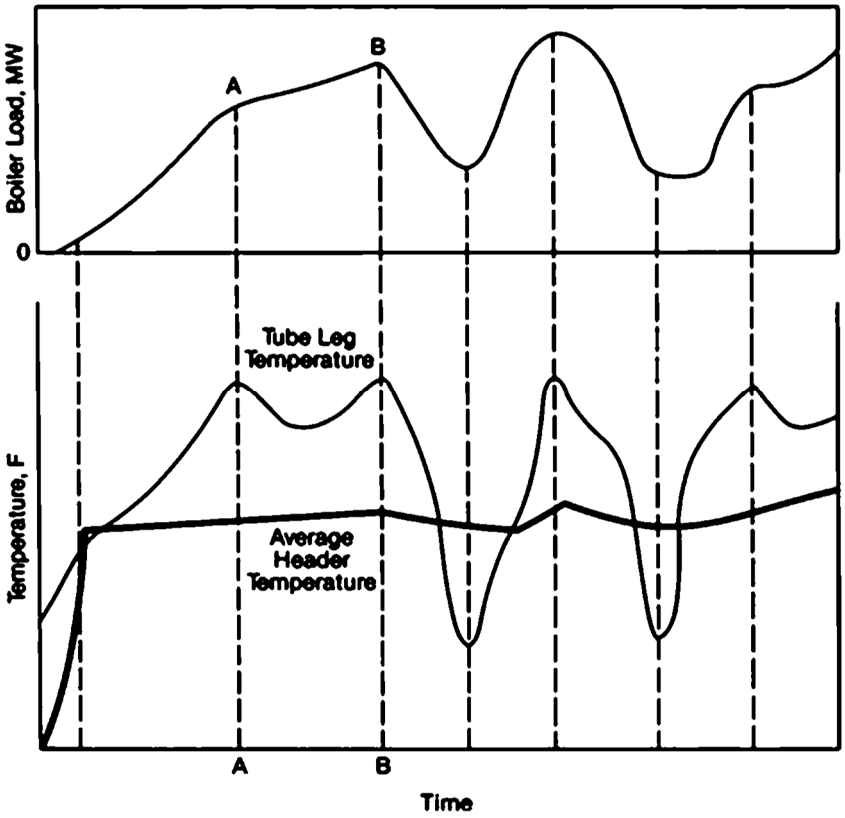

Figure 1-9: Superheater tube leg temperature variation with load [12].

There are some other quasi-steady state operational phenomena which can influence the lifetime of some components, which will be addressed below. In order to generate more power or less power from a unit of a coal fired power plant, the steam mass flow rate is increased or decreased, respectively as alluded to above. If slag builds up on the waterwalls of the combustion chamber, the furnace gas exit temperature increases. This implies that the heat exchangers downstream in the convective pass (superheaters, reheaters and economizer) might experience higher temperatures than they were designed for, hence an increase in the amount of heat absorbed. Thus, in order to maintain the designed outlet superheated steam temperature attemperation water has to be increased. If a heat exchanger in the convective pass is fouled, the amount of heat it absorbs drops thus more coal must be burnt to get the desired outlet steam temperature. Once the fouled heat exchanger has been cleaned using soot blowers, the heat it absorbs increases thus less coal must be burnt. All these factors that have an influence on the performance of the heat exchangers in the convective pass emphasise the importance of capturing the behaviour of these heat exchangers. This will help to improve the quality of control for the superheated steam temperature as well as to analyse the effect of such factors on the conditions of the tubes and headers of the heat exchanger.

1.1. Problem statement

From the discussion above it should be evident that in coal-fired power plants, final stage superheaters may experience severe conditions associated with high metal temperatures, high temperature gradients and cycling during transient operations. The outlet headers of the final superheaters are especially susceptible to these problems. Failure of such components results in an increase in maintenance costs for the plant. So, as a first step to determine how the operational conditions affect the life span of the components, a better understanding is required of the relationship between the operational conditions and the metal temperatures. For this, it is necessary to be able to model the thermofluid processes of final stage radiant superheaters in steady state and transient operations.

There is therefore a need for a thermofluid process model that can predict the flow and heat transfer of the steam inside the heat exchanger tubes and headers, the heat conduction through the tube and header walls, as well as the flue gas flow outside the tubes, in an integrated manner. The results should be provided in such a way that it facilitates the study of the resultant thermal stresses in the tube and header walls to better understand, predict and manage how the operational conditions affect the life span of the components.

The model should strike an appropriate balance between simplicity and accuracy so that it may be applied in real-life to gain an understanding of typical problems and to investigate the risks and impacts associated with intermittent operation, load following and variations in coal quality. This, together with appropriate and sufficiently accurate measurements of key parameters, could inform decision making for operating and maintenance strategies to improve component availability and reliability, and to reduce the cost of power produced.

1.2. Project hypothesis

The hypothesis of this research is that a network approach can be employed to construct integrated thermofluid process models of radiant superheater heat exchangers that provide results of outlet steam flows and temperatures that can be used as boundary values for Computational Fluid Dynamics (CFD) and Finite Element Method (FEM) analyses to determine the resultant stresses in headers. This will in turn serve to better understand, predict and manage how steady state and transient operational conditions affect the life span of these components.

1.3. Project objectives

The overall objective of this project is to develop a modelling methodology for radiant superheaters heat exchangers in steady state and transient operations. The methodology should integrate the thermofluid phenomena occurring in the superheater, which includes the fluid flow and heat transfer phenomena.

The enabling objectives of this work are:

- Develop a methodology to model the thermofluid processes of a heat exchanger in the convective pass of a coal-fired boiler.
- Apply the methodology in modelling a specific heat exchanger.
- Develop a methodology to validate the developed thermofluid process model.
- Verify and validate the developed heat exchanger model.
- Investigate the effect of operational anomalies on the tube metal and steam temperatures.
- Investigate the effect of operational anomalies on the flue gas and steam flow distribution.
- Investigate the effect of transients such as load changes on the tube metal and steam temperatures.

1.4. Project scope

The scope of this project is to develop a modelling methodology for radiant superheaters based on the one-dimensional network approach supported with high-level models to obtain input data for the heat exchanger models. These high-level models are applied to the other sub-systems of the boiler that are not of direct interest in the analyses, but still influences some of the conditions in the heat exchanger of interest.

The purpose of this study is not to produced three-dimensional computational fluid dynamics models of the superheater heat exchangers in coal fired boilers, or to determine the actual stresses in the headers.

1.5. Format of the report

Chapter 1 presented the problem statement, the project hypothesis and the objectives of the project.

Chapter 2 presents a review of literature associated with the modelling of heat exchangers, mainly in coal-fired boilers, for both steady state and transient operations.

In Chapter 3 the network modelling methodology is developed. Chapter 4 presents a demonstration case study, where the network methodology is applied to a convective primary superheater heat exchanger. The geometrical and performance data for this case study was obtained from the literature.

Chapter 5 explores the flue gas side modelling in more detail and considers some limitations associated with the one-dimensional network approach when modelling three dimensional phenomena.

Chapter 6 discusses further refinement of the modelling methodology, which is then applied to a radiant final superheater heat exchanger. The performance data for this case study was obtained from real plant measurements. The chapter also presents the high-level models needed for generating additional flue gas side input data to the radiant superheater model, as well as the validation of the modelling methodology based on plant design C-schedule data. Chapter 7 then presents the application case study of the refined model, where the real plant data is employed.

Chapter 8 concludes the report and presents some recommendations for future work.

2. LITERATURE REVIEW

This chapter presents a review of literature on the modelling of heat exchangers with a focus on heat exchangers in the convective pass of coal-fired boilers. The chapter begins by looking at simplified modelling methods which are mainly used to assess the overall performance of the heat exchanger. Two-dimensional (2-D) models which model one tubesheet/serpentine/element are then reviewed. Since a heat exchanger is a three-dimensional (3-D) system, some 3-D modelling methodologies and techniques are also reviewed. In addition, literature on the simulation of the dynamic behaviour of heat exchangers in coal fired boilers is reviewed. The chapter finishes with the review of literature dealing with the modelling of the flue gas side of the heat exchangers.

2.1. Lumped heat exchanger modelling

Thermo-fluid process models are often employed to determine the performance of a heat exchanger and sometimes also for online condition monitoring. In many instances the complete heat exchanger is lumped together and viewed as a generally counter-current flow, co-current flow, cross-flow or hybrid flow arrangement.

The most common simplified or lumped methodologies for modelling heat exchangers are the Logarithmic Mean Temperature Difference (LMTD) method and the effectiveness-number of transfer unit (NTU) method [13, 14]. For the LMTD method an experimentally determined correction factor is used to account for different types of heat exchangers or different flow arrangements. For the effectiveness-NTU method, different correlations are employed for the effectiveness-NTU relationship of different heat exchanger layouts. Kays and London [15] graphically presented the relationship between the NTU and the effectiveness for several different heat exchangers.

Diez et al. [16] highlighted the importance of lumped models for online calculations. Online calculations require simple models which are quick to run. They modified the conventional LMTD lumped model and integrated it with offline CFD predictions to improve the online modelling technique. The LMTD model was modified to account for direct radiation fluxes. Cantrell and Idem [17] employed the effectiveness-NTU method to the model the online performance of heat exchanger assemblies in a typical coal-fired boiler. The model calculated instantaneous heat transfer in different sections of the boiler to determine the local cleanliness factor. Information obtained from such models was used to make informed decisions on which section of the convective pass was to be cleaned.

There are limitations to these lumped models, especially if a detail analysis of the heat exchanger performance is required. They also cannot model with accuracy heat exchangers with complex flow arrangements. These models are usually not set up in such a way that the flow and temperature maldistribution amongst the tubes and within the headers can be identified. They also do not account for pressure drop and/or momentum conservation.

2.2. Single tubesheet modelling

In addressing the limitation of lumped models in capturing the geometry of a heat exchanger, more detailed models of one whole tubesheet of the heat exchanger may be developed. For these models the assumption is that there is no variation of flow and temperature amongst the different tubesheets along the width of the boiler.

Taler et al. [4] used mass and energy conservation equations to develop a one-dimensional (1-D) transient numerical heat transfer model for a dual-tube 12 pass primary superheater heat exchanger tubesheet of a 50-MW coal-fired utility boiler. The superheater tubesheet was discretised into a network of 1-D control volumes in the flow path connected such that they capture the complex flow arrangements as shown in Figure 2-1.

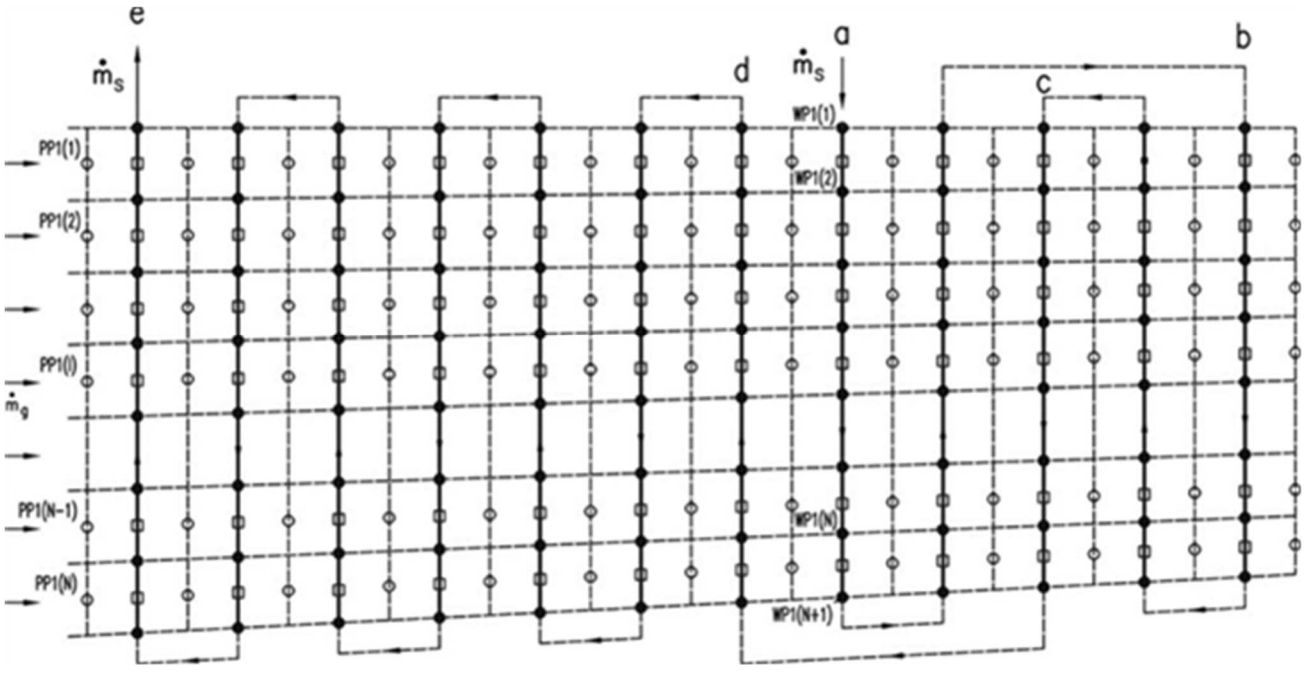

Figure 2-1: Heat exchanger flow arrangement and division into control volumes [4].

The flue gas side flow was assumed to be flowing in parallel flow channels, hence no mixing. For each pass the two tubes in parallel were lumped together and modelled as a single larger tube with equivalent

flow and heat transfer areas. The transient form of the 1-D partial differential equations for mass and energy conservation were employed for each control volume, including the heat transfer between the steam and flue gas streams. They employed a finite-volume method (FVM) to obtain the discretized equations and an explicit (forward) Euler method was then proposed for the temporal integration. The Gauss-Seidel method was used to iteratively solve the system of equations. However, they did not present results of transient analyses for this case.

The model used the convection heat transfer coefficient correlation given by Trojan and Taler [18] and Taler et al. [19]. Radiation heat transfer was accounted for through an effective heat transfer coefficient which was proposed by Taler and Taler [20]. This radiation heat transfer coefficient was then added to the convection heat transfer coefficient resulting in an equivalent heat transfer coefficient on the flue gas side. In the initial version of the model, momentum conservation was not taken into account. In an updated version of the model presented by Trojan and Taler [18] the pressure drops were also taken into account. The simplifying assumptions applied in the model by these authors are as follows: the steam and flue gas flow is 1-D; the flue gas flows in channels with no mixing; the physical properties of fluids are functions of temperature; axial conduction in tube wall is negligible; fluid conduction in the direction of flow is negligible; the flue gas and steam temperatures and the flue gas velocity are assumed to be uniform over the cross section at the inlet; and heat transfer coefficients on the inner and outer surfaces are uniform across the width of the heat exchanger [18].

The model of Taler et al. has the capability to account for scaling and an ash deposit layer of constant thickness. The ash deposit layer was accounted for separately, but the scaling layer can only be accounted for through a corrected internal heat transfer coefficient. Great care needs to be taken in accounting for the geometry on the inside of the tube if scaling is present. The model was verified against an analytical model of a one tube heat exchanger. It was then applied on a convective superheater of a coal-fired boiler, simulating the distribution of steam, tube wall, soot layer and flue gas temperatures on the different tubes in steady state for different scenarios. Their results were compared to real plant data for a single design case. They assumed a uniform thickness distribution of the ash fouling layer and to obtain good comparison with plant data they adjusted the fouling layer thickness in the model. This demonstrates one of the major difficulties in using real plant data for validation. The distribution and thickness of the fouling layer is not known and practically impossible to measure, and it changes continuously during operation.

Trojan and Taler [18] also investigated the effect of an uneven flue gas temperature distribution across the width of the superheater. This was done by modelling the one tubesheet that experienced the highest flue gas temperature and then comparing the results to that of a tubesheet from the case with uniform flue gas temperatures which was experiencing lower temperatures. In these models, the relationship between the steam mass flow and pressure drop was highlighted. In order to maintain the same pressure drop in both these models the steam mass flow rate in the case with higher flue gas temperature was reduced. This therefore approximates the effect of steam mass flow maldistribution. However, they did not connect all the different tubesheet models across the width of the header and include the integrated solution of the momentum conservation equations. Thus, the flow rate needs to be specified for each of the flow increments and the maldistribution in the flow cannot be predicted, either on the steam side or on the flue gas side. They also adjusted the fouling layer thermal resistance until they obtained a good comparison between the calculated and measured steam outlet temperature for steady state scenarios. They did not present any results of transient analysis.

Taler et al. [21] and Trojan et al. [22] combined the superheater model of Taler et al. [4] with an evaporator model to model the larger boiler for analysing the impact of ash and scaling. The model was applied as a boiler slagging and fouling simulator and was used successfully together with on-line measurements to guide soot blower operations for the combustion chamber and superheater heat exchangers in Skawina Power Plant in Poland.

The radiation heat transfer coefficient of Taler and Taler [20] was derived on the basis of a diffusivity model of radiation heat exchange. Their radiation heat transfer coefficient calculation method was compared to other methods using the commercial CFD package FLUENT 6.2 based on the Discrete Ordinates method and the Discrete Transfer Radiation Method. It showed good accuracy for a wide range of flue gas temperatures, making it suitable for both radiant type and convective type heat exchangers in the convective pass of a coal-fired boiler.

Trojan [23] modelled in detail the same superheater as that of Taler et al. [4] using the commercial CFD package, ANSYS-CFX. HyperMesh 11 was used to create the mesh for the CFD calculations. For verification purposes two meshes were used: a mesh of 7 809 105 elements and a slightly finer mesh of 8 490 342 elements. The $k-\varepsilon$ turbulence model was used to model the flue gas and steam flows. The model only focused on one tubesheet. Local and mean values of flue gas temperature after the primary superheater, tube wall temperatures and outlet steam temperatures were determined for both clean and fouled tubes. The outlet steam temperature results were verified against results from

the Taler et al. [4] model as well as validated against plant measurement data. The model clearly showed areas with the maximum tube wall temperatures. The comparison of the results from the two models with different meshes was satisfactory proving that the meshes was selected properly. Taler et al. [24] used the CFD superheater model of Trojan [23] to verify a numerical superheater model based on the energy conservation equation similar to the model of Taler et al. [4]. The heat exchanger overall performance results of the two models compared well.

Coelho [25] presented the theory of a 2-D mathematical model for simulating flow and heat transfer in the convection chamber of a utility boiler in steady state. The flow field simulation was based on the mass and momentum conservation equations in conjunction with the CFD porous media approach to account for tube bundles and control dampers. The $k-\varepsilon$ eddy viscosity/diffusivity model was employed to cater for turbulence. The pressure drop of the cross flow through the tube bundles was estimated using the correlation of Zukauskas [26]. Energy balances were performed along the tubes to account for convective heat transfer and fouling resistance on both sides of the tube, as well as radiation on the gas side. A highly simplified zonal method presented by Coelho [27] was used to incorporate radiation heat transfer. The flow and heat transfer are iteratively coupled by the solution algorithm.

The simplified formulation for calculating radiative heat transfer based on the zonal method presented by Coelho [27] conceptually divided the convection chamber into cavities and heat exchangers. Fictitious planes were placed immediately upstream and downstream of every heat exchanger as shown in Figure 2-2. A cavity was defined as a region in the convective pass not occupied by heat exchangers and enclosed by fictitious planes and the walls of the boiler. In the general formulation, the following simplifying assumptions were adopted: neglecting scattering; gray medium; uniform chemical composition of the gas; uniform temperature and emissivity of the walls bounding a cavity or heat exchanger; as well as uniform gas temperature within a cavity. Instead of calculating the direct exchange areas, a simplified formulation was derived through assuming that the tubes were infinitely long, ignoring the wall bounding a heat exchanger and using the average mean beam lengths to perform the radiative calculations.

Coelho [28] applied the mathematical model on the convective pass of an oil-fired 250 MWe power station. The computational domain consisted of a chain of heat exchangers, namely the final superheater, primary superheater, reheater and economiser. The predicted gas temperatures at a few access ports and the exit water/steam temperatures of each heat exchanger were presented. The steam temperatures were compared to experimental data and good agreement was obtained. The model was

further used to perform a sensitivity study to investigate the influence of some input variables which included the inlet conditions, the angle of the plates of the control dampers and the fouling resistances.

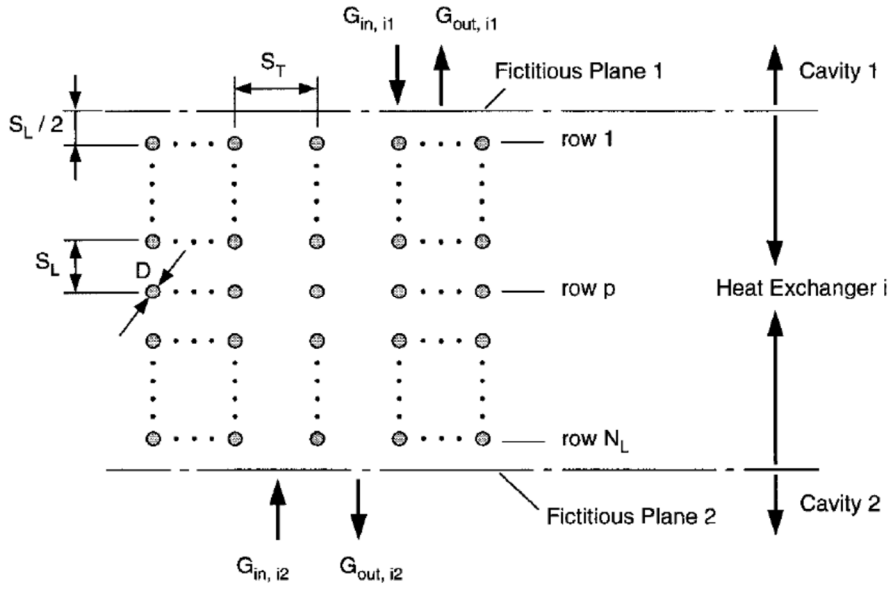

Figure 2-2: A schematic of a heat exchanger with the fictitious planes for the computation of radiation heat transfer [25].

Xu et al. [29] developed a single tube model for evaluating the wall temperature profiles of superheater and reheater tubes in power plants. The model uses the FVM to discretise the 2-D heat conduction equation. They ignored circumferential heat conduction in the tube wall. In addition, the change of diameter and material of one tube was ignored. Empirical correlations were used to account for heat transfer on both the flue gas and steam side. Radiation heat transfer on the flue gas side was accounted for through an effective heat transfer coefficient. Momentum and mass conservation equations were not solved on either of the two streams. They investigated the effect of inner fouling, steam temperature distribution and gas temperature distribution on the tube wall temperature.

2.3. Complete heat exchanger modelling

Developing a complete model of a heat exchanger in the convective pass of a boiler enables the simulation of maldistribution of flow and temperature on the outlet headers of these heat exchangers. With certain models the so called “M-type” outlet steam temperature profile can be modelled. Such complete heat exchanger models have to capture the 3-D phenomena present in the heat exchanger.

Prieto et al. [30] developed a steady state 3-D numerical model for simulating flow and heat transfer in a reheater of a utility boiler. The model was developed in the commercial CFD software code

PHOENICS V3.1. The porosity concept was employed to model the tube bundles. In addition, turbulence was accounted for. On the gas side the model solved the conservation equations of mass, momentum and energy. However, on the tube side only the energy equation was solved. Thus, steam velocity was derived from the specified mass flow rates and the geometry of the serpentines. They employed empirical correlations to incorporate convection and radiation heat transfer. The outside heat transfer coefficient accounts for both convection and radiation heat transfer. The model was developed such that it can use measured values of velocity, temperatures and gas composition in the reheater as inlet/outlet boundary conditions. The focus of the model was on the characterisation of the thermal behaviour of tube serpentines (tubesheets).

In an accompanying paper, Prieto et al. [31] presented the application of the model to investigate the maldistribution of flow and temperature across the width of the reheater. At first the model was run with an assumption of uniform steam mass flow rate in all the tubes. When the temperature results at the outlet of each serpentine were compared to experimental data the distribution was different as shown in Figure 2-3. This clearly showed that the assumption of a uniform steam mass flow distribution was not valid. In order to obtain a temperature distribution from the model that compares well with the experimental results, as shown in Figure 2-4, the model had to be re-run with different steam mass flow rates in each serpentine. This is one of the limitations of a model based on a commercial CFD code because in order for it to solve, the velocity or mass flow has to be specified. Thus, the mass flow distribution must be known beforehand to be able to produce a realistic temperature distribution.

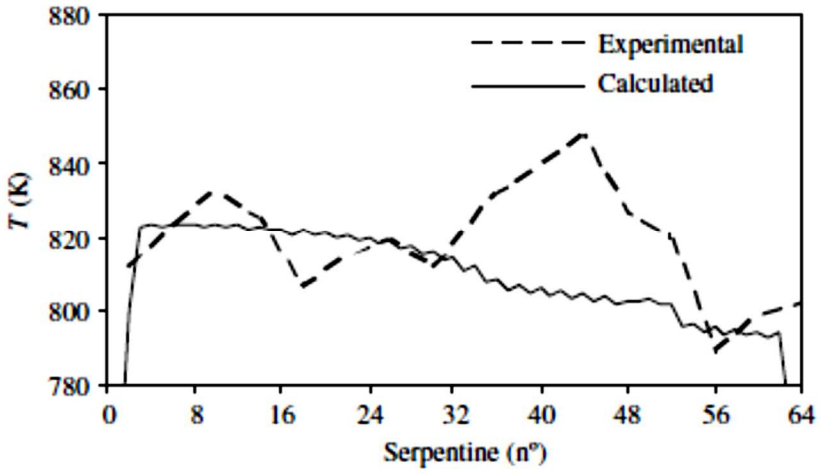

Figure 2-3: A comparison between calculated and experimental temperature results from each serpentine at the outlet of the reheater for a uniform steam mass flow rate assumption on the model [31].

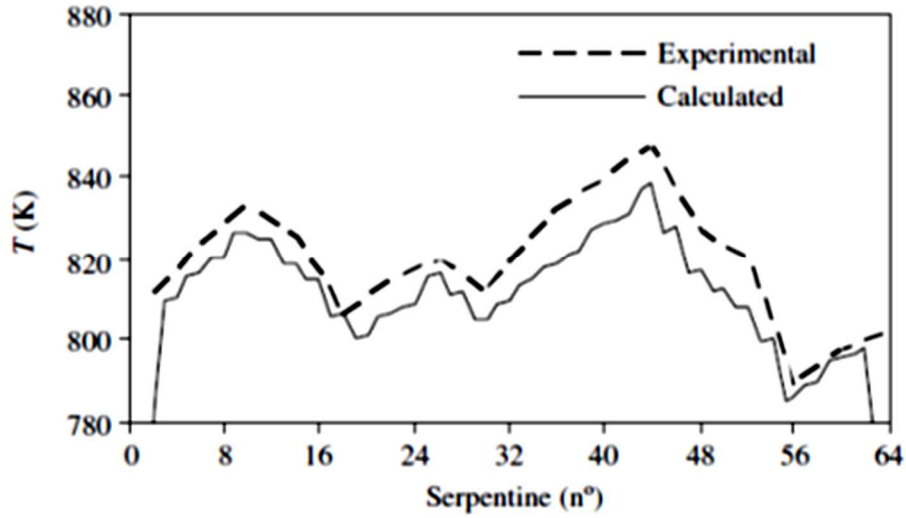

Figure 2-4: A comparison between calculated and experimental temperature results from each serpentine at the outlet of the reheater for a non-uniform steam mass flow rate assumption on the model [31].

Gonzalez et al. [32] did experimental work on the same reheater to determine the causes of the temperature maldistribution. They investigated the effect of load changes, orientation of burners and the activation of burners. Their results demonstrated that the outlet temperature for reheater tubes decreases with decrease in load as shown in Figure 2-5. However, the temperature maldistribution across the width of the reheater still persisted even under low loads. Likewise, variations in the burner configuration did not change the temperature maldistribution at the outlet of the reheater.

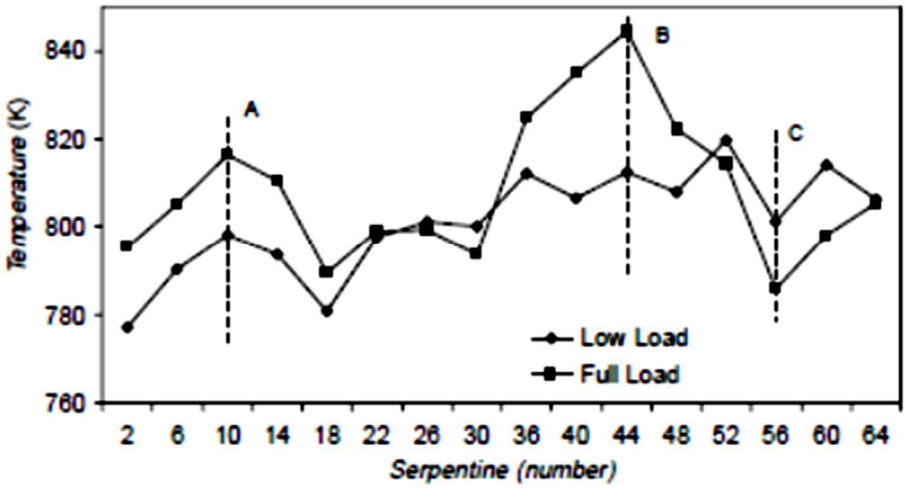

Figure 2-5: Variation of temperature profile with load [32].

Gomez et al. [33] developed a mathematical model on PHOENICS V2.2 that can be used to simulate the fluid flow and heat transfer in the convective pass of a power station boiler. The model allowed the integration of the simulation of the shell side, tube side and the metal thermal fields. On the gas side

the model solved the continuity, momentum and enthalpy conservation equations. The tubes were represented as sub-grid features based on the distributed resistance concept developed by Patankar and Spalding [34]. On the tube side, only the energy conservation equation was solved. Steam mass flow was calculated locally using geometrical calculations. The model was verified for two distinct aspects. Firstly, it was checked whether the geometrical features of the model such as connectivity options and the conservation of the overall tube-side mass flow were working correctly. Secondly, the model was verified against analytical models for geometrically simple configurations (i.e. single pass cross flow heat exchanger configuration). These simple configurations were analysed using the LMTD or the effectiveness-NTU method. The comparison of the predicted overall heat transfer rates was satisfactory.

The model was then applied on the convective chamber of a 350MWe power station boiler, beginning at the furnace exit where uniform temperatures and velocity profiles were assumed. In this model, the tube side heat transfer resistances were neglected. For the gas side, the semi-empirical approach proposed by Cortes et al. [35] was used. This semi-empirical approach is a formulation of lumped models coupled with energy balances in a section by section analysis. For the model results, on the gas side 2-D flow fields and temperature contours for two different load cases were shown. For the corresponding load cases, the tube side temperatures were also shown. Despite plant measurements being available for the safe operation and control of the utility boiler, it was discovered that such information was neither complete nor reliable enough to validate a thermofluid process model. Thus, a plan to improve and extend the instruments and measurement procedure was designed and implemented as detailed by Diez et al. [36]. Heat transferred and outlet steam temperatures at different load cases for each heat exchanger in the convective pass compared well to the gathered plant data.

The rationale of the measurement procedure of Diez et al. [36] was to improve the quality and reliability of experimental data obtained from large utility boilers for validating thermofluid models. This is done because there are limitations associated with laboratory scale methods, since the physical processes involved in a coal-fired boiler are not necessarily scalable. Building pilot demonstration plants is also not an option due to very high investment and maintenance costs. Thus, the only way to get experimental validation data is to obtain measurements from the full-scale utility boiler itself. The limitation of this approach is that data acquired under industrial operation conditions in large boilers lack the quality and completeness provided by laboratory data. Thus, a methodology to improve that was devised. The methodology involves the examination of the reliability of the existing process data, and the design of new instruments and measurement procedures to gather additional information which

might supplement or improve the quality of the available data. For some aspects of data acquisition which may prove difficult to measure such as the gas flow, simple Mass and Energy Balances (MEB) were recommended.

Xu et al. [37] developed a thermal load deviation model to simulate the temperature maldistribution at the outlet of superheaters and reheaters across the width of a utility boiler. The model was based on the power plant in situ thermodynamics parameters, thermal deviation theory and flow rate deviation theory. The thermal deviation model is obtained by an iterative procedure based on three parts; the structural deviation model, the flow rate deviation model and the thermal deviation model. The structural deviation describes the geometry of the superheater or reheater. The flow rate deviation model simulates the flow rates and the heat absorbed by each tube in the heat exchanger. The thermal deviation model accounts for heat absorbed on the outer surfaces of the tubes. Thus, this model mainly focuses on energy balance and flow analysis. It does not solve the momentum and continuity equations on both streams. The calculated results of this model compared well with experimental data.

Tilton and Ratnam [38] developed a 1-D modelling methodology based on the network paradigm for simulating and predicting the performance of the tube-side of the heat exchangers in the convective pass. In this methodology the tube banks are subdivided into a number of modules. For each module, a set of equations consisting of mass, pressure and energy balances were derived, which were then solved using a sparse matrix method. Their model was not validated against real plant data.

2.4. Transients

Mathematical models that can capture the dynamic behaviour of heat exchangers can range from lumped analytical models to custom developed numerical models as well as software based numerical models. In broad terms these models are sometimes referred to as lumped-parameter and distributed-parameter models. The details captured by a dynamic model depends on the purpose of the model as highlighted in the earlier sections of this chapter. Most of the dynamic models that were developed in the early 1950s were focused on the steam outlet temperatures for process control purposes.

Paynter and Takahashi [39] developed a modelling method based on statistical principles to approximate exact solutions for evaluating the dynamic response of counter-flow and parallel flow heat exchangers. Gvozdenac [40, 41] developed transient response analytical models for gas-to-gas parallel flow, counter flow and cross flow heat exchangers. The model solution was based on the Laplace transform method and the modified Bessel functions. Temperature distribution results for both the fluids and the wall were shown. Yin and Jensen [42] also developed an analytical model to simulate

the transient response of a heat exchanger in which one fluid is single phase and the other has a constant temperature. In their model, the dynamic behaviour of the heat exchanger is approximated by an integral method assuming that the single-phase fluid and wall temperature distribution can be expressed by a combination of known initial and final temperature distributions and a time function.

Enns [43] developed and compared dynamic models of a superheater of a boiler in a steam power plant. Some of the developed models were based on the lumped-parameter approach and others based on the distributed-parameter approach. For all the models, steam outlet temperature was of interest. Also, they did not solve instantaneous flow output, pressure drop and tube temperature. In addition, all the models assumed that heat addition to the tubes was independent of the tube temperature.

Kang et al. [44] developed a nonlinear lumped-parameter dynamic model of a power plant boiler superheater. Their model had high precision and low computational complexity which implied that it can simulate operating conditions when large disturbances such as large load changes occur as well as can satisfy the requirements for control system design. The model consisted of three parts which are the pressure-flowrate channel model, the enthalpy-temperature channel model and the steam thermodynamics parameter model. The model was applied on a final superheater of a 600MW boiler including its attemperation stage. The superheater was simplified to a one tube representation. Reasonable dynamic results of steam pressure and temperature were observed upon imposed disturbances.

Zima [45] developed a numerical solution of transient flow in parallel and counter flow superheaters. The numerical solution entailed iteratively solving the heat transfer equations from an energy balance on the control volumes of the superheater based on the implicit finite difference method. These equations were then solved using the method of lines coupled with Gear's method. Time and space temperature distribution for the flue gas, tube metal and steam were determined. This numerical solution was compared to a mathematical model which solved the 1-D transient forms of the conservation equations of mass, momentum and energy on the steam side. For this mathematical model the flue gas and steam temperatures were calculated by solving the energy balances over control volumes as with the first model. Again, in this model, the iterative implicit finite difference method was employed except that the momentum equation was solved on a staggered grid. The comparison between the results of these two models was satisfactory.

Zima [46] then applied the mathematical model that solves the 1-D conservation equations of mass, momentum and energy on the steam side on superheaters of a coal fired boiler. Each superheater was

modelled as a 1-D counter-flow heat exchanger. This simplification was achieved through assuming that the conditions in each tube element along the length of the header do not vary leading to a 2-D superheater. This 2-D superheater was then approximated using the 1-D model. The results of this model were compared to experimental data obtained from the boiler during acceptance tests, start-up and shutdown. The comparison was satisfactory and hence validated the model.

Zima [47, 48] applied the mathematical model that only solves the energy conservation equation and neglects the mass and momentum conservation equations on the platen superheater and economizer of a coal-fired boiler. For the platen superheater outlet steam temperature results compared well with plant data during a shutdown. Also, the economizer feed water temperature results compared well with plant data from acceptance tests. This model is important in the aspect of digital temperature control of the outlet steam temperature because it is quick to solve. In addition, Zima [48] successfully compared the model with analytical solutions for a tube with the temperature step function of the fluid at the tube inlet and for a case with the heat flux a step function on the outer surface.

Although the models of Zima are applicable for digital outlet steam temperature control, the simplifications of heat exchangers with complex geometry to a counter flow or parallel flow limits the capability of the model to assess damage caused by the transients on a specific tube or region.

Gwebu [49] and Gwebu et al. [50] investigated the possibility of modelling the dynamic behaviour of a boiler heat exchanger using an integrated thermo-fluid process modelling software Flownex. The emphasis of the work was placed on modelling the dynamic behaviour of a tube since by mass a boiler heat exchanger consists of more tubes than headers. Thus, most of the dynamic behaviour comes from the tubes. The focus was on radial heat transfer on the thickness of the tube, thus solving the 1-D heat conduction equation. In the investigation analytical solutions based on the Bessel function were used to verify a custom developed numerical solution based on the FVM. The verified numerical solution was then used to verify the software Flownex. Flownex allows the use of time depended boundary conditions on either side of the tube thickness. The modelling strategy systematically showed the limitations of each method, beginning with the analytical solution and then the custom developed numerical solution. However, limited transient cases were studied using Flownex to fully demonstrate its ability to capture transients of fluids flowing on each side of the tube as well as the propagation of those transients through the tube thickness.

2.5. Flue gas side flow modelling

In a typical coal-fired boiler's convective pass heat exchanger, the flue gas flow is complex due to the presence of numerous tubes in the path of the flow. These densely populated tubes increase the resistance to the flow. The arrangement of these tubes in the heat exchanger influences the extent of mixing of the flue gas within the heat exchanger.

In this section, a review of literature on modelling the flue gas pass in boiler heat exchanger or the shell side of a shell and tube heat exchanger is presented. The literature is systematically presented in accordance with the timeline of the development of the tools used. It begins by analysing the application of conventional Computational Fluid Dynamics (CFD); the application of the full Navier-Stokes equations and its limitations. The limitations of the conventional CFD are then addressed by adapting the full Navier-Stokes equations through the CFD porous media approach. The porous media approach is founded upon the distributed resistance concept. For further advantages, this distributed resistance concept is adapted into a 1-D network approach, which is used to model two-dimensional and three-dimensional phenomena.

2.5.1. Conventional Computational Fluid Dynamics (CFD)

According to Runchal [51], the origins of Computational Fluid Dynamics can be traced as far back as the 1928's or even earlier. Back then, many researchers developed concepts to what eventually became CFD. Despite being around for a couple of decades before, the wide availability and accessibility of digital computers as a tool in the early 1960's assisted in the development of CFD. In addition, the work done by a team led by Professor Brian Spalding at Imperial College in London on the Navier-Stokes equations and computer codes also contributed immensely in the development of CFD. In 1969, they published their work in a book [52] which promoted the use of CFD as an engineering tool. This led to this team being credited for creating CFD as an engineering tool, since they applied CFD in solving engineering problems [51, 53]. Furthermore, their work significantly contributed to the development of most of the commercially CFD software packages available today.

Spalding's team reinvented the upwind concept which fostered the thinking in terms of fluxes rather than the state of variables at a given grid point [54]. This followed the work of Barakat and Clark [55] and Gentry et al. [56]. However, the upwind concept was first put forward by Courant et al. [57]. This concept gave rise to the tank-and-tube analogy where a node (control volume) is viewed as a tank

exchanging fluxes with adjacent tanks via tubes (grid). This led to the development of the Finite Volume concept which is widely applied today.

Due to the tremendous improvement in computational power over the years, researchers continued to improve CFD and its applications. It is applied across a wide variety of industrial sectors including aerospace, defence, automotive, medical, chemical, manufacturing and processing, environmental, fire and safety, marine, nuclear power and fossil-fuel power industries [53].

Since computers of the 1960's were not computationally powerful, novelty in generating concepts to simplify modelling of certain industrial equipment was key. This equipment included the shell and tube heat exchanger used mostly in the nuclear and fossil fuel power industry. Since the shell and tube heat exchanger has a complex geometry including a complex arrangement of tubes and baffles, it would have been computationally expensive to model it through conventional CFD over the whole 3-D computational domain. Conventional CFD refers to solving the full Navier - Stokes equations. Thus, other concepts were developed as alternatives to model such equipment. These concepts included the Subchannel Analysis and the Distributed Resistance concept (porous media) [58, 59, 60].

The subchannel analysis is suitable to model flows around obstacles that form a regular pattern such as a tube bank in a heat exchanger or a rod bundle in nuclear fuel elements. In this analysis, the space in between a cluster of three or four tubes is referred to as a subchannel. In a computational domain, one grid is equivalent to one subchannel [59]. The foundation of the method is that it explicitly assumes that one of the velocity components (e.g. axial direction) in a certain direction is dominant compared to the other velocity components (e.g. cross flow) [58, 60]. Thus, only the dominant direction is rigorously solved, hence the only computationally expensive direction. Originally, the subchannel analysis was intended for design calculations. However, it has since been used extensively in the nuclear industry, especially for reactor safety analysis such as modelling flow blockage in the fuel assembly, as seen in references [61, 62, 63].

The subchannel method can also be used to characterise pressure drops for certain tube arrangements, thus getting resistance correlations for the distributed resistance method in cases where empirical correlations do not exist. The distributed resistance method entails less details than the subchannel analysis since it combines the porosity concept and the distributed resistance concept, thus allowing for a courser computational grid. It is addressed in detail in the next subsection.

2.5.2. CFD porous media approach: The porosity and distributed resistance concept

The distributed resistance method, just like the subchannel analysis, is an alternative method to modelling engineering equipment which often have solid obstacles such as rods, tubes and baffles through which the fluid flows. This equipment include heat exchangers, condensers, cooling towers, steam generators, nuclear fuel rod-bundle and chemical reactors.

One of the advantages of the distributed resistance method over the subchannel analysis is its economy on computer solving time and storage. This is because the distributed resistance method is based on the "continuum" approach, implying that its computational domain does not depend on the geometry of the obstacles in the equipment. The effect of the obstacle geometry is introduced through the porosity to account for variation in volume and the distributed resistance factor to account for resistance to fluid flow as well as the heat transfer to or from the fluid [64]. In essence, the flow through the equipment is treated as fluid flowing through a porous media, thus this method is also called the CFD porous media approach. This method was developed and published in 1974 by Patankar and Spalding [34]. The development and further use of the distributed resistance method is traced below.

In 1974, Patankar and Spalding [34] developed the distributed resistance concept to solve the differential equations that govern the flow of a continuous fluid. They initiated the use of this concept to model shell and tube heat exchangers. This approach regards the space within the shell as uniformly filled with fluid, through which a resistance to fluid motion is distributed on a fine scale. This resistance is due to the presence of tubes and baffles in the shell. Mathematically, this resistance is introduced in the governing equations by introducing a representative factor. They showed the governing equations in Cartesian coordinate system. An advantage of this approach is that it allows the use of a coarse grid which saves computer solving time and storage. In the paper, they presented simulation results for both steady state and transient regimes. However, no attempts were made to compare their results to experimental data.

AbuRomia et al. [65] applied the distributed resistance method in their detailed model to obtain the flow distribution on the shell side of the Clinch River Breeder Reactor Plant Intermediate Heat Exchangers. In the study, they used a lumped and a detailed model to analyse the axial/cross flow on the shell side of the heat exchangers. The lumped model utilized an overall pressure drop and flow distribution approach to determine the magnitude of the axial and cross flow components as a function of the baffle configurations. The detailed model used a fundamental approach in numerically solving the governing equations of fluid mechanics on a turbulent flowing fluid over a discretised

computational domain. The distributed resistance concept was applied to the momentum equation to account for the presence of the tube bundles and baffles. This detailed model resulted in a complete map of the fluid and pressure distribution within the tube bundle. It was concluded that the radial distribution of the cross flow can only be accurately obtained using the detailed model. This radial distribution is the mechanism responsible for fluid mixing in the tube bundle.

Patankar and Spalding [64] applied the distributed resistance method to model the three-dimensional flow and heat transfer in a steam generator. They employed the method using equations based on the cylindrical coordinate system. The porosity was explicitly included in the equations to account for the presence of the tubes in the nominal volume. They successfully calculated and plotted the three-dimensional velocity and enthalpy fields. Their results were not validated against experimental data, thus they recommended it for future research. The recommended future research also included work on empirical correlations for the distributed resistance factor.

Butterworth [66] used equations for analysing flow for anisotropic porous media to show how pressure drop data for one-dimensional flow in tube bundles may be generalised in order to provide a framework for analysing real flow problems which are often multidimensional in nature. The equations use a flow resistance tensor which accounts for flow resistance or permeability. For turbulence encountered in most tube-bundles the tensor components depend on the magnitude and direction of the superficial velocity vector. However, a simplifying assumption was made such that the tensors depend only on the magnitude of the velocity and not the direction. This resulted in isotropic flow properties for planes perpendicular to tubes arranged in square and equilateral triangle arrays. Thus, implying that the pressure drop for flow in one direction can be predicted using data from the flow in another direction. This was shown to be reasonable by comparing to experimental data.

Singhal and Spalding [67] presented the URSULA2 computer program for modelling multi-phase flow and heat transfer in steam generators. The mathematical formulation of the program was based on the Inter-Phase Slip Analyser algorithm and the distributed resistance concept, described in reference [64]. Spalding [68] presented the mathematical formulation of the fundamental governing equations of fluid flow used in the URSULA2 program. These equations incorporated the porosity and distributed resistance and were written in cylindrical-polar coordinates. The diffusion or turbulent mixing terms were neglected in the momentum conservation equation. The porosity or void fraction was calculated from the fluid density and the resident enthalpy. Empirical correlations were used to account for the resistances including the solid to fluid resistances.

Marchand et al. [69] used the URSULA2 computer program to perform two-phase, transient, three-dimensional flow and heat transfer calculations for the thermal-hydraulic performance of a steam generator. The transient was due to a power ramp from 100 to 60 percent. They were satisfied with the trends of the results; however, they did not quantitatively verify these results with experimental data. Singhal et al. [70] also applied the URSULA2 computer program to predict the thermo-hydraulic performance of a PWR steam generator using three different models; the homogeneous, the two-fluid and the algebraic-slip models. The predictions of the three different models showed significant differences especially on the circulation ratio and the flow details on the hot side of the steam generator. However, the URSULA2 program was not validated with experimental data thus its results were interpreted with caution.

Sha [60] highlighted the distributed resistance method in conjunction with porosity. This was presented in a summary of methods that can be used in rod-bundle thermal-hydraulic analysis together with the subchannel analyses and the benchmark rod-bundle thermal analysis using a body fitted coordinate system. The differences between the methods and the assumptions employed and shortcomings of each methods were clearly shown. It was concluded that the distributed resistance method eliminates the limitations of the subchannel analysis in modelling large flow disturbances. Furthermore, the distributed resistance method is applicable to a wide variety of geometries compared to the subchannel analysis. Thus, it presents a most cost-effective way of developing a computer code.

Sha et al. [71] developed a multidimensional thermal hydraulic computer code to analyse heat exchangers. The analysed heat exchangers were the shell and tube heat exchangers for liquid metal services e.g. Liquid Metal Fast Breeder Reactor intermediate heat exchangers and steam generators. The concept of distributed resistance, volumetric porosity and surface permeability were used on the shell side to modify the continuum Navier-Stokes equation to cater for the effect introduced by the presence of obstacles such as tubes and baffles. In essence, this modelled the flow in anisotropic porous media. The code was tested using experimental data. The comparison between experimental predictions and the model predictions were satisfactory.

Srikantiah and Singhal [72] presented a computer program called ATHOS which was developed for design and performance analysis of steam generators in the nuclear power industry. This program can model the geometry and internal structure including the tube bundle, tube support plates and baffles of the steam generator in considerable details. Due to symmetry, only one half of the steam generator was modelled. The porosity concept and distributed resistance concept were applied on the secondary side.

In addition, on the secondary side diffusion and turbulence were assumed to be negligible as well as the dissipation and spatial component of the pressure work in the energy equation. The final flow field for steady state simulations were plotted successfully.

Hu [73] used the distributed resistance approach to model tube bundle flow during a steam generator wet layup. The model used the concept of anisotropic porous media flow within the Darcy regime to predict the flow pattern of the tube bundle flow. The distributed resistance (fluid continuum) approach for porous media was established by introducing porosity which is the ratio of the fluid volume to the total volume. In general, a continuum approach is valid when a representative elementary volume is large enough to give a continuous statistical average of the fluid property and is small enough so that it may be considered as a material point in space [74].

In 1984, Patankar [59] established that the general heat transfer community did not sufficiently understand the computational activities associated with the distributed resistance concept when applied on the shell side flow in heat exchangers. Thus, he wrote a paper providing a review of the basic concepts associated with this type of analyses together with some illustrative examples. He explained that the shell side space is regarded as continuum which is under the action of distributed resistance due to the presence of obstacles such as tubes. In essence, the shell side flow is treated as a flow through a porous material. The presence of obstacles in the flow is accounted for via the porosity and the resistance formulas. The resistance formulas can be determined using empirical correlations.

Rhodes and Carlucci [75] presented a comparison between numerical predictions using the porous media concept, and measurements of the two-dimensional isothermal shell-side velocity distributions in a model heat exchanger. The computations and measurements were done with and without tubes present in the model to assess the efficacy of the porous media theory. The porosity, which accounts for flow volume reduction due to the tube bundle, was assumed to be locally isotropic. Their study demonstrated feasibility and validity of the porous media approach in modelling the fluid flow over obstacles. It also highlighted a discrepancy between the measured and predicted results from modelling the tube-to-baffle leakage flow. However, it was concluded that the discrepancy might have been due to the method used to estimate the leak rate from the velocity measurements.

Theodossiou et al. [76] performed a numerical study on the shell side of an experimental heat exchanger with an isothermal, steady flow distribution and incompressible fluid. The numerical study was two dimensional. The computations were done for both cases with or without tubes in the model, for Reynolds numbers less than 10 000. The distributed resistance concept was used to account for the

presence of tubes and baffles in the model. The resulting equations from the distributed resistance concept were solved using a semi-implicit predictor type scheme. The computations were run using different meshes in order to validate the code. For further validation of the distributed resistance concept, the numerical results were compared to experimental data. This comparison produced a good qualitative agreement.

Karayannis and Markatos [77] applied the distributed resistance method encapsulated in the program HERCULES to rate shell and tube heat exchangers. The HERCULES program ran under the PHOENICS CFD software package. They recommended the use of the CFD based approach to model the shell side flow field over the traditional methods which had simplifications. These simplifications included the assumptions made for mechanical design (leakages & bypass flows), thermal process (viscosity & density changes), fouling and corrosion amongst others.

Prithiviraj and Andrews [78] developed a three-dimensional, conservative, fully implicit, collocated control volume-based calculation technique for simulation of flow, heat transfer and turbulence on the shell side of shell and tube heat exchangers. This computer code, called HEATX was based on the distributed resistance method and the $k-\varepsilon$ turbulent model. Wall functions of Launder and Spalding [79] were used to compute momentum and heat transfer coefficients close to plane surface walls. HEATX also employed the volume porosities and non-homogeneous surface permeabilities to account for the presence of obstructions such as tubes and baffles in the computational domain. To account for distributed resistance across tubes in cross flow, pressure drop empirical correlations from Zukauskas [26] were used. In addition, to account for tubes in an axial flow, pressure drop correlations of Rehme [80] were used. HEATX was validated against standard benchmarks such as the driven cavity, backward facing step and sudden pipe expansion.

Prithiviraj and Andrews [81] presented the foundation and fluid mechanics behind the HEATX computer code. Equations governing fluid flow, heat transfer and turbulence were shown including the empirical correlations used to account for distributed resistance due to the presence of tubes and baffles. The code was employed to model an E shell type heat exchanger. The results agreed with experimental data. Prithiviraj and Andrews [82] presented the heat transfer part of the HEATX computer code. The shell side is coupled with the tube side of the heat exchanger. HEATX was employed to simulate a shell and tube heat exchanger. Both pressure drop and temperature difference results agreed well with experimental data.

Hueng et al. [83] used the distributed resistance method incorporated in the PHOENICS CFD software package through subroutines to model a shell and tube heat exchanger. Their main objectives were to investigate the effect of different turbulence models on the velocity field and the heat transfer coefficient as well as perform design optimisation calculations on the heat exchanger. Four different turbulence models were used; the constant turbulent viscosity model, the $k-\varepsilon$ turbulence model, the Chen – Kim $k-\varepsilon$ turbulence model and the $k-\varepsilon$ and constant turbulent viscosity model. They found that the effect of different turbulence models on the velocity distribution and heat transfer was insignificant. Thus, implying that a simple turbulence model could be used without compromising the accuracy of results. In the design optimisation of baffles in the heat exchanger, they reported that the optimum size of the baffle is about 70% of the height of the heat exchanger. This optimum size had a higher heat transfer rate and relatively lower pressure drop.

Coelho [25] presented the theory of a two-dimensional mathematical model for simulating flow and heat transfer in the convective pass of a utility boiler in steady state. The flow field simulation was based on the mass and momentum equations in conjunction with the distributed resistance concept and porosity to account for tube bundles and control dampers. The $k-\varepsilon$ eddy viscosity/diffusivity model was employed to cater for turbulence. The pressure drop of the cross flow through the tube bundles was estimated using the correlation of Zukauskas [26]. Energy balances were performed along the tubes to account for convective heat transfer and fouling resistance on both sides of the tube, as well as radiation on the gas side. The flow and heat transfer are iteratively coupled by the solution algorithm. Coelho [28] applied the mathematical model on the convection chamber of an oil-fired 250 MWe power station. The computational domain consisted of a chain of heat exchangers, namely; the final superheater, primary superheater, reheater and economiser. The results of predicted 2D velocity field were presented, however these results were not compared to experimental data.

Mirzabeygi and Zhang [84] used the distributed resistance approach to account for the flow resistance due to the presence of tubes in the shell side of a three-dimensional model of a condenser. The numerical model for this condenser was based on Eulerian – Eulerian two-phase model for solving the conservation equations.

It is evident that the distributed resistance method or CFD porous media approach to model the shell side of a shell and tube heat exchanger has been used extensively in the past four decades. Nowadays, this method is available in most commercial CFD software packages, either directly or through subroutines. Important components of this method that need careful considerations are; the choice of

empirical correlations used to account for the presence of tubes in the momentum and energy equation, porosity, and whether to account for turbulence or not.

2.5.3. Integrated Systems CFD analysis

In thermal-fluid design of systems consisting of many components connected together (e.g. nuclear reactors, coal fired power plants, etc.) engineers are continuously faced with two major challenges. The first challenge is on the ability to predict the performance of each individual component in the system. The second challenge is to predict the performance of the integrated system consisting of all the sub-systems which interact with one another [85, 86]. The modelling and analyses techniques used range from simplified one-dimensional models which do not capture all the physical phenomena [87] to the detailed large scale computational fluid dynamics models, which captures most of the significant physical phenomena but cannot simulate the entire plant as an integrated model [88].

An integrated Systems Computational Fluid Dynamics (SCFD) Approach was developed such that it can tackle these challenges in thermal-fluid design of complex systems [86]. The underlying philosophy of the SCFD methodology is that for the modelling and analyses of large thermal-fluid systems it must be possible to link models of various levels of abstraction and various degrees of complexity together to simulate the complete integrated system. The level of abstraction and the degree of complexity of the models are determined by the nature and details of the simulation as well as the details and character of the information required. This approach provides a progressive analysis of the problem, since the complexity of the simulation can be increased gradually and selectively and eventually also the level of abstraction, until the required complexity and levels of abstraction are reached [86]. In the context of superheater modelling, the SCFD allows the gas side to be modelled using CFD and then be integrated to the tube side which is modelled using one-dimensional techniques. Over the past two decades, this philosophy has gradually evolved from a mainly 1-D network approach [89], to a more advanced strategy [90] and finally a comprehensive methodology [91].

du Toit et al. [91] presented the SCFD in which a network code, Flownex, served as the main framework to interconnect models of the various components in a system together and to control the solution as well. They applied the SCFD to model the thermo-fluid phenomena of the Pebble Bed Modular Reactor (PBMR) reactor core and core structures. The fundamental governing equations were re-formulated into forms that were suitable for use in the SCFD code. The model was based on a simplification philosophy which was to strike a balance between accuracy and simplicity as well as refrain from simply developing a detailed CFD code that does not allow quick integrated plant

simulations. The numerical results were compared to experimental data and a good comparison was observed. Rousseau et al. [92] validated the transient thermal-fluid SCFD model of the PBMR reactor. The Flownex results for four transient cases were compared with experimental results as well as results from the Thermix/DIREKT code. For the Flownex model quicker computer simulation time were observed thus illustrating that a fine balance between accuracy and simplicity was achieved.

In 2006, du Toit et al. [93] highlighted the SCFD approach. They qualified it with an illustration of its use on two examples; the simulation of the power cycle of the PBMR power plant and the analysis of a coal-fired boiler. Du Toit and Kruger [94, 95] applied the integrated SCFD approach in simulating a coal-fired boiler furnace and evaporators. Flownex was used to model the quality of the water-steam mixture in the evaporators as well as the main framework for the simulation. This Flownex model was linked to a Flo++ 3-D CFD model of the gas flow and heat generation in the furnace. The CFD model showed gas flow patterns and heat distribution in the furnace while the Flownex model showed the temperatures and steam quality inside the evaporators. The integrated SCFD proved to have an advantage over uncoupled models which often rely on assumptions in order to couple certain phenomena, since in this method the coupled phenomena are iteratively solved.

du Toit and Rousseau [86] presented an overview of the modelling of the flow and heat transfer in a packed bed High Temperature Gas-Cooled Reactor using the SCFD approach. The developments in the design and layout of the PBMR gave rise to need for the simulation of a wide range of physical phenomena. Thus, a comprehensive 2-D axisymmetric pebble bed reactor was developed through reducing and recasting the conservation equations into a form usable with a network code. This re-formulation of the conservation equations resulted in a collection of one-dimensional models that can be linked together to build a comprehensive multidimensional model of the reactor. The initial validation of this model entailed comparing the predicted results to steady state and transient experimental results. A good comparison between simulated and experimental results was obtained which showed that for the cases considered the SCFD approach accounted for all the important physical phenomena. A fine balance between speed, accuracy and simplicity was achieved from this SCFD model.

2.5.4. One dimensional network approach applied to three dimensional phenomena

In the previous subsection, the integrated system CFD approach was presented as a technique that has an advantage of combining the detailed nature of the CFD results with the simulation of a complete

plant. However as shown with some applications of the SCFD, it is also possible to take advantage of the simulation speed presented by the use of the 1-D approaches to model 3-D phenomena.

In 1994, Tilton and Ratnam [38] developed a methodology for integrating the results of 2-D or 3-D gas flow models with that of a 1-D gas and tube flow model. The 1-D model used the network approach in which the tube banks were divided into modules. The gas flow and tube flow modules were explicitly interconnected. The interconnection between these modules can be split or mixed. They stated that a set of equations was derived for each individual heat exchanger module, consisting of the conservation equation; mass, momentum and energy equation. However, they did not show these equations only referring readers to semi-empirical methods in literature. They further stated that the set of equations were solved using the sparse-matrix method within a network solution code. As part of the method, the gas flow results of the 1-D model were compared to results from a CFD gas flow model based on the distributed resistance method. The CFD results were used to determine the pattern of the gas flow distribution in the 1-D model. The method was applied on the convective pass of a boiler. However, the model was not validated against experimental data.

2.6. Summary of literature review

From the literature review the following conclusions are drawn:

- In many of the simplified models reviewed the solution of the momentum conservation equations are not included, which implies that the flow maldistribution cannot be obtained as part of the solution.
- For the CFD models, where the momentum equation is solved on the flue gas side, the inlet mass flow or velocity distribution must be specified. Thus, the flow maldistribution on both the flue gas and the steam side cannot be obtained automatically.
- There are few available dynamic models that capture the detail geometry of the heat exchanger. Usually, lumped parameter models are used in dynamic simulations. Lumped parameter models cannot capture the dynamic behaviour of different tubes or regions within a heat exchanger.
- Several 1-D models have been applied for modelling heat exchangers in coal-fired boilers to reasonable levels of detail.
- Some models based on the 1-D approach modelled the flue gas as if it was flowing in parallel channels. Thus, they do not account for mixing.

- The need for large boiler heat exchanger model verification and validation is highlighted in literature. However, it is not clear how to do this in a structured and methodical way.
- The distributed resistance method or CFD porous media approach has been used extensively by researchers and engineers to model heat exchangers in an industrial setting.
- Only a few researchers attempted to use the 1-D network approach to model 3-D phenomena. This approach aims to take advantage of the increased simulation speed presented by the 1-D network approach.

3. ONE DIMENSIONAL NETWORK METHODOLOGY

Disclaimer: The conceptual idea of the modelling methodology was introduced in reference [1] *which was published as part of the proceedings of the 7th IASTED International Conference on Modelling, Simulation and Identification, Calgary, 2017. Further development of the methodology was published in the journal Heat Transfer Engineering* [2]. *The candidate is indebted to his supervisor together with whom the concept was developed.*

The network approach employed here is encapsulated in an integrated process modelling software suite called Flownex Simulation Environment (Flownex SE). The Flownex SE software platform (shown in Figure 3-1) was developed by M-Tech Industrial [96] in South Africa.

3.1. Flownex software overview

This section is included for completeness and serves to introduce a reader who is not familiar with the Flownex software, the platform on which the models have been built. Readers who are already familiar with the platform may wish to proceed directly to section 3.2.

This software platform is built on a system-level one-dimensional thermo-fluid network methodology [97, 98]. In its library this software contains several pre-configured components such as pipes, heat exchangers, flow resistors, compressors, pumps, turbines, etc which can be systematically connected together in any complex manner to model a complete thermo-fluid system. The thermo-fluid system can be a complete power plant, heating or cooling system or a subsystem of a thermo-fluid system. In addition, a range of "primitive" heat transfer components are also available. These components include 1-D planar conduction heat transfer elements, surface convection heat transfer elements as well as surface and spatial thermal radiation heat transfer elements which can be connected to create any complex heat transfer network. Flownex is also capable of handling user-defined re-usable compound components built from systematically combining the pre-configured components or primitive components in its library [98, 99].

The software also allows flexible coupling with other software tools which gets inputs from Flownex to solve and send results back to Flownex and vice versa. These software tools include Matlab and Simulink or any other tool with an Application Programming Interface (API) functionality and have specific capabilities to embed models or calculations developed in Excel, Mathcad, Engineering Equation Solver (EES), Relap or C# scripts. In addition, Flownex contains tools such as a system designer (similar to goal seeking), optimizer and sensitivity analysis [49, 98, 99].

Figure 3-1: Flownex Simulation Environment process modelling platform (M-Tech Industrial, 2014).

Flownex solves the transient form of the fundamental conservation equations together with built-in fluid property relations and component characteristics representative of all the types of components. In a network made of these components, control elements can be added to obtain a complete integrated dynamic system simulation model of a plant, sub system or component. A range of working fluids are available. These include the homogeneous model of water-steam according to the International Association for the Properties of Water and Steam (IAPWS) formulations. The Flownex solver provides as output the fluid properties such as temperature, pressure or quality at each point in the system together with the mass flow rates, heat transfer rates and power for all components. Some properties are a product of the solution scheme and others are obtained through post-processing [98, 99].

The integrated process modelling capability encapsulated within Flownex entails the simultaneous solution of the transient one-dimensional forms of the conservation equations for mass, energy and momentum, combined with the applicable closure relations, boundary values and initial values. The closure relations include models for the component specific characteristics and all the modes of heat transfer as well as the fluid property relationships. The network methodology can be described in terms of the node and element schematic shown in Figure 3-2. By convention, in a network methodology diagram, elements are represented by circles and nodes represented by squares.

In this approach an element is essentially a control volume which may represent any type of physical component such as a pipe, valve, heat exchanger, boiler, turbine, etc. Each element has one inlet and one outlet and the properties within the element are assumed to be represented by a single weighted average value between the inlet and the outlet. An element may also represent a single subdivision or

increment of a physical component that is discretized into several control volumes. It may therefore represent a pipe increment or heat exchanger increment [98].

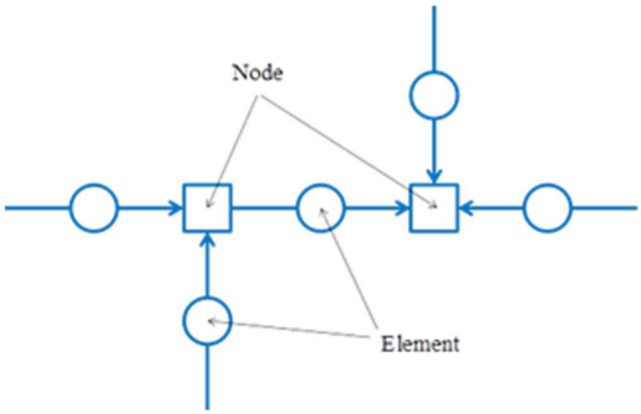

Figure 3-2: Network of nodes and elements applied in Flownex [98].

The nodes represent the connection points between elements, which may also be a physical reservoir or tank. Nodes may therefore have multiple inlets and outlets with the properties within a node assumed to be uniform and represented by a single averaged value. In the solution of the integrated network all the fluid volume, and therefore all the fluid mass, is assumed to be contained within the nodes, but the net change of momentum between all the inlets and outlets of a node is assumed to be negligible. Mass may be added to or removed from a node via mass sources or sinks. Energy may also be added to or removed from a node via power and heat transfer terms.

On each element, half of the volume is allocated to the inlet and outlet nodes respectively, implying that mass and energy can only accumulate in nodes, not in elements. However, elements accommodate the total (stagnation) pressure changes due to power inputs and outputs or frictional losses occurring within the specific component. The mass and energy conservation equations are therefore solved for each of the nodes, while momentum conservation is solved for each of the elements. In addition, Flownex solves for the mass flow rates due to pressure drops, and determines the resultant operating points of pumps, fans, compressors and turbines [98].

The spatially integrated transient partial differential forms of the mass and energy conservation equations without internal sources that are solved for each node are given in simplified format by

$$\frac{\partial \rho}{\partial t} = \frac{1}{V}\left(\sum \dot{m}_i - \sum \dot{m}_e\right) \tag{3.1}$$

$$\frac{\partial h_0}{\partial t} = \frac{1}{\rho V}\left(\sum \dot{m}_i \left(h_{0i} + g z_i\right) - \sum \dot{m}_e \left(h_{0e} + g z_e\right) + \dot{Q} - \dot{W} + V\left(\frac{\partial p}{\partial t} - h_0 \frac{\partial \rho}{\partial t}\right)\right) \tag{3.2}$$

Here ρ is the density and h_0 the specific stagnation or total enthalpy of the fluid defined as $h+\frac{1}{2}v^2$. h is the specific static enthalpy, v the weighted average velocity in the control volume, V the volume, t the time, $\dot{m}$ the mass flow rate, z the elevation and p the static pressure. Wherever there is no subscript it refers to the averaged property value within the control volume, while the subscripts i and e refer to the properties at the inlets and outlets respectively. $\dot{Q}$ is the rate of heat transfer to the control volume, $\dot{W}$ is the power output from the control volume and g is the gravitational acceleration.

The transient one-dimensional form of the momentum conservation equation (for incompressible flow) that is solved for each element is given by

$$\frac{\partial \dot{m}}{\partial t}=\frac{A}{L}\left(\left(p_{0i}-p_{0e}\right)+\rho g\left(z_i-z_e\right)+\Delta p_{0W}-\Delta p_{0L}+Lv\frac{\partial \rho}{\partial t}\right) \tag{3.3}$$

Here p_0 is the total pressure defined as $p+\frac{1}{2}\rho v^2$, A the average cross-sectional flow area, L the representative length Δp_{0W} and Δp_{0L} are the total pressure increase or decrease due to work and losses respectively. For compressible and homogeneous two-phase flows eq. (3.3) will contain additional terms. For elements such as pipes, ducts, bends and valves the total pressure loss term is often expressed in the form of a loss coefficient, K multiplied by the dynamic pressure represented as follows

$$\Delta p_{0L}=K\left(\frac{1}{2}\right)\rho v^2 \tag{3.4}$$

Equations (3.1), (3.2) and (3.3) may be integrated over a discrete time step Δt using an Euler integration scheme to obtain

$$\rho=\rho^o+\left(\left(1-\alpha\right)S_c^o+\alpha S_c\right)\Delta t \tag{3.5}$$

for the new density,

$$h_0=h_0^o+\left(\left(1-\alpha\right)S_e^o+\alpha S_e\right)\Delta t \tag{3.6}$$

for the new total enthalpy and,

$$\dot{m}=\dot{m}^o+\left(\left(1-\alpha\right)S_m^o+\alpha S_m\right)\Delta t \tag{3.7}$$

for the new mass flow rate through the components. The superscript o refers to the values at the previous time. The terms $S_c(t)$, $S_e(t)$ and $S_m(t)$ are the time dependent source terms emanating from the mass, energy and momentum conservation equations, respectively [98]. The weighting factor α which determines the characteristics of the integration scheme is between 0.0 (fully explicit) and 1.0 (fully implicit) for the source terms at the previous time step and current time step. This therefore determines the degree of forward or backward Euler integration. A weighting factor of 0.7 is often applied since it produces a good balance between accuracy and stability.

As illustrated schematically in Figure 3-3, the network methodology essentially reduces to the calculation of new values for the density and total enthalpy in each node based on the "old" values (with superscript o) and the mass flow rates into and out of the nodes. The mass flow rates are dictated by the elements connected to the nodes. With the enthalpy and density known within the node, the pressure may be derived from the appropriate fluid property relationship $p = f(\rho, h)$. The pressures in the nodes in turn dictate the new values of the mass flow rate in each of the elements. The primary dependent variables that are solved for are p_0, h_0 and ρ.

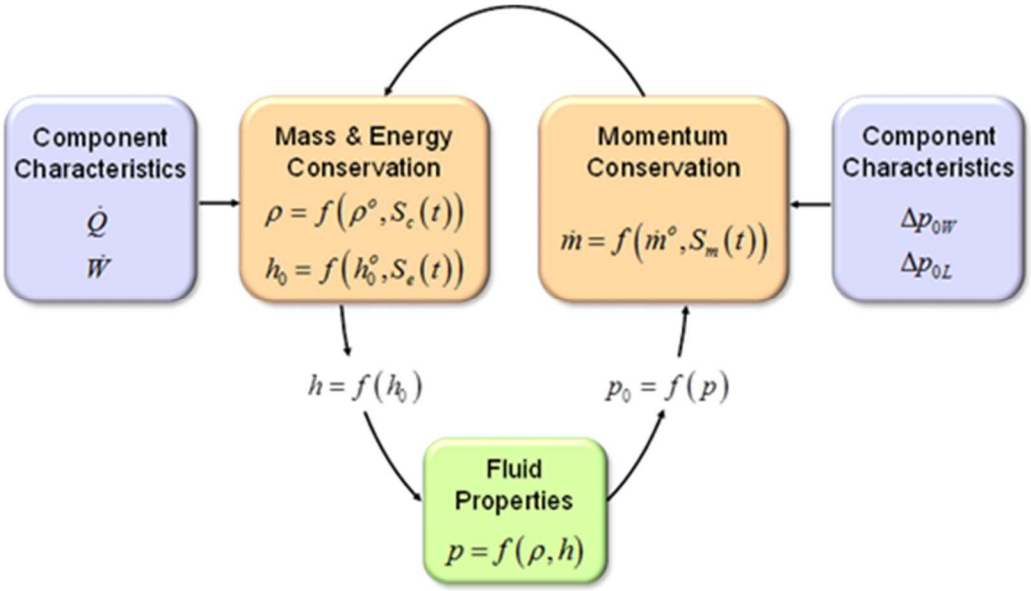

Figure 3-3: Schematic of Flownex transient network solution methodology [98].

The numerical solution scheme applied in Flownex is an Implicit Pressure Correction Method (IPCM). It is based on combining the mass and momentum conservation equations to obtain a total pressure matrix which, after a Newton-Raphson-type linearization, produces a total pressure correction solution

matrix. A more detailed description of the numerical solution scheme is presented by Greyvenstein [100].

It is important to note that while the conservation equations will be the same for all the nodes and elements, the component characteristics ($\dot{Q}, \dot{W}, \Delta p_{0W}$ and Δp_{0L}) will be totally different, depending on the component of interest. The level of complexity at which each component is modelled is really determined by the level of complexity that is encapsulated in the component characteristic formulations. Interestingly, there can be a very wide variation in the level of complexity, even for the same type of component operating with the same working fluid and the same boundary values [98, 101].

Besides solving the transient form of the conservation equations, Flownex also has the ability to directly solve the steady-state form of the equations, i.e. with the $\partial/\partial t$ terms set equal to zero. This implies that the steady-state solution can be obtained directly and quickly without having to run a transient from a given set of initial conditions until steady-state is eventually reached.

In terms of heat transfer, Flownex is capable of handling conductive, convective and radiative heat transfer. Flownex solves both the Cartesian form and cylindrical form of the 2-D transient heat conduction equation. The 2-D Cartesian form of the transient heat conduction equation is given by

$$\rho c \frac{\partial T}{\partial t} = \frac{\partial}{\partial x}\left(k \frac{\partial T}{\partial x} \right) + \frac{\partial}{\partial y}\left(k \frac{\partial T}{\partial y} \right) \tag{3.8}$$

Solving the Cartesian form of the equation implies that the area discretisation is done using standard averages [97]. This capability allows Flownex to solve for heat conduction through any shape, provided the shape is sufficiently discretised.

For the cylindrical form, the circumferential heat conduction is neglected, thus it solves radial and axial conduction heat transfer. The cylindrical form of the 2-D heat conduction heat is given by

$$\rho c \frac{\partial T}{\partial t} = \frac{1}{r}\frac{\partial}{\partial r}\left(rk \frac{\partial T}{\partial r} \right) + \frac{\partial}{\partial z}\left(k \frac{\partial T}{\partial z} \right) \tag{3.9}$$

with k the thermal conductivity, c the specific heat capacity and r is the radius of the component. Solving the cylindrical form of the equation implies that linear area change discretisation is used [97]. The heat conduction equation, Cartesian or Cylindrical, is solved using the FVM on a grid with half control volumes at the end as illustrated in Figure 3-4.

The convection heat transfer is accounted for through empirical correlations. This convective heat transfer is set to be constant throughout an element or an increment if the element is discretised axially [96]. Radiation heat transfer is accounted for through solving the standard radiation heat transfer equation given by

$$\dot{Q}_{rad} = A_o F \sigma \left(T_{fg}^4 - T_{fo}^4 \right) \tag{3.10}$$

with A_o the outer fouled tube surface area and F the view factor.

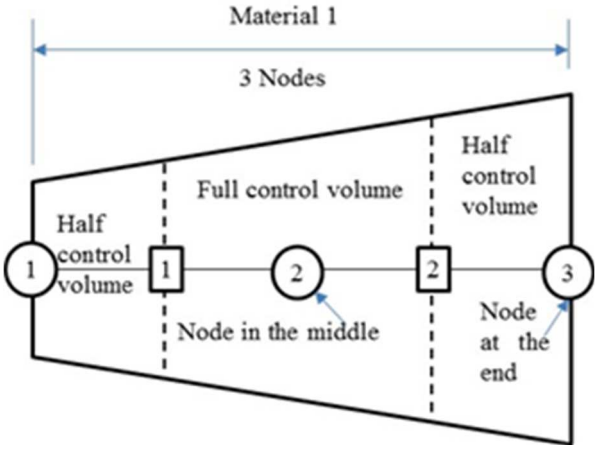

Figure 3-4: Representation of the discretisation of the thickness of the component on the heat transfer element [49].

Figure 3-5 shows the basic Flownex components which are a pipe element, a composite heat transfer element, a boundary condition and a node, while Figure 3-6 presents the primitive heat elements for conduction, convection and radiation.

The pipe element shown in Figure 3-5a) can be used to model flow in pipes and ducting with non-constant, arbitrary cross-sectional area. It takes into account both friction and secondary losses. The technical capabilities of this component include the ability to handle gas, liquid and two-phase flows, the ability to model both steady-state and transient flows, the capability of handling the effects of gravity as well as the capability of allowing the user to discretise the computational domain into a number of increments. The 1-D convective acceleration term in the momentum equation is retained in the calculations. For transient flows, the inertia terms are also retained in the calculations [102].

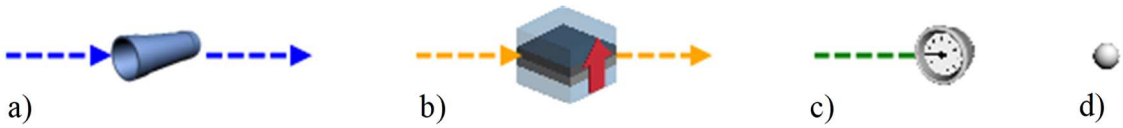

Figure 3-5: Flownex components; a) Pipe, b) Composite Heat Transfer Element, c) Boundary Condition and d) Node.

The Composite Heat Transfer element (CHT) shown in Figure 3-5b) is used to model heat transfer in a solid structure resulting from an interaction with its surroundings. The CHT can account for conduction, convection and radiation heat transfer to and from the solid structure. It can account for different solid materials which are modelled by dividing the structure into different material layers for the conduction heat transfer. The capabilities of modelling conduction heat transfer on both Cartesian and cylindrical coordinate systems are described in the preceding subsection. In essence, the CHT element can account for both thermal resistance and thermal inertia. Its ability to allow for the interaction of the solid structure with the surroundings implies that it can connect to flow elements or flow nodes with either single or two-phase flows [102].

The Boundary Condition component shown in Figure 3-5c) is used to specify the boundary conditions of a network. This defines the interface between the network and the surroundings. These may be inlet conditions, outlet conditions, etc. The boundary condition component can only be connected to a node component in which the specified conditions are applied. The conditions that can be specified at the boundary include pressure (static or total), temperature, quality, enthalpy and mass source. The nodes (illustrated in Figure 3-5d)) are end points of elements. However, nodes can also be used to model tanks or reservoirs [102].

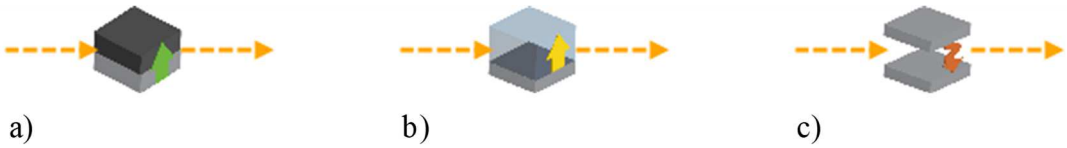

Figure 3-6: Primitive heat transfer element; a) conduction, b) convection and c) surface and spatial radiation heat transfer elements.

To allow for flexibility in modelling certain heat transfer problems, a combination of two or more primitive heat transfer elements is preferred over the CHT element. The purely Conduction primitive heat transfer element shown in Figure 3-6a) is used only for linear, 1-D heat transfer in mostly solid structures. Figure 3-6b) shows the Convection primitive heat transfer element which serves as a heat

exchange link between a fluid and a solid structure. The Convection primitive heat transfer element can be connected to either a non-discretised flow element or a flow node on one side and on the other side it is always connected to a solid node. It cannot be connected between two flow nodes or two flow elements or a combination of a flow element and a flow node. On the Convection heat transfer element, the user specifies the heat transfer area as well as the method for calculating the convection heat transfer coefficient. The heat transfer coefficient can either be calculated using the Dittus-Boelter correlation or Gnielinski correlation or be specified as a constant. Figure 3-6c) presents the Surface Radiation primitive heat transfer element that is used to model radiation heat transfer between surfaces. The Surface Radiation element can be connected between two solid nodes or between a solid node and a flow node or between two flow nodes. The radiation heat transfer element cannot be connected to a flow element. In the calculation, the radiation heat transfer element solves the standard radiation heat transfer equation shown in the preceding subsection [102].

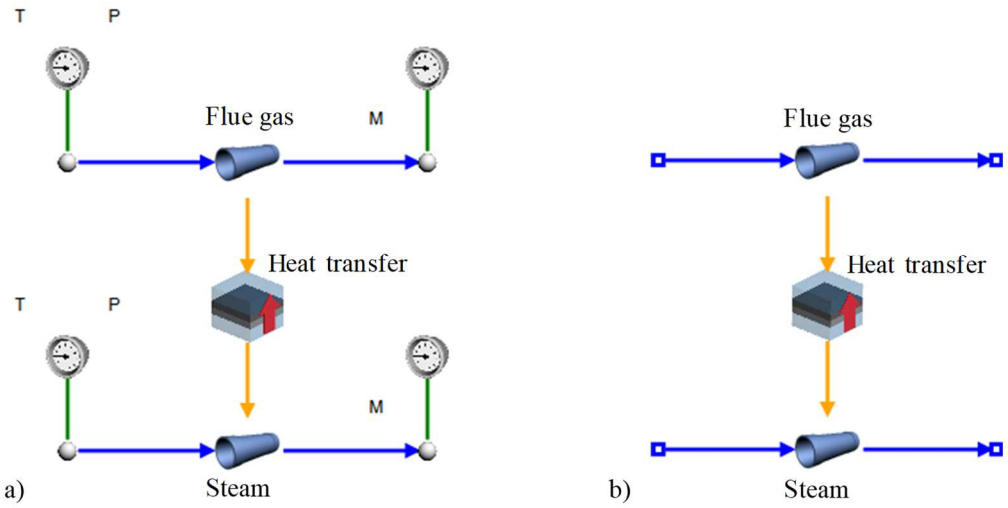

Figure 3-7: Examples of simple Flownex networks in which heat is transferred from a flue gas stream to a steam stream: a) Complete standalone Flownex network and b) Compound component which represents the repeatable part of a network.

Figure 3-7a) presents a simple Flownex setup where by convention (because of heat transfer arrow) heat is transferred from the flue gas stream to the steam stream via the CHT element. If the heat transfer direction is opposed to the prescribed direction, then the heat transfer value will be a negative. On both streams, inlet temperature and pressures are prescribed and a mass sink at the outlet of each flow element is prescribed. If this simple Flownex network is repeatable in a bigger network, for instance if the computational domain is discretised to smaller increments for better accuracy, then the repeatable part can be lumped together to form a Compound component as shown in Figure 3-7b). This

Compound component is then used a building block for the bigger network. Geometrical information can differ between different Compound components. It can be seen that the compound component no longer has the nodes and boundary conditions at both the inlet and outlet of each stream. These components are replaced by the open fibre component (small squares at each end of both streams) which implies that the compound component can be treated like an element on which boundary conditions are not specified.

3.2. Tube modelling methodology

In order to model a specific heat exchanger in the convective pass of a coal fired boiler using the network approach encapsulated in Flownex, a specific methodology was developed. This developed methodology is generic such that it can be applicable to any heat exchanger of interest in the convective pass of a coal-fired boiler. In this methodology the basic building blocks remain the same, while only the geometrical information and tube arrangements will vary according to the specific heat exchanger geometry.

Since most heat exchangers in the convective pass of a coal-fired boiler are mostly made of plain tubes, the methodology is centred around modelling a tube or a bundle of tubes. Now consider a plain tube with steam flowing inside and flue gas cross-flowing over it as shown in Figure 3-8.

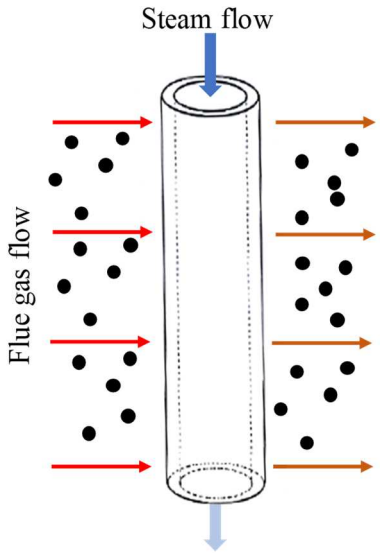

Figure 3-8: Representation of a tube with steam flowing inside and flue gas cross-flowing over it.

In order to correctly model the fluid flow and heat transfer in this tube on Flownex one should focus on the cross-section of the thickness of the tube as shown in Figure 3-9. The directions of the arrows shown in Figure 3-9 represent the assumed direction of heat transfer, which may initially be unknown.

The actual direction of the heat transfer will be part of the solution and if it is different from the assumed direction, the calculated value of the heat transfer will simply be negative. This approach ensures that the directions of the heat transfer are always correctly calculated rather than being specified, since the directions may in fact change during a transient event.

The heat transfer through the pipe wall is assumed to be axially symmetric and for the thin-walled superheater tube it is assumed that heat conduction is in the radial direction only. The vertical arrows in Figure 3-9 represent the steam (st) and flue gas (fg) flow paths respectively. $h_{0,sti}$ and $h_{0,ste}$ are the total enthalpy of the steam at the inlet and outlet respectively. $h_{0,fgi}$ and $h_{0,fge}$ are the total enthalpy of the flue gas inlet and outlet, respectively.

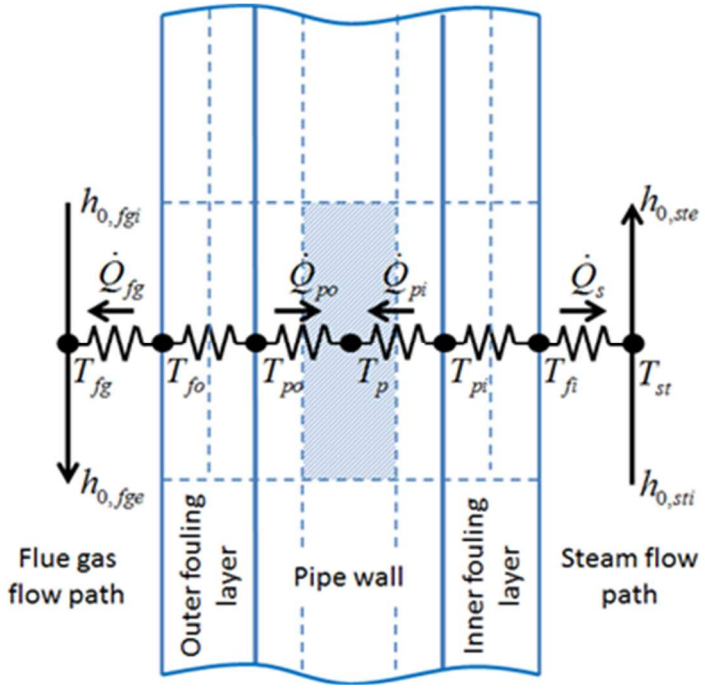

Figure 3-9: Schematic of a single heat exchanger pipe increment (not to scale) [1].

The thermal inertia associated with the mass contained in the control volume of each node is also accounted for by solving the transient form of the energy conservation equation for the node. For example, for the cross-hatched control volume in Figure 3-9 the energy conservation would be

$$\frac{\partial T_p}{\partial t} = \frac{\dot{Q}_{pi} + \dot{Q}_{po}}{(\rho V c)_p} \tag{3.11}$$

with $(\rho V c)_p$ the heat capacity of the pipe wall material within the control volume, and $\dot{Q}_{pi}$ and $\dot{Q}_{po}$ the heat transfer rates into the control volume from the inner and outer pipe wall surface temperature

nodes respectively. The conductive heat transfer rates are calculated using a simple Fourier conduction heat transfer equation in cylindrical form.

The representation of the fluid flow and heat transfer in a tube on Flownex is shown in Figure 3-10. This represent the display of the compound component which is a heat exchanger increment. Such heat exchanger increments are connected one after the other until the desired geometry and level of discretisation is achieved. The compound component can represent one tube or a tube bundle. The lumping of tubes into one is demonstrated in Figure 3-11.

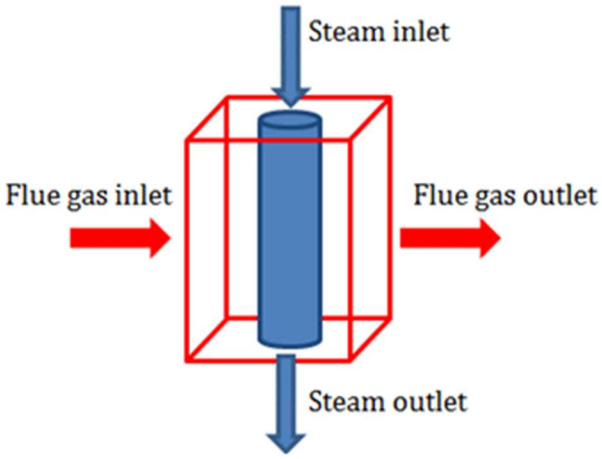

Figure 3-10: Representation of a heat exchanger increment [1].

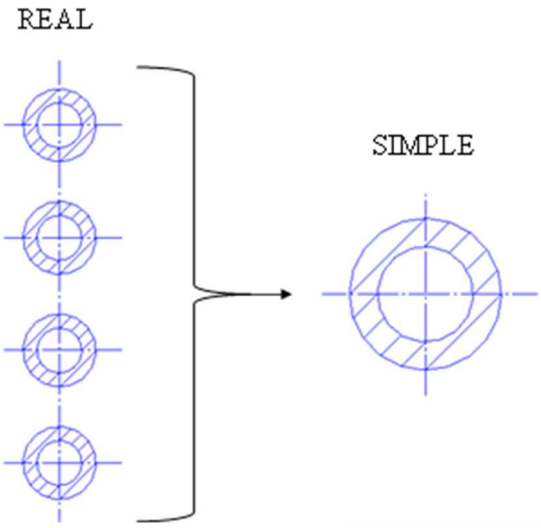

Figure 3-11. Schematic of bundling inline tubes into one tube (the four tubes were selected for demonstration purposes) [49].

If the heat exchanger element represents a tube bundle, then great care must be taken in accounting for surface area, free flow area and diameter. The surface area is important for correctly capturing the heat transfer into the tubes, thus it should be the sum of all the surface areas in the grouped tubes. The free flow area is important to characterise the amount flowing in the tube bundle thus it should also be the sum of the free flow areas of all the tubes. On the other hand, the hydraulic diameter should be the same as that of a single tube since it is used in the calculation of the heat transfer coefficients. The hydraulic diameter is kept the same as that of one tube through manipulating the inlet circumference/perimeter on the Flownex inputs using the following equation

$$P = \frac{4A_{freeflow}}{D_{tube}} \tag{3.12}$$

with P , $A_{freeflow}$ and D_{tube} the perimeter, free flow area and hydraulic diameter, respectively.

Figure 3-12 shows the heat exchanger increment sub-network within Flownex which is embodied in the compound component shown in Figure 3-10.

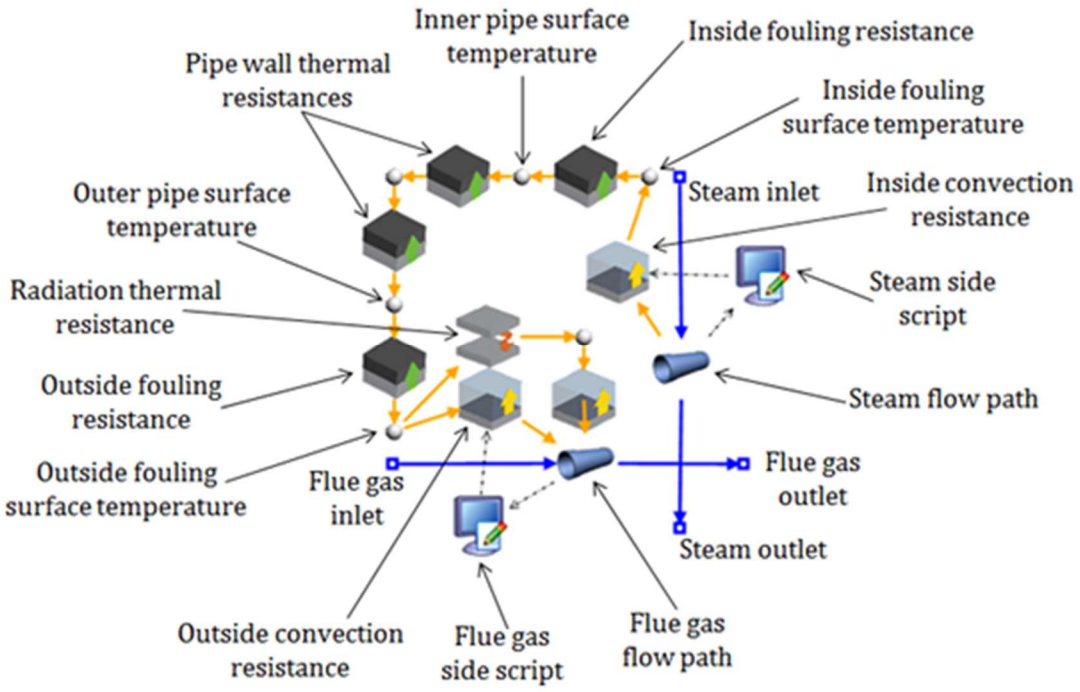

Figure 3-12: Schematic of the heat exchanger increment sub-network in Flownex.

The different elements are: the steam flow path; the inside convective heat transfer resistance; the inner fouling layer (IFL) conduction heat transfer resistance and associated thermal inertia; two conduction heat transfer resistances and thermal inertia components, each associated with half of the pipe wall

thickness; an outer fouling layer (OFL) conduction heat transfer resistance and associated thermal inertia; the outside convective heat transfer resistance; the outside gas radiative heat transfer resistance; and the flue gas flow path. As mentioned in the subsection above, since the Surface Radiation primitive heat transfer element cannot be connected to a flow element, it is connected to a node. Then the node is connected to a convection primitive heat transfer element which in turn connects to the flow element on the flue gas side. The heat transfer coefficient in this "pseudo" convection heat transfer element is set to be very high, thus it induces negligible thermal resistance on the system. Note that in this compound component the set direction for heat transfer is from the steam side to the flue gas side. If the calculated heat transfer direction is in the opposite direction, then the heat transfer value will be a negative.

It is important to mention that at this stage only the radiation from the surrounding flue gas is considered, hence referred to as gas radiation. Long range radiation that originates upstream of the heat exchanger of interest, henceforth referred to as direct radiation is not considered here. However, the direct radiation will be considered as part of the modelling methodology refinement process in chapter 6 and implemented in chapter 7.

3.3. Summary of the modelling methodology

In this chapter, the network methodology which is encapsulated in the Flownex software was described. In addition, the Flownex components that are used in the model development were also highlighted. Furthermore, a model for a generic cross-flow heat exchanger increment was developed that can be used to construct a heat exchanger of any complex layout. This heat exchanger increment is a building block which is used in this work to build models of different superheater heat exchangers of coal-fired boilers. Such heat exchanger increments can be connected one after the other until the desired geometry and level of discretisation is achieved. It accounts for all the thermal resistances in the heat exchanger including inner and outer fouling resistances using experimental correlations or specified constant values. The resulting heat exchanger model can simulate steady state and transient operations of the heat exchanger. At this stage the heat exchanger increment only falls short of accounting for direct radiation which originates upstream of the heat exchanger of interest. However, that phenomenon is addressed in chapter 6 where the modelling methodology is refined.

4. METHODOLOGY DEMONSTRATION

Disclaimer: A significant amount of the work documented in this chapter was published in the journal Heat Transfer Engineering in reference [2]. *The candidate is indebted to his supervisor together with whom the concept was developed.*

In order to demonstrate the modelling methodology described in the previous chapter, it is applied in this chapter to model the primary superheater of a 50-MW coal fired power plant. This superheater was also modelled by Taler et al. [4] as well as other researchers in Poland. This superheater was chosen because most of its geometrical and flow information is available in literature. Some of the results reported in the literature were also used for model verification.

4.1. Geometrical and flow information

The primary superheater is the heat exchanger on the right in the convective pass of the coal fired boiler as shown in Figure 4-1. Based on its location in the convective pass, it is a convective superheater since its most dominant mode of heat transfer is convection.

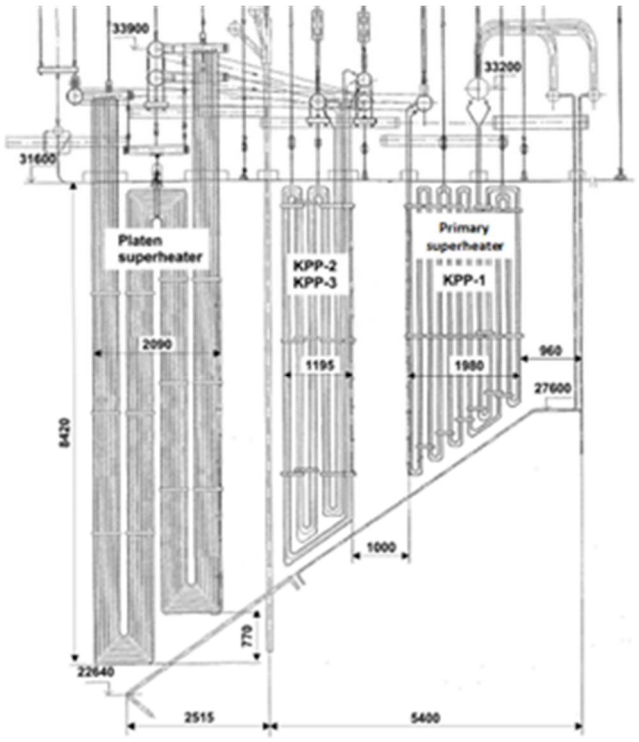

Figure 4-1: The convective pass of a 50-MW coal-fired boiler system [48].

Figure 4-2 shows the schematic of a single tubesheet/element of the primary superheater. It is a 12-pass dual-tube superheater heat exchanger where each pass consists of two tubes in "parallel" with a complex flow arrangement inside the boiler. These inline tubes are connected on one end to the same

inlet header and to an outlet header on the other end forming one tubesheet. Therefore, a tubesheet is made up of 24 tube passes along the length of the flue gas flow path.

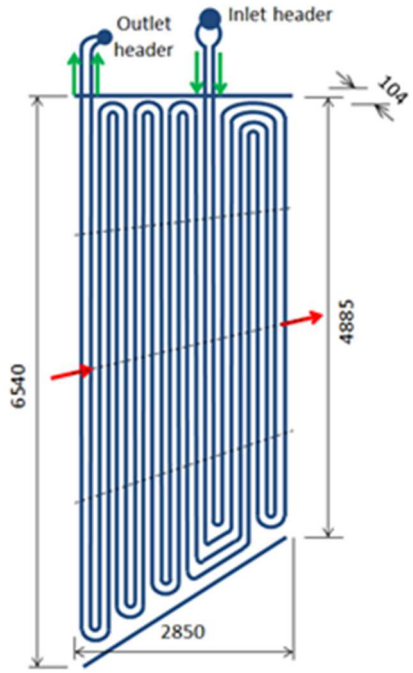

Figure 4-2: Schematic of the layout of a single tubesheet of the superheater [2].

The inlet header is connected to the 8th pass from the flue gas inlet side and the tubes then follow a complex arrangement with the outlet header connected to the 1st pass at the flue gas inlet side. The superheater consists of 74 such tubesheets in parallel across the width of the flue gas duct, and the width of the flue gas flow path associated with each tubesheet is 104 mm. All the tubes have an outer diameter of 42 mm and wall thickness of 5 mm. The heights of the first and the last tube with respect to the flue gas flow are 5.34 m and 4.46 m, respectively. The height of tubes in between is assumed to be linearly distributed.

At nominal operation the steam capacity of the boiler is 210 x 10^3 kg/h. The live steam parameters at the outlet of the final superheater are: pressure of 9.61 MPa and temperature of 532.8 °C [103].

4.2. Superheater Flownex models

A characteristic of the Flownex network modelling approach is that the steam flow model traces the path travelled by the steam in the superheater. The flue gas flow model also traces the flue gas flow path. However, in this work the subchannel approach was adopted on the flue gas side. The foundation of the subchannel approach is that it explicitly assumes that one of the velocity components in a certain direction is dominant compared to the other velocity components [58, 60]. Thus, only the dominant

direction is rigorously solved, hence the only computationally expensive direction. In this case, the flow is predominantly flowing from the inlet of the heat exchanger to the outlet, thus that is the flow direction adopted. This implies that flow in the vertical direction or across the width of the heat exchanger is ignored. Thus, mixing and recirculation in certain cases cannot be accounted for. This assumption can be relaxed at a later stage of the modelling. A more detailed study of the flue gas side modelling will be presented in Chapter 5 of this work.

The input data required for these models are inlet temperatures, inlet pressures and mass flow rates for both the steam and flue gas streams. In addition, geometrical information of the superheater is required.

4.2.1. Single tubesheet

Figure 4-3 shows a schematic of the 1-D network model of a single tubesheet. It consists of 24 columns of tubes along the flue gas flow path.

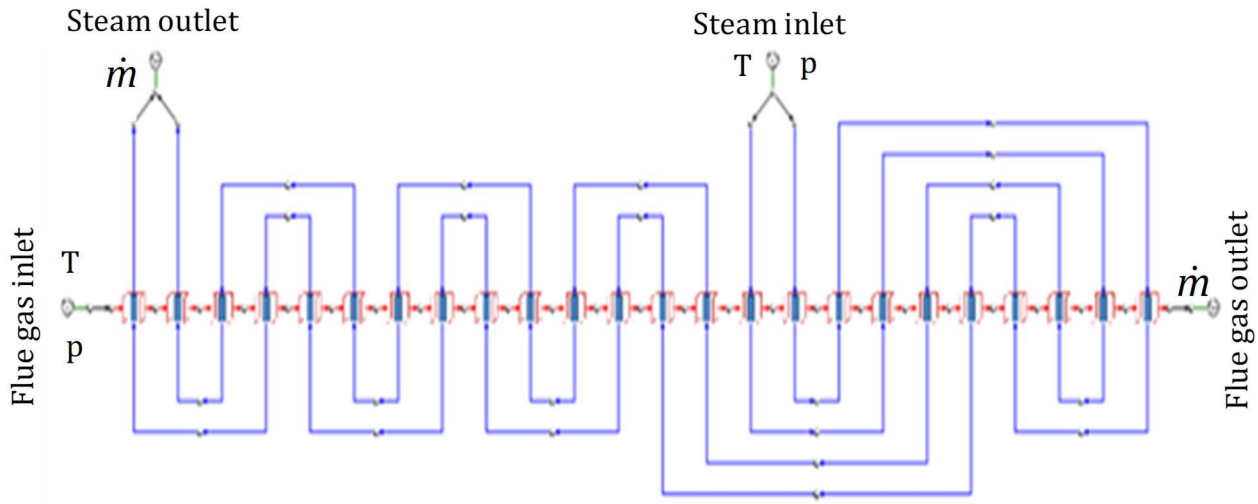

Figure 4-3: Schematic of a tubesheet model in Flownex with tubes that are not discretised.

The flow path layout on the steam side reflects the complex layout in accordance to the geometrical information shown in Figure 4-1 and Figure 4-2. In the tubesheet model shown in Figure 4-3, the tubes are not discretized along the length in each steam pass. In order to obtain a refined computational domain, the tubes may be discretised along the length in each pass as shown in Figure 4-4. Figure 4-4 also shows a single tubesheet model but with each of the tubes in each pass discretized into four increments along the length of the tube. The specific number of four increments is for illustrative purposes only and therefore in this case a single tubesheet is represented by 96 individual heat

exchanger increments. A representation of one such a heat exchanger increment was presented in Figure 3-10.

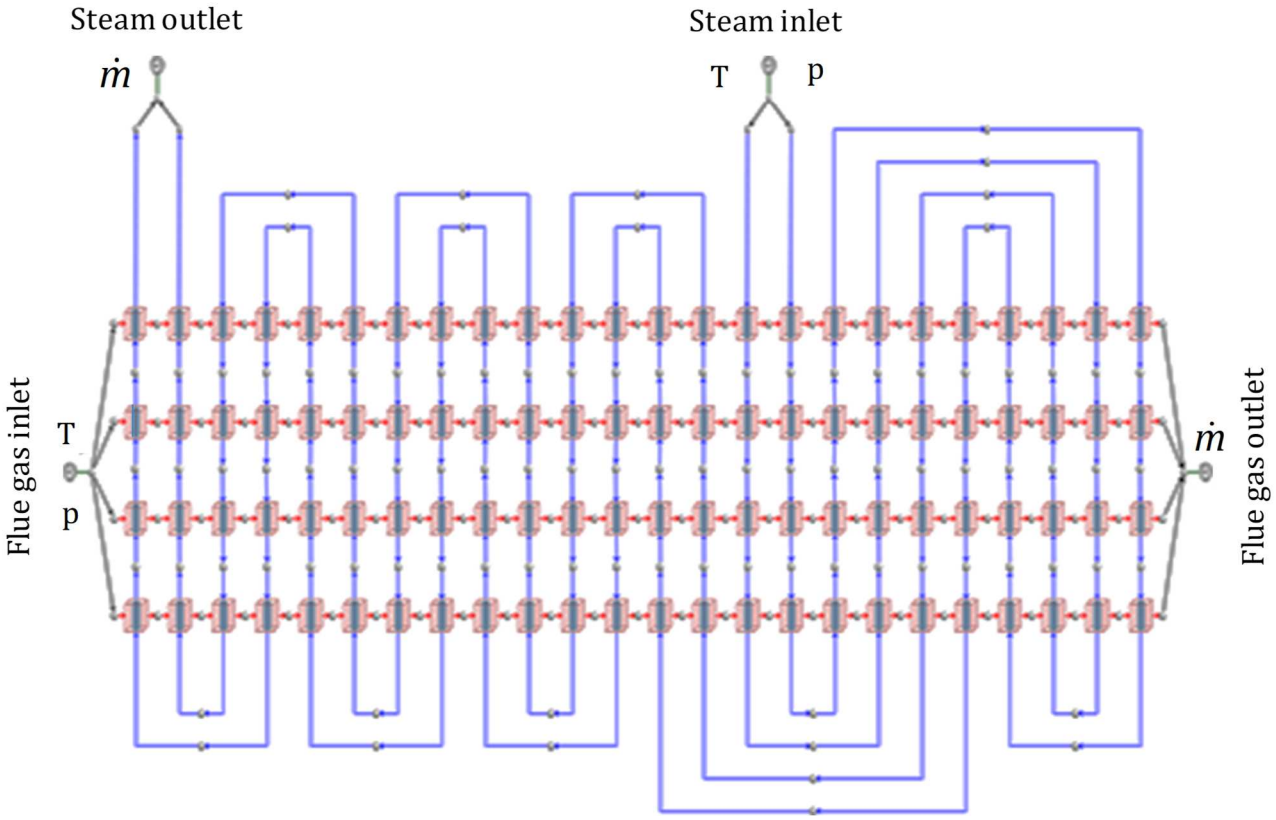

Figure 4-4: Schematic of a discretised tubesheet model in Flownex.

From the single node representing the extraction point on the inlet header the flow splits into two separate nodes, each representing the inlet of one of the two tubes in the 8th pass. Each of the two tube outlets in the 1st pass is also represented by a node which then converge into a single node representing the connection to the outlet header. The gauge-like symbols connected to the inlet and outlet nodes represent boundary values. The boundary values provided at the inlet node are the inlet steam pressure and temperature. The outlet boundary value is a mass sink. Although the outlets of the two tubes converge into a single node, there may be different resultant mass flow rates and temperatures emanating from each. We may therefore detect flow and temperature maldistribution between the two tubes due to different heat transfer and pressure drop conditions that may occur.

On the flue gas side, the overall inlet and outlet are each also represented by a single node. At the inlet this implies an assumption of a uniform pressure and temperature distribution over the height of the flue gas duct. This assumption is temporarily adopted for demonstration purposes but can be relaxed later. The flue gas inlet pressure and temperature boundary values are specified. From the single inlet

node, the flow splits to individual inlet nodes to each of the flue gas flow increments along the height of the flue gas duct. The boundary value specified for the single node at the outlet of the flue gas flow path is a mass sink. The single node implies that a uniform pressure distribution is assumed, which may also be relaxed later on. This single overall outlet node is fed by a convergence from the outlet nodes of each of the flue gas increments. The mass flow rates and temperatures coming from the outlet of each of the flue gas increments may be different due to different heat transfer and pressure drop conditions. Possible flow and temperature maldistribution along the height of the flue gas duct may therefore also be detected.

Note that for now it is also assumed that there is no mixing in the vertical direction between the flue gas increments as it flows through the heat exchanger. This assumption may also be relaxed by adding interconnecting flue gas flow path elements in the vertical direction between the various inlet and outlet nodes of the flue gas increments. In order to obtain the appropriate detailed flue gas flow pattern within the tubesheet it will require the specification of appropriate representative flow resistances within the horizontal and vertical flow path elements. However, for the purpose of demonstrating the modelling methodology the vertical mixing will be assumed to be negligible, as was done by Taler et al. [4].

4.2.2. Multiple tubesheets

In order to investigate the effect of maldistribution of flow and temperature across the width of the superheater heat exchanger a 3-D model was developed. This showed the extended capabilities of the 1-D network approach. In this 3-D model a tubesheet with one heat exchanger increment (not discretised) was used, as shown Figure 4-5. A wide selection of input temperature data can be postulated for both fluid streams. This includes postulating both uniform and non-uniform temperature profiles for the flue gas inlet temperature. For this model as well, mass flow rate is set up as a sink at the end of each stream. The mass flow is allowed to redistribute in accordance to the heat transfer and pressure drops in the system.

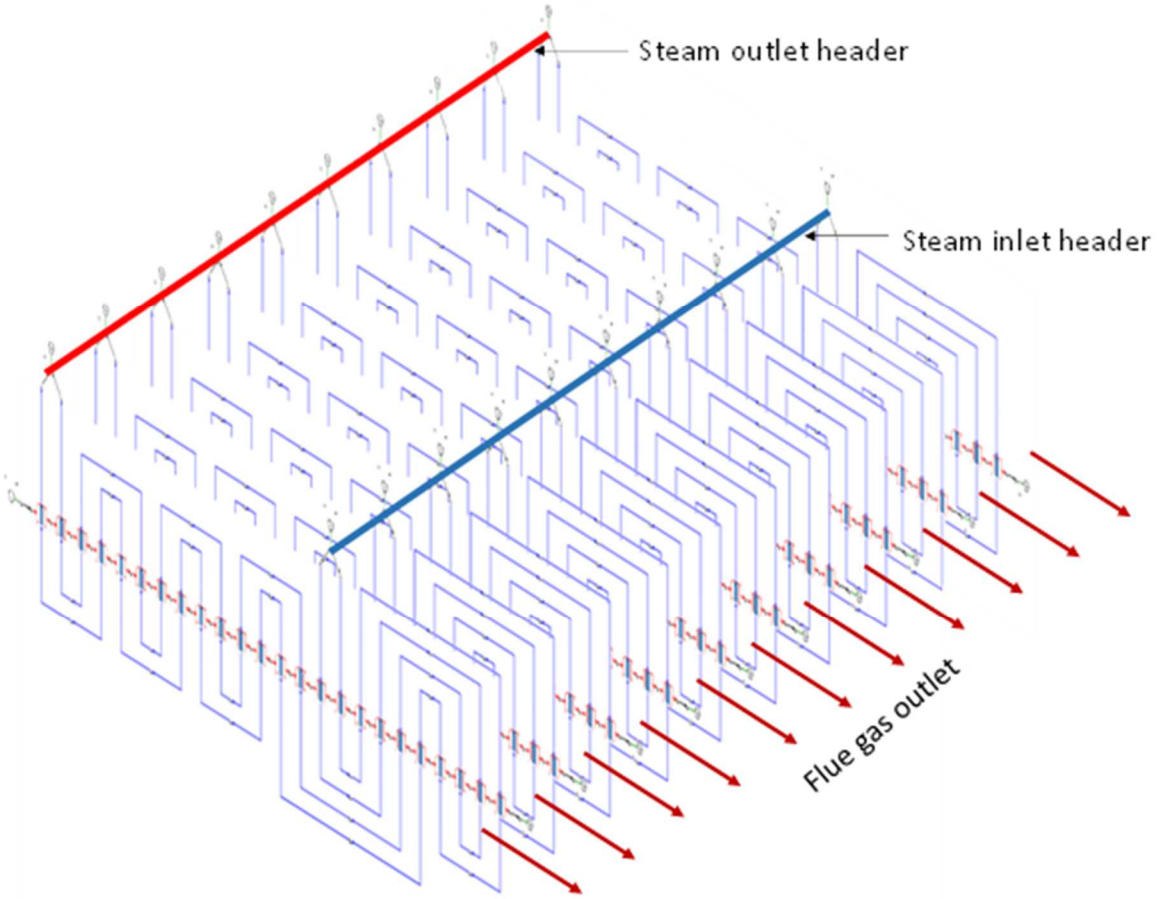

Figure 4-5: Demonstration of header flow modelling [2].

4.3. Heat transfer models, pressure drop models and fluid properties

The following subsections will describe the models applied for each of the heat transfer and flow elements shown in Figure 3-12 in more detail.

4.3.1. Inside convective heat transfer element

The inside convective heat transfer is calculated using the Gnielinski [104] correlation for heat transfer during turbulent flow of gases and liquids through pipes. The equations are incorporated in the element using the steam side C# script as illustrated in Figure 3-12. This correlation is given by

$$Nu = \frac{(\xi/8)\,\mathrm{Re}\,\mathrm{Pr}}{1+12.7\sqrt{\xi/8}\left(\mathrm{Pr}^{2/3}-1\right)}\left[1+\left(d_i/l_t\right)^{2/3}\right] \tag{4.1}$$

where

$$\xi = \left(1.8\log_{10}\mathrm{Re}-1.5\right)^{-2} \tag{4.2}$$

Here, Nu, Re and Pr are the dimensionless Nusselt, Reynolds and Prandtl numbers, respectively. d_i and l_t are the fouled inner tube diameter and the length of the tube respectively. The ranges of validity for this correlation are as follows

$$10^4 \le \mathrm{Re} \le 10^6$$
$$0.1 \le \mathrm{Pr} \le 1000$$
$$d_i / l_t \le 1$$

4.3.2. Conductive heat transfer elements

The tubes are made of carbon steel with a constant density and specific heat capacity with the value of $7832\,kg/m^3$ and $0.29\,kJ/(kg \cdot K)$, respectively. The thermal conductivity of the tube material was given by Taler et al. [4] in $\mathrm{W/(m \cdot K)}$ as

$$k_t = 35.54 + 0.004084 \cdot T - 2.0891 \times 10^{-5} \cdot T^2 \tag{4.3}$$

with the temperature T given in °C. Unfortunately, no information was provided about the accuracy of the correlation, but for the temperature range of $300°C \le T \le 500°C$ considered in this work, the thermal conductivity variation is small, namely $32.4 \le k \le 34.9\ \mathrm{W/(m \cdot K)}$, with an average value of $33.8\ \mathrm{W/(m \cdot K)}$. The thermal conductivity of the outer fouling ash layer was also taken from Taler et al. [4] and its value is $k_{ash} = 0.07\ W/(m \cdot K)$. The inner scaling thermal conductivity was taken from Trojan and Taler [105] and its value is $k_{scale} = 0.15\ W/(m \cdot K)$.

4.3.3. Outside convective heat transfer element

The outside convective heat transfer is calculated using the Gnielinski [106] correlation for cross-flow around a single tube incorporated using the flue gas side C# script. This correlation is given by

$$Nu_l = 0.3 + \sqrt{Nu_{l,lam}^2 + Nu_{l,turb}^2} \tag{4.4}$$

Here, Nu_l is the overall Nusselt number and $Nu_{l,lam}$ and $Nu_{l,turb}$ are the resultant laminar and turbulent Nusselt numbers given by

$$Nu_{l,lam} = 0.664 \sqrt{\mathrm{Re}_l} \sqrt[3]{\mathrm{Pr}} \tag{4.5}$$

and

$$Nu_{l,turb} = \frac{0.037\,\mathrm{Re}_l^{0.8}\,\mathrm{Pr}}{1+2.443\,\mathrm{Re}_l^{-0.1}\left(\mathrm{Pr}^{2/3}-1\right)} \tag{4.6}$$

The validity ranges for correlations given by eq. (4.5) and (4.6) are as follows

$$10 < \mathrm{Re}_l < 10^6$$
$$0.6 < \mathrm{Pr} < 10^3$$

where the Reynolds number is given by

$$\mathrm{Re}_l = \frac{\rho v l}{\mu} \tag{4.7}$$

Here, ρ, v and μ are the fluid's density, velocity and dynamic viscosity, respectively. l is the streamed length given by

$$l = \frac{\pi}{2} d_o \tag{4.8}$$

where d_o is the fouled outer tube diameter.

4.3.4. Outside radiative heat transfer element

The radiation heat transfer from the flue gas to the outer surface of the outer fouling layer is accounted for using Taler and Taler's [107] radiation heat transfer coefficient given by

$$h_{ro} = \frac{\sigma \cdot \varepsilon_{eq} \cdot \alpha \cdot s}{\alpha \cdot s + \varepsilon_{eq}} \left(\frac{T_{fg}^4 - T_{fo}^4}{T_{fg} - T_{fo}} \right) \tag{4.9}$$

with σ the Stefan-Boltzmann constant given as $5.67\times10^{-8}\,W/\left(m^2K^4\right)$. The equivalent emissivity of the tube, ε_{eq} is given by

$$\varepsilon_{eq} = \frac{2\varepsilon_w}{2-\varepsilon_w} \tag{4.10}$$

with ε_w the emissivity of the outer tube wall or the outer surface of the OFL. The geometric mean beam length, s is given by

$$s = C\frac{V}{A} \tag{4.11}$$

V is the volume around the tube occupied by the flue gas and A is the outer surface area of the fouled tube. According to Jones [108] in many practical systems the constant C is taken as 3.6. The absorptivity coefficient α is given by

$$\alpha = -\frac{\ln(1-\varepsilon_g)}{s} \tag{4.12}$$

The total emissivity of the gas ε_g is determined using the weighted sum of gray gases (WSGG) model from Hottel and Sarofim [109]. The total emissivity for the WSGG model is calculated from

$$\varepsilon_g = \sum_{i=0}^{I} a_{\varepsilon,i}(T)\left[1 - e^{-\kappa_i \cdot p_g \cdot s}\right] \tag{4.13}$$

where $a_{\varepsilon,i}$ denotes the emissivity weighting factor for the *i-th* gray gas, which is based on the gas temperature T. The quantity in square brackets in eq. (4.13) is the emissivity of the *i-th* gray gas, with absorption coefficient κ_i, partial pressure p_g and geometric mean beam length s. The weighting factor $a_{\varepsilon,i}$ is the fraction of the amount of black-body energy in the spectral regions where a gray gas of absorption coefficient κ_i exists. For the "transparent" windows in the spectrum between the spectral bands of high absorption, the absorption coefficient is assigned a value of zero. This transparent window is treated as a gas at $i = 0$, with a weighting factor given as

$$a_{\varepsilon,0} = 1 - \sum_{i=0}^{I} a_{\varepsilon,i} \tag{4.14}$$

This implies that only I values of the weighting factors have to be determined. Smith et al. [110] presented a polynomial for evaluating the temperature-dependent emissivity weighting factor which is given by

$$a_{\varepsilon,i} = \sum_{j=1}^{J} b_{\varepsilon,i,j} T^{j-1} \tag{4.15}$$

where $b_{\varepsilon,i,j}$ are the emissivity gas temperature polynomial coefficients. For this model the emissivity coefficients given by Smith et al. [110] for a typical flue gas mixture were used and are given in Table 4-1. These coefficients are applicable for gas and irradiation temperatures within the range 600 to 2400 K and partial pressure-path length product within the range of 0.001 to 10.0 atm-m.

Table 4-1: Coefficients for emissivity [110].

i	k_i	$b_{i,1}\times10^{1}$	$b_{i,2}\times10^{4}$	$b_{i,3}\times10^{7}$	$b_{i,4}\times10^{11}$
1	0.4201	6.508	-5.551	3.029	-5.353
2	6.516	-0.2504	6.112	-3.882	6.528
3	131.9	2.718	-3.118	1.221	-1.612

The default radiation heat transfer element within Flownex solves the standard radiation heat transfer equation given by eq. (3.10)

$$\dot{Q}_{rad} = A_o F \sigma \left(T_{fg}^4 - T_{fo}^4 \right)$$

with A_o the outer fouled tube surface area and F the view factor. This standard radiative heat transfer element is used in the current model but with the view factor given by

$$F = \frac{\sigma \cdot \varepsilon_{eq} \cdot \alpha \cdot s}{\alpha \cdot s + \varepsilon_{eq}} \sigma^{-1} \tag{4.16}$$

Using this view factor together with eq. (3.10) is equivalent to employing the effective radiation heat transfer coefficient given by eq. (4.9).

4.3.5. Steam side pressure drop

The pressure drop on the steam side is calculated according to eq. (3.4) which can be further expressed as

$$\Delta p_{0L} = \left(\frac{f l_t}{d_i} \right) \left(\frac{1}{2} \right) \rho v^2 \tag{4.17}$$

where f is the friction factor and for turbulent flows it is given by Swamee and Jain [111] as

$$f = \frac{0.25}{\left[\log\left\{ \left(e/(3.7 d_i) \right) + \left(5.74/\mathrm{Re}^{0.9} \right) \right\} \right]^2} \tag{4.18}$$

with e the inside wall surface roughness in $[\mu\mathrm{m}]$. The validity ranges of friction factor correlation are as follows

$$5000 \le \mathrm{Re} \le 10^8$$

$$10^{-6} \le \left(\frac{e}{d_i}\right) \le 10^{-2}$$

4.3.6. Flue gas side pressure drop

The pressure drop on the flue gas side is accounted for using the following equation

$$\Delta p = Eu \frac{\rho v^2}{2} z \tag{4.19}$$

where z is the number of tube rows and Eu is the Euler number which was experimental determined and given graphically in Zukauskas and Ulinskas [112].

4.3.7. Steam properties

The model used the built-in steam properties in Flownex. These properties are based on the standards of the International Association for the Properties of Water and Steam (IAPWS) [113].

4.3.8. Flue gas properties

The flue gas specific heat capacity was calculated from the measured values using the energy balance between the steam and the flue gas as follows

$$cp_{fg} = \frac{-\dot{Q}_s}{\dot{m}_{fg}\left(T_{fge} - T_{fgi}\right)} \tag{4.20}$$

where $\dot{Q}_s$ is the heat transferred to the steam and $\dot{m}_{fg}$ is the mass flow rate of flue gas. T_{fgi} and T_{fge} are the inlet and outlet flue gas temperatures, respectively.

The flue gas density was accounted for using the ideal gas law given as

$$\rho_{fg} = \frac{p_{fg}}{R_{fg} T_{fg}} \tag{4.21}$$

where p_{fg}, T_{fg} and R_{fg} are the pressure and the specific gas constant, respectively.

The flue gas dynamic viscosity was given as a constant. This constant value was the average of the inlet and outlet dynamic viscosities each calculated using the following formula

$$\mu_{fg} = \frac{T_{fg}}{1.2635\times10^7 + 1.2618\times10^4 T_{fg} - 1.6929 T_{fg}^2} \tag{4.22}$$

with the temperature given in Kelvin [114].

The flue gas conductivity was specified as a constant. This constant value was the average of the inlet and outlet conductivities each calculated using the following formula

$$k_{fg} = 9.1446 \times 10^{-5} \times 0.99958^{T_{fg}} \times T_{fg}^{1.0148} \tag{4.23}$$

with the temperature given in Kelvin [114].

4.4. Results

This section presents some results to demonstrate the capability of the model. At first a comparison is made with the results presented by Taler et al. [4]. For reference purposes another comparison is then made with results from lumped models while assuming different simplified heat exchanger flow configurations. Following this, results are presented for low load operation and for transients due to load changes. In these cases, only one tubesheet is modelled with the assumption that the flows and inlet temperatures are evenly distributed across the superheater. Lastly, results of a study on the maldistribution of flow and temperature are presented.

4.4.1. Comparison to results of Taler et al. [4]

This section provides a comparison between the results obtained using the new model for the 50 MW coal-fired boiler's primary superheater tubesheet with the results provided by Taler et al. [4]. Taler et al. [4] presented the overall temperatures and flow rates for both the steam and the flue gas side at the nominal operating conditions. This information is valuable since it is usually very challenging to obtain suitable measured data from real operating power plants for model validation purposes. However, the information available has some limitations due to the lack of detail and therefore it is not really possible to provide a definitive validation based on this. Nevertheless, this comparison does at least provide qualitative proof of the validity of the new model. The main limitation in the available data is that the magnitude and distribution of the outer fouling layer thickness are not known. For this reason, Taler et al. [4] assumed a uniform thickness distribution throughout the whole of the heat exchanger and then adjusted the outer fouling layer thickness in the model until the computed and known steam temperature differences over the whole superheater were equal. This same approach was therefore applied here for the Flownex model.

The input conditions for the Flownex model are the same as those in the model of Taler et al. [4] and are given in Table 4-2. According to Taler et al. [4] the resulting outlet steam and mean outlet flue gas

temperatures were 400.9 °C and 558.6 °C respectively. At a fouling layer thickness of 1.02 mm, the corresponding outlet steam and outlet flue gas temperatures obtained with the Flownex model are 400.8 °C and 558.2 °C respectively. The detail temperature results obtained with the Flownex model are compared to that of Taler et al. [4] for the steam, OFL and mean flue gas, as shown in Figure 4-6. These were obtained using the Flownex model which was not discretised along the tube length as illustrated in Figure 4-3.

Table 4-2: Input conditions for a complete superheater model with outer fouled tubes at full load.

Details	**Units**	**Value**
Inlet steam temperature	°C	337.7
Inlet steam pressure	kPa	9600
Steam mass flow rate	kg/s	46.2
Inlet flue gas temperature	°C	632.6
Inlet flue gas pressure	kPa	100
Flue gas mass flow rate	kg/s	64.5

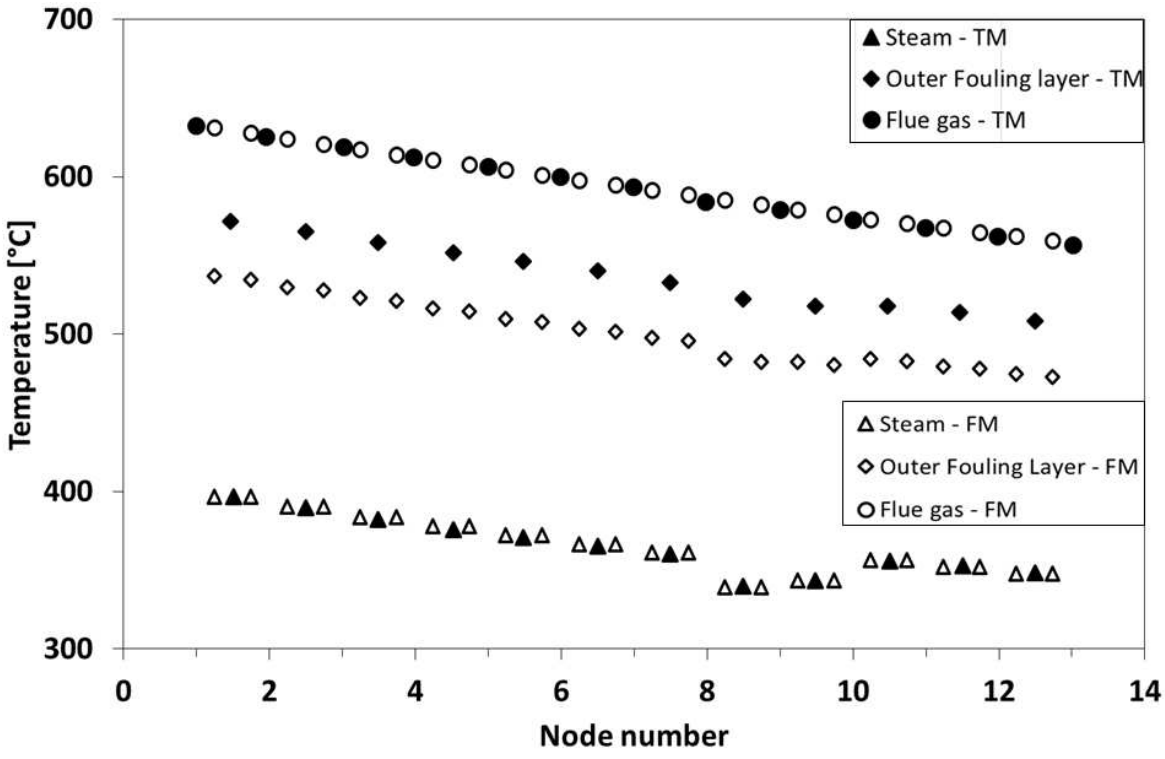

Figure 4-6: Comparison of the Flownex model (FM) results with the results of Taler et al. [4] (TM).

The results shown in Figure 4-6 illustrate that there is good agreement between the steam and flue gas temperature profiles. Note that in the Taler model the two tubes in each pass were lumped together and therefore it only provided one averaged value per tube pass. In the Flownex model the two tubes are modelled separately and therefore it provides two distinct values per tube pass. For the steam side all the average values of the two distinct temperatures determined with the Flownex model are within 2.7 °C of the averaged values from the Taler model, and also within 2.7 °C for the flue gas side.

However, there is a marked difference between the temperatures obtained for the outer fouling layer surface. Possible contributing factors to this discrepancy include the following: the difference introduced by the different convection coefficient correlations used in each model, the difference in the flue gas properties used in each model, as well as the way in which radiation heat transfer was accounted for in each model.

Heat is transferred from the flue gas to the OFL outer surface via convection and radiation heat transfer. The distribution of the different modes of heat transfer through the fouled tubesheet as calculated with the Flownex model is shown in Figure 4-7. The radiation contribution on the flue gas side is smaller than that of convection and it also decreases with the flue gas temperature. Since this heat exchanger is at the back of the boiler convective pass it is not unexpected that convection contributes more than radiation. The total of the convection and radiation heat transfer is conducted through the outer fouling layer and tube wall as shown in Figure 4-7. The calculated amount of heat transferred by one tubesheet of the superheater with all tubes having a constant outer fouling layer of 1.02 mm thickness is 138.7 kW. This duty of the superheater tubesheet presents an error of 0.5% when compared to the actual duty of 138 kW given by the Taler et al. [4] results.

A sensitivity study was performed to determine the effect of discretization along the length of each tube by comparing the results obtained with one, two, three, four and five increments respectively. The results obtained for the 12^{th} pipe situated in the sixth pass of the tubesheet was chosen for comparative purposes. The results are summarized in Table 4-3. It can be seen that the change in temperatures from the model with one heat exchanger increment to that with five increments is less than one percent. This implies that for steady-state scenarios the effect of discretization is negligible if uniform inlet flow conditions and uniform outer fouling are assumed. For convenience, a one increment heat exchanger model is used for the rest of the case studies presented here.

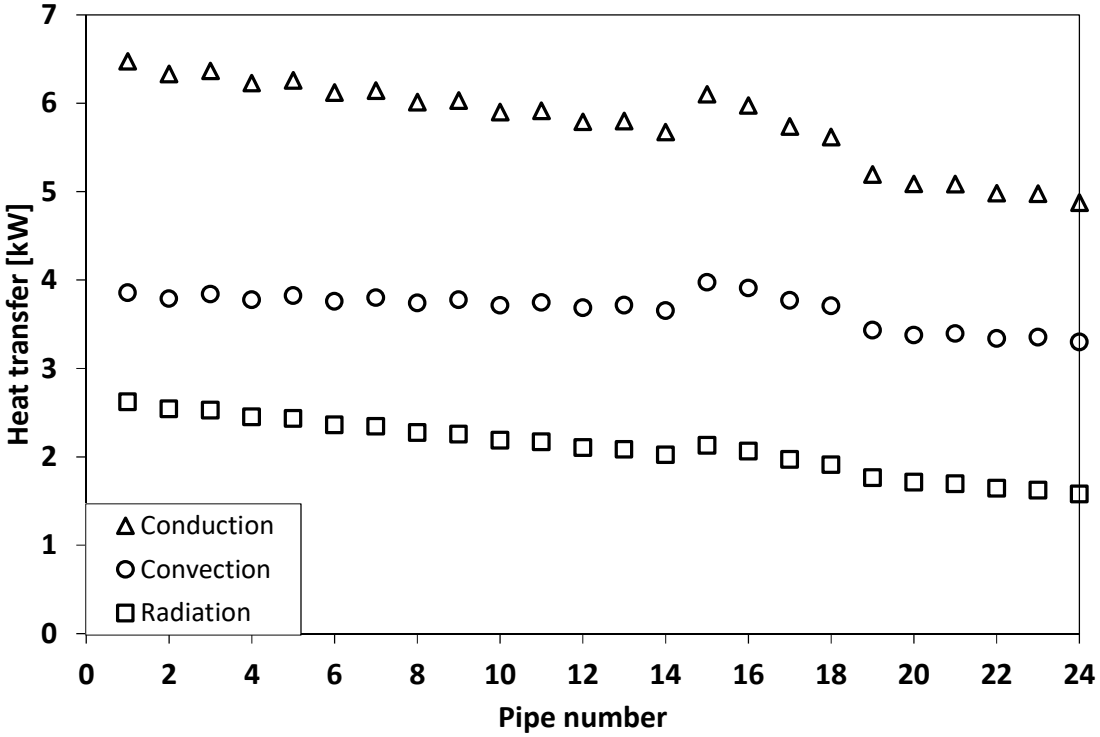

Figure 4-7: A comparison between the different modes of heat transfer.

Table 4-3: 1.02 mm OFL thickness - The sensitivity of the outlet steam, tube, outer fouled layer and outlet flue gas temperature to level of discretisation of the superheater tube sheet with uniform inlet flow conditions.

Number of heat exchanger increments	Outlet steam temperature (°C)	Average temperature for pipe 12 on the 6th pass (°C)				Outlet flue gas temperature (°C)
		Inner pipe surface	Centre of the pipe	Outer pipe surface	Outer fouled pipe surface	
1	400.79	373.27	374.19	375.00	501.89	558.22
2	400.70	372.78	373.70	374.51	501.25	558.31
3	400.51	372.68	373.59	374.40	500.78	558.50
4	400.76	372.65	373.57	374.37	500.76	558.25
5	400.78	372.49	373.41	374.21	501.09	558.23

4.4.2. Comparison to results from lumped parameter models

As shown in Figure 4-2 the complex flow arrangement of the superheater actually consists of 24 cross-flow heat exchangers configured in a combination of overall parallel flow and overall counter flow configurations. This complex arrangement cannot be accounted for in any single one of the conventional lumped parameter models. It is however instructive to systematically compare the results of the complex model with that of the lumped models while assuming different simplified heat exchanger flow configurations. The calculations for the lumped models are based on the Effectiveness

– Number of Transfer Units $(\varepsilon - NTU)$ method. The detail calculations performed here are shown in Appendix A.

At first, an overall heat transfer coefficient (UA) value of $0.682\ {}^{kW}/_{K}$ was calculated from the known average properties for one tubesheet based on the detail geometry and model described in Section 4.3. The duties obtained with each of the conventional lumped parameter models while using this calculated UA value are presented in Table 4-4 together with the resulting errors when compared to the known duty of one tubesheet, namely 138 kW. The resulting errors vary depending on the configuration assumed. The lowest error of +4.2% is obtained with the cross flow – both fluids unmixed configuration and the highest error of +8.9% with the counter flow configuration. This raises the question of whether these errors are indeed due to the fact that the complex flow configuration is not taken into account, or whether it is simply due to the averaging of the overall UA value?

Table 4-4: Heat transfers and errors resulting from the different lumped parameter heat exchanger models based on an overall AU value obtained from the average flow properties for one tubesheet.

Heat exchanger flow configurations	**Heat transfer (kW)**	**Error (%)**
Counter flow	150.226	8.9
Parallel flow	146.097	5.9
Cross flow - Steam (C_{max}) mixed, flue gas (C_{min}) unmixed	148.265	7.5
Cross flow - both fluids unmixed	143.753	4.2

In order to evaluate this, another approach was followed. An overall UA value of $0.609\ {}^{kW}/_{K}$ was calculated based on a summation of the incremental UA values calculated in the detail Flownex model. This re-calculated UA value therefore is not based on averaged properties as before, but rather take into account the variation in the properties from tube to tube. The duties and errors obtained with the different lumped parameters models when using this new overall UA value are provided in Table 4-5. In this instance, the error associated with the pure counter flow model is lowest at only -0.07% while the cross flow – both fluids unmixed error is highest at -4.2%. This shows that the overall counter flow model can be used with confidence for steady-state normal operation, provided that an appropriate value of the overall UA value is known, despite the fact that the complex flow arrangement is not accounted for. This is not totally unexpected since it is generally accepted that the overall counterflow approach provides good results for heat exchangers with four or more tube rows in series having a

"generally" counter flow arrangement. This also provides further qualitative evidence of the validity of the detailed incremental model when using the same overall UA value.

Table 4-5: Heat transfers and errors resulting from the different lumped parameter heat exchanger models based on an overall AU value obtained from addition of the incremental UA values calculated in the Flownex model for one tubesheet.

Heat exchanger flow configurations	**Heat transfer (kW)**	**Error (%)**
Counter flow	137.864	-0.07
Parallel flow	134.739	-2.3
Cross flow - Steam (C_{max}) mixed, flue gas (C_{min}) unmixed	136.375	-1.1
Cross flow - both fluids unmixed	132.104	-4.2

It can therefore be concluded that the earlier higher errors were mainly due to the inaccurate overall UA value that was obtained based on the known average properties, rather than being due to the assumed simplified flow configuration. One could now argue that by employing a simple logarithmic temperature profile for the steam and flue gas sides (which is consistent with the lumped parameter model assumptions) it would be possible to accurately calculate the incremental fluid properties. Therefore, one should be able to obtain a more accurate overall UA value without having to take into account the complex flow arrangement. However, the simple logarithmic temperature profile will not properly "track" the changes in the fluid properties since it does not correspond to the actual temperature profile. This is demonstrated in Figure 4-8. Figure 4-8 also shows that the logarithmic temperature distribution inherent in the lumped model cannot account for the fact that the steam inlet header is connected to the 15^{th} and 16^{th} tubes rather than at the back end of the heat exchanger.

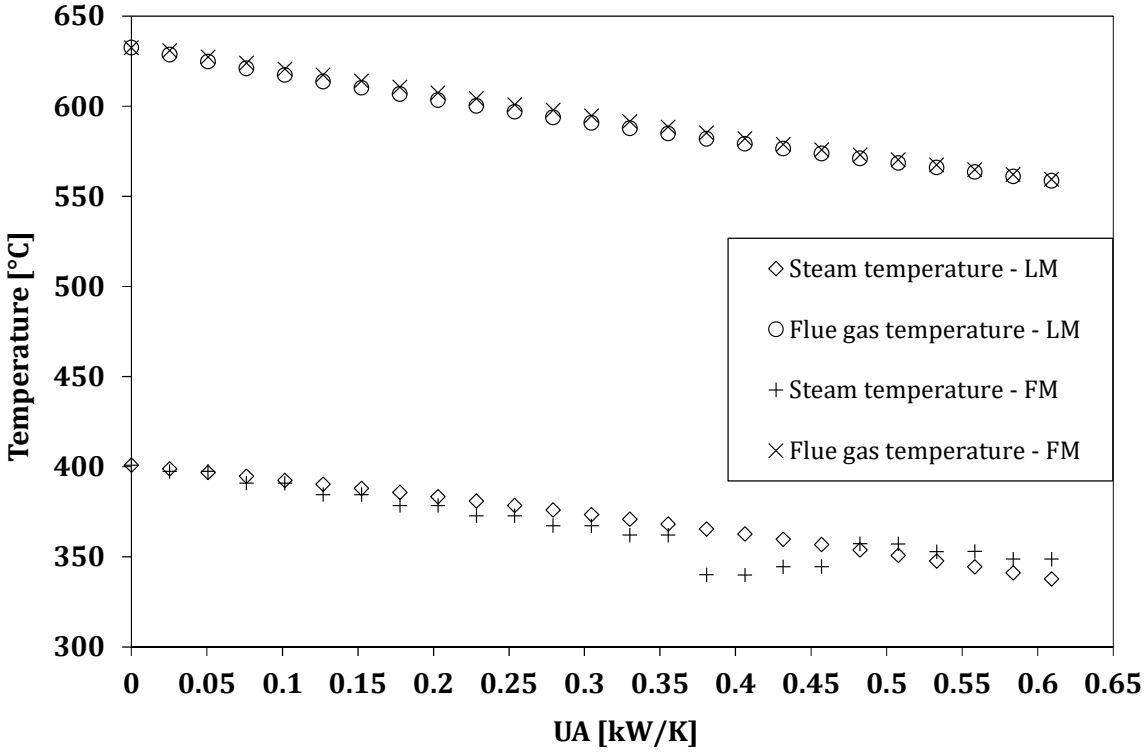

Figure 4-8: A comparison of steam and flue gas temperatures for the counter-flow lumped model (LM) and the detail Flownex Model (FM).

The shortcomings of the lumped model can be further demonstrated for more complex situations. One such case is where there is a partial blockage of the steam flow in one of the two tubes. The results of this are shown in Figure 4-9. Again, the inherent logarithmic temperature distribution of the lumped model cannot predict the steam temperature distribution in this case. It seems logical that this limitation of the lumped approach will also exist in even more complex cases such as non-uniform fouling or scaling and during transient operations. Therefore, the lumped parameter models have limited scope in the development of advanced tools for on-line process condition monitoring.

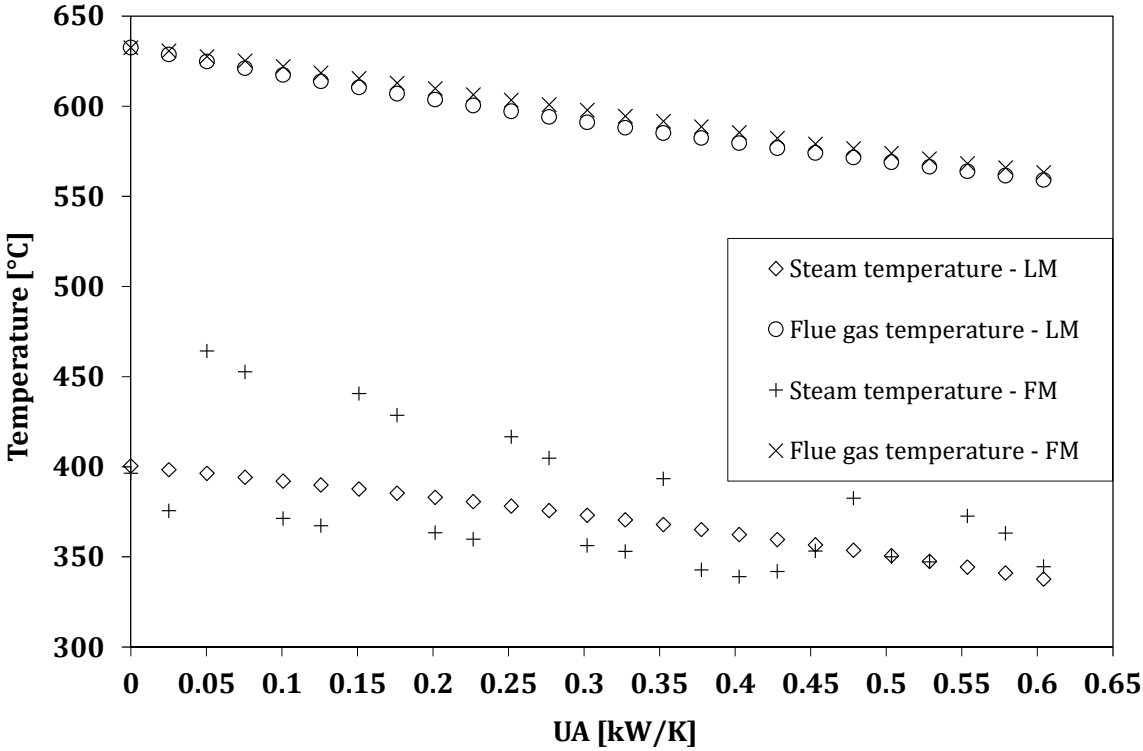

Figure 4-9: A comparison of steam and flue gas temperatures for the counter-flow lumped model (LM) and the detail Flownex Model (FM) where one steam tube is experiencing a partial flow blockage.

4.4.3. Load changes and low load operation

Due to the introduction of more intermittent renewable energy plants on the electricity supply grid, coal-fired plants are forced to change their mode of operation from base load to variable load operation. This will often involve ramp up or ramp down of the plant as well as running continuously at low load. However, low load operations of coal-fired plants are not only due to the increase in renewable energy generation. It is sometimes implemented simply to balance low demand on the grid. In addition, coal plants sometimes run on low load if a draft group, mill or a feed pump has tripped.

If the steam temperature cannot be controlled adequately during load changes, for example if attemperator sprays are already 100% open, the tube metal temperatures can increase to values which might be above the design limit [115]. In certain cases, the firing rate may also not respond quickly enough during a ramp down. Peet and Leung [116] demonstrated that during a quick load ramp up the outlet steam temperature sharply increases to values above the design limit.

Load changes – from 100% to 50% in 15 minutes

The Flownex tubesheet model with clean tubes was extended to investigate the effect of load changes on steam and tube metal temperatures. The input conditions given in Table 4-6 were used. In this case a linear ramp down from 100% to 50% of the steam mass flow in 15 minutes was assumed. When the outlet steam temperature moved above 421 °C it triggered a linear decrease in the flue gas mass flow until the outlet steam stabilizes back to a temperature close to the set 421 °C.

Table 4-6: Input conditions for a complete superheater with clean tubes at full load.

Details	**Units**	**Value**
Inlet steam temperature	°C	337.7
Inlet steam pressure	kPa	9600
Steam mass flow rate	kg/s	46.2
Inlet flue gas temperature	°C	632.6
Inlet flue gas pressure	kPa	100
Flue gas mass flow rate	kg/s	40

The response of the outlet steam as well as the first pipe (with respect to flue gas flow path) and second pipe wall temperatures are shown in Figure 4-10. The increase in outlet steam temperature corresponds to an increase in the tube metal temperature. This has the potential to result in short term overheating. The temperature response in Figure 4-10 demonstrates that the model does take into account the thermal inertia of the system.

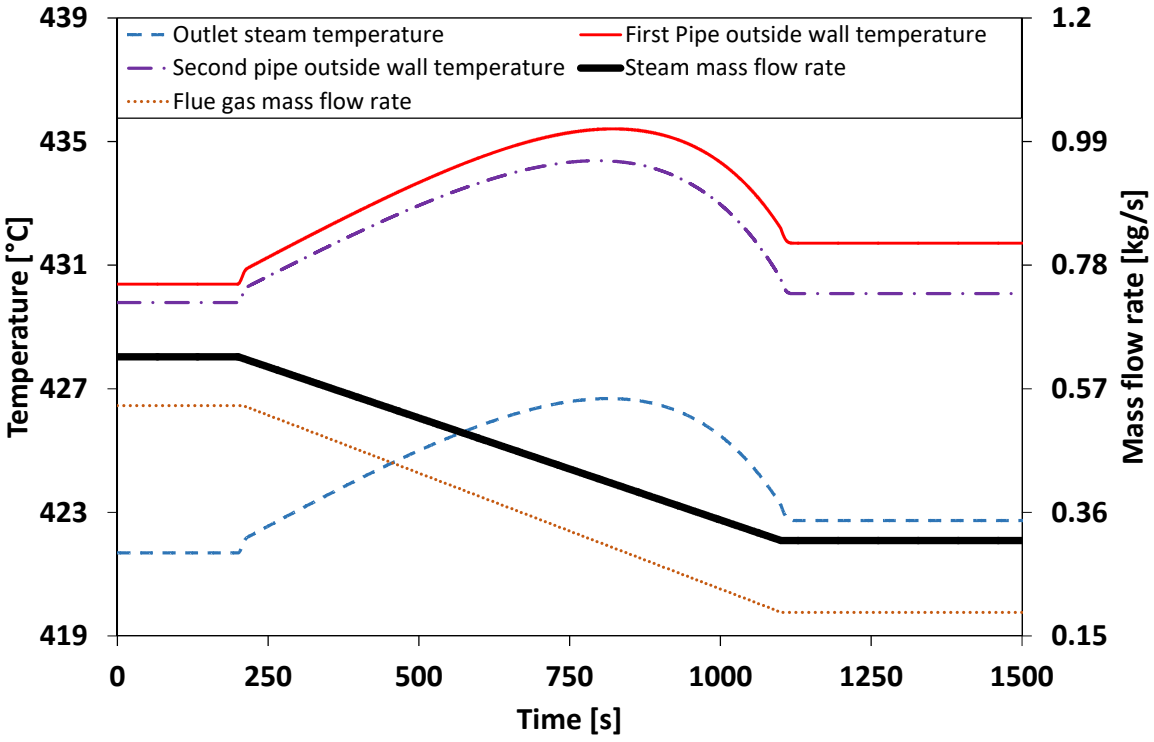

Figure 4-10: The response of the primary superheater to a duty ramp down from 100% to 50% in 15 minutes.

Load changes – from 100% to 50% in 2 minutes

The detail Flownex model can also be employed to investigate the effect of different ramp rates on the tube metal temperatures. Consider the same case with clean tubes as above and with the same initial conditions as given in Table 4-6. If the load is now ramped down from 100% load to 50% in 2 minutes rather than 15 minutes, the resulting temperatures are shown in Figure 4-11. Comparing the temperature results in Figure 4-11 to that of Figure 4-10 shows that for a quicker ramp rate the tube temperatures can reach higher values during the load change.

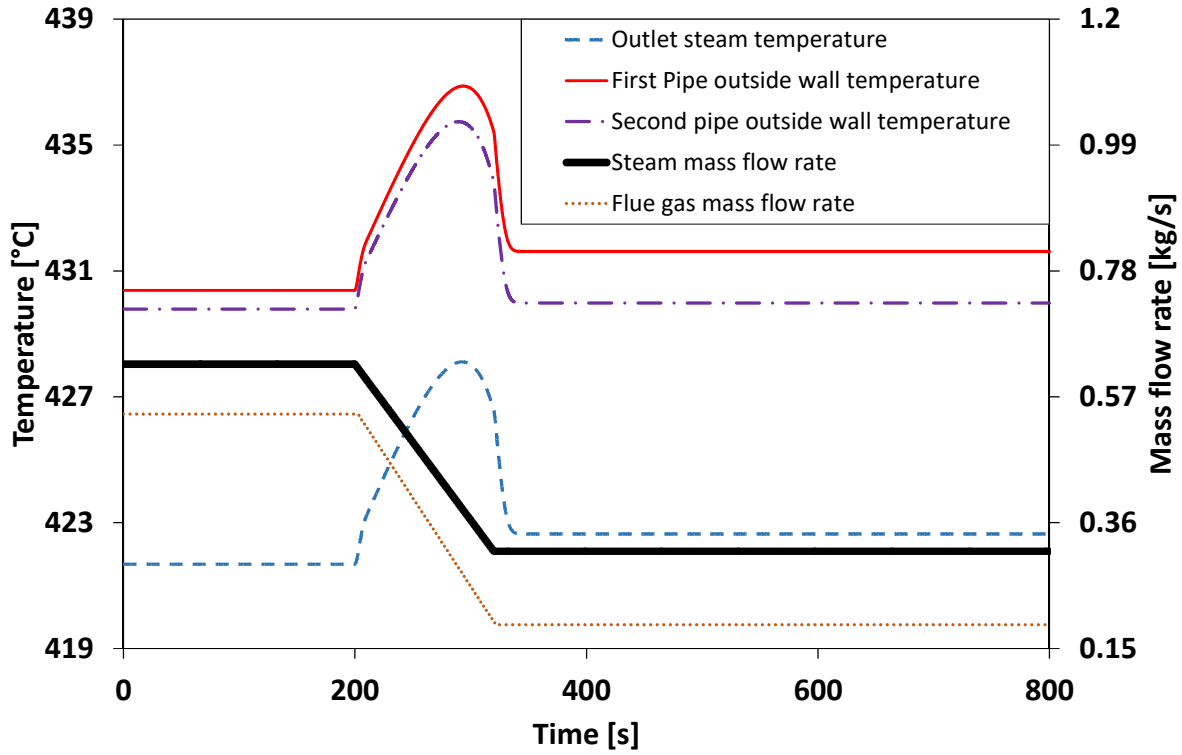

Figure 4-11: The response of the primary superheater to a duty ramp down from 100% to 50% in 2 minutes.

Figure 4-12 illustrates that different tubes in the heat exchanger experiences different metal temperature changes due to the heat exchanger duty change. For pipe number 1, which is at the inlet of the flue gas path and outlet of the steam path, the metal temperature first increases and then reduces to a value higher than the initial value. This response is different to that of pipe number 16 which is at the inlet of the steam path and pipe number 24 which is at the outlet of the flue gas path. This figure illustrates the importance of tube-by-tube discretisation along the flue gas path if detail tube analyses is of interest. In such scenarios, lumped models will again fall short.

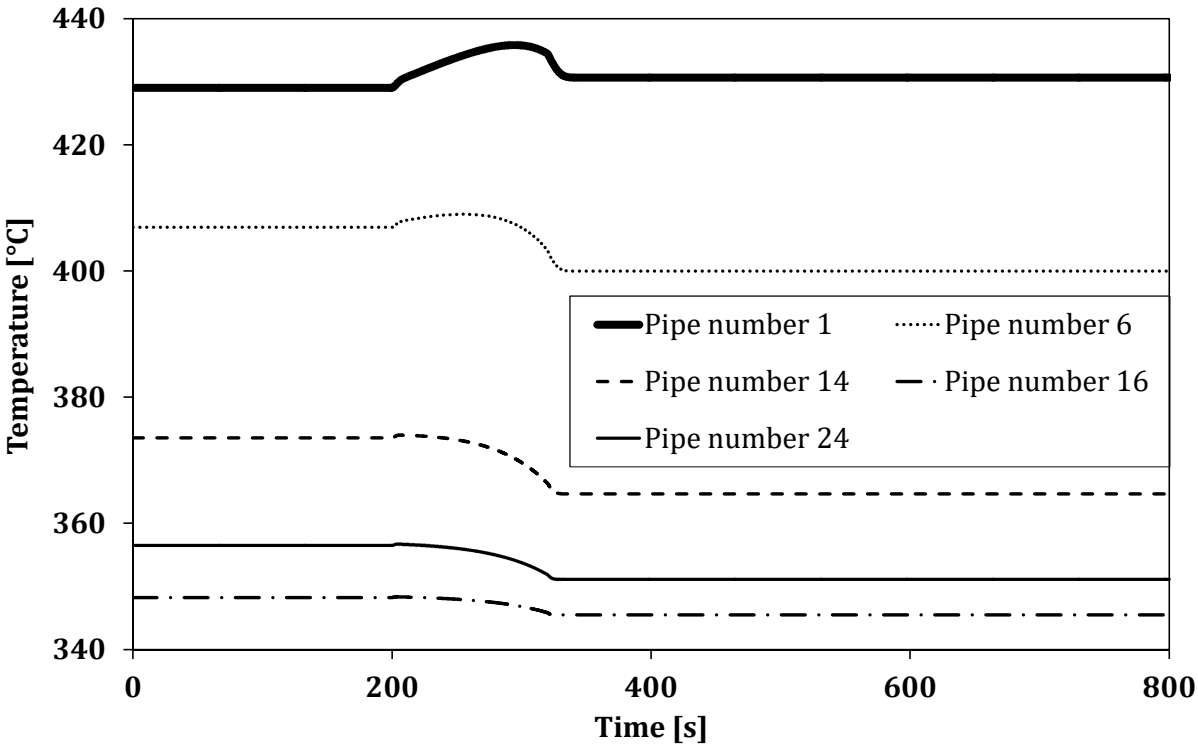

Figure 4-12: The metal temperature response at the centre of selected pipes in the primary superheater to a duty ramp down from 100% to 50% in 2 minutes.

4.4.4. Maldistribution of flow and temperature in the superheater header

Due to processes that occur upstream of the primary superheater in the boiler, flow and temperature maldistribution may be present across the cross section of the duct. This maldistribution in turn leads to maldistribution of steam flow and temperature going into the outlet header. These upstream processes may include the firing pattern of burners, slagging on the water walls and the outer fouling of heat exchangers preceding the primary superheater in the convective pass. The outer fouling pattern of the primary superheater itself can also influence the flue gas flow and temperature profile across the width of the heat exchanger. The experimental results shown by Gonzalez et al. [32] demonstrate the typical temperature maldistribution profile across the width of the heat exchanger in the convective pass that can be expected during operation.

A Flownex model made up by linking several individual tubesheet models was used to model the effect of a postulated parabolic flue gas inlet temperature maldistribution. Only half of the boiler width is modelled while assuming symmetry across the other half of the boiler. The results show the impact on the flue gas flow distribution across the width of the boiler as well as the steam flow and temperature distribution going into the outlet header.

A schematic representation of the superheater model covering more than one tubesheet is shown in Figure 4-5. Common nodes are created at the outlet of each stream, representing a section of the outlet header on the steam side and a section of the duct on the flue gas side. Flow is pulled through the heat exchanger on both the steam and flue gas sides by specifying negative mass sources at the respective outlets. This allows the flow to redistribute in both streams with respect to the specified flue gas inlet temperature profile and the interaction between the two streams. The steam inlet header temperature is assumed to be uniform.

Parabolic inlet flue gas temperature profile – clean tubes

Consider a case of a parabolic flue gas inlet temperature profile as shown in Figure 4-13. It is assumed that tubesheet 1, which is at the end near the water walls, experiences the lowest flue gas temperature while the highest temperature is at the centre line of the flue gas duct. This can be expected since the water walls are significant heat sinks. The boundary conditions are as follows: an average flue gas inlet temperature of 787.3 °C, a total flue gas mass flow rate of 57.5 kg/s, a uniform steam inlet temperature of 317.2 °C and a total steam mass flow rate of 49.5 kg/s.

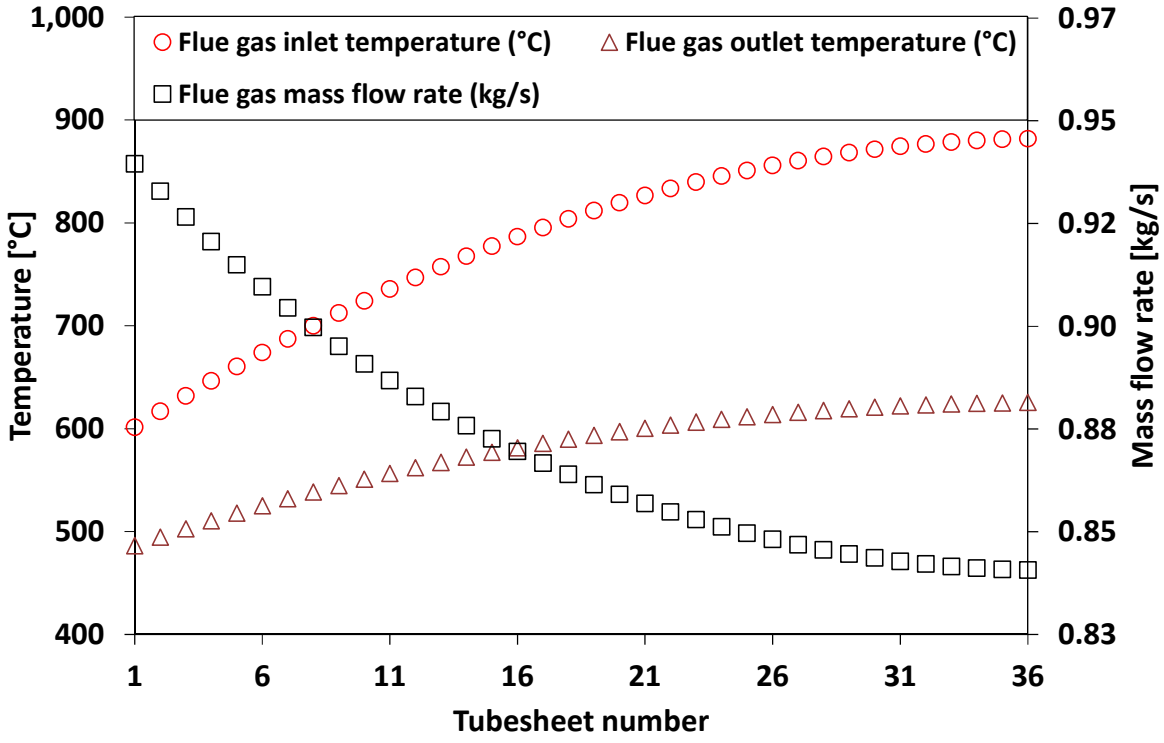

Figure 4-13: Flue gas flow and temperature distribution from the different tubesheets along the half header length.

The outlet flue gas temperature for clean tubes is expected to follow the same parabolic profile as shown in Figure 4-13. The flue gas mass flow automatically redistributes such that more mass flows through the region with lower temperature. Corresponding to the higher flue gas temperature towards the middle of the superheater, the outlet steam temperature is higher in that region compared to the sides, as demonstrated in Figure 4-14. The steam mass flow is also lower in the region with higher temperatures.

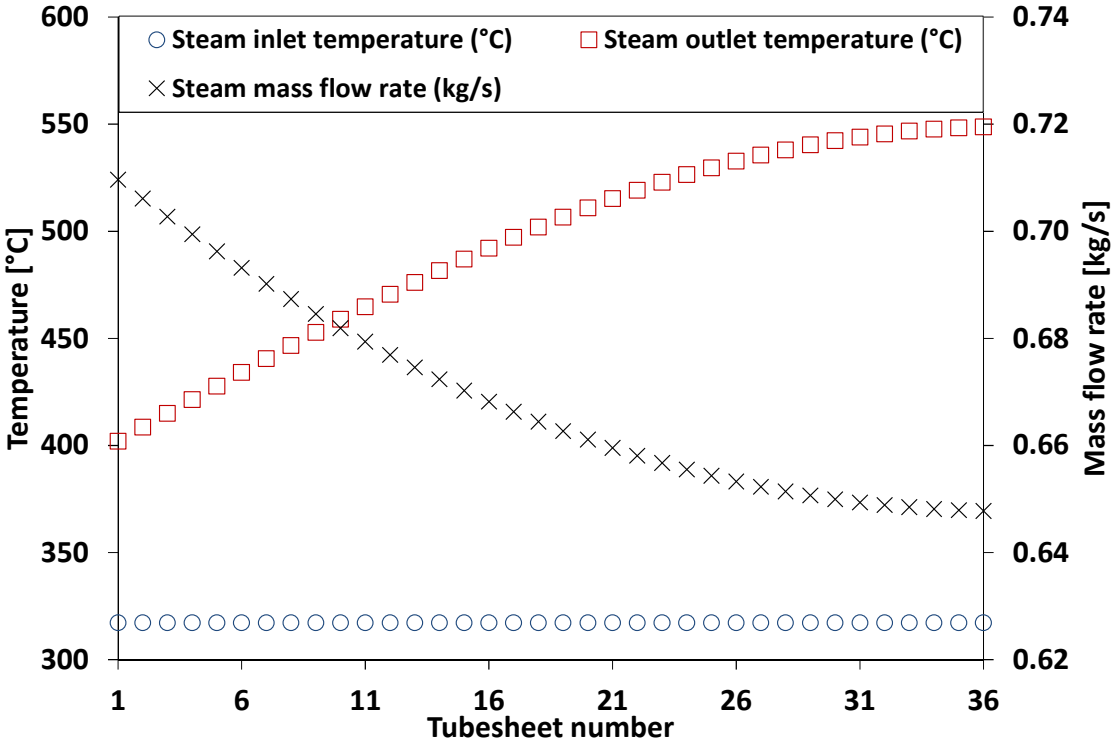

Figure 4-14: Steam flow and temperature distribution from the different tubesheets along the half header length.

The mass flow maldistribution in both the steam and flue gas passes is due to variations in the heat transfer rates, which result in variations in the fluid properties such as the density. This in turn influences the respective velocities and pressure drop characteristics that are taken into account in the momentum conservation equations.

Figure 4-15 shows the top view map of the associated flue gas temperature distribution across half of the flue gas duct. It clearly shows the higher temperatures in the middle compared to the sides.

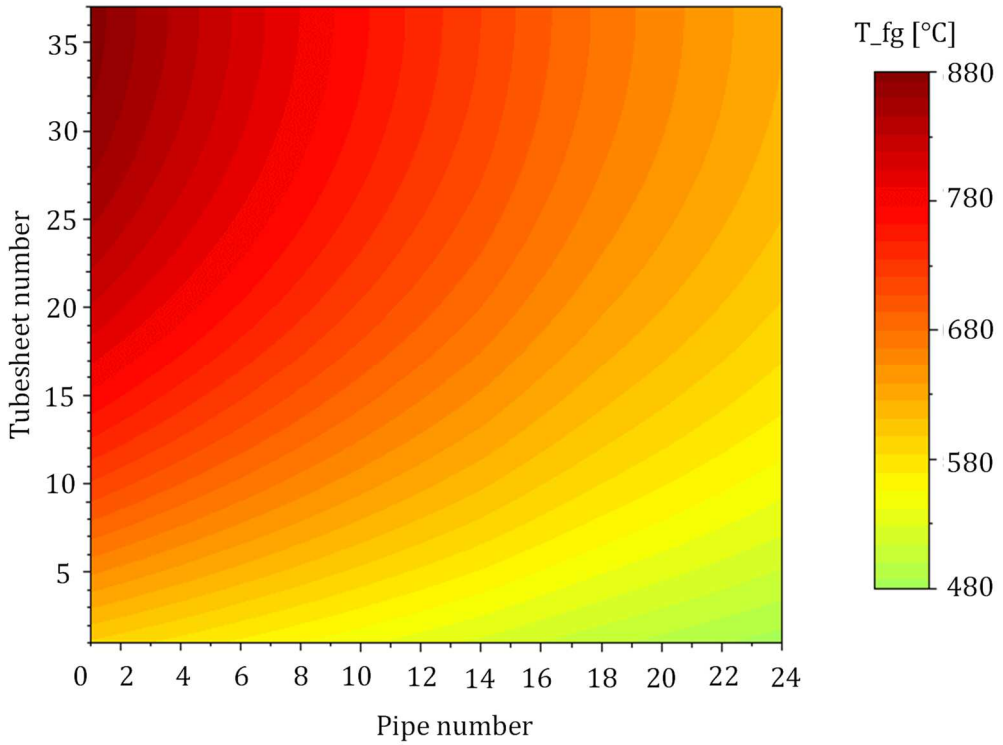

Figure 4-15: Top view of the flue gas temperature distribution across half of the superheater.

Parabolic inlet flue gas temperature profile – outer fouling around the centre line

During operation outer fouling usually begins to occur on the tubesheets situated closer to the centre line of the flue gas duct. This is one of the factors that result in the so-called M-type outlet steam temperature profile, where the outlet steam temperature profile has two or more peaks along the outlet header. This can be seen in the experimental results of Gonzalez et al. [32]. Such a temperature maldistribution leads to uneven expansion of the outlet header, thus contributing to thermal fatigue through the development of bending stresses. This bending can also contribute to tube-to-header weld cracks.

Using the half superheater model with the inlet conditions the same as those given for the clean case above, outer fouling of varying thickness was postulated from tubesheet number 31 to 36. Figure 4-16 demonstrates that the outlet steam temperature peaks around tubesheet number 30 and then dips towards the centre line of the superheater. This corresponds to an increase in flue gas outlet temperatures for tubesheets numbers 31 to 36 as shown in Figure 4-17.

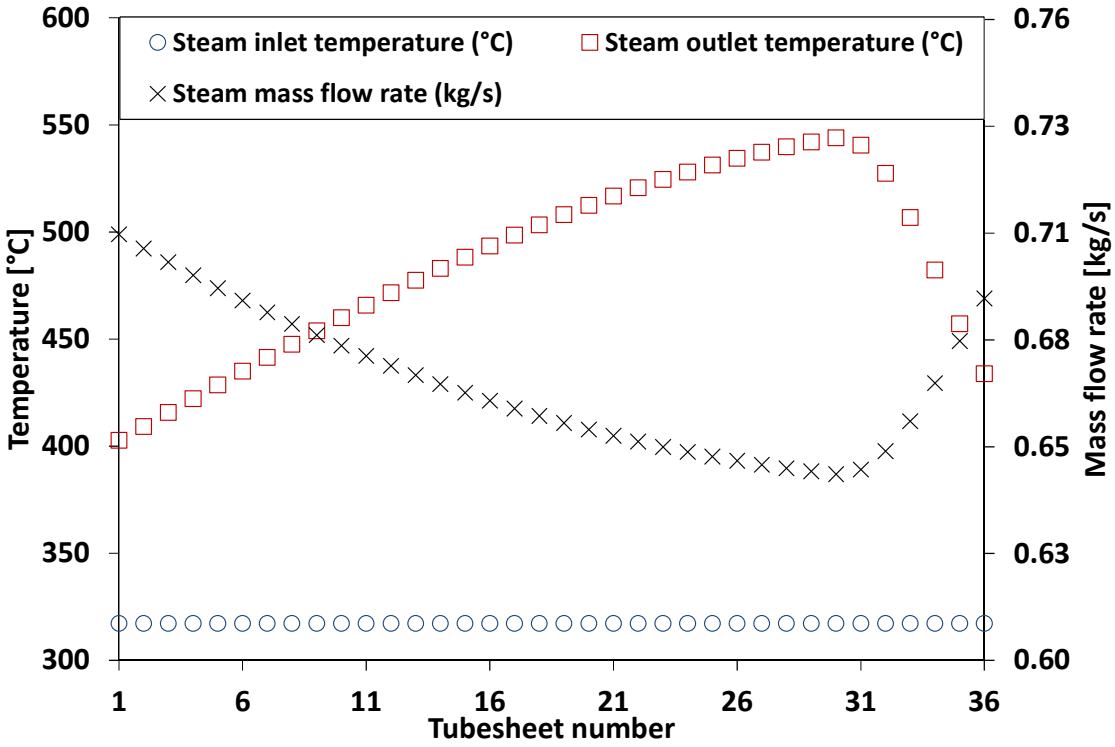

Figure 4-16: Steam flow and temperature distribution from the different tubesheets along the half header length with outer fouling on the middle tubesheets.

Figure 4-18 shows the top view map of the flue gas temperature distribution across half of the flue gas duct that resulted due to the outer fouling. Comparing Figure 4-18 to Figure 4-15 it can be seen that the higher temperatures in the middle region where there is more fouling propagates further downstream due to less heat transfer in the centre region.

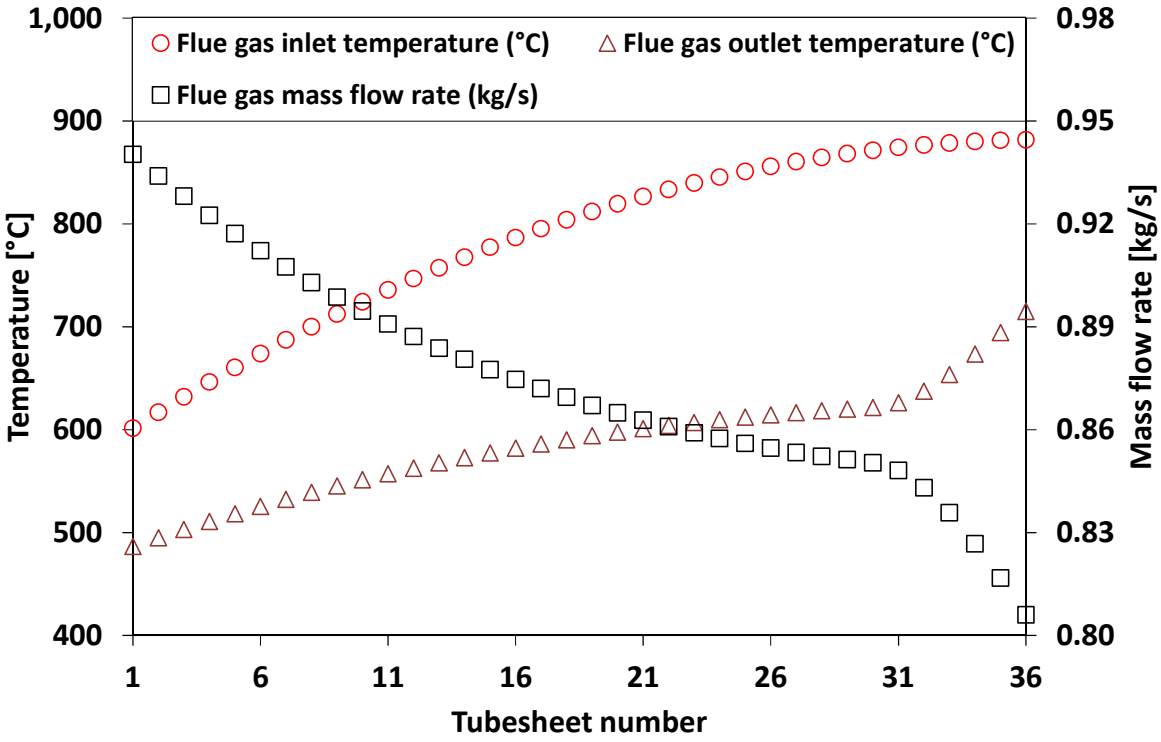

Figure 4-17: Flue gas flow and temperature distribution from the different tubesheets along the half header length with outer fouling on the middle tubesheets.

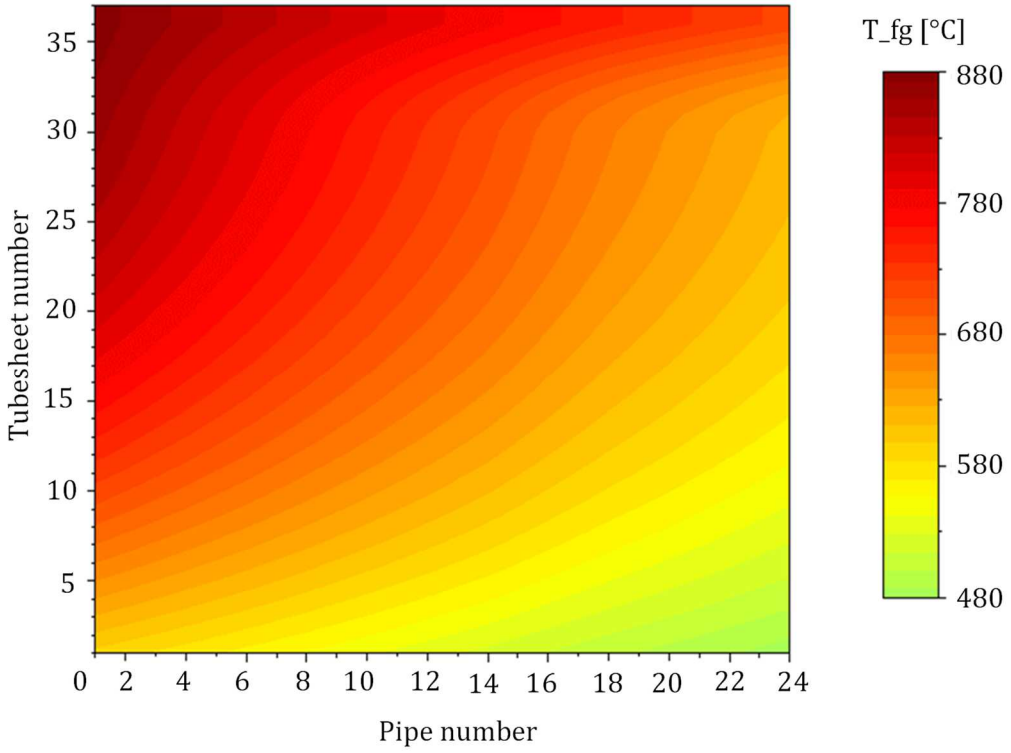

Figure 4-18: Top view of the flue gas temperature distribution across half the superheater with increased outer fouling around the centre line.

4.5. Summary: Application case study

This chapter presented the application of a one-dimensional network approach to model a superheater heat exchanger with complex geometry. This approach consists of iteratively solving the transient mass, energy and momentum conservation equations for each of the one-dimensional increments that are used to construct the complex three-dimensional geometry.

The heat exchanger geometry is discretized along the flue gas flow path as well as along the steam flow path. Each heat exchanger increment contains the appropriate geometrical information and thermal resistance characteristics. Empirical correlations were employed to model the inner and outer convective heat transfer. An effective heat transfer coefficient was used to account for radiation heat transfer. The emissivity of the gas was calculated using the weighted sum of gray gases model.

The results of a case with outer fouling were compared with results provided by Taler et al. [4]. The comparison was satisfactory for both the steam and flue gas temperatures. However, discrepances were observed in the predicted outer fouling layer temperatures. This is most probably due to the differences in the heat transfer correlations, flue gas properties and thermal radiation models used in the two different approaches. This comparison provides at least a qualitative validation of the model since a definitive validation is not possible due to a lack of detail data. This also highlights the need for more detailed real plant data in order to facilitate model validation studies.

Some of the advantages of the discretized Flownex model were illustrated when compared to lumped models based on the effectiveness-NTU method. The “black box” approach inherent in the lumped models falls short if detailed analysis of the temperature distributions through the heat exchanger is required. For instance, the lumped models cannot correctly predict the steam temperature distribution with a steam inlet that is not situated at the end of the heat exchanger, as well as when there is partial steam flow blockage in one of the tubes. However, for the most simple steady-state normal operation case the results of the discretized model corresponds very well with the overall counter flow model, provided that the correct overall UA value is employed in the lumped parameter model. This provides further confidence in the validity of the discretized model.

The capability of the model to study the effect of different ramp rates during load change on the tube metal temperatures was demonstrated. The results showed that higher metal temperatures are predicted on some tubes at increased ramp rates, even during load reduction. In addition, the tube by tube discretisation makes it possible to observe the different responses of the different tubes during load

changes. The ability to calculate the flow and temperature maldistribution within a tubesheet as well as across the width of the superheater was also demonstrated. The results showed the formation of an M-shaped outlet steam temperature profile due to increased outer fouling near the centre line of the flue gas duct.

It is envisaged that models based on a transient one-dimensional network approach such as the one proposed here, can be employed to study complex thermofluid process phenomena that may occur during intermittent, transient and low load operation of power plants. This could form the basis for improving operations and for the development of advanced tools for on-line process condition monitoring in support of preventative maintenance and outage planning.

5. FLUE GAS SIDE MODELLING

Up to this point in the dissertation, the sub-channel approach has been adopted in conjunction with the pipe network approach on the flue gas side modelling of the heat exchanger. In essence, only the dominant flow direction is modelled [58, 60]. This chapter investigates the limitations inherent in the network approach to fully account for the momentum conservation on the flue gas side within the heat exchanger, in an effort to illuminate the applicability of the proposed model.

In the convective pass of most boilers, the flue gas flows in a cross-flow configuration over several tubes and exchanges heat with the steam inside the tubes via convection and radiation. In principle, these arrays of tubes that are making passes in the boiler are obstructing the flue gas flow. This flue gas flow is governed by the fundamental physical principles of fluid dynamics. These principles are mathematically represented by the mass, momentum and energy conservation equations, which govern computational fluid dynamics (CFD) [117]. It is generally accepted that to obtain realistic flow patterns on the shell side of heat exchangers the conventional CFD approach with finely discretised meshes on a body-fitted coordinate system must be used. However, in engineering practise it is particularly time consuming to employ the conventional CFD approach in modelling the flue gas flow side, thus often alternative approaches are used. The CFD porous media approach and distributed resistance approach are some of the alternative approaches used.

It has been established that in literature there is no consensus in the terminology used to refer to these alternative approaches. Gomez et al. [33] employed the porous media approach yet stated that they used the conventional CFD technique for their model. Also, there has not been any clear distinction between the distributed resistance and porous media approaches. In most cases they have been considered to imply the same concept as in the case of Coelho [25], who used the porous media approach equations yet stating that he used the distributed resistance concept. The distributed resistance concept was established in 1974 by Patankar and Spalding [34] to simplify the modelling of shell and tube heat exchangers. In their initial equations, the effects of viscous diffusion were not included. However, they stated that the inclusion of such effects in the calculation procedure presented no difficulty. They also highlighted the possibility of such effects being neglected in densely-filled spaces such as in shell and tube heat exchangers. Patankar [59] emphasized this where he initially included the viscous action, effects of body forces and distributed resistance for the momentum

equations and the effects of diffusion on the energy equation. He then stated that for a densely packed volume, the diffusion terms can be ignored.

For consistency in this study the CFD porous media approach implies the approach that includes the viscous diffusion terms, body forces and the distributed resistance term. The distributed resistance approach implies the approach that eliminates the viscous terms since their effect is assumed to be negligible compared to that of the distributed resistance coefficients. However, the body forces are still present. In essence, the assumption that the volume is densely packed is adopted. Thus, the equations are the same as those in the initial paper by Patankar and Spalding [34]. This brings into focus the distributed resistance terms.

This chapter systematically investigates the applicability of the network approach in modelling two- or three-dimensional flows. The adopted systematic approach consists of two parts; the conceptual development and an illustrative example on a simplified model problem. The conceptual development begins with the fundamental governing equations for the conventional CFD approach, then the porous media approach, followed by the distributed resistance approach and then comparing the distributed resistance approach with the pipe network approach. Therefore, the narrative flows from the general to the simplified approach.

5.1. The governing equations

For the purposes of this study the flow is assumed to be isothermal and therefore the focus will be on the mass and momentum conservation equations only.

Continuity equation

$$\frac{\partial(\varepsilon\rho)}{\partial t}+\nabla\cdot\left(\varepsilon\rho\overline{u}\right)=0 \tag{5.1}$$

with ε , ρ and $\overline{u}$ representing the local porosity, density and volume averaged velocity vector, respectively. Furthermore, t is time and ∇ is the divergence or vector gradient operator.

The local porosity is defined as the ratio of the volume of the void spaces where the fluid flows to the bulk volume of a porous medium [74] and it is given as

$$\varepsilon=\frac{V_{fluid}}{V_{bulk}} \tag{5.2}$$

where V_{fluid} is the volume of the fluid and V_{bulk} is the total volume of the system.

Momentum equation

$$\frac{\partial(\varepsilon\rho\bar{u})}{\partial t}+\nabla\cdot(\varepsilon\rho\bar{u}\otimes\bar{u})=-\varepsilon\nabla p+\bar{f}+\delta\varepsilon\mu\nabla^2\bar{u}+\psi\varepsilon\bar{R}\bar{u} \tag{5.3}$$

where μ represents the dynamic viscosity and a Newtonian fluid is assumed. $\bar{f}$ represents the body forces and $\bar{R}$ represents the coefficients of the hydraulic distributed resistance due to the matrix structure obstructing the fluid flow. δ and ψ are constants which are either zero or one depending on which modelling approach is used.

The generalised mass and momentum conservation equations respectively given by eq. (5.1) and eq. (5.3) represent the equations for the conventional CFD, porous media and distributed resistance approaches. The difference for each approach depends on the choice of ε, δ and ψ as shown in Table 5-1. These differences are further discussed below.

Table 5-1: Summary of the corresponding constants to the governing equations.

Details	ε	δ	ψ
Conventional CFD approach	1	1	0
Porous media approach	$0 < \varepsilon < 1$	1	1
Distributed resistance approach	$0 < \varepsilon < 1$	0	1

5.1.1. Conventional CFD approach

The fundamental governing equations for the conventional CFD approach inherently characterised in eq. (5.1) and eq. (5.3) in conjunction with Table 5-1 can be applied on an infinitesimally small element fixed in space, shown in Figure 5-1, represented in a Cartesian coordinate system. Employing these governing equations in modelling the flue gas in the convective pass of a boiler is always time consuming in practise. This is due to catering for all the shear terms around the tube bank obstruction, as illustrated by the velocity gradient shown in Figure 5-2. In addition, this would require a finely discretised model, similar in topology but much finer than the one shown in Figure 5-3 for flow over one tube. This makes the model computationally expensive. Thus, for practical engineering cases, especially for online condition monitoring applications, an alternative approach has to be employed.

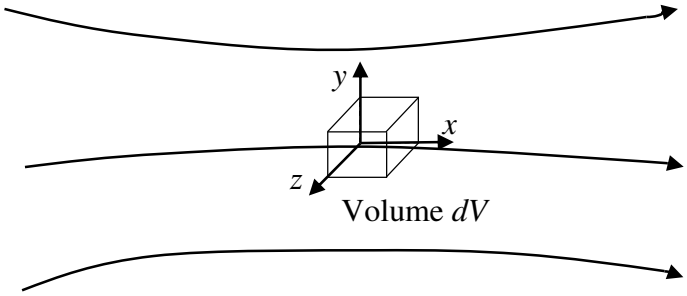

Figure 5-1: Infinitesimal fluid element fixed in space with fluid moving through it.

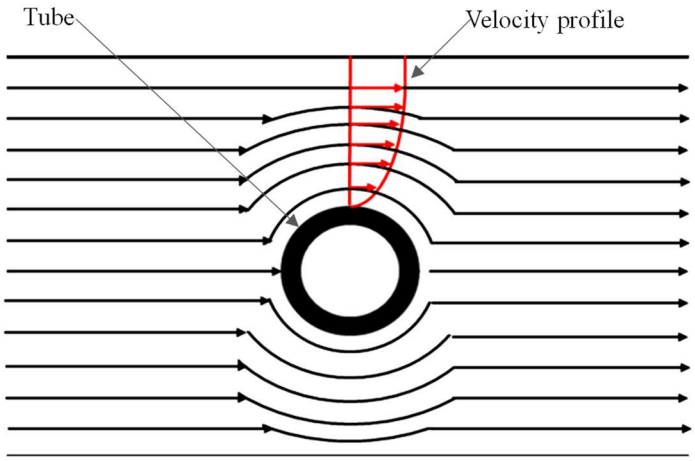

Figure 5-2: An example of a fluid flow case that can be modelled with the conventional CFD equations.

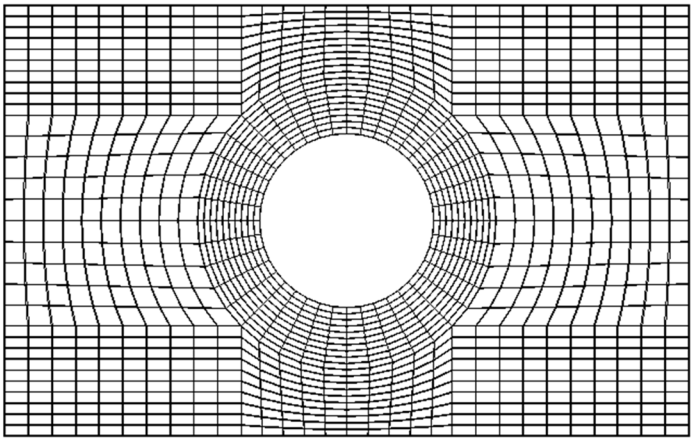

Figure 5-3: An example of a particularly course CFD grid for simulating flow over a cylindrical object.

5.1.2. Porous media approach

The porous media approach has been widely used as an alternative approach in engineering practise to model fluid flow in complex equipment with obstructions to flow e.g. shell and tube heat exchangers. It is based on the continuum approach which regards the volume within the shell of the heat exchanger as uniformly filled with fluid with distributed resistance to fluid flow [34, 74]. In essence, it models the fluid as if it is flowing through a porous media where fine scale turbulence effects are modelled via porous matrix resistance coefficients.

This approach allows for the use of a coarser grid similar to the one shown in Figure 5-4, compared to that of the conventional CFD approach shown in Figure 5-3, hence improving the economy of computer solving time and storage [34]. Another advantage of this approach is that it simplifies the modelling of the fluid flow over the porous structure through incorporating the porosity and a function that characterises the distributed resistance to flow. Usually, the functions to characterise the distributed resistance to the flow due to the solid matrix are determined experimentally.

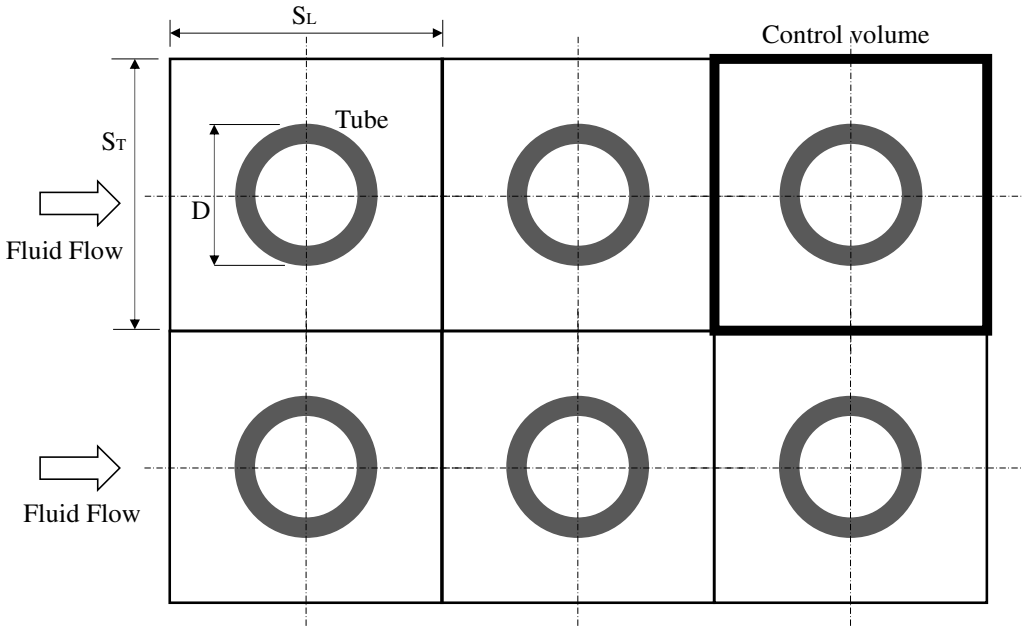

Figure 5-4: An example of a computational grid for the porous media approach applied in an inline tube arrangement.

The governing equations for this approach are similar to those of the conventional CFD approach (eq. (5.1) and eq. (5.3)) with the addition of the porosity and the adjustment to incorporate the distributed resistance as characterised in Table 5-1.

5.1.3. Distributed resistance approach

The distributed resistance approach is a simplified version of the porous media approach, with the only difference being that it does not account for the volume averaged superficial viscous actions as characterised in eq. (5.3) in conjunction with Table 5-1. However, the underlying continuum approach to fluid flow is also adopted in this approach.

The equations of the distributed resistance approach are solved on a computational grid similar to that of the porous media approach illustrated in Figure 5-4. In these equations, the local porosity and the coefficients of the hydraulic distributed resistance are based on the physical geometry of the enclosure and obstacles through which the fluid is flowing. These may vary from location to location in the enclosure depending on the variation in geometry. The determination of these two variables is explained in detail below.

5.1.4. Porosity

In illustrating the local porosity determination, consider the local flow over a tube as shown in Figure 5-5 in either inline or staggered tube arrangement. Employing eq. (5.2) leads to a porosity of

$$\varepsilon = 1 - \frac{\pi D^2}{4 S_L S_T} \tag{5.4}$$

This formulation is depended on the chosen control volume.

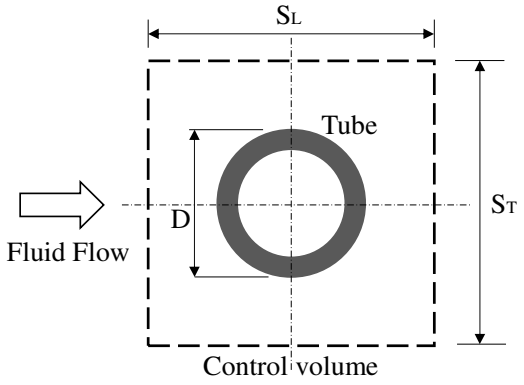

Figure 5-5: A control volume around a tube.

5.1.5. Distributed resistance coefficients

The coefficients of the hydraulic distributed resistance are algebraically related to the solid geometry, fluid properties and local velocity components. According to Patankar and Spalding [34] these coefficients can be given by dimensional analyses as follows

$$\frac{R_x \ell}{\rho u} = F_x\left(\rho\frac{u\ell}{\mu}, \frac{v}{u}, \frac{w}{u}\right) \tag{5.5}$$

with ℓ representing a local length dimension, e.g. the tube diameter. u, v and w represents the local velocity components in the x, y and z directions, respectively in accordance to the Cartesian coordinates system. From the dimensional analysis groups, a number of empirical correlations have been developed by researchers in the past. Bell [118], Zukauskas [119], Oka et al [120], and Rhodes and Carlucci [75] were amongst those researchers who contributed to this study.

Patankar [59] stated that the distributed resistance coefficients R_j for the $j-$ direction momentum can be obtained from the friction factor correlations. The correlations are given in the form

$$R_j = -\left(\frac{1}{2}\right)\left(\frac{\xi_j \rho v}{D_h}\right) \tag{5.6}$$

with v representing the magnitude of the resultant local volume averaged velocity, D_h representing the hydraulic diameter of the interspaces between obstacles and ξ representing the friction factor. The latter is usually given by the formula of the form

$$\xi = c\mathrm{Re}^n \tag{5.7}$$

where c and n are constants and Re is the local Reynolds number.

A further simplification of the distributed resistance approach would constitute the pipe-network approach. These are compared next.

5.2. Distributed resistance approach versus the pipe network approach

In this section, the fundamental equations for the distributed resistance approach are compared with that of the one-dimensional pipe network approach.

5.2.1. Continuity equation

For the distributed resistance approach, the continuity equation is given by eq. (5.1) as

$$\frac{\partial(\varepsilon\rho)}{\partial t} + \nabla \cdot \left(\varepsilon\rho\bar{u}\right) = 0 \tag{5.8}$$

Integrating this equation over the control volume which is fixed in space (an illustration shown in Figure 5-1) leads to

$$\iiint_V \frac{\partial(\varepsilon\rho)}{\partial t} dV + \iiint_V \nabla \cdot \left(\varepsilon\rho\bar{u}\right) dV = 0 \tag{5.9}$$

Applying the divergence theorem from vector calculus, the second volume integral on eq. (5.9) can be expressed as a surface integral as shown below.

$$\iiint_V \nabla \cdot \left(\varepsilon\rho\bar{u}\right) dV = \iint_S \left(\varepsilon\rho\bar{u}\right) \cdot d\bar{s}$$

where $\bar{s} = \bar{n}S$. Here, $\bar{n}$ is the outward pointing unit vector to the surface area S of the control volume.

Since the control volume used in these derivations is fixed in space, the limits of integration are constant so the time derivative $\partial/\partial t$ can be placed outside the integral as shown below.

$$\iiint_V \frac{\partial(\varepsilon\rho)}{\partial t} dV = \frac{\partial}{\partial t} \iiint_V \left(\varepsilon\rho\right) dV$$

Thus, eq. (5.9) becomes

$$\frac{\partial}{\partial t} \iiint_V \left(\varepsilon\rho\right) dV + \iint_S \varepsilon\rho\bar{u} \cdot d\bar{s} = 0 \tag{5.10}$$

The first term represents the rate of change of mass within the control volume and the second term represents the net outflow of mass from the control volume.

Now, the continuity equation given by eq. (5.10) is applied on the network approach. Figure 5-6 shows a computational domain for the network approach in three-dimensions. Here, the squares represent nodes and circles represent elements. In the network approach, the conservation of mass is applied on the nodes. A node represents a volume that contains a fluid with multiple mass flows into and out of it. After the integration of eq. (5.10) over a 3-D control volume and simplifying the effective volume represented by εV to V , the continuity equation can be simplified to

$$\left.\frac{\partial \rho}{\partial t}\right|_P = \frac{1}{V}\left(\sum \dot{m}_i - \sum \dot{m}_e\right) \tag{5.11}$$

since the second term in eq. (5.10) represents the sum of all the mass flows out minus the sum of the mass flows into the control volume. The continuity equation given by eq. (5.11) is exactly the same as eq. (3.1) which was introduced in chapter 3 for the network approach.

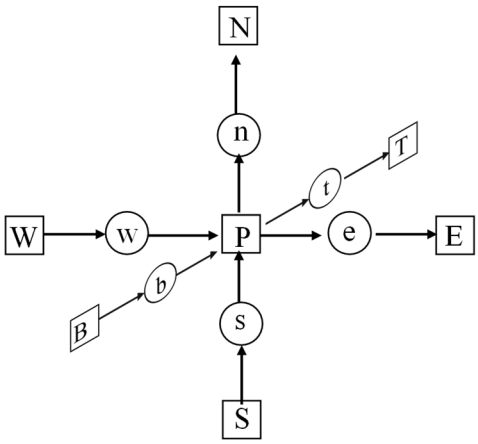

Figure 5-6: A demonstration of the pipe network approach applied on a three-dimensional computational domain.

The continuity equation for the distributed resistance approach may be solved on a similar staggered grid as for the pipe network approach. Figure 5-7a) shows a control volume on a two-dimensional grid on which the continuity equation of the pipe network approach, given by eq. (5.11), is solved. Figure 5-7b) shows a control volume on a two-dimensional grid on which the continuity equation of the distributed resistance approach, given by eq. (5.1), is solved. Comparing the two diagrams shows that the continuity equations for the two approaches are exactly equivalent.

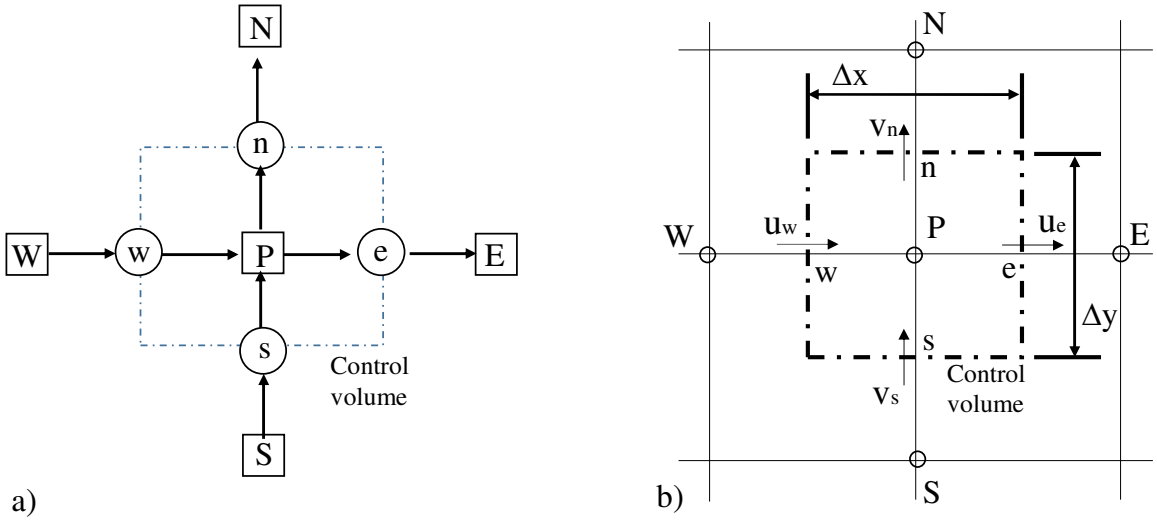

Figure 5-7: A control volume on a two-dimensional grid on which the continuity equation for a) the network approach and b) the distributed resistance approach is solved.

5.2.2. Momentum equation

The momentum equation of the distributed resistance approach, given by eq. (5.3) in conjunction with Table 5-1, can be represented as

$$\frac{\partial(\varepsilon\rho\bar{u})}{\partial t}+\nabla\cdot(\varepsilon\rho\bar{u}\otimes\bar{u})=-\varepsilon\nabla p+\bar{f}+\varepsilon\bar{R}\bar{u} \tag{5.12}$$

This equation can be transformed into an integral form using the Reynolds Transport Theorem, resulting in

$$\frac{\partial}{\partial t}\iiint_V \bar{u}\varepsilon\rho dV+\iint_S \bar{u}(\varepsilon\rho\bar{u}\cdot d\bar{s})=\sum\bar{F} \tag{5.13}$$

The terms position in the equation corresponds to their positions in the partial differential form of the equation given by eq. (5.12). The first term on the left represents the rate of change of momentum within the control volume. The second term on the left represents the net flow rate of momentum out of the control volume. The term on the right represent the sum of all the forces acting on the fluid within the control volume, including the distributed resistance terms.

Now, consider a one-dimensional control volume fixed in space as shown in Figure 5-8. Since the length of this control volume is very small and the change in area is also very small, the volume can be approximated by $Ad\ell$.

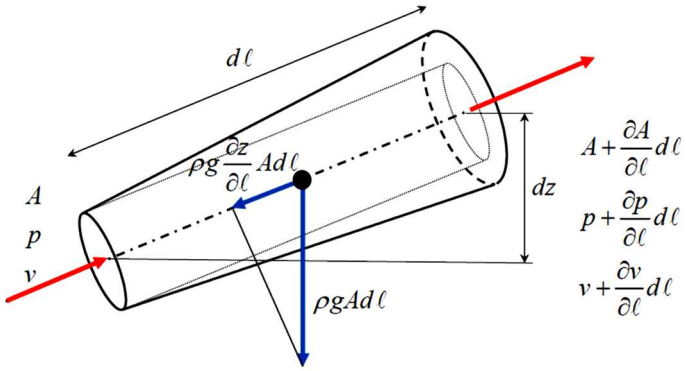

Figure 5-8: An arbitrary infinitely small one-dimensional control volume where A is the effective area [121] fixed in space.

If it is assumed that the unit vector is always in line with the direction of the flow, eq. (5.13) can be transformed from a vector equation to a scalar equation as illustrated below. In the 1-D control volume shown in Figure 5-8, the rate of change of momentum is then transformed as follows

$$\frac{\partial}{\partial t}\iiint_V \bar{u}\varepsilon\rho dV = \frac{\partial}{\partial t}(\rho v) A d\ell$$

with $A d\ell = \varepsilon dV$ which is the effective volume and A representing the effective cross-sectional area in the porous structure.

The net flow rate of momentum out of the control volume is also transformed as follows

$$\iint_S \bar{u}\left(\varepsilon\rho\bar{u}\cdot d\bar{s}\right) = \left[\rho v^2 A + \frac{\partial}{\partial \ell}\left(\rho v^2 A\right) d\ell\right] - \rho v^2 A$$

$$= \frac{\partial}{\partial \ell}\left(\rho v^2 A\right) d\ell$$

The forces acting on the fluid in the control volume can be classified as surface and body forces. The surface forces are due to physical contact with the fluid in the control volume and include forces due to static pressure, frictional and secondary losses as well as pressure rises. Body forces are the forces that do not need direct contact with fluid in the control volume and they include forces due to gravity, magnetic field and electric field. In the network approach, only the component of the forces that are aligned with the flow direction are considered. The forces can therefore be represented by scalars rather than vectors. The net force due to static pressure on the fluid in the control volume is given by

$$-\frac{\partial p}{\partial \ell} A d\ell$$

The net force due to frictional and secondary losses where there is contact with the wall is given by

$$-\frac{\partial p_{0L}}{\partial \ell} A d\ell$$

with p_0 representing the total pressure. The total pressure is the sum of the static pressure and dynamic pressure given by $p_0 = p + \frac{1}{2}\rho v^2$. The net force due to pressure rise associated with work done on the control volume is given by

$$\frac{\partial p_{0W}}{\partial \ell} A d\ell$$

The component of the body force due to gravity that is aligned with the flow direction is represented as

$$b\varepsilon\rho dV = -\rho g \frac{\partial z}{\partial \ell} A d\ell$$

Combining all these terms on a per unit volume basis in accordance with eq. (5.13) leads to

$$\frac{\partial}{\partial t}(\rho v) + \frac{1}{A}\frac{\partial}{\partial \ell}\left(\rho v^2 A\right) = -\frac{\partial p}{\partial \ell} - \frac{\partial p_{0L}}{\partial \ell} + \frac{\partial p_{0W}}{\partial \ell} - \rho g \frac{\partial z}{\partial \ell} \tag{5.14}$$

valid for both compressible and incompressible flows. With further mathematical manipulations together with the application of mass conservation, eq. (5.14) reduces to

$$\rho\frac{\partial v}{\partial t} + \rho v\frac{\partial v}{\partial \ell} + \frac{\partial p}{\partial \ell} = \frac{\partial p_{0W}}{\partial \ell} - \frac{\partial p_{0L}}{\partial \ell} - \rho g \frac{\partial z}{\partial \ell} \tag{5.15}$$

For incompressible flows, the second term on the left-hand side which represents the convective momentum in the direction of the flow can be manipulated as follows

$$\rho v\frac{\partial v}{\partial \ell} = \frac{\partial\left(\frac{1}{2}\rho v^2\right)}{\partial \ell}$$

Now, inserting this into eq. (5.15) and combining it with the static pressure term leads to

$$\rho\frac{\partial v}{\partial t} + \frac{\partial\left(p + \frac{1}{2}\rho v^2\right)}{\partial \ell} = \frac{\partial p_{0W}}{\partial \ell} - \frac{\partial p_{0L}}{\partial \ell} - \rho g \frac{\partial z}{\partial \ell} \tag{5.16}$$

Thus, the equation can be written in terms of total pressure as follows

$$\rho\frac{\partial v}{\partial t} + \frac{\partial p_0}{\partial \ell} = \frac{\partial p_{0W}}{\partial \ell} - \frac{\partial p_{0L}}{\partial \ell} - \rho g \frac{\partial z}{\partial \ell} \tag{5.17}$$

Integrating eq. (5.17) over a one-dimensional control volume with a finite length L between the inlet i and the outlet e with an average cross-sectional area A leads to

$$\rho L \frac{\partial v}{\partial t} + \left(p_{0e} - p_{0i} \right) = \rho g \left(z_i - z_e \right) + \Delta p_{0W} - \Delta p_{0L} \tag{5.18}$$

Further manipulations of the transient term results in

$$\frac{\partial \dot{m}}{\partial t} = \frac{A}{L} \left(\left(p_{0i} - p_{0e} \right) + \rho g \left(z_i - z_e \right) + \Delta p_{0W} - \Delta p_{0L} + Lv \frac{\partial \rho}{\partial t} \right) \tag{5.19}$$

This is the transient one-dimensional form of the momentum equation for incompressible flow that was introduced in chapter 3, eq. (3.3). This is now a single scalar equation aligned with the flow, whereas the momentum equation for the distributed resistance approach consist of vector equations.

If a staggered grid approach is adopted in solving the governing equations of the distributed resistance approach given by eq. (5.1) and eq. (5.3), in two dimensions the grid will be as shown in Figure 5-9. The continuity equation is solved on the grid points as shown by its control volume while both the x and y momentum equations are solved in between the grid points. The advantage of the staggered grid is that it eliminates checkerboard solutions [122]. Furthermore, the pipe network approach adopted in this work is based on a similar strategy. For the network approach, the governing equations given by eq. (5.11) and eq. (5.19) are solved on the grid shown in Figure 5-10 which is imposed on the two-dimensional staggered grid. In Figure 5-10 it is shown that the continuity equation is solved around the nodes while the momentum equations are solved around the elements. As mentioned above, for the continuity equation the terms solved for on the distributed resistance approach and the pipe network approach are identical. However, for the momentum equation it is not the case. The difference is mainly on the term which represents the net flow rate of momentum out of the control volume.

For further analyses, the term representing the convective momentum (second term in eq. (5.3)) in the distributed resistance approach is expanded on the Cartesian coordinate system in three-dimensions. Now, consider the component of this term in the x direction as shown below.

$$\frac{\partial(\varepsilon \rho u u)}{\partial x} + \frac{\partial(\varepsilon \rho v u)}{\partial y} + \frac{\partial(\varepsilon \rho w u)}{\partial z}$$

It illustrates that in addition to the momentum convected in the direction of the flow, it includes the contribution of the momentum from the convected flux in the y and z directions.

For the one-dimensional pipe network approach, the contribution of the y and z fluxes to the scalar momentum equation cannot be taken into account at the east and west faces. This is because the term representing the net flow rate of momentum out of the control volume (second term in eq. (5.14)) is

$$\frac{1}{A}\frac{\partial}{\partial \ell}\left(\rho v^2 A\right)$$

which only accounts for the flux in the direction of the flow. This term is then manipulated to represent the dynamic pressure component and then added to the static pressure to form the total pressure.

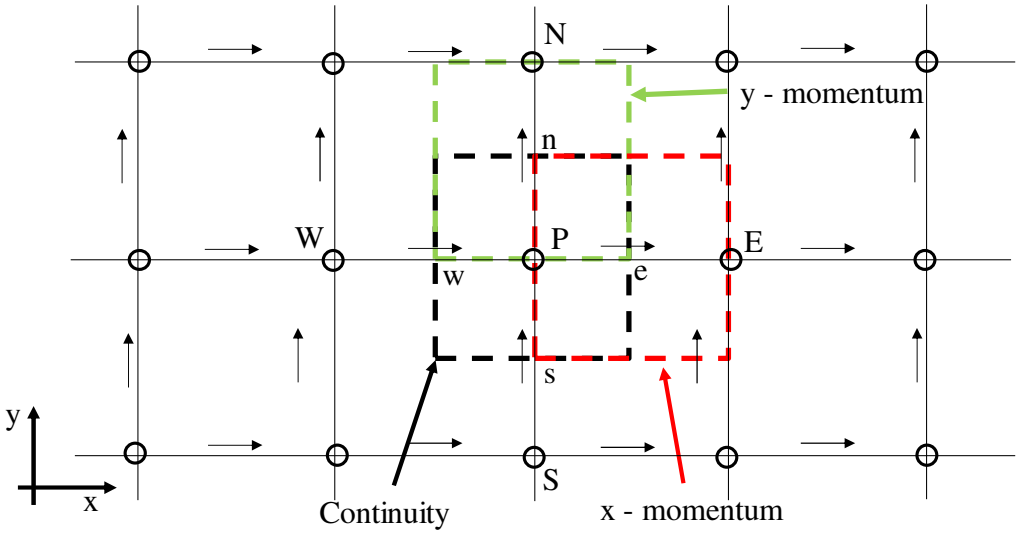

Figure 5-9: A two-dimensional staggered grid in the Cartesian coordinate system.

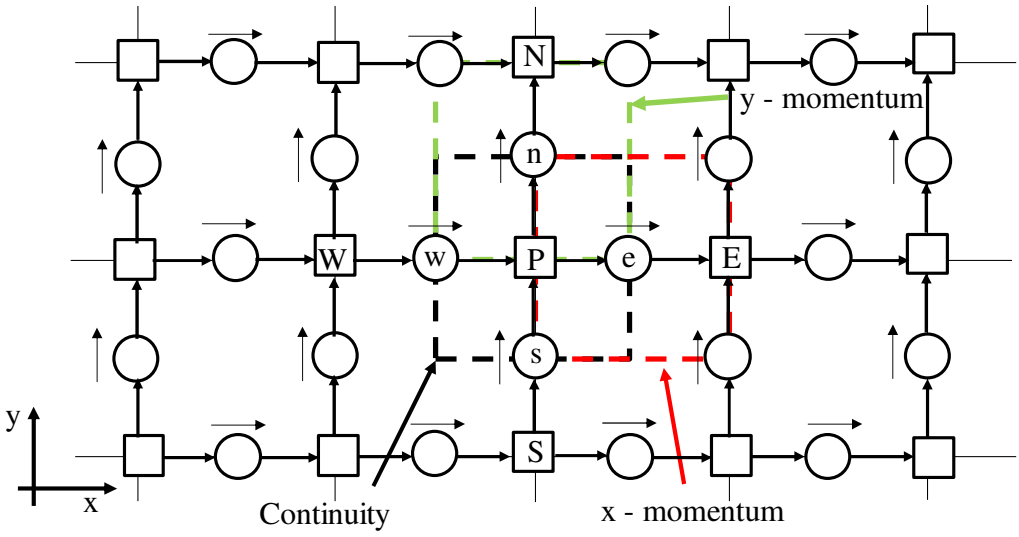

Figure 5-10: Imposing the one-dimensional network approach grid on the two-dimensional staggered grid.

According to Greyvenstein [100], solving for total pressure in the network approach presents an advantage as it retains the convective momentum term in the direction of the flow but eliminates it in the solution technique. However, accounting for only the convective momentum in the direction of the flow implies that if the network approach is employed in two- or three-dimensional flows in an open space might result in some inaccuracies. The magnitude of the error is flow physics dependent.

Furthermore, for the pipe network approach the pressure drop due to the pipe wall friction is given by

$$\Delta p_{oL} = \left(\frac{1}{2}\right)\frac{fL}{D_h}\rho v^2 \tag{5.20}$$

where f is the friction factor and D_h is the hydraulic diameter. On the other hand, integrating the x momentum equation for the distributed resistance approach, which can be derived from eq. (5.3), over a control volume with finite length L and an average cross sectional area A the resulting distributed resistance force per unit area from eq. (5.6) is given by

$$R_x uL = \left(\frac{1}{2}\right)\frac{\xi L}{D_h}\rho u^2 \tag{5.21}$$

Equating eq. (5.21) to eq. (5.20) shows that

$$\xi = f$$

Thus, the distributed resistance coefficient of the distributed resistance approach can be correlated to the friction factor in the pipe network approach.

5.3. Case study to systematically illustrate the differences between the approaches

This section aims to further analyse the applicability of the one-dimensional network approach in modelling two-dimensional or three-dimensional fluid flow. To scrutinize the applicability of the network approach, it is compared to other modelling approaches. A case specific quantitative analyses is undergone to magnify the differences.

5.3.1. Model problem

To qualify and quantify the differences, the illustrative example which is schematically shown in Figure 5-11 is used. This case is isothermal; thus, the energy equation is not solved. This example involves an incompressible Newtonian fluid flowing through a single 2-D control volume of dimensions one metre by one metre. The inlet x and y velocities are specified as 5 m/s and 1 m/s,

respectively. The outlet static pressures are also specified as zero Pascals (this is relative to a reference pressure as is the custom in CFD codes). The density of the incompressible fluid is given as 1 kg/m^3.

In the following subsections, the various modelling approaches are used in a systematic format viz.: distributed resistance approach, simplified distributed resistance approach, network approach and custom developed 1-D steady state flow exact solutions.

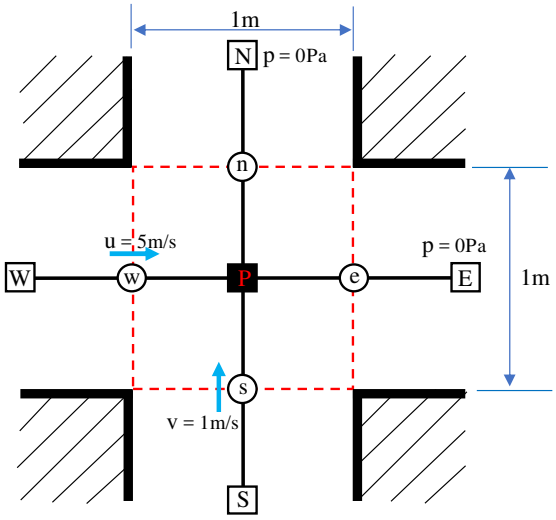

Figure 5-11: A single 2-D control volume for an incompressible fluid.

Computational domain discretisation

For comparison purposes, this example is solved on a single 2-D computational cell using a staggered grid as shown in Figure 5-12 for CFD and pipe network approaches.

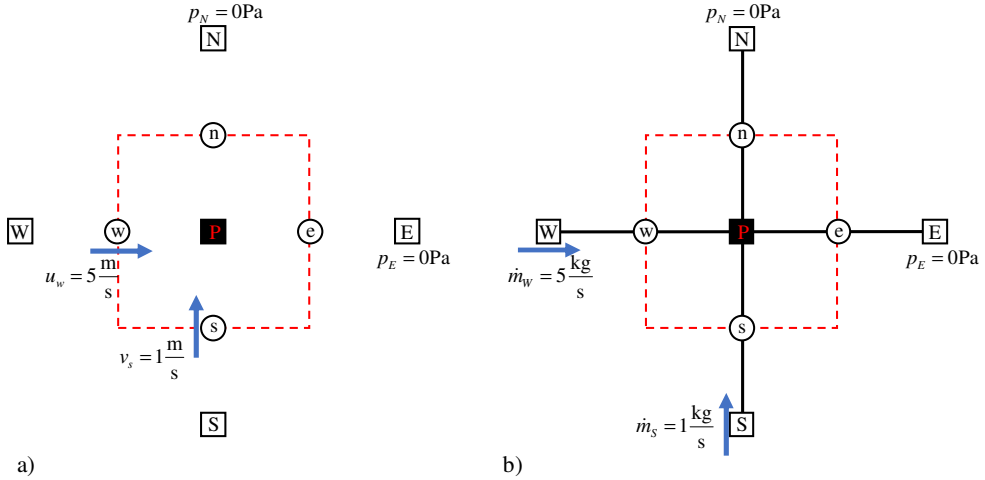

Figure 5-12: Model problem on the two computational domains: a) 2-D CFD staggered grid and b) the pipe network staggered grid.

The governing equations

The general governing equations for the distributed resistance approach and simplified distributed resistance approach are shown below for the 2-D incompressible and isothermal case. The continuity equation is given by

$$\frac{\partial u}{\partial x}+\frac{\partial v}{\partial y}=0 \tag{5.22}$$

and the x and y momentum equations are given by

$$\begin{aligned}\frac{\partial(\rho u)}{\partial t}+\frac{\partial(\rho uu)}{\partial x}+\psi_{SDR}\frac{\partial(\rho vu)}{\partial y}&=-\frac{\partial p}{\partial x}+\beta_x\rho|u|u\\ \frac{\partial(\rho v)}{\partial t}+\psi_{SDR}\frac{\partial(\rho uv)}{\partial x}+\frac{\partial(\rho vv)}{\partial y}&=-\frac{\partial p}{\partial y}+\beta_y\rho|v|v\end{aligned} \tag{5.23}$$

with ψ_{SDR} being a constant which is one for the distributed resistance approach and zero for the simplified distributed resistance approach.

Distributed Resistance Approach

The distributed resistance (DR) approach is a form of the CFD porous media approach where the non-matrix diffusion terms are ignored. This is due to the assumption that in a computational domain with several obstacles most of the resistance to flow will come from the obstacles (porous matrix) rather than the shear in the fluid. The 2-D equations of this approach are also generically given by eq. (5.22) and eq. (5.23) with the constant $\psi_{SDR}=1$.

Simplified Distributed Resistance Approach

The simplified distributed resistance (SDR) approach is a version of the distributed resistance approach that only solves for convective momentum in the direction of the flow. Thus, it neglects the cross convective momentum terms. The equations associated with the simplified distributed resistance approach are also generically given by eq. (5.22) and eq. (5.23) but with the constant $\psi_{SDR}=0$.

1-D Network Approach: Flownex

The network approach used in this work is encapsulated in Flownex. Flownex solves the 1-D conservation equations of mass and momentum. The governing equations that Flownex solves are as follows; the continuity at the intersection is given by

$$\sum \dot{m}_e - \sum \dot{m}_i = 0 \tag{5.24}$$

and the momentum equation is given by

$$\rho \frac{\partial v}{\partial t} + \frac{\partial p_0}{\partial \ell} = \frac{\partial p_{0L}}{\partial \ell} \tag{5.25}$$

where

$$\Delta p_{oL} = \beta \rho v^2$$

with

$$\beta = -\frac{f}{2}\frac{L}{D_H}$$

Some similarities can be drawn from the simplified distributed resistance approach and the network approach; however, their solution techniques differ, as emphasised below.

The pressure projection methodology is used as a solution technique for the distributed resistance approach and the simplified distributed resistance approach. In this solution scheme the governing continuity and momentum equations are solved on a staggered grid computational domain. The pressure projection methodology is explained below. The network approach employs the Implicit Pressure Correction Method on a staggered grid computational domain as explained in chapter 3.

Pressure projection methodology

Since the case modelled here is isothermal and incompressible, then the pressure projection methodology involves three steps:

Step 1: Compute $\Delta \overline{w}^*$ from

$$\frac{\Delta \overline{w}^*}{\Delta t} = -\nabla \cdot \left(\overline{w}^n \otimes \overline{u}^n \right) + \mu \nabla^2 \overline{u}^n \tag{5.26}$$

where

$$\overline{w} = \begin{bmatrix} \rho u \\ \rho v \end{bmatrix}$$

and

$$\Delta \overline{w}^* = \overline{w}' - \overline{w}^n$$

with $\overline{w}'$ an intermediate momentum term.

Step 2: Solve for pressure implicitly from

$$0 = \nabla \cdot \overline{u}^n - \frac{\Delta t}{\rho} \nabla^2 p^{n+1} + \frac{1}{\rho} \nabla \cdot \left(\Delta \overline{w}^* \right) \tag{5.27}$$

using $\Delta \overline{w}^*$ computed in Step 1.

Step 3: Finally compute the velocity $\overline{u}^{n+1}$ which is at the next time step form

$$\overline{u}^{n+1} = \overline{u}^n - \frac{\Delta t}{\rho} p^{n+1} + \frac{1}{\rho} \Delta \overline{w}^* \tag{5.28}$$

where the pressures are as computed in Step 2 and $\Delta \overline{w}^*$ computed in Step 1.

5.3.2. Inviscid flow

Consider an inviscid flow scenario of the model problem shown in Figure 5-11. The analytical solution is trivial i.e. undisturbed flow. Applying the network approach using the computational grid shown in Figure 5-12b), the computed velocity and static pressures are presented in Table 5-2. The network approach predicts that the flow will split equally in both the x and y directions at the outlets. However, practically this will not be the case, as the flow will continue undisturbed in this case. The full calculations for this are detailed in Appendix B. Also evident from Table 5-2 are that both the distributed resistance (DR) and simplified DR approaches achieve the exact solution in terms of predicted flow velocities. However, only the DR method computes the static pressures correctly. In the case of the simplified DR approach this is attributed to the cross convective momentum terms being neglected.

Table 5-2: A comparison of the summary results from the network approach, simplified distributed resistance approach and distributed resistance approach for a steady state case with inviscid flow.

Details	**Symbols**	**Units**	**Network approach**	**Simplified DR**	**Distributed resistance (DR)**
x outlet velocity	u_e	m/s	3	5.000	5.000
y outlet velocity	v_n	m/s	3	1.000	1.000
Internal static pressure	p_P	Pa	-2.22	0.000	2.500
Inlet x static pressure	p_W	Pa	-8	0.000	5.000
Inlet y static pressure	p_S	Pa	4	0.000	5.000

To further gain some insights on the modelling approaches, the x and y streams in the model problem are decoupled as shown in Figure 5-13. These streams are then solved separately using basic fluid mechanics techniques. This is not far off from what most CFD codes do, but it falls-short because the two streams are not then linked back to each other. The summary results for this scenario are presented in Table 5-3.

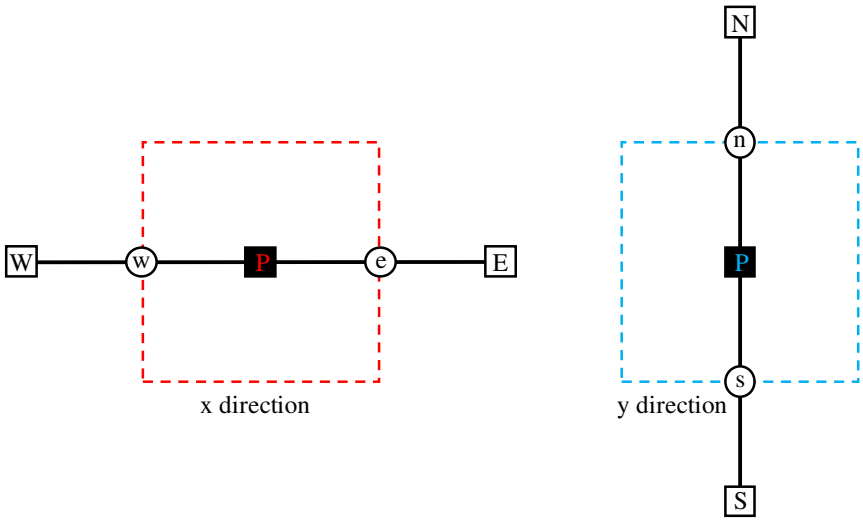

Figure 5-13: Decoupled x and y flow streams.

It is shown on Table 5-3 that the total pressures calculated from each stream are different, i.e.

$$p_{0xP} = 12.5\text{Pa} \quad p_{0yP} = 0.5\text{Pa}$$

Thus, if a solution technique which solves for a common total pressure at the common node **P** were to be applied, the results from that method will be different from the 1-D exact solution results. Hence, the difference in the network approach results for such a case presented in Table 5-2, since it solves for total pressure rather than the static pressure. It is further shown in Table 5-3 that the static pressures at the common node **P** are the same and exactly zero. That is

$$p_{xP} = 0\text{Pa} \quad p_{yP} = 0\text{Pa}$$

This implies that the results from the simplified distributed resistance approach should be the same as that of the two decoupled streams and that is confirmed by Table 5-2 and Table 5-3. Thus, despite having the same variation of the governing equations, the solution techniques used for the network approach and the distributed resistance approach led to different results in this case. This analysis also brings forth that at the common node **P**, static pressure is a scalar, yet total pressure is a vector. Thus, the results of the simplified distributed resistance approach are governed by the directionality of the

flow which is encapsulated by the physics in the x and y momentum equations. This illustrates the short-comings of the network approach for such a case, since it solves for total pressure rather than the static pressure. The inherent 1-D momentum equation of network approach neglects the directionality of the total pressure at the common node **P**, thus solving for total pressure as if it is a scalar quantity at that common node.

Table 5-3: x and y streams results at the nodes from the 1-D exact solutions for inviscid flows.

x direction							
Details	**Nodes**	**W**		**P**		**E**	
	Units	**Symbols**	**Values**	**Symbols**	**Values**	**Symbols**	**Values**
Velocity	m/s	u_W	5	u_P	5	u_E	5
Static pressure	Pa	p_W	0	p_{xP}	0	p_E	0
Total pressure	Pa	p_{0W}	12.5	p_{0xP}	12.5	p_{0E}	12.5
y direction							
Details	**Nodes**	**S**		**P**		**N**	
	Units	**Symbols**	**Values**	**Symbols**	**Values**	**Symbols**	**Values**
Velocity	m/s	v_S	1	v_P	1	v_N	1
Static pressure	Pa	p_S	0	p_{yP}	0	p_N	0
Total pressure	Pa	p_{0S}	0.5	p_{0yP}	0.5	p_{0N}	0.5

5.3.3. Resistance to flow

In this dissertation, however flow subjected to resistances due to the presence of tube bundles is considered. Therefore, now consider the model problem shown in Figure 5-11 which has some resistance to the flow. For this analysis the Flownex model shown in Figure 5-14 was set-up. Initially, a small resistance to flow is introduced. The resistance is introduced in Flownex as a friction factor in all directions and the value is

$$f = 0.01$$

Figure 5-14 and the first results column in Table 5-4 show the summary of the results from the Flownex simulation. Notable in the network approach results column in Table 5-4 is that the x and y outlet velocities are the same still as was for the inviscid flow case. They just split equally in both directions.

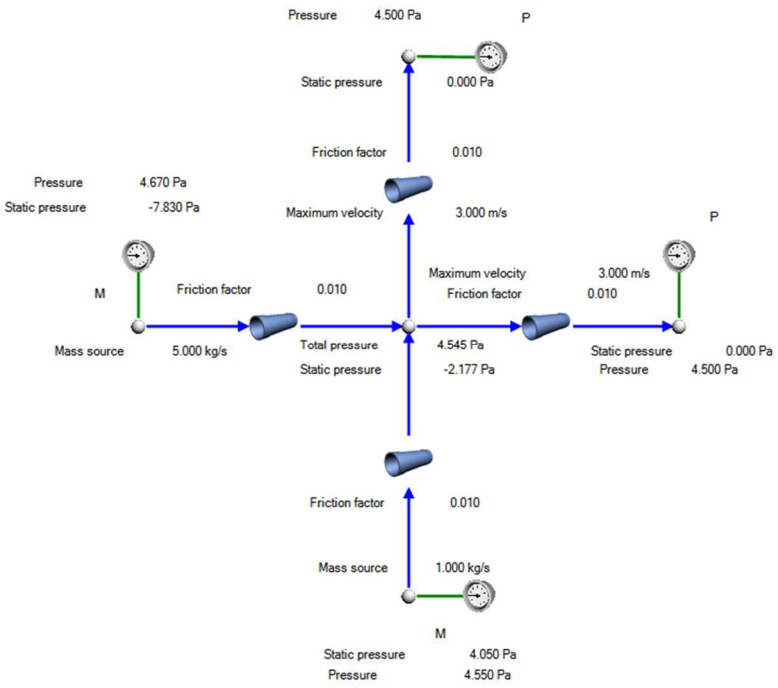

Figure 5-14: Flownex results for the case with low resistance.

Again, for comparison purposes the simplified distributed resistance approach is employed. In this case, the distributed resistance factors are the same for all the momentum control volumes. In order to correspond to the friction factor for the network approach, the distributed resistance factor is calculated to be

$$\beta_x = \beta_y = -0.005\frac{1}{m} \tag{5.29}$$

Applying the pressure projection methodology, the velocity and static pressure results are summarised in the middle results column in Table 5-4. Again, the results from the simplified distributed resistance approach do not correspond to that of the network approach. The results of the simplified distributed resistance approach demonstrate a flow with directionality whereas the results from the 1-D network approach does not take directionality into account. For further emphasis on the directionality of the flow, for the simplified distributed resistance approach the components of directional total pressure in the common node **P** are given as

$$p_{0x_P} = p + \frac{1}{2}\rho u^2 = 0.024 + \frac{1}{2}\times 1\times\left(\frac{5+4.987}{2}\right)^2 = 12.49Pa$$

$$p_{0y_P} = p + \frac{1}{2}\rho v^2 = 0.024 + \frac{1}{2}\times 1\times\left(\frac{1+1.013}{2}\right)^2 = 0.53Pa$$

Yet for the network approach, the total pressure is a scalar and as shown in Figure 5-14. It is given as

$$p_{0_P} = 4.545 Pa$$

The directionality of the total pressure is due to the dynamic pressure component due to the convective momentum in the direction of the flow for 1-D cases. Since for the network approach this dynamic pressure is absorbed in the formulation of the momentum equation using total pressure, it is unable to manifest the directionality of the flow. Instead, the total pressure at the common node is calculated using a weighted averaged velocity as illustrated in Appendix B for the inviscid case. For the network approach, static pressures are obtained through post-processing, hence the reason some negative values as shown in Figure 5-14.

Again, to illustrate the effect of the additional convective momentum terms on the solution for this model problem, the distributed resistance approach was employed. The results from the distributed resistance approach are shown on the far-right column in Table 5-4. As was the case with the inviscid flow, again for this case only the static pressure values were affected. These static pressures are higher than those from the simplified distributed resistance approach. The flow patterns are exactly the same.

Table 5-4: A comparison of the summary results from the network approach, simplified distributed resistance approach and distributed resistance approach for a steady state case with resistance to flow.

Details	**Symbols**	**Units**	**Network approach**	**Simplified DR**	**Distributed resistance**
x outlet velocity	u_e	m/s	3.00	4.987	4.987
y outlet velocity	v_n	m/s	3.00	1.013	1.013
Internal static pressure	p_P	Pa	-2.177	0.025	2.551
Inlet x static pressure	p_W	Pa	-7.830	0.117	5.176
Inlet y static pressure	p_S	Pa	4.050	0.037	5.056

For further analysis, 1-D exact solutions of the separated x and y streams as shown in Figure 5-13 are again used to help gain some further insights. From basic fluid mechanics calculations, some results for the x and y flow streams are shown in Table 5-5 for the nodes. These results are different to those from the inviscid flow case (Table 5-3) because both the static pressures and the total pressures at the common node (**P**) are different. Thus, in this case both techniques that solves for static pressure and total pressure for the model problem will result in different results to that of the 1-D exact solutions.

Table 5-5: x and y streams results at the nodes from basic fluid mechanics.

x direction							
Details	**Nodes**	**W**		**P**		**E**	
	Units	**Symbols**	**Values**	**Symbols**	**Values**	**Symbols**	**Values**
Velocity	m/s	u_W	5	u_P	5	u_E	5
Static pressure	Pa	p_W	2.50	p_{xP}	1.25	p_E	0
Total pressure	Pa	p_{0W}	15.00	p_{0xP}	13.75	p_{0E}	12.5
y direction							
Details	**Nodes**	**S**		**P**		**N**	
	Units	**Symbols**	**Values**	**Symbols**	**Values**	**Symbols**	**Values**
Velocity	m/s	v_S	1	v_P	1	v_N	1
Static pressure	Pa	p_S	0.10	p_{yP}	0.05	p_N	0
Total pressure	Pa	p_{0S}	0.60	p_{0yP}	0.55	p_{0N}	0.5

From the results of the 1-D basic solutions on two separate streams, the static pressure values for the common node **P** were found not to be the same and they are given as

$$p_{xP} = 1.25\text{Pa} \quad p_{yP} = 0.05\text{Pa}$$

Thus, this signals that the resulting solutions from the simplified distributed resistance approach will be different to that of the 1-D separate stream exact solutions. That is evident from the simplified distributed resistance results shown in Table 5-4 when compared to the results of the 1-D exact solutions shown in Table 5-5. As practically expected, the simplified distributed resistance approach shows that some flow from the x direction is diverted to the y direction due to a higher resistance in the outlet x momentum direction.

The introduction of resistance in the flow paths illustrates some changes to the static pressures at the common nodes. Thus, stemming from this, next an investigation on the influence of the resistance factor on the accuracy of the network approach. Flow resistance is added to both directions and by equal amounts, increasing from zero to five per meter. For this investigation the results of the network approach were compared to those of the distributed resistance approach. The results are depicted in Figure 5-15, illustrating that as the distributed resistance factor increases equally in both directions, the flow distribution percentage error reduces.

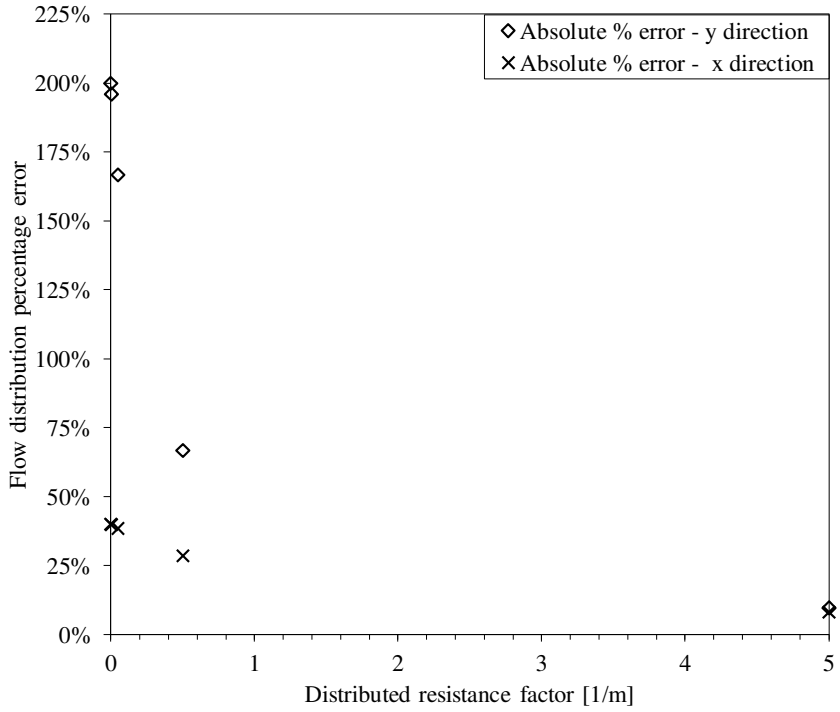

Figure 5-15: The flow distribution percentage error behaviour corresponding to equal variation of the distributed resistance factor in both directions.

However, the considered heat exchangers in this dissertation do not have equal resistances to flow in both directions. In this heat exchangers, the highest resistance is due to the tube bundles in the dominant direction of the flow. Thus, the network approach will present some limitations in modelling the 2-D or 3-D phenomena of the flue gas side flow of these heat exchangers. Here, the network approach would depict the flow choosing the path of least resistance which would not conform to real life observations.

5.4. The applicability of the network approach to heat exchangers in boilers

The insight gained from the study above demonstrated some limitations in using the network approach for two-dimensional and three-dimensional flows especially those with low resistance to flow. Since, for this project the network approach is selected as the modelling approach, then going forward the subchannel approach that was used in chapter 3 will be used to model the radiant final stage superheater heat exchangers. So, there will be no flue gas side vertical connections to allow for flow mixing. The flow is assumed to be flowing in channels perpendicular to the tubes. Now, one may ask what are the practical implications for this?

In practice the superheater heat exchangers close to the furnace (typically platen types) have large transversal pitch, which means that the flue gas side looks more like open space with low resistance to flow. Thus, using the network approach to model the flue gas flow one would not be able to determine the correct flow patterns. In addition, the flow through these superheaters are typically not perpendicular to the tubes. So, assuming simple flow perpendicular to the tubes will be erroneous. However, the correct flow pattern is not very important at all since these heat exchangers are totally dominated by radiation rather than convection. So correctly accounting for the direct radiation from the furnace and the gas radiation from the high temperature flue gas in the superheater region is key for thermal performance determination.

Moving further away from the furnace (towards the final superheater heat exchanger analysed in the case considered in chapter 6) the transversal pitch becomes smaller and the flow in the convective pass becomes more perpendicular to the tubes. Therefore, as convection heat transfer becomes more important and therefore the flow pattern becomes more important, the network approach with flow specified near perpendicular to the tubes becomes more and more suitable. However, one should recognise that some adjustment to the convection coefficient correlations may be necessary to slightly compensate for the flow pattern that might have not been specified correctly (and cannot be predicted using the network approach). This also brings forth the physical structure factor in the modelling aspects. Boiler designs and so the heat exchangers in the convective pass vary from station to station.

Therefore, in this work the limitations of network approach encapsulated in Flownex are recognised based on a fundamental understanding of the simplifications involved. However, from the insight gained from this study an understanding of the implications of adopting the network approach for the practical problems modelled here was developed. Thus, it will be used responsibly going forward while always keeping in mind these limitations.

5.5. Chapter summary

The objective of this chapter was to investigate the applicability of the network approach encapsulated in the Flownex software in modelling the flue gas side of a superheater heat exchanger in a coal fired boiler. The study was carried out systematically. It began with a conceptually analyses of most of the modelling approaches that can be used where the assumptions from one approach to the next were highlighted. The governing equations of the network approach were compared in-depth to those of the distributed resistance approach. In the comparison, it was pointed out that the network approach neglects the convective momentum terms that are not in the direction of the flow since it only focuses

on one-dimensional flows. Due to the one-dimensional assumption, the convective momentum term is combined with the static pressure term, allowing for the use of the total pressure in the solution scheme.

To further illuminate some of the limitations of the network approach, a model problem was considered. The network approach was mainly compared to the distributed resistance approach; however, some intermediate approaches were used to assist in gaining further insights. For the studied model problem, the effect of neglecting the convective momentum terms not in the direction of flow were noticed on the static pressures rather than flow distribution. The major limitation was due to the solution technique adopted by the network. Due to the inherent assumption of one-dimensional flow in the network approach, the approach solves for total pressure as a non-directional parameter even at common nodes in cases of two-dimensional flows. This led to the software being used outside its inherent computational domain characteristics which is flows in pipes.

After gaining insights on the limitations of the network approach in modelling the open spaces on the flue gas side of the heat exchangers it was concluded that the philosophy of the subchannel approach should be used going forward. The subchannel approach philosophy provides better accuracy than allowing for mixing in the network approach. This implies that flue gas flow computations should be done in the predominant direction of the flow. Thus, no mixing of the flow in between streams should be allowed on the network approach model.

6. REFINED METHODOLOGY: MODEL DESCRIPTION

In Chapters 3 and 4 a network modelling methodology was proposed and demonstrated for convective superheaters with gas radiation. However, it only accounted for radiation to the heat exchanger tubes from the gas surrounding it. It did not account for any direct radiation that originated elsewhere (such as the furnace exit plane or gas contained in a neighbouring heat exchanger) that may pass through the surrounding gas without being absorbed and then impinge directly on the tubes. This chapter describes the further refinement of the proposed network methodology to include this direct radiation phenomenon and presents a practical case study applied to a final stage radiant superheater in a coal-fired boiler. The information provided include the relevant geometry, heat exchanger arrangements and the detail description of the Flownex model for the final stage superheater and its process flow conditions.

High-level models are employed to attain the flue gas conditions and these models are described in this chapter as well. These high-level models are lumped models or overall performance models of the systems or subsystems that influence the behaviour of the final stage radiant superheater heat exchanger. They include the boiler mass and energy (MEB) and parts of the boiler design method which is known as the Gurvich Method.

6.1. Coal-fired boiler geometry and heat exchanger arrangements

The final stage radiant superheater heat exchanger for a 600 MW class coal-fired power plant is considered. This final superheater is a sub-system in the convective pass of the coal-fired boiler shown in Figure 6-1. Figure 6-1 shows a schematic of the overall layout of the drum-type two-pass boiler with the relevant subsystems.

In the arrangement of the heat exchangers in the convective pass, the final superheater of interest in this work is located in between two heat exchangers as shown in Figure 6-2. Upstream of the final superheater is the platen superheater and downstream is the secondary/final reheater. The subsystems upstream and downstream have an influence on the operation of the final superheater. Figure 6-2 also shows that the flue gas cross flow area reduces as the flow moves towards the back-pass. This cross-flow area reduction is mostly around the final stage superheater and the final stage reheater.

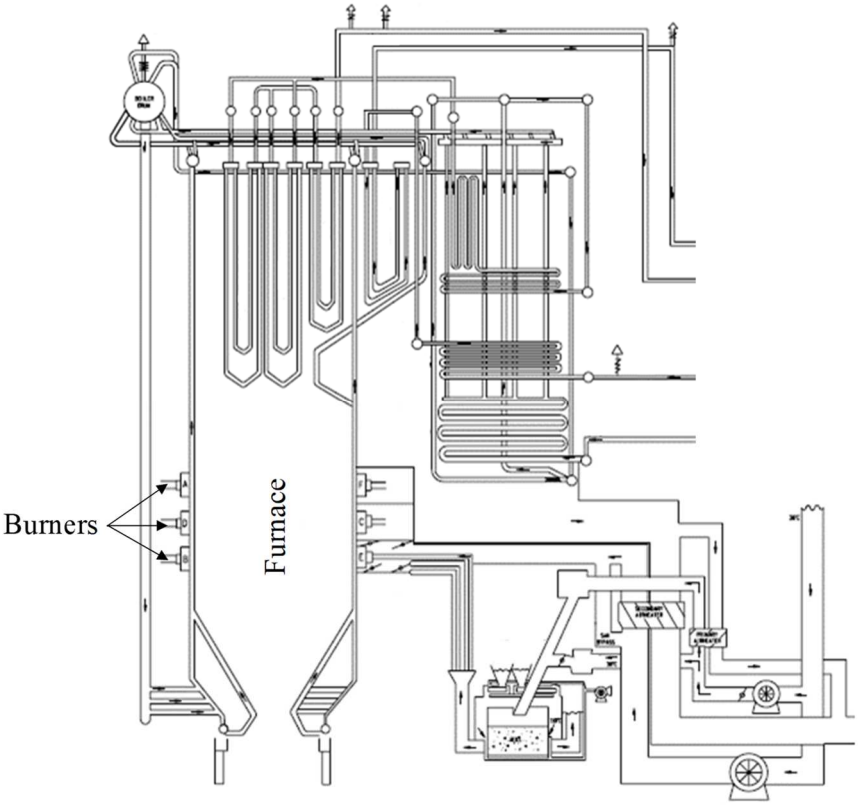

Figure 6-1: The overall layout of the boiler including the furnace and the convective pass (Courtesy of Eskom).

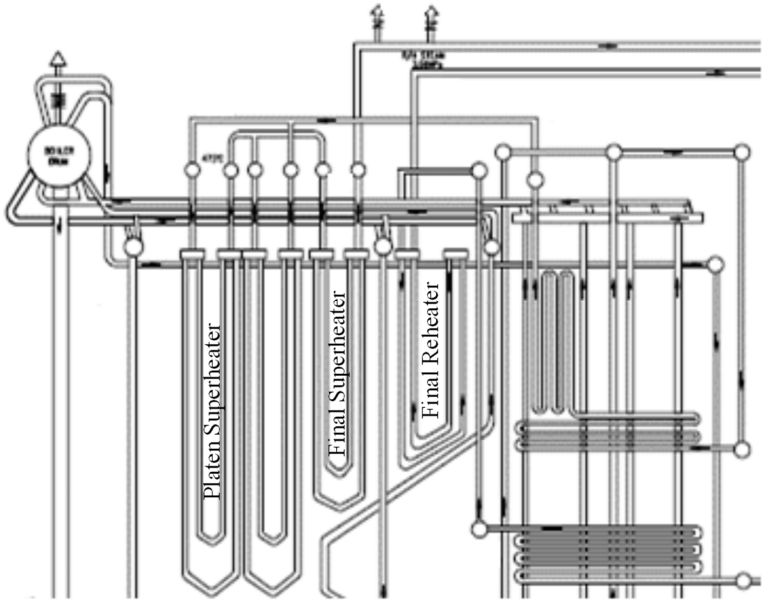

Figure 6-2: The arrangement of the heat exchangers in the convective pass (Courtesy of Eskom).

6.1.1. Final superheater heat exchanger geometry

A solid model of the final superheater geometry is shown in Figure 6-3. This superheater consists of 28 tubesheets/elements suspended from the roof of the boiler. Each element has 34 inline U-shaped tubes connected to the inlet and outlet stub-headers. Each U-shaped tube makes two passes inside the boiler and consists of three different tube sections in series having the same outer diameter, but with different wall thicknesses, as highlighted in Figure 6-4 and Table 6-1. The common outer diameter is 44.5 mm while the respective tube wall thicknesses are 6.3, 8.8 and 11 mm. The total height and width of each element are 15.878 m and 3.921 m, respectively.

Two pipes connect each of the 28-inlet stub-headers and 28-outlet stub-headers to the four inlet and two outlet main headers, respectively as shown in Figure 6-4. The connecting pipes on the inlet and the outlet are equally distributed into four legs namely leg A, B, C and D, as illustrated in Figure 6-3. Pairs of two of these legs connect to each of the outlet main headers.

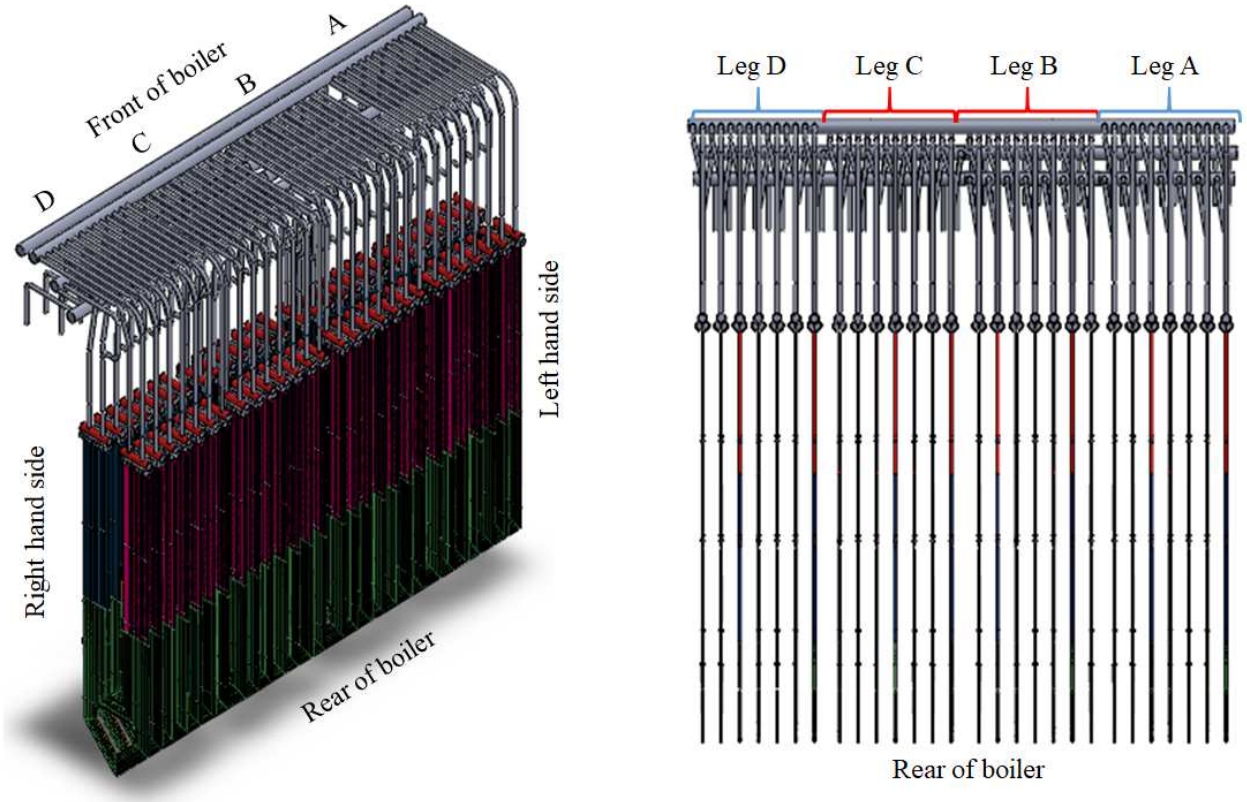

Figure 6-3: The final superheater.

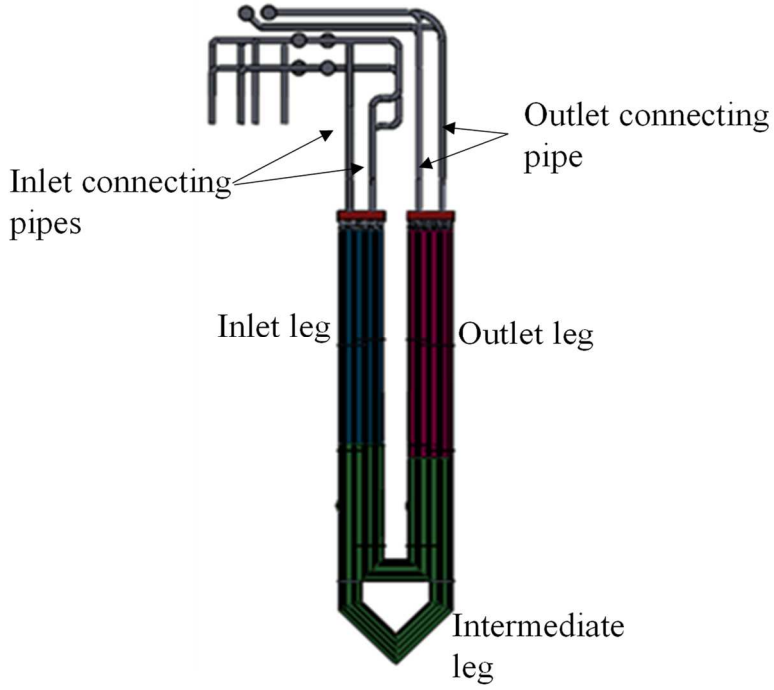

Figure 6-4: Side elevation (looking from the right-hand side) of the final superheater.

Table 6-1: Geometrical information of each leg in a tube sheet.

Details	**Units**	**Inlet leg (blue)**	**Intermediate leg (green)**	**Outlet leg (red)**
Outer diameter	mm	44.5	44.5	44.5
Thickness	mm	6.3	8.8	11
Design temperature	°C	527	559	584
Design pressure	MPa	19.04	19.04	19.04

6.2. Superheater model development

The model is based on the 1-D network approach introduced in Chapter 3, that involves the solution of the 1-D mass, energy and momentum conservation equations. In applying this approach, the physical layout of the tube passes in each element is represented by the layout of the network as shown in Figure 6-5. To limit the complexity, bundles of tubes may be grouped together and discretised depending on the level of detail required. The 1-D network approach allows for the mass flow rates and temperatures to redistribute in the heat exchanger in accordance to the interaction between the steam flow, flue gas flow and the tube material. In this model, all the relevant modes of heat transfer

are accounted for. The model is built using specific building blocks which consist of heat exchanger increments for regions containing tubes, and open flow channels for regions without tubes as shown in Figure 6-6a and Figure 6-6b, respectively. As concluded in chapter 5, on the flue gas side the model does not attempt to model the flow patterns due to the limitations of the underlying network approach it is based on. Thus, the flue gas is modelled as if it is flowing in channels in the predominant direction of the flow. However, due to the one-directional nature of the steam flow in the tubes, the model building blocks are connected such that they trace the steam path as is in the real plant.

In this case the 34 parallel tubes per pass in each tubesheet are grouped together in four bundles along the flue gas flow path. Consider the inlet leg that is modelled using four bundles: the first two of these bundles each consist of eight tubes and the last two each consist of nine tubes. These tubes are grouped together with great care, to ensure that tubes with similar inner diameters are bundled together since this is a requirement for correct calculation of the heat transfer coefficients that depend on the local flow velocity via the Reynolds number. The total effective tube outer heating surface area for one tubesheet in the discretized Flownex model is 133.25 m^2.

Note the differences between this final superheater heat exchanger when compared to the primary superheater heat exchanger that was studied in the previous case study in chapter 4. These differences allow for the application of a slight variation of the modelling approach when grouping tubes together and discretization along the height of the final superheater.

In addition to geometrical information, the inputs in this model are inlet temperatures and pressures for both the flue gas and steam streams, the mass flow rates of these streams, and the direct radiation heat transfer from the flue gas in the furnace and the platen superheater spaces. Again, in this model, the mass flow rates were given as negative sources at the outlet, thus effectively drawing the correct total mass flow through the heat exchanger. This allows the mass flow to automatically distribute along the flow paths with respect to the thermophysical phenomena occurring in the heat exchanger. Such a model is capable of analysing maldistribution of mass flow and temperatures within an element as well as the entire heat exchanger in both steady state and transient operations.

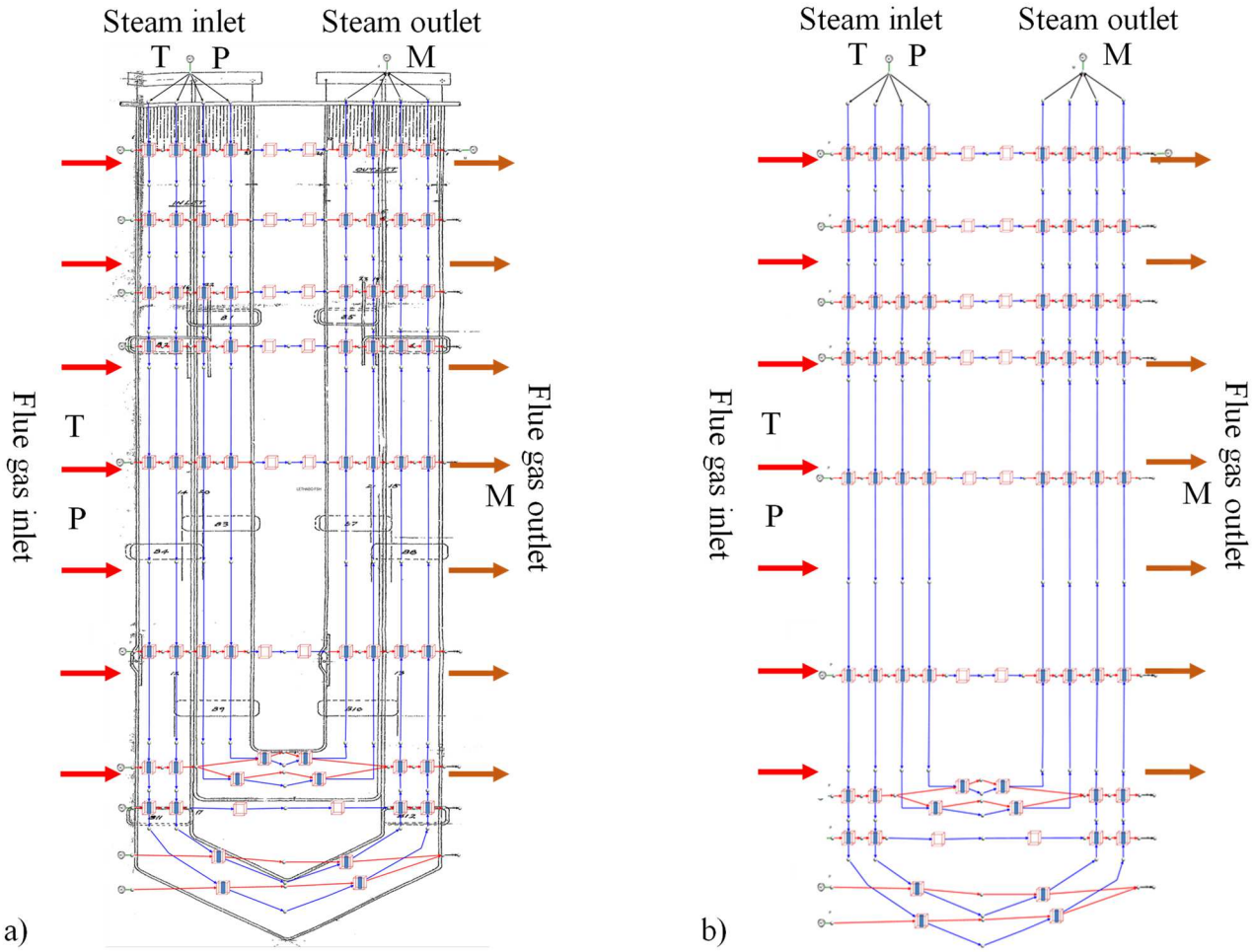

Figure 6-5: Model layout of one tubesheet/element of the heat exchanger: a) Flownex model imposed on the physical layout of the final superheater in the plant and b) A stand-alone Flownex model of the superheater to maximize the details of the model.

As described in Chapter 3 each heat exchanger increment is again made up of a sub-network of nodes and 1-D flow and heat transfer elements. As shown in Figure 3-9 and Figure 3-12 the different elements are: the steam flow path; the inside convective heat transfer resistance; the inner scaling layer conduction heat transfer resistance and associated thermal inertia; two conduction heat transfer resistances and thermal inertia components that each represent half of the pipe wall thickness; an outer fouling layer conduction heat transfer resistance and associated thermal inertia; the outside convective heat transfer resistance; the outside radiative heat transfer resistance; and the flue gas flow path. The direct radiation into the final superheater is accounted for via a heat addition on the node for the surface of the outer fouling layer.

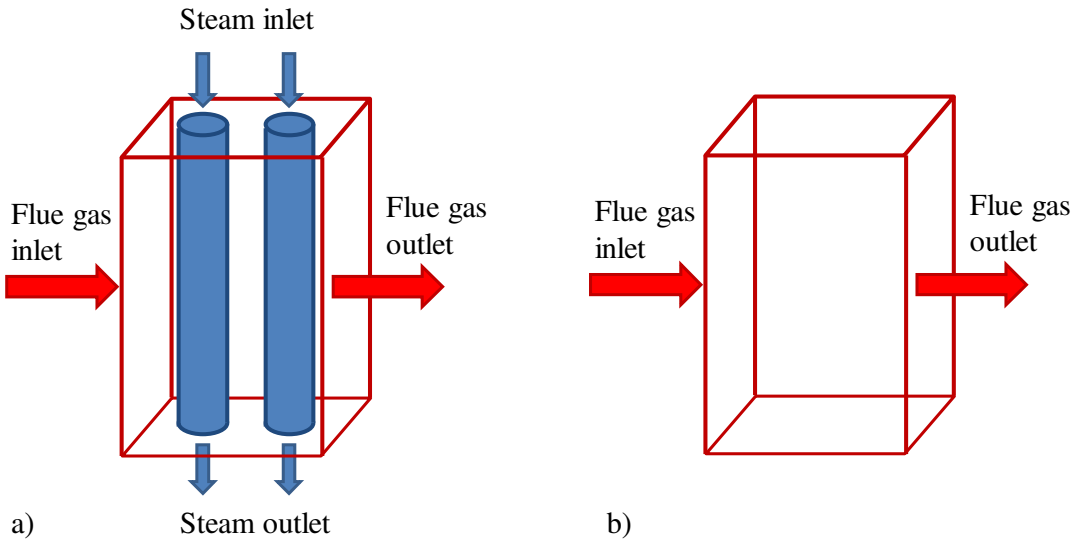

Figure 6-6: The building blocks of the model: a) Heat exchanger increment with two lumped tubes and b) Flow channel for areas without the presence of tubes.

The modelling methodology also allows for the modelling of the complete heat exchanger by interconnecting the models of the various elements. The complete heat exchanger model can be discretised to a level required by the purpose of the model. Here the superheater was discretised into four sections across the width of the boiler corresponding to the four legs A, B, C and D as explained in the subsection above. This means that the seven tubesheets contained in each of the four legs are assumed to be similar and are therefore modelled via one representative tubesheet model that correctly accounts for the total steam and flue gas flow rates through the whole leg. The schematic representation of the model is shown in Figure 6-7.

It is highly desirable to demonstrate the applicability of the model based on real plant data. Limited plant measurements are usually available from the Distributed Control System (DCS) for various operational conditions. These typically include steam flow rates and temperatures at the inlet and outlet of each heat exchanger. However, the flue gas mass flow rates and temperatures are rarely measured directly. An exception is the low temperature economizer heat exchanger at the outlet of the convective pass where the outlet flue gas temperature is typically measured before it enters the air heater. The oxygen content is also measured at this point to monitor and control the excess air provided for combustion.

Since the flue gas flow rate and properties as well as the inlet temperatures and direct radiation are required to compare the model results with real plant data, separate high-level models must be employed to obtain such input information. These include developing and verifying a boiler mass and

energy balance (MEB) that can be used to calculate the flue gas flow rate and properties that are not directly measured. The mass flow rate of the coal, hot humid air and flue gas calculated from the boiler MEB are then used in a high-level thermal model of the furnace and the platen superheater. This high-level thermal model (the Gurvich method) is then used to obtain the inlet flue gas temperature into the final superheater as well as the lumped direct radiation that impinges onto the final superheater. Finally, the lumped direct radiation is systematically cascaded over the rows of the heat exchanger. Each row or group of tubes in rows absorbs some fraction of the direct radiation that impinges on it.

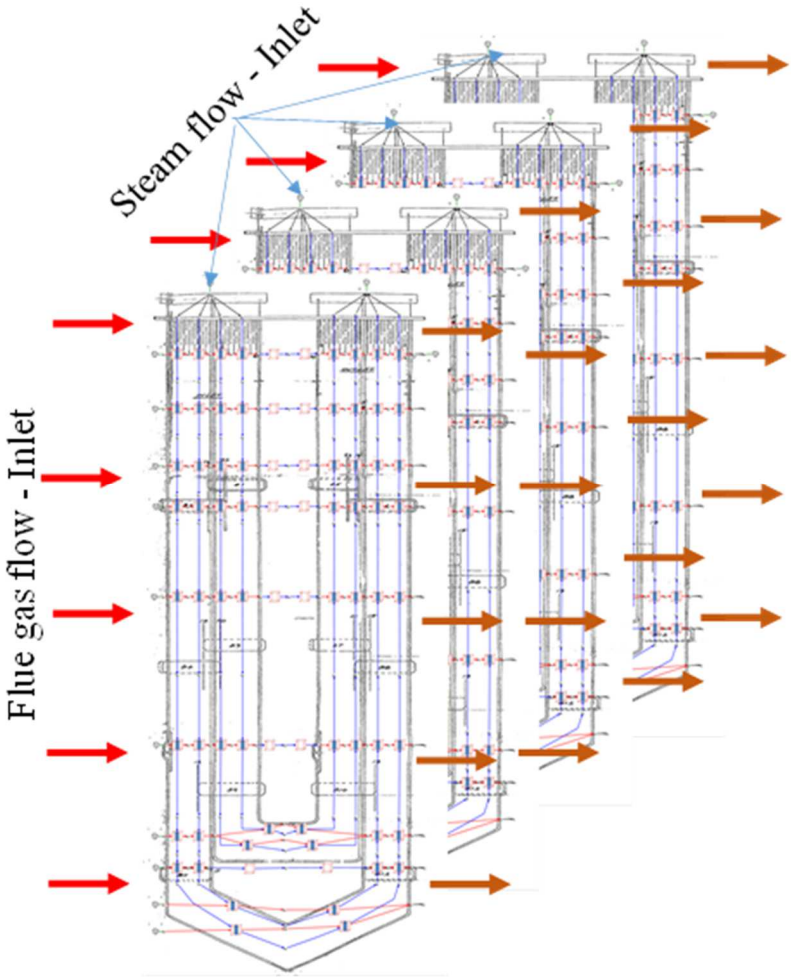

Figure 6-7: A representation of the Flownex model for a complete superheater modelled with only four Flownex element models.

6.3. Heat transfer model, pressure drop model and fluid properties

The section presents the various correlations used to describe the flow and heat transfer phenomena in the model.

6.3.1. Inside convective heat transfer model

For the inside convection heat transfer coefficient, the Dittus-Boelter's correlation [13] is used. The Nusselt number for this correlation is given as

$$Nu = 0.023\,\mathrm{Re}_{ID}^{0.8}\,\mathrm{Pr}^{0.4} \tag{6.1}$$

It is valid for fully developed turbulent flow in smooth tubes for fluids [13] with the following range of conditions, $0.6 \le \mathrm{Pr} \le 160$, $\mathrm{Re}_{ID} \ge 10000$ and $L/ID \ge 10$ [123].

6.3.2. Conduction heat transfer

All tubes were assumed to be made of Chromium (low) Steel - (1Cr-0.5Mo). The thermal conductivity of the outer fouling ash layer was taken from Taler et al. [4] and its value is $\lambda_{ash} = 0.07\ \ W/(m \cdot K)$.

6.3.3. Outside convective heat transfer model

The outside convection heat transfer is accounted for using the Zukauskas correlation [124] and the Nusselt number is given as

$$Nu_{OD} = C\,\mathrm{Re}_{OD}^{m}\,\mathrm{Pr}^{n}\left(\frac{\mathrm{Pr}}{\mathrm{Pr}_w}\right)^{0.25} \tag{6.2}$$

where the values of the constants C, m and n depend on Reynolds numbers. For an in-line tube bundle arrangement, $0.7 < \mathrm{Pr} < 500$, $0 < \mathrm{Re}_{OD} < 2\times10^{6}$ and for 16 or more tube rows these constants are shown in Table 6-2. The Prandtl number Pr_w is evaluated at the conditions of the tube wall. The convection heat transfer coefficient is then given by

$$h_{g.\varphi=0} = \frac{Nu_{OD}\lambda_{fg}}{OD} \tag{6.3}$$

provided the flue gas angle of attack is zero. If the angle of attack is not zero, then the flue gas convection heat transfer coefficient is given by

$$h_{fg.\varphi} = \varepsilon_{\varphi} h_{fg.\varphi=0} \tag{6.4}$$

The correction factor, ε_{φ} is given by Figure 6-8.

For the final superheater heat exchanger addressed here, the flue gas flow is assumed to be following the direction of the mid-plane of the trapezoidal flue gas flow channel. Thus, the flow angle of attack, φ is determined as illustrated in Figure 6-9. From basic trigonometry

$$\tan\theta = \frac{y_2 - y_1}{x_2 - x_1} \tag{6.5}$$

and the angle of attack is given by

$$\varphi = 90 - \theta \tag{6.6}$$

Table 6-2: Constants for the Zukauskus correlations for an inline tube arrangement and 16 or more rows [124].

Range of the Reynolds number	**C**	**m**	**n**
0 - 100	0.9	0.4	0.36
100 - 1000	0.52	0.5	0.36
1000 - $2x10^5$	0.27	0.63	0.36
$2x10^5$ - $2x10^6$	0.033	0.8	0.4

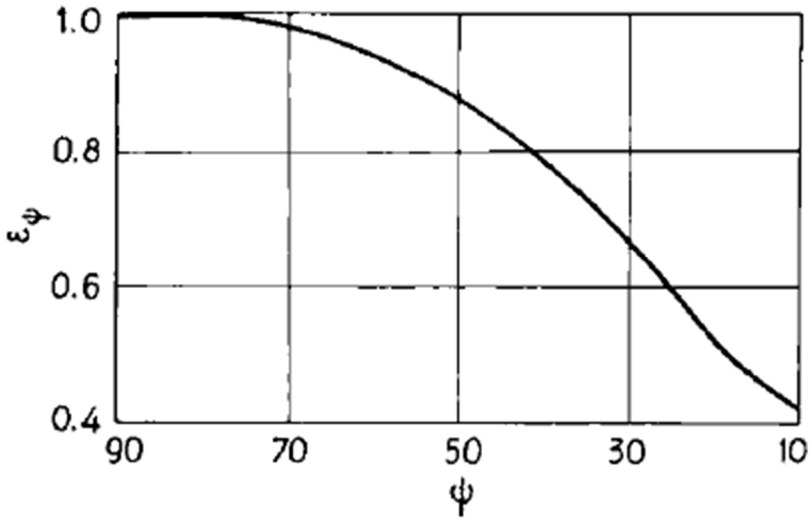

Figure 6-8: Dependence of heat transfer of banks on the angle of attack [125].

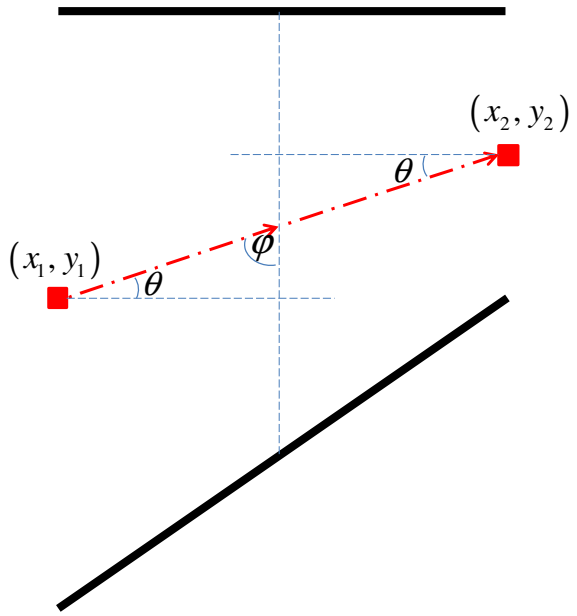

Figure 6-9: An illustration on the characterization of the angle of attack on the flue gas side of the final superheater heat exchanger.

6.3.4. Radiation heat transfer model

In the model that was presented in chapter 4, only the radiation heat transfer from some gaseous combustion products were considered, thus simplifying the model. These gaseous products were carbon dioxide, water vapour and a transparent gas. The transparent gas accounted for the bands where the two gases were not radiating any energy. However, the radiation from pulverised-coal combustion products is a more complex heterogeneous system. It involves radiation heat transfer from the gaseous products and the solid disperse phase. Most of the radiation heat transfer in a boiler takes place in the furnace with the thermal radiation from the pulverised-coal flame. In the furnace, the radiative transfer is due to both band emission from CO_2 and H_2O as well as some trace amounts of CO and SO_2. This transfer of energy is coupled with the continuous emission from the different types of particles in the flame. These particles that are entrained in the combustion gas can be classified as carbonaceous (coal, char and soot) and inorganic (fly ash). Most of the carbonaceous particles are confined in the firebox region [126]. The fly ash may be the only particle remaining in the heat absorption region as well as moving with the gaseous products to the convective pass.

Since this section focuses on modelling radiant heat exchangers in the convective pass of a coal fired boiler, the radiation of the particle-gas flow mixture only considers the radiation from fly ash particles in conjunction with the radiation from the gases. This is because fly ash is the dominant type of particles present in the convective pass, with only traces of the other particles. This work will mainly

focus on the radiation model used in the Gurvich boiler thermal calculation model [127] which is based on the former Soviet Union's standards. However there are other models from literature which include that of the VDI heat atlas [128, 129] and Blokh [130].

The radiation heat transfer coefficient used in the Gurvich method is given by

$$h_r = \sigma_0 \left(\frac{\varepsilon_w + 1}{2} \right) \varepsilon_g \left(\frac{T_g^4 - T_w^4}{T_g - T_w} \right) \tag{6.7}$$

where σ_0 , T_g and T_w are the Stefan – Boltzmann constant, average flue gas temperature [K] and average outer fouled wall temperature [K], respectively. ε_w is the emissivity of the outer fouled wall and ε_g is the emissivity of the flue gas, which consists of the gases and particles.

The flue gas emissivity is given by

$$\varepsilon_g = 1 - \exp\left(-KL_{mb}\right) \tag{6.8}$$

where L_{mb} and K are the mean beam length and the overall extinction coefficient of the flue gas, respectively. The mean beam length for the superheater region is given by

$$L_{mb} = \frac{C_{rad}}{2\left(\frac{1}{b} + \frac{1}{h} + \frac{1}{S_T} \right)} \tag{6.9}$$

where b , h and S_T are the width, height and transverse pitch of the heat exchanger, respectively. According to Jones [108] in many practical systems the constant C_{rad} is taken as 3.6. The overall extinction coefficient is given by

$$K = K_g + K_{fa} \tag{6.10}$$

where K_g is the extinction coefficient of the gas and K_{fa} is the extinction coefficient of the fly ash. The extinction coefficient of the gas is given by

$$K_g = k_g r_n p \tag{6.11}$$

where p and r_n are the total pressure in the convective pass and volume fraction of the triatomic gases, respectively. The gas coefficient, k_g in $1/(\mathrm{m} \cdot \mathrm{Pa})$ is given by

$$k_g = \left(\frac{0.78 + 1.6 r_{H_2O}}{\sqrt{\frac{p_n}{p_0} L_{mb}}} - 0.1 \right) \left(1 - 0.37 \frac{T_g}{1000} \right) \times 10^{-5} \tag{6.12}$$

with r_{H_2O}, p_n and p_0 the volume fraction of water vapor, the partial pressure of triatomic gas and the reference pressure, respectively.

The extinction coefficient of the fly ash is given by

$$K_{fa} = k_{fa} \mu_{fa} p \tag{6.13}$$

where k_{fa} and μ_{fa} are the fly ash coefficient and concentration, respectively. The fly ash coefficient is given by

$$k_{fa} = \frac{4300 \rho_g}{\sqrt[3]{T_g^2 d_{fa}^2}} \times 10^{-5} \tag{6.14}$$

where ρ_g and d_{fa} are the gas density and the diameter of the fly ash particles given in μm, respectively.

The fly ash concentration is given by

$$\mu_{fa} = \frac{\%FA x_{ash}}{G_g} \tag{6.15}$$

where $\%FA$ is the fraction of the fly ash after combustion, x_{ash} is the fuel ash content on an as-received basis and G_g is the flue gas mass excluding the fly ash.

Discretised Flownex model

The default radiation heat transfer element within Flownex solves the standard radiation heat transfer equation given by

$$\dot{Q}_{rad} = A_o F \sigma_0 \left(T_g^4 - T_w^4 \right) \tag{6.16}$$

with A_o the outer fouled tube surface area and F the view factor. This standard radiative heat transfer element is used in the current model but with the view factor given by

$$F = \left(\frac{\varepsilon_w + 1}{2} \right) \varepsilon_g \tag{6.17}$$

Using this view factor together with eq. (6.16) is equivalent to employing the effective radiation heat transfer coefficient given by eq. (6.7).

Comparison to the VDI heat atlas model

The radiation heat transfer coefficient given by eq. (6.7) as

$$h_{r.Gurvitch} = \sigma_0 \left(\frac{\varepsilon_w + 1}{2} \right) \varepsilon_g \left(\frac{T_g^4 - T_w^4}{T_g - T_w} \right)$$

was compared to the radiation heat transfer coefficient given by the VDI heat atlas model [128, 129] as

$$h_{r.VDI} = \sigma_0 \left(\frac{\varepsilon_w}{\alpha_g + \varepsilon_w - \alpha_g \varepsilon_w} \right) \left(\frac{\varepsilon_g T_g^4 - \alpha_g T_w^4}{T_g - T_w} \right) \tag{6.18}$$

where α_g is the absorptivity of the flue gas, which consists of the gases and the ash particles.

Using values given in the plant design documents (C-schedule) for a 100% boiler MCR case shown in Table 6-3, the radiation heat transfer coefficients compared well as shown in Table 6-4. These values are within 11%. The full calculation for the 100% MCR case from the C-schedule is documented in Appendix C for the VDI heat atlas model and Appendix E for the Gurvich model.

Table 6-3: Input data from C-schedule for the radiation models at 100% boiler MCR.

Details	**Units**	**Value**
Average flue gas temperature	K	1274
Average outer fouled wall temperature	K	791
Particle loading	kg/m^3	0.046
Outer fouled wall emissivity	--	0.7

Table 6-4: Comparison between the heat transfer coefficient used in the Gurvich method to that of the VDI heat atlas for the same temperature values.

Details	**Radiation heat transfer coefficient** $\left(W/m^2K\right)$
Gurvich method	82.94
VDI heat atlas	91.99

6.3.5. Pressure drop models

The steam side pressure drop was accounted for in the same way as in Section 4.3.5. The pressure drop on the flue gas side was accounted for using eq. (4.19) which is repeated below for completeness as

$$\Delta p = Eu\frac{\rho v^2}{2}z$$

where z is the number of tube rows and Eu is the Euler number [112]. The Euler number can also be determined using the power law. For inline tube banks with Reynolds numbers ranging between 10^4 and 2 x 10^5 it can be given as

For $\left(b-0.8\right)/\left(a-1\right)\geq 1$

$$Eu = 0.52\left(\frac{b-0.8}{a-1}\right)^{1.5}\mathrm{Re}^r \tag{6.19}$$

For $\left(b-0.8\right)/\left(a-1\right)\leq 1$

$$Eu = 0.52\left(\frac{b-0.8}{a-1}\right)\mathrm{Re}^r \tag{6.20}$$

where the exponent r is given by

$$r = 0.12\left(\frac{b-1}{a-1}\right)^{0.5} \tag{6.21}$$

In addition, a and b are the pitch-to-diameter ratios or the relative pitches. The relative transverse pitch $a = S_T / OD$ and the relative longitudinal pitch $b = S_L / OD$ where S_T is the transversal pitch and S_L is the longitudinal pitch.

6.3.6. Fluid properties

The steam and flue gas properties were accounted for in the same way as in Sections 4.3.7. and 4.3.8., respectively in chapter 4. In the calculation of the flue gas density using the ideal gas law, the specific gas constant was calculated from the universal gas constant $(8.314\ J/mol \cdot K)$ and the molar mass of the flue gas. This molar mass was calculated based on the flue gas composition sampled from the plant together with calculations from the boiler Mass and Energy Balance (MEB).

6.4. Mass and Energy Balance (MEB)

In simple terms, the Mass and Energy Balance (MEB) calculates the amount of coal required to produce the necessary energy to heat water of a specific mass flow rate to the required temperatures at specific pressures. In general, from the energy balance around the boiler boundary shown in Figure 6-10, the mass flow rate of coal $(\dot{m}_{coal})$ can be calculated as follows

$$\dot{m}_{coal} = \frac{\dot{Q}_{input} + \dot{Q}_{loss} - \dot{Q}_{credits}}{\sum_{flows} FR_{flow} h_{flow} + CV_{coal}} \tag{6.22}$$

where, $\dot{Q}_{input}$ is the net heat transferred to the Rankine Cycle. This is the total heat transferred into the water/steam circuit via the respective heat exchangers. The steam from this circuit turns the turbines to produce power. $\dot{Q}_{loss}$ is the total boiler heat losses i.e. the radiation losses through the surface. $\dot{Q}_{credits}$ is the combined electrical power into the auxiliaries such as the mills, air heater, primary air fans and forced draft fan depending on whether they are included in the overall boiler MEB boundary. The CV_{coal} is the calorific value of the coal, which is the Higher Heating Value (HHV). FR_{flow} are the mass flow ratios of each specific stream per kg of coal flow. For streams going into the boundary, the mass flow ratios are positive and negative for streams going out of the boundary. Lastly, h_{flow} represents the enthalpy of the specific flow streams evaluated at the temperature on the boundary of the overall MEB [101, 131, 132], as listed on the right in Figure 6-10.

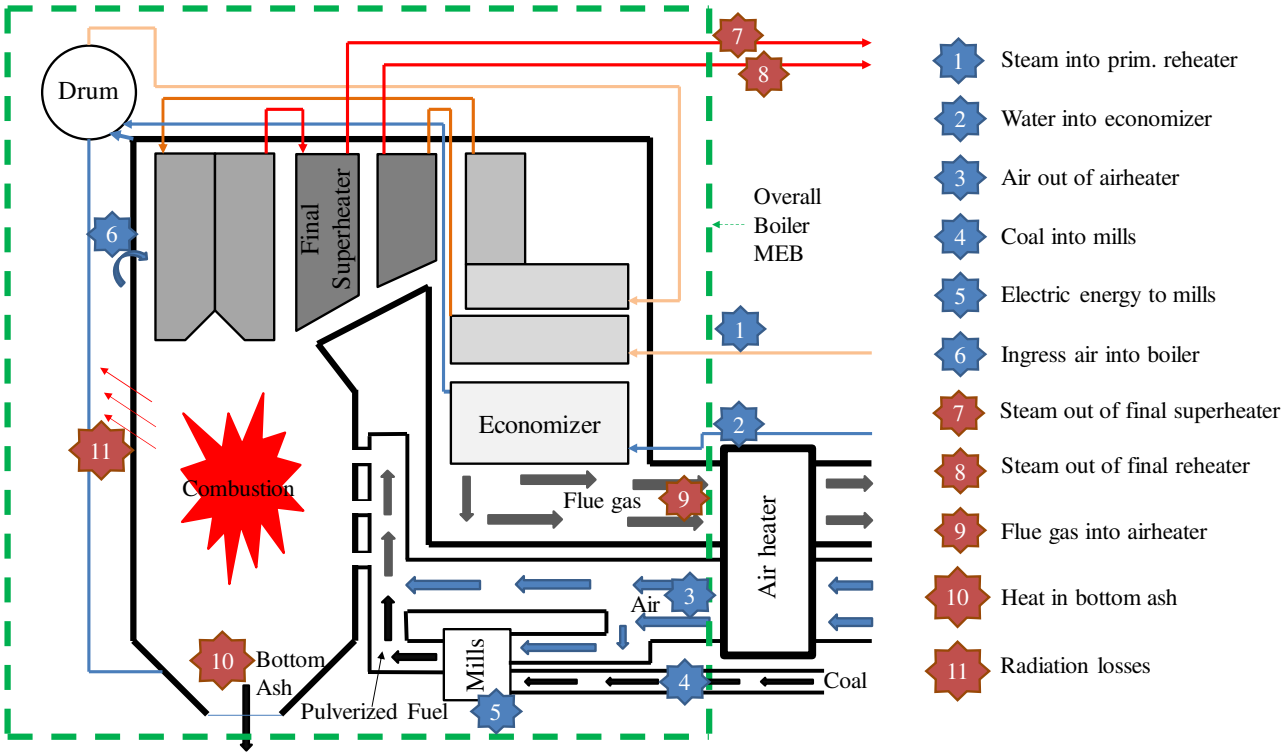

Figure 6-10: Mass and Energy Balance boundaries.

Implicit in eq. (6.22) is the amount of air required to combust the coal constituents which are usually referred to as the CHONS. C for carbon, H for hydrogen, O for Oxygen, N for Nitrogen and S for Sulphur. From stoichiometry, the Theoretical Air Required (TAR) to fully combust the CHONS is given as

$$TAR = \frac{M_{air}}{y_{O2/air}} \sum_i St_i \frac{x_i}{M_i} \tag{6.23}$$

Where $i = C,\ H,\ O,\ N,\ S$. St_i represents the stoichiometric coefficients of O_2 required to combust each $i-th$ constituents. $M,\ x$ and $y_{O2/air}$ represents the molar mass, mass fractions and the mole fraction of O_2 in the air, respectively. In order to ensure complete combustion in real boilers an additional quantity of excess air is added. Thus, the Dry Air Required (DAR) is given as

$$DAR = TAR\left(1 + f_{EA}\right) \tag{6.24}$$

With f_{EA} the percentage of excess air per kg of the TAR. In addition, the air going into the boiler has to account for the water vapor content in the atmosphere. Thus, the Humid Air Required (HAR) is given as

$$HAR = DAR(1 + w) \tag{6.25}$$

with w the percentage amount of water vapor present in the atmospheric air. The mass flow rate of the hot humid air into the boiler would therefore be given as

$$\dot{m}_{ha} = HAR \cdot \dot{m}_{coal} \tag{6.26}$$

If a control volume around the combustion process in the furnace is considered, then from mass balance the flue gas mass flow ratio (FGR) per mass flow rate of coal is given by

$$FGR = HAR + 1 - x_{ash} f_{BA} \tag{6.27}$$

where x_{ash} is the fraction of ash in the coal and f_{BA} is the percentage of ash that falls to the bottom of the boiler normally referred to as Bottom Ash. Thus, the flue gas mass flow rate is given by

$$\dot{m}_{fg} = FGR \cdot \dot{m}_{coal} \tag{6.28}$$

6.4.1. Input data to the Mass and Energy Balance

The inputs and assumptions for the overall boiler Mass and Energy Balance are detailed in Table 6-5. The full names of the abbreviations are as follows: ATT, EC, SH, RH, AH and FW which imply the attemperator, economizer, superheater, reheater, air heater and feedwater, respectively.

To verify the custom developed boiler MEB, it was applied for a boiler MCR case that is provided in the plant design C-schedule data. The values of the inputs and assumptions for this boiler MCR case are shown in Table 6-5.

Table 6-5: Inputs and assumptions to the MEB for an MCR case given by the C-schedule.

Parameter	**Units**	**Value**
Excess air	%	17.36
Ingress air	%	1.86
Coal CV (HHV)	kJ/kg	16410
Feedwater flow rate	kg/s	487.841
Cold reheat flow rate	kg/s	467.995
ATT 1 flow rate	kg/s	16.826
ATT 2 flow rate	kg/s	5.096
ATT 3 flow rate	kg/s	10.69
EC water inlet temperature	°C	249
SH 3 steam outlet temperature	°C	540
RH 1 steam inlet temperature	°C	329
RH 2 steam outlet temperature	°C	540
ATT 1 spray water temperature	°C	249
ATT 2 spray water temperature	°C	249
ATT 3 spray water temperature	°C	165
EC flue gas outlet temperature	°C	334
Ambient air temperature	°C	44
AH air outlet temperature	°C	288
FW pressure	MPa	19.44
RH pressure	MPa	4.178
Seal air flow rate	kg/s	4.856

6.4.2. Mass and Energy Balance Results

The aim of the overall boiler MEB here is to obtain the mass flow rate of coal, hot humid air and flue gas. For the boiler MCR case given in the C-schedule, the developed boiler MEB compared well with the C-schedule data as shown in Table 6-6. This gives confidence in the use of the MEB at different operating load cases of the real power plant. The full calculation for the MCR case from the C-schedule is documented in Appendix D.

Table 6-6: Comparison of the results from the boiler MEB to the C schedule at 100% MCR (Input values were the same as that from the C schedule).

Details	Units	C schedule	MEB + C-sch. Inputs	Error (%)
Mass flow rate of coal	kg/s	98.4	97.6	0.76
Mass flow rate of humid air into the furnace	kg/s	637.2	621.9	2.40
Mass flow rate of flue gas at economizer exit	kg/s	715.8	728.4	-1.76

6.5. Thermal Calculations and Energy Balances

To determine the final superheater inlet flue gas temperature and the inlet direct radiation from the furnace and the platen superheater, an existing boiler design methodology is used. This Gurvich boiler design method was documented by Zhang et al. [127], Basu et al. [133] and Kakac [134]. It is important to note that this method was developed to design boilers from design specifications. However, in this work the method is used to do performance calculations on an existing boiler, thus all the basic sizing models are not used. In addition, the coal mass flow rate, hot air mass flow rate, flue gas mass flow rate and the flue gas properties are already available as determined using the MEB that was presented in the previous section.

6.5.1. Furnace model

The work flow process diagram of the furnace model which is used to calculate the Furnace Exit Temperature (FET) and the heat absorbed by the furnace is shown in Figure 6-11. The model is centred around the calculation of the FET, T_{FE} which is determined via trial and error as illustrated in Figure 6-11. It is first guessed and then later calculated using the following equation

$$T_{FE} = \frac{T_{flame}}{M\left[\frac{\sigma_0 T_{flame}^3 \varepsilon_{furnace} A_{furnace} \psi_{ave}}{\varphi_{furnace} \dot{m}_{coal} Cp_{furnace}}\right]^{0.6} + 1} \tag{6.29}$$

where T_{flame} is the flame temperature, M is the flame centre modification factor, σ_0 is the Stefan-Boltzmann constant and $\varepsilon_{furnace}$ is the furnace emissivity. $A_{furnace}$ represents the projected area of the furnace which absorbs the radiated heat, ψ_{ave} is the average thermal efficiency coefficient, $\varphi_{furnace}$ is

the heat preservation coefficient, $\dot{m}_{coal}$ is the mass flow rate of coal and $Cp_{furnace}$ is the mean overall heat capacity of the combustion products in the furnace.

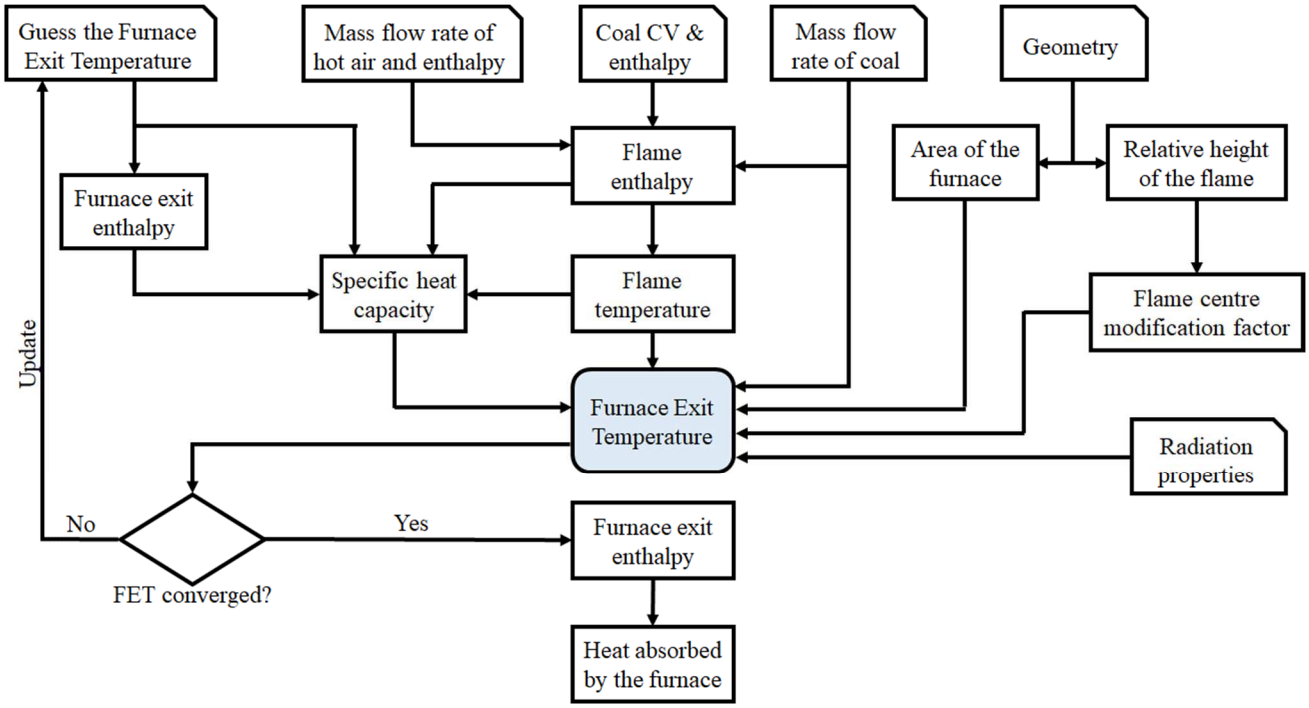

Figure 6-11: A flow diagram for the calculation of the Furnace Exit Temperature (FET) and the heat absorbed by the furnace.

The theoretical adiabatic flame temperature, T_{flame} that results from the combustion of the coal in the furnace is calculated by performing a Mass and Energy Balance around the combustion process control volume [101] as shown in Figure 6-12.

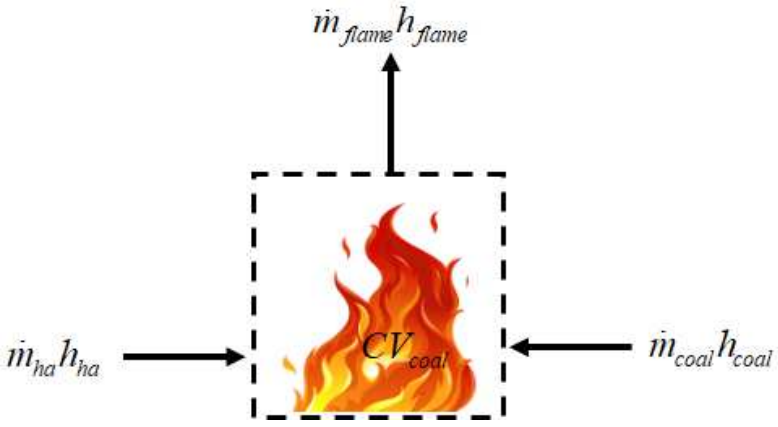

Figure 6-12: Flame energy balance [101].

From the mass balance around the process control volume, the flame outlet "mass flow" rate can be given as

$$\dot{m}_{flame} = \dot{m}_{ha} + \dot{m}_{coal} \tag{6.30}$$

where $\dot{m}_{ha}$ is the mass flow rate of the hot humid air.

The adiabatic flame outlet enthalpy is determined by performing an energy balance around the combustion process as shown in Figure 6-12. Thus, the flame outlet enthalpy, h_{flame} is given as

$$h_{flame} = \frac{\dot{m}_{ha} h_{ha} + \dot{m}_{coal}\left(h_{coal} + CV_{coal}\right)}{\dot{m}_{flame}} \tag{6.31}$$

where h_{ha} is the enthalpy of the hot humid air, h_{coal} is the enthalpy of the coal and CV_{coal} is the calorific value of the coal. The theoretical adiabatic flame temperature is then determined from the flue gas properties developed in the boiler MEB.

Using the guessed FET, the furnace exit enthalpy, h_{FE} is also determined. The mean overall heat capacity of the combustion products, $Cp_{furnace}$ in per unit mass of coal is obtained by

$$Cp_{furnace} = \frac{h_{flame} - h_{FE}}{T_{flame} - T_{FE}}\left(\frac{\dot{m}_{fg}}{\dot{m}_{coal}}\right) \tag{6.32}$$

The flame centre modification factor, M which is also referred to as the temperature field coefficient, accounts for the temperature distribution in the furnace [133]. It is a function of the relative burner levels as well as the type of fuel burnt. Thus, the flame centre modification factor is given as

$$M = B - Cx_{flame} \tag{6.33}$$

For a suspension-firing boiler burning anthracite and mean pulverized coal, the constants B and C are 0.56 and 0.5, respectively [127]. The relative flame centre position, x_{flame} is given by

$$x_{flame} = x_b + \Delta x \tag{6.34}$$

with Δx an adjustment parameter to account for the burner firing type and the relative burner height, x_b given by

$$x_b = \frac{h_b}{h_F} \tag{6.35}$$

where h_b and h_F are the burner height and the height from the dry bottom hopper to the centre of the furnace exit, respectively.

The radiation heating surface area or projected area of the furnace, $A_{furnace}$ is given by

$$A_{furnace} = X_{furnace}\left(A_{furnace.total} - A_{mh}\right) \tag{6.36}$$

where $X_{furnace}$ is the furnace configuration factor, $A_{furnace.total}$ represents the entire furnace area as shown in Figure 6-13 and A_{mh} represents the area of doors and holes.

The radiation properties in Figure 6-11 represents the gas inputs needed to account for the radiation in the furnace. The furnace emissivity, $\varepsilon_{furnace}$ is given by

$$\varepsilon_{furnace} = \frac{\varepsilon_{flame}}{\psi_{ave}\left(1-\varepsilon_{flame}\right)+\varepsilon_{flame}} \tag{6.37}$$

where ε_{flame} is the furnace flame emissivity. ψ_{ave} is the average thermal efficiency coefficient which is given by

$$\psi_{ave} = \zeta_{slag} X_{furnace} \tag{6.38}$$

where ζ_{slag} is the water wall fouling factor.

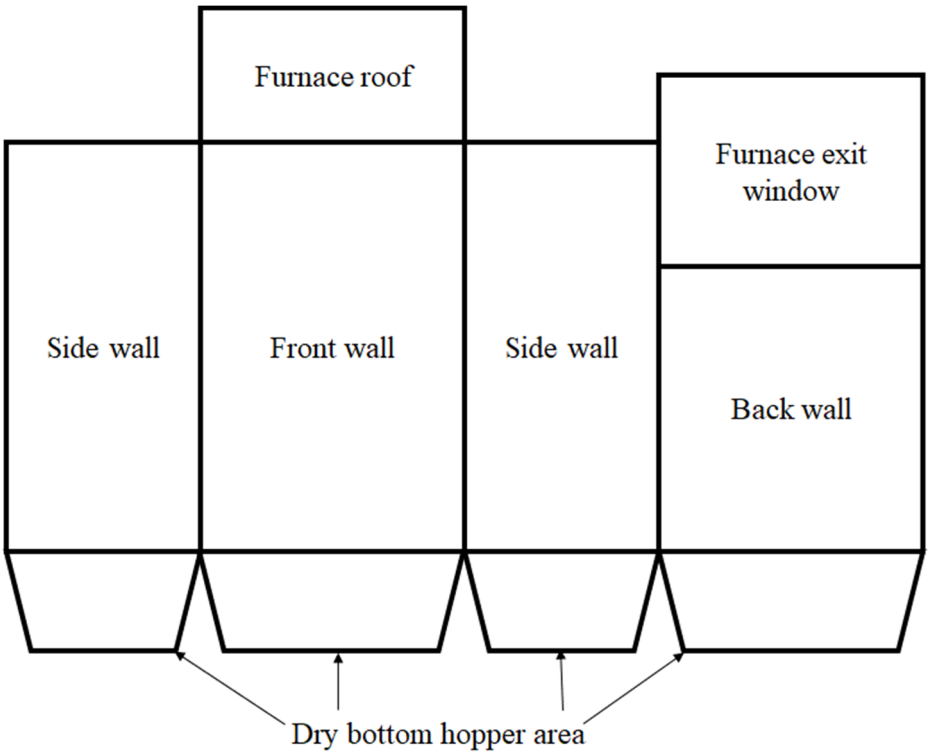

Figure 6-13: Schematic of the projected area of the boiler used for furnace heat absorption calculations.

The furnace flame emissivity is given by

$$\varepsilon_{flame} = 1 - \exp(-K_{flame} p_{furnace} L_{mb.furnace}) \tag{6.39}$$

where $p_{furnace}$ is the furnace pressure. The furnace mean beam length, $L_{mb.furnace}$ is given as

$$L_{mb.furnace} = 3.6 \frac{V_{furnace}}{A_{furnace.total}} \tag{6.40}$$

with $V_{furnace}$ is the volume of the furnace.

The radiant absorption coefficient of the flame radiation is given as

$$K_{flame} = k_g r_g + k_{fa} \mu_{fa} + k_{co} x_1 x_2 \tag{6.41}$$

where k_g is the radiant absorption coefficient of the gas, r_g the volume fraction of triatomic gases, k_{fa} the radiant absorption coefficient of fly ash, μ_{fa} the dimensionless fly ash concentration and k_{co} the radiant absorption coefficient of coke particles. x_1 and x_2 are dimensionless numbers determined by the type of fuel and the firing method, respectively [133].

In eq. (6.29) the heat preservation coefficient is given by

$$\varphi_{furnace} = 1 - Loss_{rad} \tag{6.42}$$

with $Loss_{rad}$ being the percentage heat loss due to furnace wall radiation and convection.

Once the FET has converged via trial and error, it is then used in conjunction with flue gas properties to calculate the correct furnace exit enthalpy. Then, the radiative heat absorbed by the furnace in per unit mass of burnt fuel is obtained through

$$q_{r.furnace} = \varphi_{furnace}\left(h_{flame} - h_{FE}\right)\left(\frac{\dot{m}_{fg}}{\dot{m}_{coal}}\right) \tag{6.43}$$

The thermal load of radiation heating surface per unit area is then given by

$$Q_{r.furnace} = \frac{\dot{m}_{coal} q_{r.furnace}}{A_{furnace}} \tag{6.44}$$

Figure 6-14 summaries the mass and energy balances around the furnace control volume. Some energy is lost from the system to the surroundings via the radiation loss, $Q_{Loss.rad}$ and the bottom ash, $\dot{m}_{ba}h_{ha}$. The water walls absorb some of the radiated heat represented by Q_{ww}.

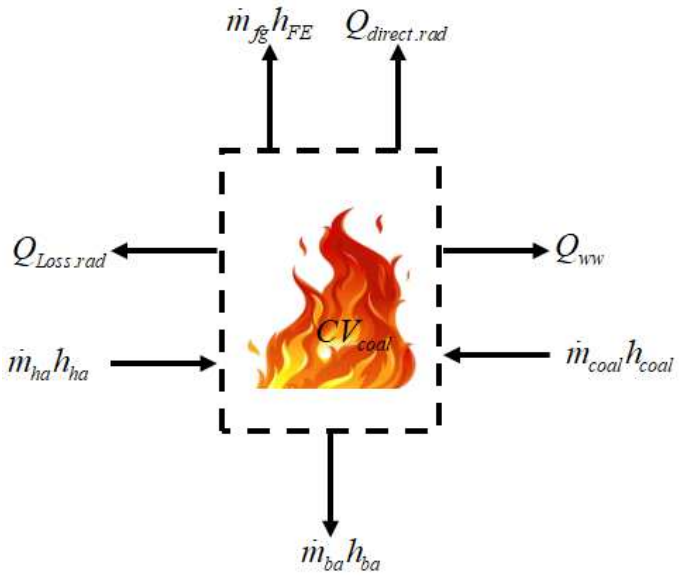

Figure 6-14: Mass and Energy Balance control volume around the furnace.

Figure 6-14 shows that the heating surfaces after the furnace experiences both the energy of the flue gas exiting the furnace, $\dot{m}_{fg}h_{FE}$ and the direct radiation, $Q_{direct.rad}$ which escapes through the furnace exit window.

6.5.2. Platen superheater model

Effectively the platen superheater receives energy from the combustion via two streams; namely flue gas energy and direct radiation as illustrated by separating them in Figure 6-15. It is important to mention that the two streams are separated in this figure for illustration purposes only, in the boiler the processes are intertwined. Considering the flue gas control volume around the platen superheater, the flue gas stream exchanges heat with the platen superheater steam, the roof in the platen region and the water walls in the platen region. These exchanges are predominantly driven by flue gas radiation heat transfer, however there is also some convection heat transfer taking place. In this model, it is assumed that all the direct radiation absorbed in the platen superheater regions is absorbed by the platen superheater steam stream. The unabsorbed direct radiation falls onto the final superheater downstream. The flue gas stream interacts with the final superheater in two ways. Firstly, since the flue gas in the platen superheater matrix is at high temperatures, it also radiates heat to the final superheater. Then, the unabsorbed energy in the flue gas stream also passes through to the final superheater.

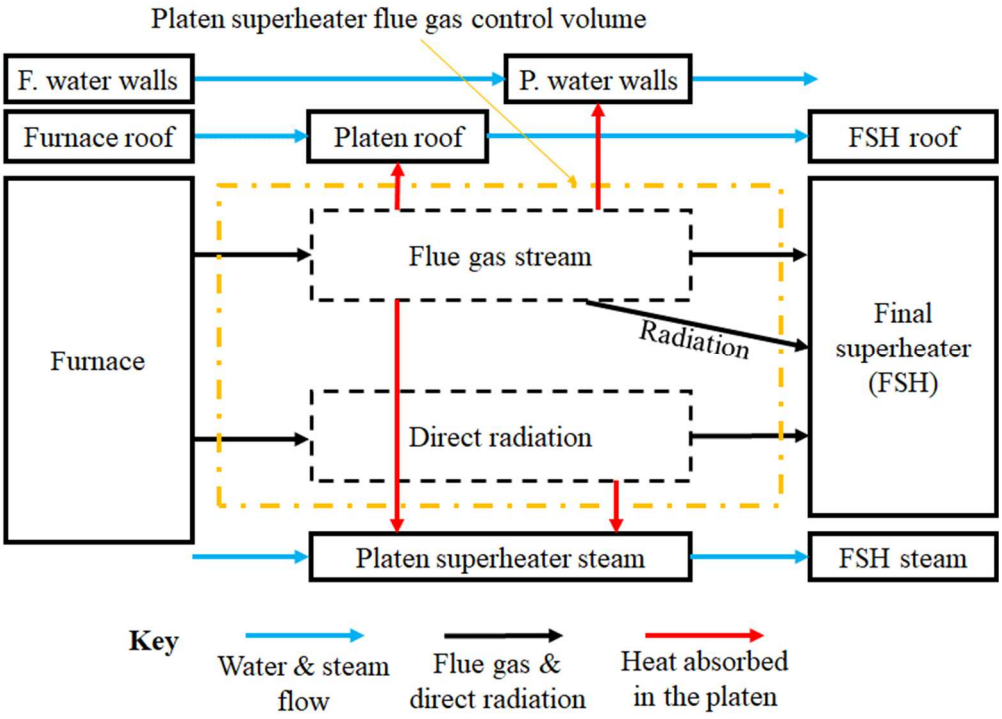

Figure 6-15: A process flow diagram for the platen superheater with a control volume around the flue gas stream.

The direct radiation absorbed by the platen superheater steam stream is given by

$$Q_{r.plat} = \left(q'_{r.plat.in} - q'_{r.plat.out}\right)\dot{m}_{coal} \tag{6.45}$$

where $q'_{r.plat.in}$ and $q'_{r.plat.out}$ are the direct radiation from the furnace into the platen superheater and passing through the platen superheater, respectively. The direct radiation coming into the platen superheater is given by

$$q'_{r.plat.in} = \frac{q_{r.plat.in.cor} A_{rad.plat.in}}{\dot{m}_{coal}} \tag{6.46}$$

with $A_{rad.plat.in}$ the inlet radiation area for the platen superheater and $q_{r.plat.in.cor}$ the corrected radiative intensity into the platen superheater. The corrected radiative intensity is given by

$$q_{r.plat.in.cor} = \beta_{plat} q_{r.plat.in} \tag{6.47}$$

where β_{plat} is a coefficient accounting for reradiation. $q_{r.plat.in}$ is the radiation heat flow into the platen and it is given by

$$q_{r.plat.in} = \frac{\eta_{plat} q_{r.furnace} \dot{m}_{coal}}{A_{furnace}} \tag{6.48}$$

with η_{plat} the thermal load distribution coefficient for the platen. $q_{r.furnace}$ and $A_{furnace}$ are the radiative heat absorbed by the furnace in per unit mass of burnt fuel and radiation heating surface area of the furnace, respectively.

In eq. (6.45), the furnace radiation heat leaking out of the platen superheater is given by

$$q'_{r.plat.out} = \frac{q'_{r.plat.in}\left(1-\varepsilon_{g.plat}\right)\varphi_{plat}}{\beta_{plat}} \tag{6.49}$$

with φ_{plat} the configuration factor from inlet to outlet of the platen. The emissivity of the flue gas in the platen is calculated from

$$\varepsilon_{g.plat} = 1-\exp\left(-K_{g.plat} p_{plat} L_{mb.plat}\right) \tag{6.50}$$

The radiant absorption coefficient of the flue gas in the platen only accounts for the gas and fly ash as shown below.

$$K_{g.plat} = k_{g.plat} r_g + k_{fa.plat} \mu_{fa.plat} \tag{6.51}$$

and the mean beam length for the platen is given by

$$L_{mb.plat} = \frac{1.8}{\left(\frac{1}{b_{plat}} + \frac{1}{h_{plat}} + \frac{1}{S_{T.plat}}\right)} \tag{6.52}$$

with b_{plat}, h_{plat} and $S_{T.plat}$ the depth, height and average transverse pitch for the platen superheater.

On the flue gas stream, the heat radiated by the gas in the platen superheater matrix onto the final superheater in per mass of fuel burnt basis is calculated using

$$q_{rl} = \frac{\sigma_0 \alpha_{g.plat} A_{rad.FSH.in} T_{g.plat.ave}^4 \zeta_r}{\dot{m}_{coal}} \tag{6.53}$$

where σ_0 is the Stefan-Boltzmann constant, $\alpha_{g.plat}$ is the absorptivity of the gas in the platen, $A_{rad.FSH.in}$ is the radiation inlet area for the final superheater and ζ_r is the correction factor of the fuel. The average flue gas temperature of the platen is given by

$$T_{g.plat.ave} = \frac{T_{g.plat.in} + T_{g.plat.out}}{2} \tag{6.54}$$

where $T_{g.plat.in}$ is the furnace exit temperature and $T_{g.plat.out}$ is the flue gas exit temperature out of the platen superheater into the final superheater.

The total direct radiation into the final superheater is the sum of eq. (6.49) and eq. (6.53) multiplied by the mass of fuel burnt resulting in

$$Q_{direct.rad.FSH} = \left(q'_{r.plat.out} + q_{rl}\right)\dot{m}_{coal} \tag{6.55}$$

In this model, the flue gas exit enthalpy of the platen superheater is calculated via the trial and error iteration method. The governing equation of the iteration is given by

$$h_{g.plat.out} = \frac{\dot{m}_{fg} h_{FE} - q_{rl}\dot{m}_{coal} - Q_{c.plat} - Q_{ww.plat} - Q_{roof.plat}}{\dot{m}_{fg}} \tag{6.56}$$

where $\dot{m}_{fg} h_{FE}$ and $q_{rl}\dot{m}_{coal}$ represents the flue gas energy from the furnace into the platen and the heat radiated from the flue gas in the platen superheater matrix onto the final superheater, respectively. $Q_{c.plat}$ represents the amount of heat transferred from the flue gas into the platen superheater steam stream via convection and gas radiation. $Q_{ww.plat}$ and $Q_{roof.plat}$ represent the amount of heat absorbed via convection and gas radiation by the water walls and the roof around the platen superheater,

respectively. In the model, $Q_{c.plat}$, $Q_{ww.plat}$ and $Q_{roof.plat}$ are first guessed, then calculated using lumped parameter methods in a trial and error iteration scheme together with the flue gas exit temperature due to the non-linearity of their relationship.

However, if the conditions and mass flow rates of the steam stream in the platen superheater are known, then the heat transferred from the flue gas stream via convection and gas radiation heat transfer can be obtained as

$$Q_{c.plat} = Q_{plat.tot} - Q_{r.plat} \tag{6.57}$$

where $Q_{plat.tot}$ and $Q_{r.plat}$ are the heat duty of the platen superheater and the direct radiation absorbed by the platen, respectively.

If the platen steam stream conditions are unknown, then the lumped parameter Logarithmic Mean Temperature Difference (LMTD) method can be used to calculate the heat transferred from the flue gas into the steam stream. The representation of heat transfer calculation using the LMTD method is given by

$$Q_{c.plat} = U_{plat} A_{g.plat.conv} \Delta T_{LMTD.plat} \tag{6.58}$$

where U_{plat} is the overall heat transfer coefficient of the platen, $A_{g.plat.conv}$ is the surface area for heat transfer consistent with the definition U_{plat} and $\Delta T_{LMTD.plat}$ is the Logarithmic Mean Temperature Difference across the platen superheater. The overall heat transfer coefficient is calculated as follows

$$U_{plat} = \frac{h_{g.plat}}{1 + \left(1 + \frac{Q_{r.plat}}{Q_{c.plat}}\right)\left(\mathrm{E}_{ash.plat} + \frac{1}{h_{s.plat}}\right) h_{g.plat}} \tag{6.59}$$

where $h_{g.plat}$, $h_{s.plat}$ and $\mathrm{E}_{ash.plat}$ representing the flue gas heat transfer coefficient, steam heat transfer coefficient and ash deposition coefficient, respectively. The term $Q_{r.plat} / Q_{c.plat}$ accounts for the increase in temperature of the ash deposit layer due to the radiant flux from the furnace which in turn reduces the amount of heat transferred by both convection and radiation on the flue gas side.

The heat transfer coefficient of the steam is given by

$$h_{s.plat} = \frac{Nu_{s.plat} \lambda_{s.plat}}{ID_{plat}} \tag{6.60}$$

with ID_{plat} representing the average inner diameter of the tubes in the platen superheater and $\lambda_{s.plat}$ the thermal conductivity of the steam. The steam side Nusselt number is

$$Nu_{s.plat} = 0.023 C_{d.plat} R_{s.plat}^{0.8} \Pr_{s.plat}^{0.4} \tag{6.61}$$

where $C_{d.plat}$, $\mathrm{Re}_{s.plat}$ and $\Pr_{s.plat}$ represents the correction coefficient of tube diameter, the Reynolds number and the Prandtl number on the steam side.

The flue gas heat transfer coefficient, $h_{g.plat}$ in eq. (6.59) is a combination of the convection heat transfer coefficient, $h_{g.conv.plat}$ and the radiation heat transfer coefficient, $h_{g.rad.plat}$ and is given by

$$h_{g.plat} = \zeta_{g.plat} \left(\frac{\pi OD_{plat}}{2S_{L.plat}} h_{g.conv.plat} + h_{g.rad.plat} \right) \tag{6.62}$$

$\zeta_{g.plat}$, OD_{plat} and $S_{L.plat}$ represents the utilization coefficient of the platen superheater, outer diameter of the platen tubes and average longitudinal pitch of the platen, respectively. In eq. (6.62), the term in front of the convection heat transfer coefficient, $\pi OD_{plat} / 2S_{L.plat}$ accounts for different heat transfer surface areas used in the correlations.

The flue gas convective heat transfer coefficient is given by

$$h_{g.conv.plat} = \frac{Nu_{g.plat} \lambda_{g.plat}}{OD_{plat}} \tag{6.63}$$

with OD_{plat} representing the outer diameter of the tubes in the platen superheater and $\lambda_{g.plat}$ the thermal conductivity of the flue gas. The flue gas side Nusselt number is

$$Nu_{g.plat} = 0.2 C_{z.plat} C_{s.plat} C_{w.plat} R_{g.plat}^{0.65} \Pr_{g.plat}^{0.33} \tag{6.64}$$

where $\mathrm{Re}_{g.plat}$ and $\Pr_{g.plat}$ are the Reynolds number and Prandtl number for the flue gas. $C_{z.plat}$, $C_{s.plat}$ and $C_{w.plat}$ represents the correction factor for the tube rows, geometric arrangement, and flue gas composition and temperature, respectively.

In eq. (6.62), the radiation heat transfer coefficient is

$$h_{g.rad.plat} = \sigma_0 \left(\frac{\varepsilon_w + 1}{2} \right) \left(\varepsilon_{g.plat} T_{g.plat.ave}^3 \right) \left(\frac{1 - \left(T_{w.plat} / T_{g.plat.ave} \right)^4}{1 - \left(T_{w.plat} / T_{g.plat.ave} \right)} \right) \tag{6.65}$$

with σ_0 , ε_w and $\varepsilon_{g.plat}$ representing the Stefan-Boltzmann constant, tube wall fouling emissivity and flue gas emissivity in the platen, respectively. $T_{g.plat.ave}$ is the average flue gas temperature in the platen calculated in eq. (6.54). The temperature of the ash deposit layer on the tubes is given by

$$T_{w.plat} = T_{s.plat} + \left(\mathrm{E}_{ash.plat} + \frac{1}{h_{s.plat}} \right) \left(\frac{Q_{r.plat} + Q_{c.plat}}{A_{g.plat.conv}} \right) \tag{6.66}$$

where $T_{s.plat}$ being the average steam temperature in the platen. The term

$$\left(\mathrm{E}_{ash.plat} + \frac{1}{h_{s.plat}} \right) \left(\frac{Q_{r.plat} + Q_{c.plat}}{A_{g.plat.conv}} \right)$$

accounts for the increase in temperature of the ash deposit layer.

The heat absorbed by the water walls and the roof in the platen superheater region is calculated using the overall heat transfer coefficient given by eq. (6.59). Thus, the heat absorbed by the water walls is given by

$$Q_{ww.plat} = U_{plat} A_{ww.plat} \Delta T_{ww.plat} \tag{6.67}$$

where $A_{ww.plat}$ is the heat transfer surface area for the water walls around the platen region. The average temperature difference for heat transfer is simplified to

$$\Delta T_{ww.plat} = T_{g.plat.ave} - T_{s.ww.plat} \tag{6.68}$$

with $T_{s.ww.plat}$ representing the water temperature of the water wall around the platen superheater region.

The heat absorbed by the roof around the platen region is given by

$$Q_{roof} = U_{plat} A_{roof.plat} \Delta T_{roof.plat} \tag{6.69}$$

with $A_{roof.plat}$ representing the heat transfer surface area for the roof in the platen superheater region. The average temperature difference for heat transfer is given by

$$\Delta T_{roof.plat} = T_{g.plat.ave} - T_{s.roof.plat.ave} \tag{6.70}$$

where $T_{s.roof.plat.ave}$ is the average steam temperature within the roof of the platen superheater.

6.5.3. Final superheater model

The final superheater lumped thermal calculation model is effectively similar to that of the platen superheater, as schematically shown in Figure 6-16. However, it is important to note that almost all the direct heat transfer leaking from the platen is absorbed by the final superheater panels. This includes both the direct radiation leaking out from the furnace and the direct radiation from the gas in the platen superheater matrix.

On the other hand, if the gas temperature inside the final superheater is high enough, there could also be direct radiation leaking out at the back of the final superheater. This will be the heat radiated by the gas in the final superheater matrix onto the final reheater downstream on the flue gas side. However, in this work this radiation will be neglected since there are no obvious models available of how to distribute the radiation between the different heat exchanger increments. Only the effect of this radiation on the outlet flue gas temperature will be addressed at the end.

In calculation of the area around the water walls, there is an additional area due to the water walls below the final superheater.

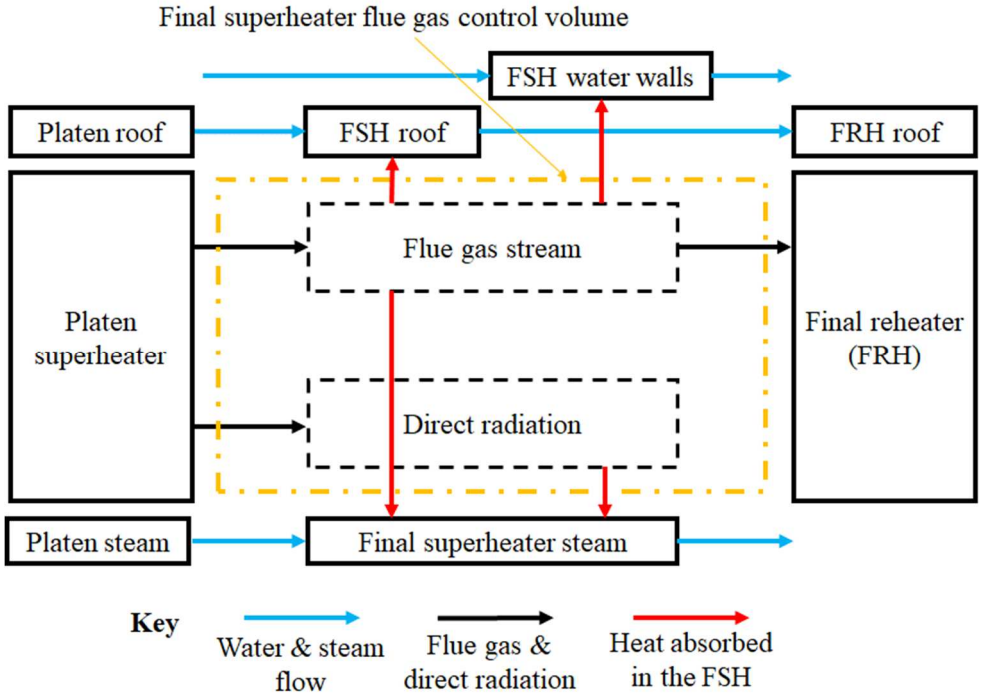

Figure 6-16: A process flow diagram for the final superheater with a control volume around the flue gas stream.

6.5.4. Results from the thermal calculations

The main aim of the high-level thermal calculations of the furnace and platen model was to obtain inputs to the detailed discretized final superheater model. These inputs are the inlet gas temperature and direct radiation falling onto the final superheater. For the MCR case given in the C-schedule, the results are shown Table 6-7. The outlet flue gas temperature was also calculated so that it could be used to compare with the results from the discretized Flownex model. The full calculation for the MCR case from the C-schedule is documented in Appendix E.

Table 6-7: Inputs to the final superheater calculated from the Gurvich Method for the MCR case.

Details	**Units**	**Gurvich Method values**
Inlet direct radiation	MW	27.078
Gas radiation view factor	--	0.315
Inlet flue gas temperature	°C	1059.1
Outlet flue gas temperature	°C	942.6

6.6. Direct radiation onto the Final Superheater

The direct radiation that falls onto the tubes of the final superheater is gradually absorbed from the front tube rows until the back rows. The lumped amount of direct radiation calculated in the subsection above is therefore cascaded over the tube rows. According to Ganapathy [135], the fraction of energy absorbed by the first row is given by

$$a_{FSH}(0) = 3.14\frac{OD_{FSH}}{2S_{T.FSH}} - \frac{OD_{FSH}}{S_{T.FSH}}\left[\sin^{-1}\left(\frac{OD_{FSH}}{S_{T.FSH}}\right) + \left(\sqrt{\left(\frac{S_{T.FSH}}{OD_{FSH}}\right)^2 - 1}\right) - \frac{S_{T.FSH}}{OD_{FSH}}\right] \tag{6.71}$$

and the fraction of the energy absorbed by the subsequent rows is given by

$$a_{FSH}(i) = \left[1 - \left(\sum_{i=0}^{i-1} a_{FSH}(i)\right)\right] a_{FSH}(0) \tag{6.72}$$

6.6.1. Direct radiation inputs to the final superheater

As shown in Figure 6-5 the Flownex model of each element/tubesheet in the final superheater was discretized into four regions per pass. Applying the direct radiation cascading method given by eq.

(6.71) and eq. (6.72) on the direct radiation given in Table 6-7 for the boiler MCR case, results in the distribution shown in Table 6-8.

Table 6-8: Amount of direct radiation absorbed by the different rows in the final superheater Flownex model for the MCR case.

Row numbers	**Units**	**Amount of radiation**
Rows 1 - 8	kW	13 200.81
Rows 9 - 16	kW	6 765.18
Rows 17 - 25	kW	3 759.21
Rows 26 - 34	kW	1772.09
Rows 35 - 43	kW	835.36
Rows 44 - 52	kW	393.79
Rows 53 - 60	kW	171.2
Rows 61 - 68	kW	87.74

Since the discretized model groups the tube rows in a bundle of eight or nine tubes, then the highest direct radiation is experienced by the first bundle. From there it reduces, as it cascades toward the back of the heat exchanger. In a bundle, the direct radiation is assumed to be evenly distributed along the height of the bundle. Thus, in the Flownex model shown in Figure 6-5 the input direct radiation in each heat exchanger building block is correlated to the area it represents with respect to the total area along the height of the bundle. This is dependent on the discretisation employed. As per the description in chapter 3, each heat exchanger building block is a compound component that consists of a network of 1-D elements as shown Figure 6-17. In this heat exchanger building block, the direct radiation is introduced as a lumped heat input on the node at the outer fouling layer surface. This direct radiation increases the temperature of the outer surface of the outer fouling layer. This in turn has an influence on the flue gas radiation and convection heat transfer. The full calculation of the direction radiation for the MCR case from the C-schedule are documented in Appendix E.

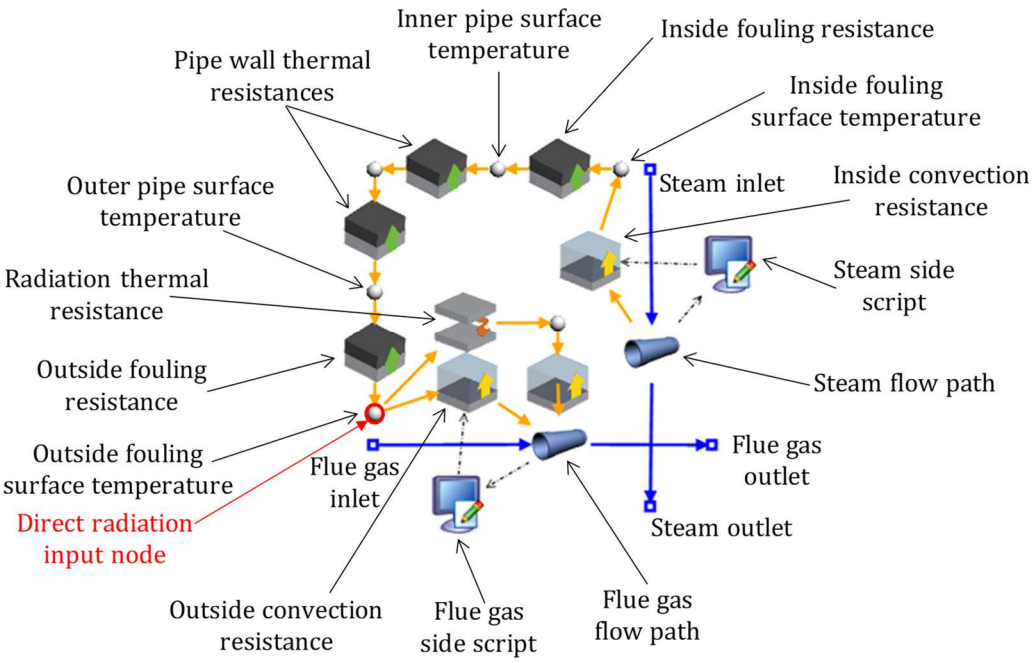

Figure 6-17: Schematic of the heat exchanger increment sub-network in Flownex as shown in Figure 3-12 but with an illustration of the node on which the direct radiation is introduced.

6.7. Model validation

Disclaimer: The conceptual idea of the model validation methodology was introduced in reference [3] *which was published as part of the proceedings of the 16th International Heat Transfer Conference. The candidate is indebted to his supervisor together with whom the concept was developed.*

In this chapter, a refined modelling methodology was developed that may help to better understand the relationship between the operational conditions and metal temperatures encountered in boiler heat exchangers. To further establish confidence in the results produced with this methodology it should be validated. However, detailed validation of heat exchanger process models in a real power plant poses significant challenges. These include the sheer size and complex geometry of the equipment, and the fact that the relevant steam and flue gas flow rates and temperatures are not always directly measured. It is also not possible in an industrial setting to simply install additional measurement equipment. Therefore, the methodologies and results of such validation studies are rarely found in open literature.

Here, a validation methodology is proposed and applied to the developed radiant final superheater process model. The validation methodology employs a combination of the plant design data (C

schedules), the boiler Mass and Energy Balance (MEB) and the Gurvich boiler design method to obtain the various inputs as well as the outputs for comparison purposes. The steam temperatures and pressures are readily available from the C-schedules. However, some flue gas values are determined using a combination of the MEB and the Gurvich method.

6.7.1. Model validation methodology

The systematic validation methodology proposed here is based on a combination of C-schedule data, a boiler MEB and the Gurvich method which are used to obtain the necessary data. This methodology is as follows;

Step 1: Run the model in steady state for the 100% MCR (Maximum Continuous Rating) case while prescribing the same boundary values for the total steam mass flow rate, inlet temperature and pressure as well as the same flue gas properties, total flue gas mass flow rate and inlet temperature and pressure. Here, it is assumed that the steam and flue gas temperatures and pressures are uniformly distributed at the inlets and that the tube surfaces are perfectly clean with no outer fouling, inner scaling or flow blockages. Compare the calculated total heat exchanger duty with that of the C-schedule.

Since the C-schedule data is usually based on a typical operational scenario where there is already some degree of plant degradation (typically fouling on the outside of the tubes, etc), it can be expected that the calculated duty for the clean heat exchanger will be greater than that specified in the C-schedule.

Step 2: Therefore, the model is now calibrated by adjusting the overall heat transfer coefficient (UA) across the whole heat exchanger until the calculated duty matches that of the C-schedules. The adjustment of the UA value involves a systematic and careful adjustment of the thickness of the outer fouling layer.

The rationale behind adjusting the outer fouling layer is that during operation there will be build-up of ash particles on the outer surface of the tubes. However outer fouling might not be the only effect which can influences the change in the UA value. During normal operation, the flue gas flow is not uniform across the inlet cross sectional area of the heat exchangers. Thus, these flow patterns have an influence on the convection heat transfer process. On the other hand, the heat exchanger of interest is a radiant superheater, thus an adjustment to the convective heat transfer coefficient might not necessarily result in a significant change on the UA value. Hence, this effect is assumed to be negligible in this case.

Step 3: Run the calibrated model for the other steady state off-design load cases provided in the C-schedule. Compare the model results to the C-schedule data. A successful outcome in Step 3 without any re-calibration of the model implies that the calibration that was performed in Step 2 is not simply a case-by-case "tuning" of the model. Rather, once it was calibrated for 100% MCR the model is applicable to a broad range of well-defined off-design operational conditions at a given state of plant degradation that was assumed by the Original Equipment Manufacturer. Therefore, good comparison for all off-design cases at this stage provides suitable evidence of the validity of the model.

6.7.2. Application of the model validation methodology

This section presents the results of the validation study conducted for the Flownex model of the final stage superheater heat exchanger of the 600 MW class coal-fired power plant. The single element Flownex model present in Figure 6-5 was employed. Based on the data provided by the C-schedule, the flue gas input data including direct radiation was calculated using the boiler MEB and the Gurvich boiler design method. In this case the heat absorbed by the side and bottom water walls and roof around the superheater is assumed to be negligible.

Step 1: The model with clean tubes was used to predict the duty of the superheater for the 100% MCR case under steady state operating conditions. As expected, the model overestimated the duty by 68.2% when compared to the C-schedule data as shown in the middle column Table 6-9.

Step 2: Upon calibration via the introduction of an outer fouling layer (OFL) of 0.864 mm in thickness, the predicted duty matched that of the C-schedule as shown in the right-hand column in Table 6-9. It is important to note that there is some discrepancy in the flue gas outlet temperature which might be due to flue gas properties used or the zonal influence of the imposed direct radiation.

Step 3: The calibrated model was then used to predict the heat exchanger duty for the off-design 68.6% MCR load case as shown in Table 6-10. The predicted duty was within 2.1%. This good comparison provides suitable evidence of the validity of the model results. The resulting outlet steam temperature was also slightly higher.

Table 6-9: Comparison of the Flownex (FNX) model with clean and fouled tubes to the data derived from C-schedule information at MCR.

	Details	Units	C-schedule	FNX model - Clean	FNX model - Fouled
General	Boiler load	MCR		100%	
	Outer fouling layer	mm	--	0	0.864
	Heat Exchanger Duty	MW	107	180	107
Steam	Mass flow rate	kg/s	509.8	509.8	509.8
	Inlet pressure	MPa	17.88	17.88	17.88
	Inlet temperature	°C	473.6	473.6	473.6
	Outlet temperature	°C	540	591.9	540.1
Flue gas	Mass flow rate	kg/s	728.4	728.4	728.4
	Inlet pressure	kPa	83.5	83.5	83.5
	Inlet temperature	°C	1059.1	1059.1	1059.1
	Outlet temperature	°C	942.5	828.8	939.5

Table 6-10: Comparison of the Flownex (FNX) model with fouled tubes to the C-schedule data at low load cases.

	Details	Units	C-schedule	FNX model
General	Boiler load	MCR		68.6%
	Outer fouling layer	mm	--	0.864
	Heat Exchanger Duty	MW	72.5	74
Steam	Mass flow rate	kg/s	349.7	349.7
	Inlet pressure	MPa	16.84	16.84
	Inlet temperature	°C	472.1	472.1
	Outlet temperature	°C	540	542
Flue gas	Mass flow rate	kg/s	538.8	538.8
	Inlet pressure	kPa	83.5	83.5
	Inlet temperature	°C	937.0	937.0
	Outlet temperature	°C	829.0	825.6

6.8. Direct radiation downstream of the final superheater

As mentioned in the subsection above, if the flue gas temperature within the final superheater is high enough, it could also emit direct radiation towards the downstream final reheater heat exchanger. This heat rejection via direct radiation will influence the local flue gas temperature and therefore also the local gas radiation and convective heat transfer within the superheater. In addition, it influences the

outlet flue gas temperature of the final superheater which in turn becomes the inlet flue gas temperature for the downstream reheater heat exchanger. In this work, detailed accounting of this direct radiation is not done. However, its potential influence is considered in the following paragraphs.

Consider the 100% MCR case from the C-schedule data that was discussed above without taking into account the direct radiation from the final superheater onto the final reheater. The resulting outlet flue gas temperature was 939.5°C as shown in Table 6-9. If the direct radiation onto the final reheater is calculated using the same lumped analysis that was employed in the platen superheater, it works out to be 9.492 MW as presented in Table 6-11. If this direct radiation is also extracted from the calculated final flue gas temperature from the discretized model, the outlet flue gas temperature reduces to 925.3°C as shown in Table 6-11.

Table 6-11: Summary of the study on the influence the direct radiation from the final superheater onto the downstream final reheater has on the outlet flue gas temperature of the final superheater for the 100%MCR C-schedule case on the validated final superheater Flownex model.

Details	**Units**	**Value**
Direct radiation onto the final reheater	MW	9.492
Outlet flue gas temperature of the FSH without accounting for the direct radiation onto the final reheater	°C	939.5
Outlet flue gas temperature of the FSH with the direct radiation onto the final reheater accounted for	°C	925.3

The results show that although the potential direct radiation is roughly 9% of the total heat exchanger duty, the impact of that on the outlet gas temperature is relatively small. However, the convective heat transfer is driven by the temperature difference between the fluid streams and the gas radiation is driven by the difference in the temperatures each to the power four. The results shown in Table 6-11 imply that the convection heat transfer might be overestimated by roughly 1.4% and the gas radiation heat transfer by 2.5%. Therefore, the impact of neglecting the potential direct radiation at the outlet of the final superheater should be relatively small.

In the Gurvich model, this direct radiation is calculated as a function of the average flue gas temperature. Therefore, it does not provide a mechanism for distributing the direct radiation between the different tube rows as was the case for the incident direct radiation. Thus, a recommendation for

future work is to apply more refined methods such as the zonal model inside the areas in between the tubesheets of the platen and final superheaters to account for both the incoming direct radiation and the outgoing direct radiation. These models should be discretised and linked up to the Flownex heat exchanger building blocks, again at the outer surface temperature node as was indicated in Figure 6-17. However, the platform solution speed will be affected in the process.

6.9. Summary of the chapter

This chapter presented a refinement to the developed heat exchanger process modelling methodology. It systematically provided the information and models necessary in the application of the refined process modelling methodology on a practical case. This practical case is a final stage radiant superheater in a coal-fired boiler. The required information included the relevant geometry, heat exchanger arrangements, Flownex model description and process flow inputs. The inputs on the flue gas side are not measured in the plant, thus high-level models for attaining the input data into the final superheater model had to be employed. These high-level models included an overall boiler Mass and Energy Balance as well as the Gurvich thermal calculation method. The Gurvich method brought to light the importance of the direct radiation from the furnace and the platen superheater upstream on the final stage radiant superheater. The refined process modelling methodology is capable of accounting for this direct radiation. It accounts for it as a heat source on the node of the outer fouling layer's outer surface, thus heating the outer fouling layer as it would be the case practically. Hence influencing the local gas radiation and convection heat transfer on a discretised model.

These high-level models were applied for a boiler 100% MCR case and a 68.6% MCR case provided in the plant design C-schedule data. For completeness, inputs and results for the 100% MCR case were shown. The developed boiler MEB was successfully verified against the C-schedule data, thus creating confidence in its further use on other cases. The developed network model of the final stage radiant superheater model was also calibrated and validated against the heat transfer duty provided by the C-schedule. The successful validation of the model created confidence in the use of the model.

Further insight was gained when analysing the impact of accounting for the direct radiation originating from the flue gas in the final superheater region towards the downstream final reheater heat exchanger. This analysis showed that the impact will be small and also illuminated that for better accounting of this direct radiation, refined models such as zonal model must be used.

7. REFINED METHODOLOGY: MODEL APPLICATION

This chapter presents the application of the refined modelling methodology to the cross-flow radiant superheater heat exchanger that was described in chapter 6. The emphasis of this chapter is on the application of the superheater model on a real plant case supported by plant data. From these applications, the value added by such a model is magnified.

Limited plant measurements are usually available from the Distributed Control System (DCS) for various operational conditions. These typically include steam flow rates and temperatures at the inlet and outlet of each heat exchanger. However, the flue gas mass flow rates and temperatures are rarely measured directly. Since the flue gas flow rate and properties are required inputs for the model, the boiler MEB is employed to obtain them. To obtain the inlet flue gas temperature and the direct radiation into the final superheater, the Gurvich method is employed. In this chapter, only the direct radiation from upstream that impinges on and is absorbed by the final superheater is accounted for.

In addition, for this radiant final stage superheater heat exchanger additional measurement equipment was installed on the plant. This involved the installation of thermocouples both at the inlet and outlet of the heat exchanger as detailed in the section below. Some details of the installed thermocouples were presented by Rousseau et al. [136].

7.1. Description of plant measurements: installed thermocouples

In the plant, thermocouples were installed on the manifold headers and on the stub headers of one of the elements that is known to experience the highest temperatures. The positions of the installed thermocouples on the manifold inlet and outlet headers of the final superheater are shown in Figure 7-1. Figure 7-1 clearly illustrates that there are four manifold inlet headers and two manifold outlet headers. Each manifold inlet header corresponds to one leg of the overall heat exchanger. Each leg consists of seven elements. So, for each manifold inlet header, one thermocouple was installed on the connecting pipes to determine the inlet steam temperature. The assumption was that within the header the steam temperature will be relatively uniform [136]. To be more specific, the thermocouples were installed on one connecting pipe for elements 6, 11, 18 and 23. On the outlet, the outer legs (Leg A and D) share a manifold header and the inner legs (Leg B and C) share the other manifold header. For each of the outlet manifold headers, measurements are taken on every second connecting steam pipe. This implies that measurements are taken for each of the 28 elements, since each element has two

connecting pipes which are connected side by side on the manifold headers. It is assumed that each measurement represents the average outlet steam temperature for each of the 28 elements [136].

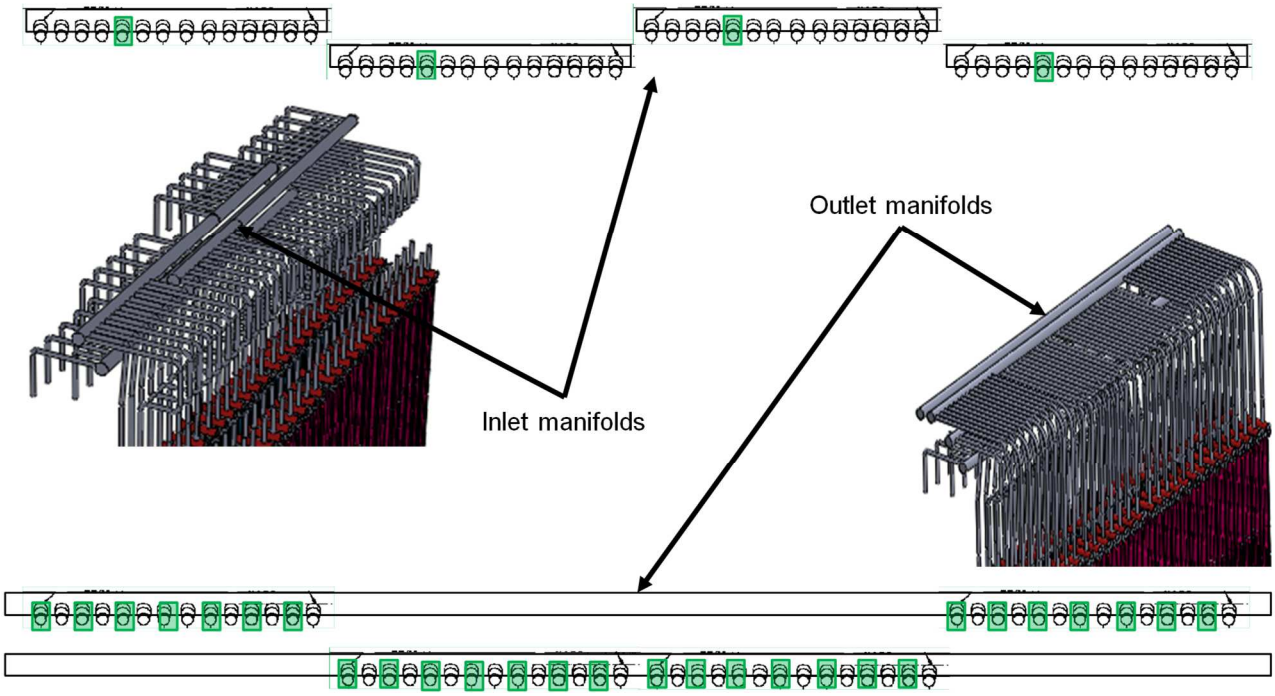

Figure 7-1: Positions of the steam pipes coupled to the inlet and outlet manifolds on which thermocouples have been installed [136].

Due to element 23 usually experiencing the highest temperatures more detailed measurements were installed on this element, shown in Figure 7-2. Thus, each of the 34 tubes had a thermocouple installed at the outlet near the outlet stub-header as shown in Figure 7-3.

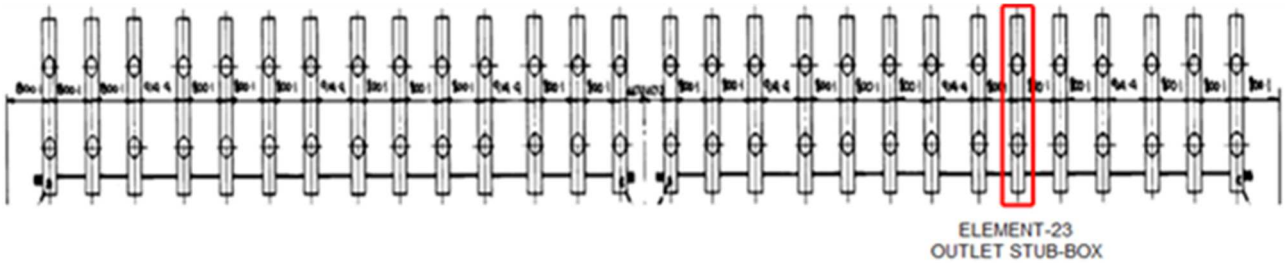

Figure 7-2: Thermocouples installed on the tubes just before the outlet stub-box of element 23 (Courtesy of Eskom).

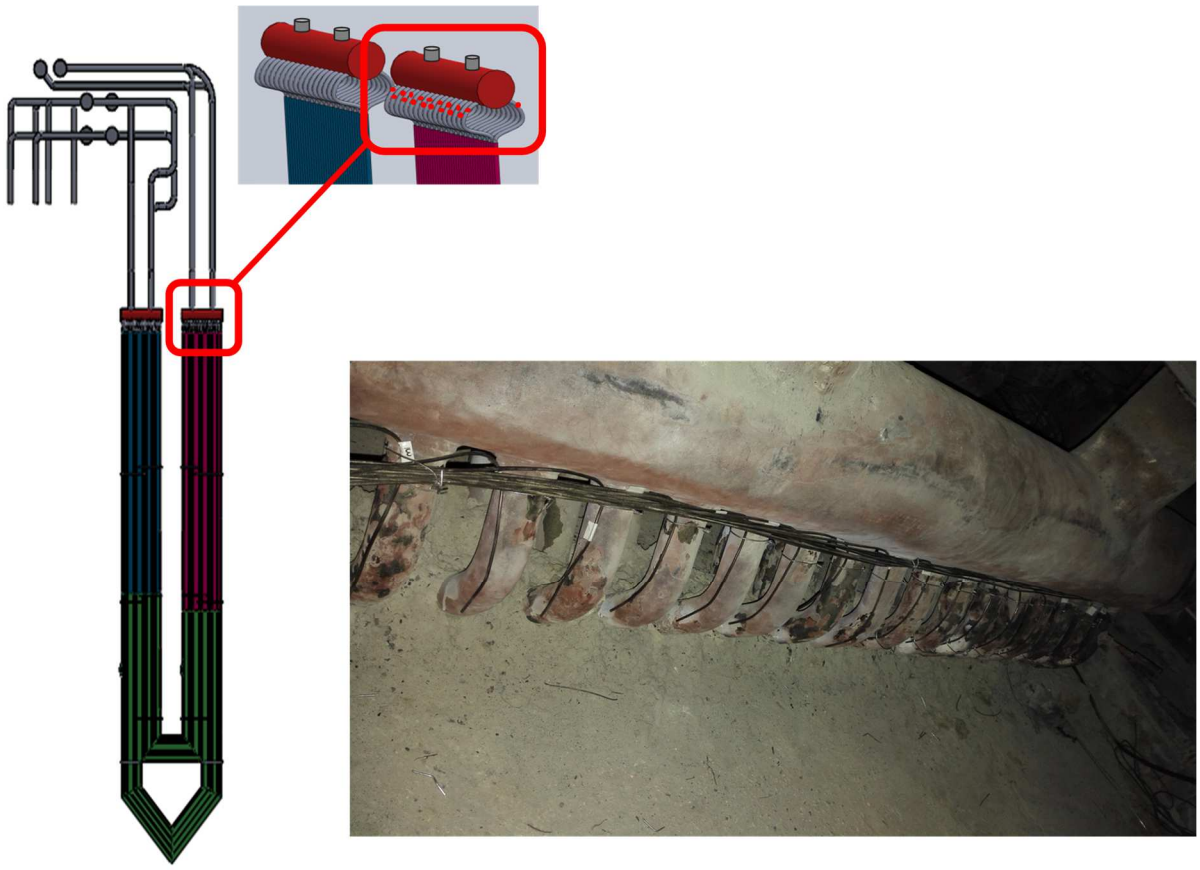

Figure 7-3: Thermocouples installed on every tube on element 23 just before the outlet stub-box (Courtesy of Jean-Piere du Preez & Professor Pieter Rousseau).

Disclaimer: The installation of thermocouples on the final stage superheater heat exchanger was part of Jean-Pierre du Preez's Master of Science in Mechanical Engineering Project registered at the University of Cape Town under the Eskom Specialisation Centre in Energy Efficiency [137]. *The installation was funded by Eskom Research, Testing and Development (RT&D) under the leadership of Dr Mark Newby. The acquisition of data both from the DCS and the installed thermocouples was part of Lethukuthula Vilakazi's Master of Technology in Mechanical Engineering Project registered at the Vaal University of Technology under the Eskom Specialisation Centre in Energy Efficiency* [138].

7.2. Input data

In addition to the installed thermocouple data, DCS data had to be obtained for the final superheater heat exchanger and the high-level models (the boiler MEB and the Gurvich method model) as discussed in the sections above. This DCS data is presented in Appendix F.

7.3. Model application: Steady state

In this section, the discretized superheater model developed and validated in the previous chapter is applied to real plant scenarios for steady state operations. Cases for both uniform and non-uniform flue gas and steam inlet conditions across the width of the superheater are analysed.

Furthermore, results of a case study at the plant full load are presented. In the acquisition of steady state real plant operation data, it is important to identify a time period during which the plant was operating at near steady state, as highlighted by Rousseau et al. [136]. In most instances, the plant hardly operates at true steady state, but achieve quasi-steady state. In the acquired plant data, a quasi-steady state period of full load plant operation was observed between 17:30 and 22:40 for the selected day, as illustrated by Figure 7-4 for the generator load. Therefore, all inputs used for the full load steady state case are based on the mean values of the respective inputs obtained within this period.

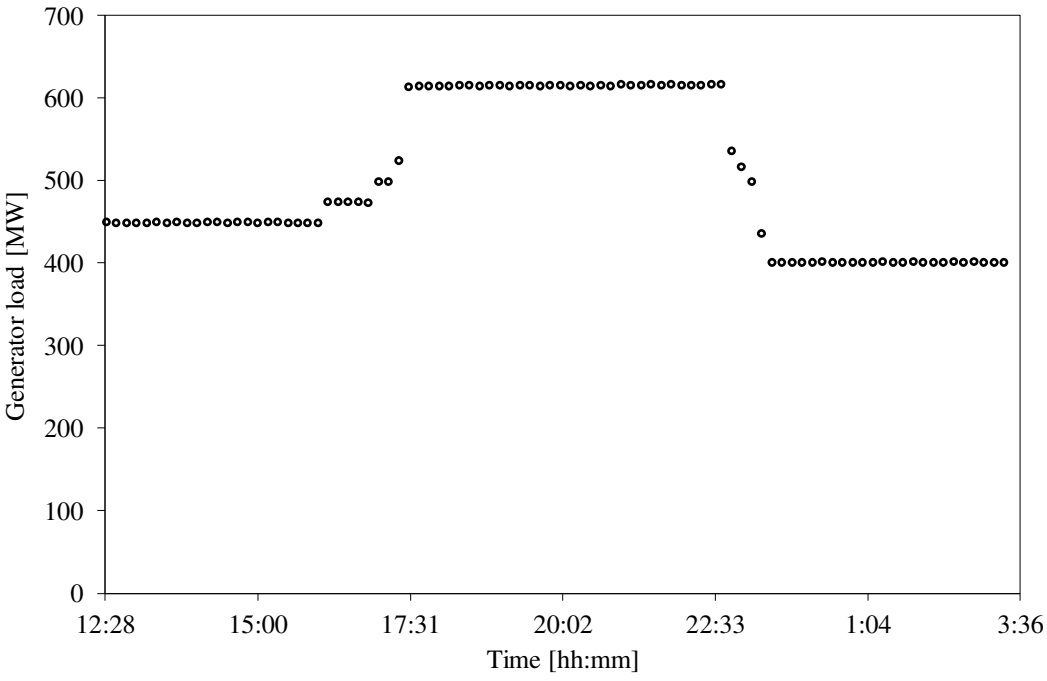

Figure 7-4: Recorded generator load data from the plant DCS, showing a full load quasi-steady state from around 17:30 until 22:40 [136].

For the discretized model, inputs for both the steam and flue gas sides are required. For the case modelled here, the input data is shown in Table 7-1. Inputs for the steam side are obtained from the recorded DCS real plant data. For the flue gas side, the high-level models, i.e. the boiler MEB and the Gurvich method, were employed to obtain the inputs. These are lumped input values, thus relevant methods of distributing them into the discretized Flownex superheater model are employed. As

illustrated in the previous chapter, the direct radiation is cascaded over the heat exchanger model using eq. (6.71) and (6.72). For each lumped bundle of tubes in the Flownex model, the direct radiation is assumed to be uniformly distributed along the length of the tubes. The input to the high-level models are presented in Appendix F. These inputs were used in the high-level models similar to those presented in Appendix D and E for the 100% MCR C-schedule case.

Table 7-1: Inputs to the final superheater from the DCS and resulting from the high level MEB and Gurvich model calculations for the full load real plant case.

Details	**Units**	**Value**
Mass flow rate of steam into the final superheater	kg/s	470.6
Inlet steam temperature	°C	485.9
Mass flow rate of flue gas out of the economizer	kg/s	839.9
Inlet flue gas temperature	°C	1030.9
Direct radiation into the final superheater	MW	22.297
Gas radiation view factor for the final superheater	--	0.259

7.3.1. Uniform inlet conditions across the superheater width

If it is assumed that all 28 elements of the superheater heat exchanger experience the same steam and flue gas inlet conditions as well as the same fouling conditions, then the one element model for the superheater shown in Figure 6-5 can be used as a representative model for the whole heat exchanger. This is the model that was calibrated and validated against plant design C-schedule data in the previous chapter.

Firstly, the model had to be run in steady state for the full load case while prescribing the same boundary values for the total steam mass flow rate, inlet temperature and pressure as well as the same flue gas properties, total flue gas mass flow rate and inlet temperature and pressure as those obtained from the DCS data together with the data generated via the boiler MEB and Gurvich method. The calculated total heat exchanger duty was then compared with that of the real plant data. Since the real plant is likely to be operating with a different degree of fouling than the C-schedule for which the model was calibrated earlier, it can be expected that the calculated duty will be different from the measured value. The results presented in Table 7-2 confirm this. Therefore, the model was then re-calibrated by further adjusting the outer fouling layer thickness uniformly across the whole heat exchanger until the calculated duty matched that of the real plant data as illustrated in Table 7-2. This

was achieved when the outer fouling layer thickness was 1.65mm. This adjustment is based on the rationale discussed in the previous chapter. In addition, there was a satisfactory comparison of the outlet lumped steam and lumped flue gas temperatures from the discretised model to those from the DCS, MEB and Gurvich method.

Table 7-2: Comparison of the results from the discretized Flownex (FNX) model which has been calibrated against the MCR of the C-schedule (left) and the re-calibrated model against the plant full load at the date and time selected in this calculation.

	Details	**Units**	**DCS, MEB & Gurvich**	**FNX model – Calibrated against C-schedule**	**FNX model – Re-Calibrated for real plant data**
General	Plant load	Full		100%	
	Outer fouling layer	mm	--	0.864	1.65
	Heat Exchanger Duty	MW	67.5	95.7	67.4
Steam	Mass flow rate	kg/s	470.6	470.6	470.6
	Inlet pressure	MPa	16.3	16.3	16.3
	Inlet temperature	°C	485.9	485.9	485.9
	Outlet temperature	°C	533.5	554.9	533.2
Flue gas	Mass flow rate	kg/s	839.9	839.9	839.9
	Inlet pressure	kPa	83.5	83.5	83.5
	Inlet temperature	°C	1030.9	1030.9	1030.9
	Outlet temperature	°C	975.9	935.2	972.0

The results of the calibrated discretized model of the superheater can then be used to study the temperatures and heat transfer trends in locations of the heat exchanger where a measuring instrument cannot be easily installed. Figure 7-5 shows some 2-D temperature profiles on a section of heat exchanger just above the U-shape. This section of interest is illustrated by the rectangular shape imposed on the superheater model on Figure 7-5a). Figure 7-5b) shows a relatively uniform variation of the flue gas temperature across the depth of the heat exchanger section. This is because the inlet flue gas temperature is assumed to be uniform across the cross-section of the inlet to the superheater. Figure 7-5c) presents the temperature profile of the outer surface metal temperatures. As expected, the temperatures are lower at the steam inlet side than the steam outlet side. Also, on the steam outlet there is a variation since the inner tubes are shorter than the outer tubes. Thus, the steam in the inner tubes is subject to less heat transfer than that on the outer tubes because of the difference in the heat transfer area.

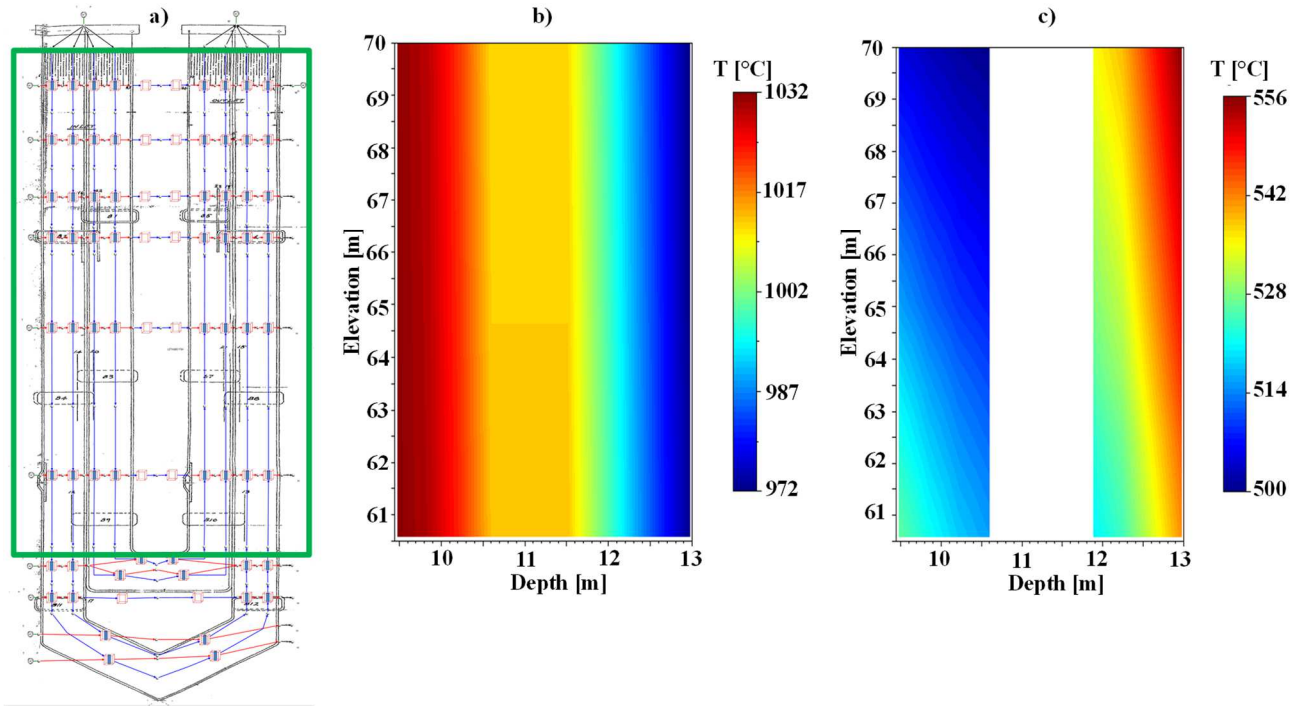

Figure 7-5: Temperature results along the depth of a section of the superheater element; a) the 2D section of interest, b) flue gas temperature profile and c) outer surface metal temperature profile.

A more detailed and comparative analyses of the temperature and heat transfer distribution is presented in Figure 7-6. The focus is on a cut away section corresponding to the discretisation of the model as illustrated in Figure 7-6a). This is an interesting section because it consists of both the inlet and outlet steam sides. Figure 7-6b) and Figure 7-6c) respectively present the temperature and heat transfer distribution for this discretised section. For each of the heat exchanger building blocks, the recorded steam and flue gas temperature values represent an average between the inlet and the outlet.

In Figure 7-6b), the inlet steam temperature is uniform since it was specified in the model and the outlet steam temperatures are slightly higher on the flue gas outlet side. The trend of the outlet steam temperature conforms to the expectation as per the geometry of the heat exchanger. The outer tubes are longer, thus have a higher heat transfer area than the inner tubes. Therefore, these outer tubes absorb more heat resulting in a higher outlet steam temperature. Due to the high thermal conductivity of the tubes, the tube outer surface temperatures are close to the corresponding steam temperatures. As explained in chapter 4, the outer fouling layer temperature is higher than that of the tube surface due to its low thermal conductivity. However, the relationship between the temperatures of the flue gas and outer fouling layer for this heat exchanger differs to that analysed in chapter 4. This is because the

final superheater analysed here is a radiant heat exchanger, while in chapter 4 a primary superheater which is a convective heat exchanger was analysed.

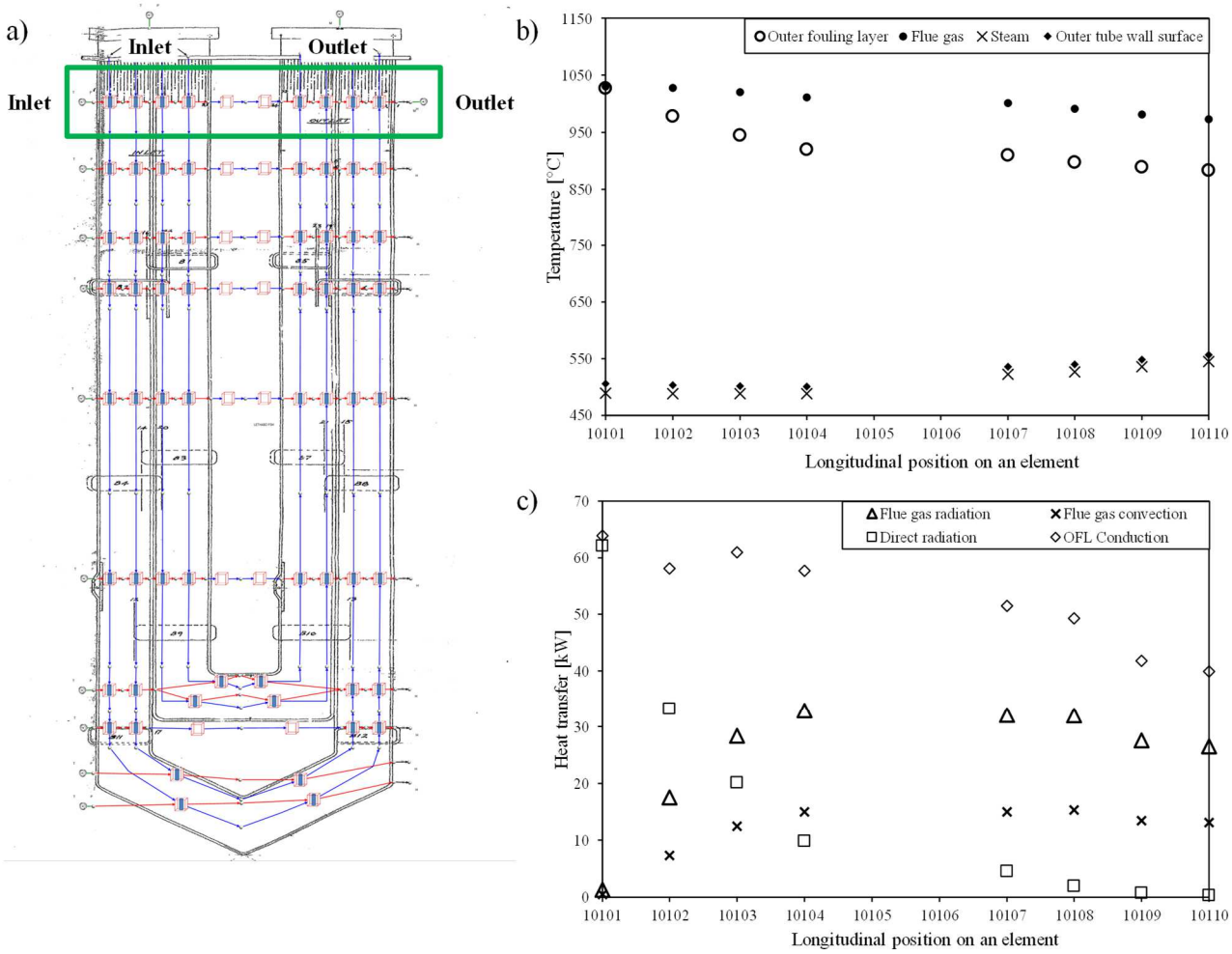

Figure 7-6: A detailed analysis of the inlet and outlet of the heat exchanger with; a) the location of the region of focus on the heat exchanger, b) the temperature distribution and c) the heat transfer distribution.

In addition to the gas radiation, direct radiation must also be accounted for in a radiant superheater as shown in Figure 7-6c). Due to the location of such heat exchangers, the luminous radiation from the furnace also leaks out and reaches these heat exchangers. Also, the long-range direct radiation from the flue gas in the platen superheater region upstream does reach the final superheater. As a result of the direct radiation heat impinging on the first bundle close to the furnace, the temperature of the outer fouling layer is almost the same as that of the flue gas, as shown in Figure 7-6b). This phenomenon corresponds to a relatively small amount of heat being convected and radiated via gas radiation from the flue gas stream onto the outer fouling layer as illustrated in Figure 7-6c). Despite this phenomenon occurring, there is still a significant amount of heat conducted into the steam flow, as indicated by the data points named “OFL Conduction”. Thus, for the first bundle almost all the heat transferred to the

steam is a result of the direct radiation. As the direct radiation gets absorbed by the tubes, its contribution decreases as the flow cascades towards the back of the superheater. This corresponds to an increase in the contribution of gas radiation and convection heat transfer as shown in Figure 7-6c), supported by the flue gas and outer fouling temperature trends shown in Figure 7-6b).

Furthermore, the direct radiation heat impinging on the first bundle close to the furnace can result in a case where the temperature of the outer fouling layer is higher than that of the flue gas. This phenomenon could then correspond to heat being convected and radiated via gas radiation away from the outer fouling layer into the flue gas stream. However, despite such a phenomenon occurring, the net heat would still be conducted into the steam flow. Thus, for the first bundle all the heat transferred to the steam would be a result of the direct radiation.

7.3.2. Non-uniform inlet conditions across the superheater width

Here, the focus is on modelling the complete superheater heat exchanger to allow for the variation of parameters and properties in three-dimensions i.e. width, depth and height. The discretized model shown in Figure 6-7 is used. This model bundles together the seven elements in each leg. In this model, the energy absorbed by the side water walls, bottom water walls and roof is assumed to be negligible.

As alluded to in the sections above, the input from the high-level MEB and Gurvich model lumps the flue gas energy at the inlet face of the superheater. However, it is well accepted that in reality the input energy at the inlet face of the superheater is not uniformly distributed, as illustrated by Babcock & Wilcox [12]. For the boiler considered in this, a CFD model which included the furnace, platen superheater and final superheater was developed separately by Dr Ryno Laubscher of the University of Cape Town. The CFD model focused on the flue gas side without solving the detailed steam flows inside the tubes. The results from this CFD model of the boiler confirmed that the inlet flue gas temperature to the final superheater varies across the face of the inlet cross-section. When the CFD model was run with inputs corresponding to the 100% boiler MCR case C-schedule data, it resulted in the normalized inlet flue gas temperature profile presented in Figure 7-7. In the CFD model, the boiler was assumed to be symmetric, hence half of the boiler was modelled. Notable is that the temperature is highest at the centre location across the width but below the midpoint along the height. In addition, the temperature reduces closer to the side water walls and the roof since some energy is absorbed there. Furthermore, due to the conservation of momentum the flow profile has an impact on where the hot spots are in the boiler. In this work the normalized inlet flue gas temperature profile shown Figure 7-7 is used to proportion the lumped input energy from the high-level Gurvich model. The resulting

temperature distribution is then used as an input to the discretized superheater model. This energy distribution is only done for the inlet flue gas temperature, not for the direct radiation.

Disclaimer: The CFD model for the boiler analysed in this work from which the inlet flue gas profile was extracted was developed by Dr Ryno Laubscher based on geometrical information and plant design C-schedule data. This is part of the wider research work done in the Eskom Specialisation Centre in Energy Efficiency under the Department of Mechanical Engineering at the University of Cape Town.

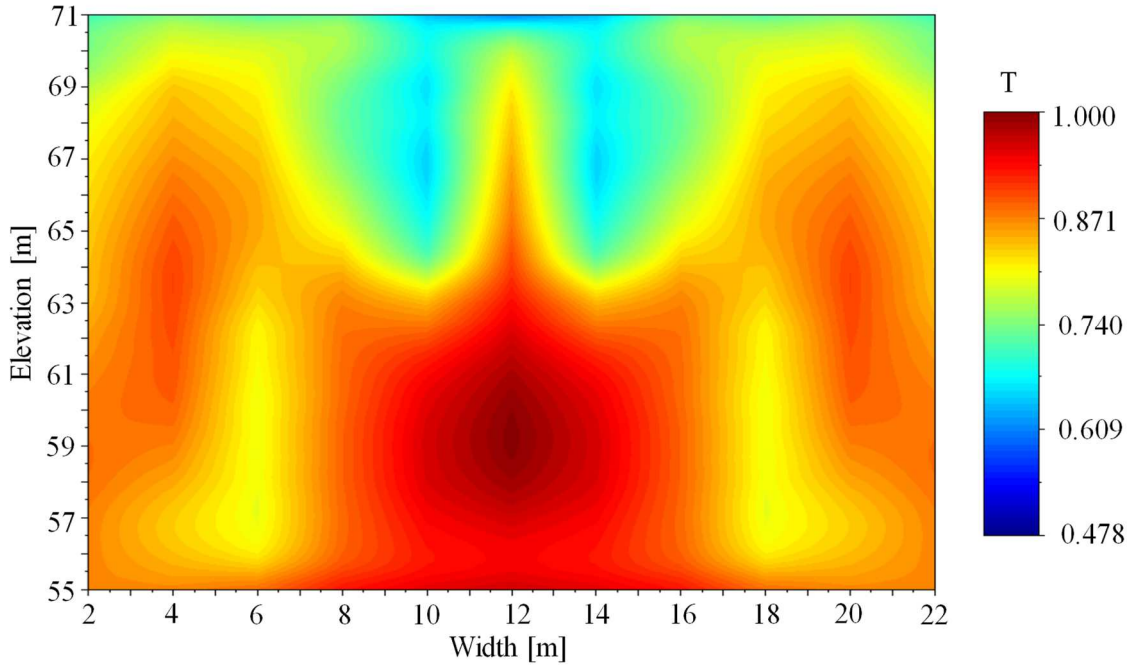

Figure 7-7: Normalized flue gas temperature plot at the inlet face of the final superheater from a CFD model with a symmetry assumption at the mid-plane of the heat exchanger (Courtesy of Dr Ryno Laubscher).

Applying the steam mass flow rate and averaged flue gas side input values presented in Table 7-1, but while accounting for the variation of the inlet steam temperature on each leg, the outlet steam temperatures shown in Figure 7-8 were obtained from the discretised model. The model results are compared to the results from the detailed thermocouple measurements shown in Figure 7-1. For this analysis, the inlet steam temperatures are assumed to correspond with the measurements from the thermocouples on the inlet headers. The rationale behind the assumption is that the thermal conductivity of the metal is high, thus the difference between the steam and metal temperatures should be negligible. In addition, it was assumed that the measured inlet temperatures are a representation of the steam temperatures in the inlet headers for each leg.

At first it was assumed that the outer fouling layer was uniform across the heat exchanger as was the case when uniform inlet conditions were imposed. Since now the inlet thermocouples temperatures

were to be used as inputs, the model used for the case with uniform inlet conditions was recalibrated. Using the average inlet temperature of 478.9°C, calibrating against an average outlet temperature of 536.9°C, a satisfactory comparison was achieved when an OFL of thickness 1.2mm was imposed. The corresponding outlet steam temperature from the discretized model was 536.7°C.

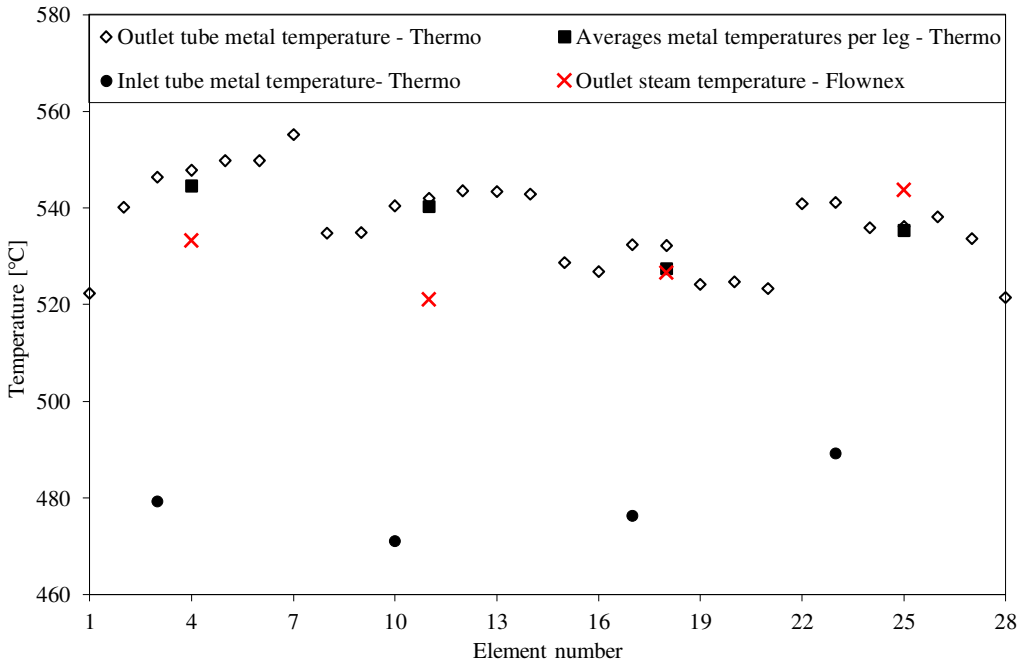

Figure 7-8: Comparison of the outlet steam temperature from the discretized model to the detailed thermocouple data with the inlet tube metal temperatures from the thermocouples used as inlet steam temperature inputs for the discretized model. For this discretized model all the legs were made up of the recalibrated model from the uniform inlet condition section above.

Hence the assumption that each leg experiences an OFL thickness of 1.2mm was employed. The resulting outlet steam temperatures from the discretised model are shown in Figure 7-8. The temperature results from the discretized model for Legs A, B and D do not correspond to those from the averages per leg from the thermocouples for those legs. With those from Legs A and B slightly lower and that from Leg D slightly higher. However, the results for Leg C are almost the same. The average of all the measured temperatures from the thermocouples at the outlet is 536.9°C, while that from the discretized model is 531.3°C. Thus, despite imposing the same OFL across all the legs on the discretized model the average outlet temperature is relatively close to the average from measurements. The slight discrepancy of about 1% can be attributed to the imposed profile on the flue gas side. This implies that the inlet energy that was provided by the uniform profile was slightly higher than the energy imposed in this case study where a non-uniform profile is imposed. Here, the inlet flue gas temperature corresponds to the CFD normalized profile which conforms to reality. Even though the

average outlet steam temperature is slightly lower, the trend of the temperatures still depicted a profile which is related to the inlet steam temperature profile.

Although the calculated outlet steam temperatures from the discretised model compared reasonably well with the measurements in the analysis above, it must be noted that an OFL of uniform thickness was still assumed for all the tubes in the representative elements for all the legs. In practice however, different OFL thicknesses will occur and therefore a separate recalibration of each leg is required to fine-tune the discretised model. After recalibration of each leg, the steam temperature results from the discretised model compared well to the average temperature results from the thermocouple measurements for each leg as shown in Figure 7-9. Such results were achieved with the following OFL thicknesses: Leg A – 0.85mm, Leg B – 0.65mm, Leg C – 1.2mm and Leg D – 1.55mm. With such satisfactory results, the respective temperatures of the lumped elements per leg can be analysed. This analysis can be done in areas of the heat exchanger where measuring equipment cannot easily be installed.

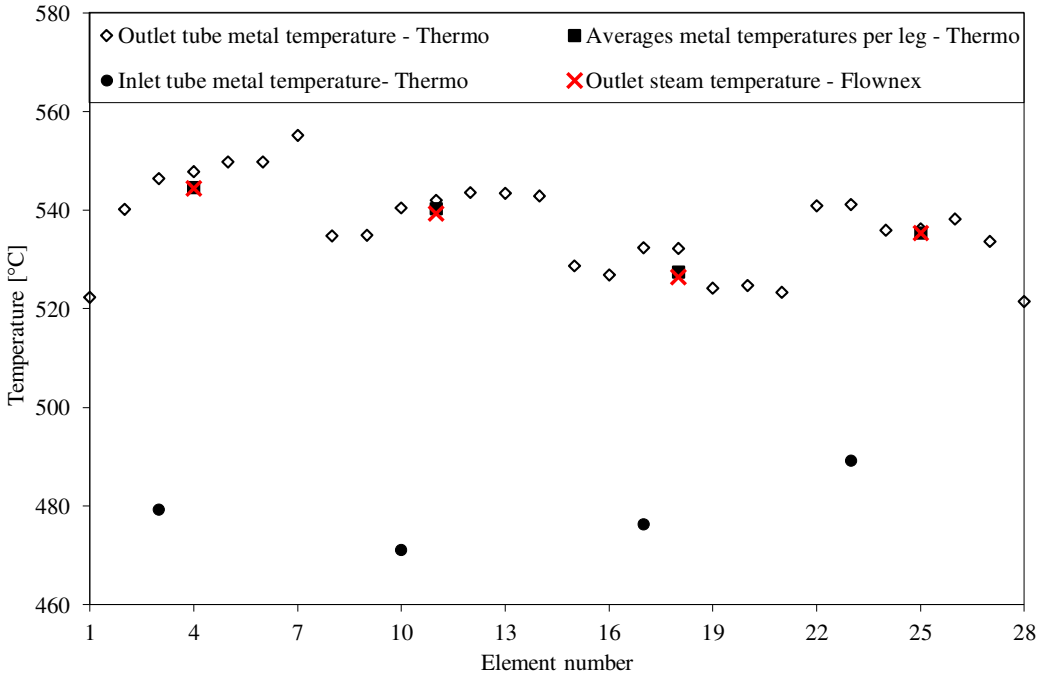

Figure 7-9: A comparison of the results from the discretized model to the detail measurements from the custom installed thermocouples after recalibration of the model for each leg.

However, note that due to the discretisation of four lumped legs across the width of the boiler, it is not possible to fully capture the "M-type" profile shown by the detailed outlet metal temperature measurements. The modelling methodology does allow for a more finely discretised complete superheater model to simulate the "M-type" outlet steam temperature profile as illustrated in chapter

4. It should be mentioned that with the level of discretisation along the height of an element, such a model would not be very quick to run. Thus, somehow eliminating some of the benefits of the 1-D network approach modelling. The building of such a finely discretised model using the developed element models of the final superheater can be done as future work for illustration purposes, thus it is deemed to be outside the scope of this work.

7.3.3. Element 23 – Non-uniform inlet conditions

For further validation of the discretised superheater model, element 23 is analysed. This element had thermocouples installed at the inlet and outlet stub headers as detailed in the sections above and illustrated in Figure 7-3. Element 23 is part of leg D in the complete heat exchanger arrangement.

As alluded above, the detailed CFD model calculations showed that the flue gas temperature is not uniform at the inlet cross-section of the final superheater but has a non-uniform profile as illustrated in Figure 7-7. Thus, for the model of element 23 as well, an inlet flue gas temperature profile has to be imposed at the inlet boundary. This inlet profile has to account for the variation of temperature along the height of the element at the inlet as illustrated in Figure 7-10a). Figure 7-10a) represents the normalised inlet flue gas temperature along the height of the inlet cross section as extracted from the CFD model results around the location of element 23. The profile illustrates that closer to the roof there are lower temperatures because some of the energy there is absorbed by the roof. There is some significant variation along the height of the element which corresponds with the flue gas flow profile as determine by the momentum conservation. The weighted normalized inlet flue gas temperature profile that corresponds to the discretisation of the Flownex model is shown in Figure 7-10b). The inlet flue gas averaged temperature of 1030.9°C calculated via the Gurvich method and presented in Table 7-1 is imposed together with the normalized inlet temperature profile shown in Figure 7-10b) to obtain the inlet flue gas temperature profile for the discretized model of element 23. This is done such that the resulting average inlet flue gas temperature is the same as the lumped temperature from the Gurvich method.

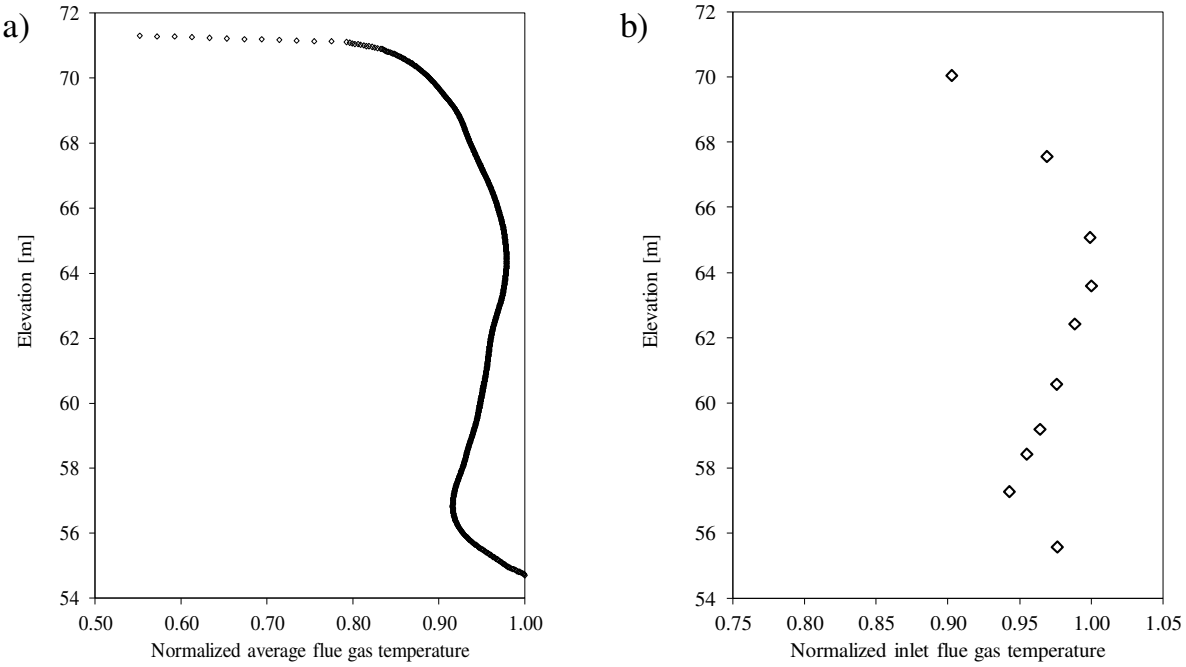

Figure 7-10: The normalized inlet flue gas temperature distribution of the final superheater along the height weighted with respect to the flow across the width of the inlet ducting before the final superheater based on detailed CFD results; a) shows the profile as extracted from the CFD and b) shows the profile that corresponds to the discretisation of the discretized Flownex model (Courtesy of Dr Ryno Laubscher).

On the steam side, input data was obtained from the DCS for leg D of the final superheater. The inlet steam temperature is presented in Table 7-3, together with the outlet steam temperature which was extracted to compare with the model results.

Table 7-3: Inlet and outlet steam temperatures from the DCS for leg D and the weighted averaged outlet steam temperature from the Flownex model of element 23.

Details	**Value [°C]**
Inlet steam temperature - DCS	494.9
Outlet steam temperature - DCS	535.7
Outlet steam temperature – Flownex model	535.5

The relevant input data from Table 7-1 and Table 7-3 was applied on the calibrated model of the final superheater heat exchanger element. After calibrating the outer fouling layer thickness to 2.05mm, the resulting steam temperature corresponded to the DCS data as illustrated in Table 7-3. The outlet metal

temperature results of the calibrated model were further compared to the values obtained from the custom installed thermocouples as illustrated in Figure 7-11. The overall trend of the tube outer surface temperature predicted by the discretized model corresponds to the trend of the readings from the thermocouples. The temperatures are slightly lower on the inner side compared to the outer side. In addition, the comparison of the discretized model results to the average values from the thermocouple recordings was satisfactory as well.

Again, 2-D profiles of the flue gas and outer tube surface temperatures for a section of element 23 above the U-shape area were plotted as shown in Figure 7-12. Figure 7-12b) illustrates the effects of the imposed inlet flue gas temperature profile. Figure 7-12c) shows the metal temperatures at the outer surface of the tubes. Despite having a flue gas profile imposed on it, the metal temperatures conform to the expected profile of lower temperatures at the inlet and higher temperatures at the steam outlet corresponding to the steam temperatures.

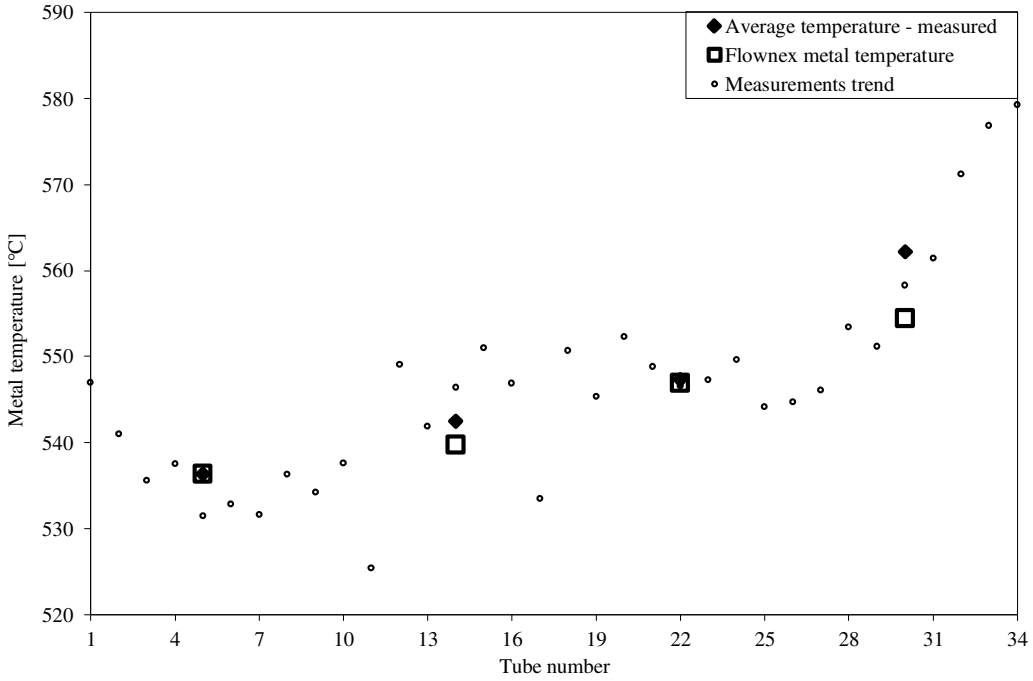

Figure 7-11: Comparison of the outlet metal temperature of the Flownex model results to the average thermocouple measurements from the plant for element 23 at plant full load.

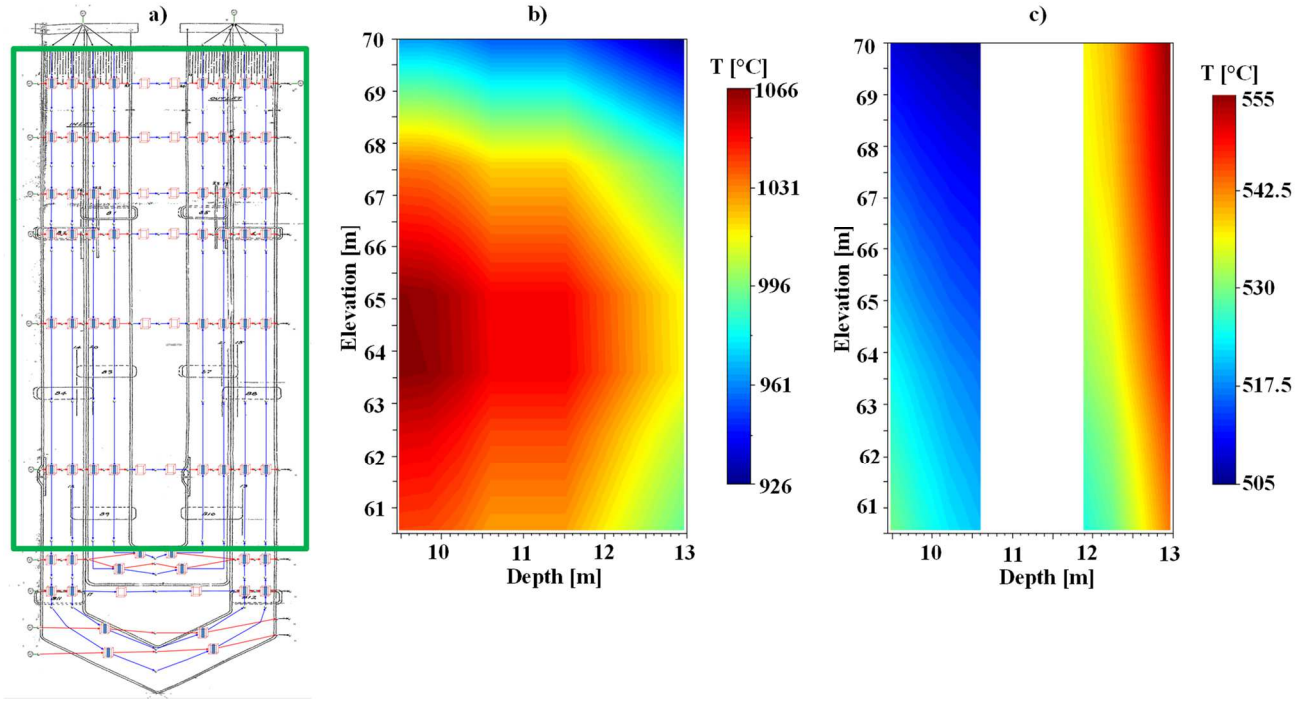

Figure 7-12: Temperature results along the depth of a section of element 23; a) the 2D section of interest, b) flue gas temperature profile and c) outer surface metal temperature profile.

7.4. Model application: Transient

This section illustrates the applicability of the refined heat exchanger modelling methodology to simulate the behaviour of a heat exchanger in response to an overall transient event of the plant. This is built on the transient scenarios that were analysed in chapter 4 where the ability of the models to simulate transients was introduced. However, in chapter 4, the focus was on behaviour analysis of the model in response to case specific disturbances introduced for sensitivity analysis purposes. Here, the focus is on the behaviour of the refined model of the final stage radiant superheater in simulating a transient event that took place in the real plant, in line with the purpose of having a model suitable for online condition monitoring. The selected real plant transient event was due to a reduction in plant load from full load at 22:40 to about 65% full load at 23:30 on the selected day as illustrated in Figure 7-13. So, the plant undergone this dynamic operation for a period of 50 minutes.

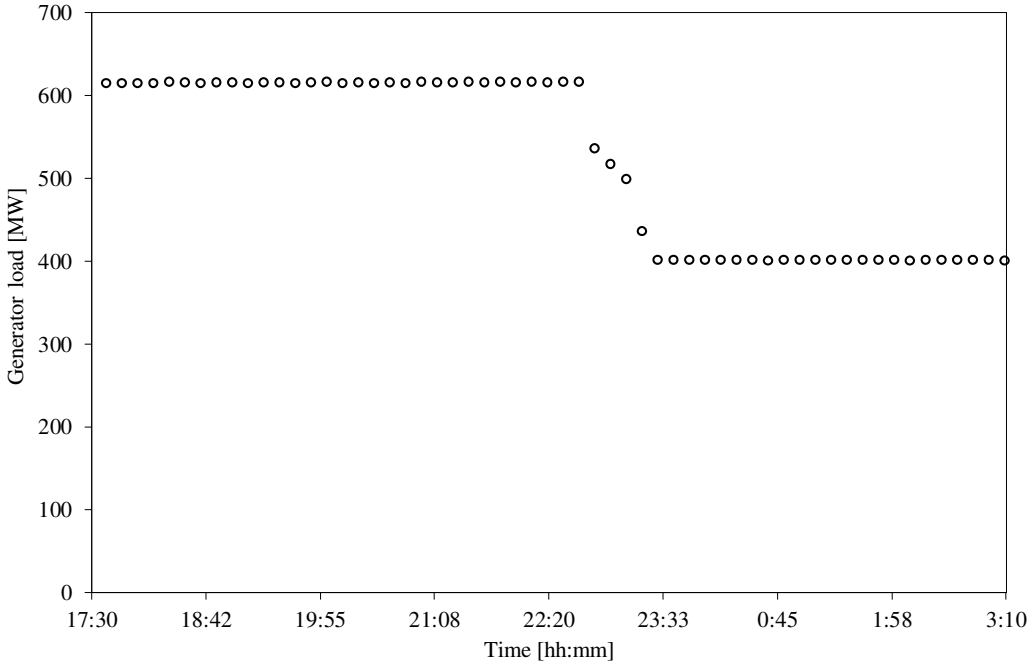

Figure 7-13: Generator load illustrating a transient event where the load drop from full load to about 65% full load between 22:40 and 23:30 on the selected days.

The transient event was sandwiched between two quasi-steady state operations; at full load from 17:30 to 22:40 (case that was analysed under the steady state section above) and at 65% full load from 23:30 to 3:10 the next day. So, the questions addressed in this section are: How did the final superheater behave during this 50-minute transient period, and was it different from the steady state operations and can the final superheater discretized model capture this behaviour?

As mentioned above, in the plant it is very rare to measure temperatures and mass flow rates on the flue gas side, hence the development of the high-level boiler MEB and Gurvich method for obtaining the flue gas side input data. However, these models are limited to quasi-steady state cases due to the cumbersome nature of the calculations and the modelling platforms on which they were developed. Thus, for the selected transient event the high-level models were employed for the two steady state cases that sandwiches it and the resulting values were presented on Table 7-4. For each steady state case, mean values over the duration of that particular operation state were used as inputs in the high-level models. The input data used is presented in Appendix F. In the final superheater discretized model for this transient case, the direct radiation and the view factor were assumed to be average values covering both the steady state cases and during the transient event. This assumption can be adapted later to account for the variation in the model if need be. For the flue gas mass flow and inlet temperature, it was assumed that they vary linearly between the two steady state cases.

Table 7-4: Model inputs for the quasi-steady state sandwiching the transient event.

Details	**Units**	**Value**	**Value**
Generator load	Full load	100%	65%
Mass flow rate of steam into the final superheater	kg/s	470.6	302.3
Inlet steam temperature	°C	485.9	461.5
Mass flow rate of flue gas out of the economizer	kg/s	839.9	531.7
Inlet flue gas temperature	°C	1030.9	919.9
Direct radiation into the final superheater	MW	22.297	16.503
Radiation view factor for the final superheater	.--	0.259	0.271

Corresponding to the reduction in the generator load for the transient event of interest as recorded by the DCS, the steam mass flow rate out of the final superheater to the high-speed turbine also reduced as illustrated in Figure 7-14. This data was obtained from the DCS on a ten-minute interval basis. As per the assumption adopted for this case, the flue gas mass flow rate for the transient event varied linearly between the two steady state events as shown in Figure 7-14. These mass flow rates were used as inputs in the final superheater discretized model.

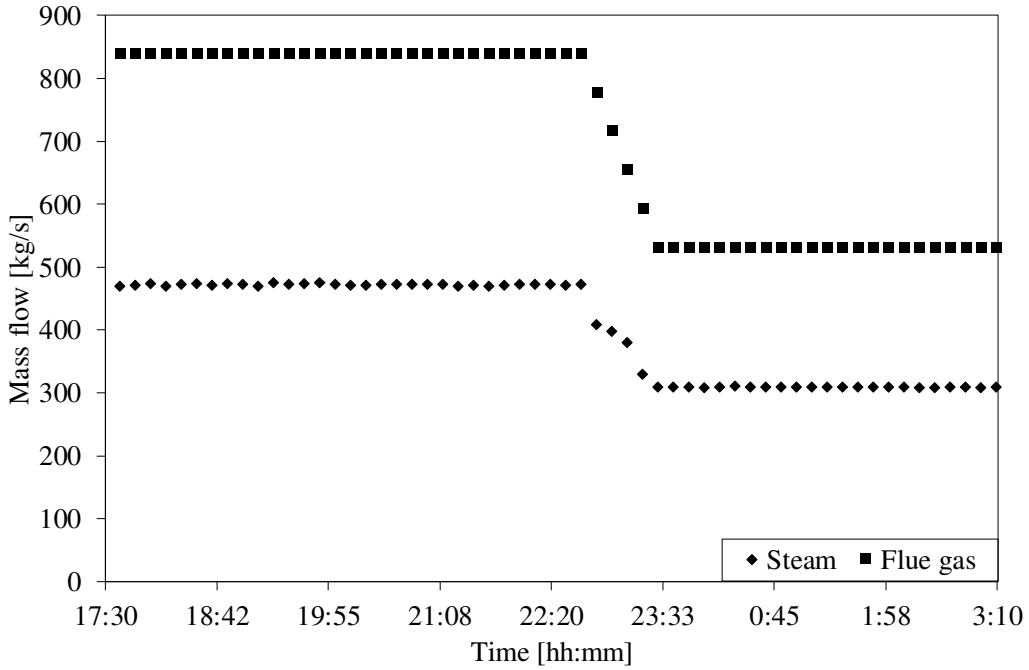

Figure 7-14: Flue gas and steam mass flow rates which corresponds to the generator load between 17:30 and 3:10 on the selected days.

Again, for simplicity it is assumed that all 28 elements of the superheater heat exchanger experience the same steam and flue gas inlet conditions across the width of the heat exchanger as well as the same fouling conditions. Therefore, the one element model for the superheater shown in Figure 6-5 can be used as a representative model for the whole heat exchanger. The input steam temperature is an average of the values from the four legs. The inlet flue gas temperature is assumed to be uniform across the width of the inlet cross-section of the heat exchanger but not along the height. This allows for the adaption of the flue gas temperature profile as illustrated in the modelling of the steady state case for element 23 in the section above.

By again extracting data from the detailed CFD model results, the inlet flue gas temperature profile illustrated in Figure 7-15a) was determined. Figure 7-15a) represents the normalised weighted average inlet flue gas temperature along the height of the inlet cross section. This profile is a weighted average with respect to the flow distribution across the width of the duct at every elevation. The normalised weighted inlet flue gas temperature profile that corresponds to the discretisation of the Flownex model is shown in Figure 7-15b). As alluded in the previous sections, the input inlet flue gas temperatures, shown in Table 7-4, obtained from the high-level Gurvich method are lumped values across the inlet cross section of the superheater. These lumped values are then imposed on the profile for the discretized model for each of the steady state cases (100% and 65% full load) as was the case for the

steady state model for element 23. For each of the inlet flue gas boundary condition, a linear distribution of the inlet flue gas temperature assumption is imposed.

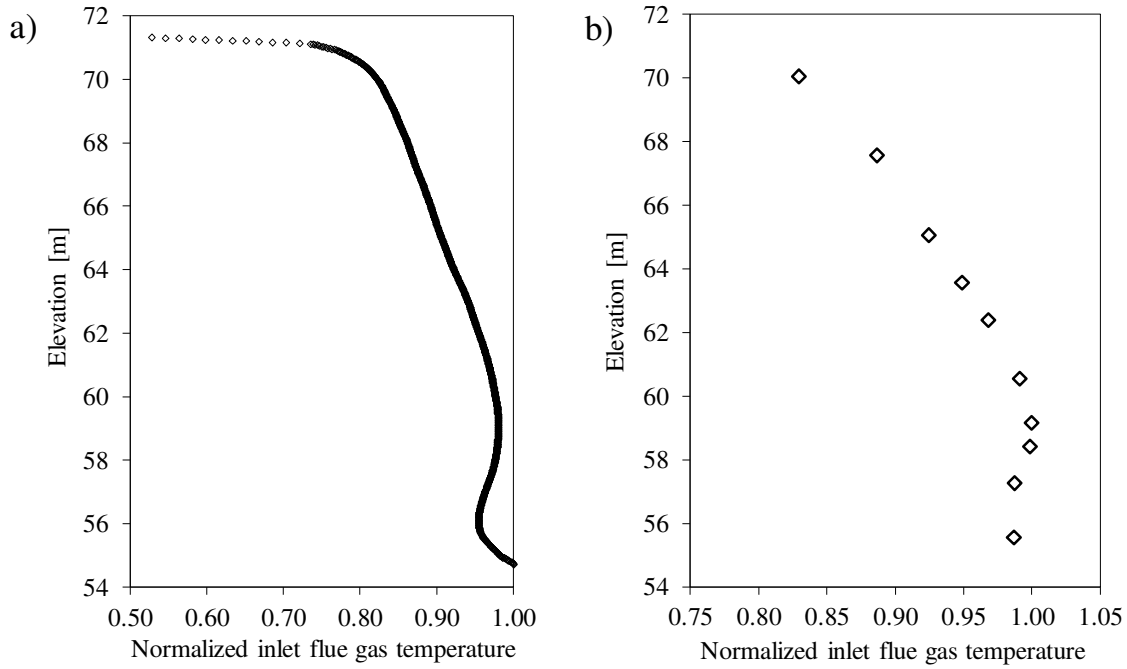

Figure 7-15: The normalized inlet flue gas temperature distribution of the final superheater along the height weighted with respect to the flow across the width of the inlet ducting before the final superheater which is based on detailed CFD results; a) shows the profile as extracted from the CFD and b) shows the profile that corresponds to the discretisation of the Flownex model (Courtesy of Dr Ryno Laubscher).

To illustrate the applicability of the final superheater discretized model for online condition monitoring, it was run for the sets of input values from 17:30 to 3:10 the next day. The model was first calibrated using the full load steady state data to account for the difference in the inlet flue gas temperature profiles and radiation characteristics when compared to the homogenous case that was modelled above.

However, before embarking on detailed analysis of the transient event it is prudent to ensure that a time-step independent solution is obtained. It is therefore necessary to start off with a study to investigate this over the computational time domain. From the DCS, the input data is reported in 10 minutes intervals, thus the maximum allowable time-step size in order to avoid missing important details is 10 minutes. For ease of reporting and comparison, time-step sizes which are mathematical factors of 10 minutes are considered. A C sharp script that was developed by Willie Le Grange [139] was used to import the DCS 10 minutes intervallic data in to the boundary conditions of the Flownex

models. This script allows for linear interpolation on the data points to get values at a desired point in time.

Figure 7-16 demonstrates the time-step size dependence of the results obtained from the model. It is presented in terms of the normalised error squared results for various time-step sizes. The error squared for each time-step size was determined by summing the square of the difference between the model results and measured outlet steam temperatures at 10 minutes intervals. The resulting errors squared were then normalized using the maximum error squared. The nearly corresponding values for the smaller time steps of less than 5 minutes, indicate that a further reduction in the time-step size will not results in a variation in the results, and therefore time-step independence is obtained. For further analyses in this work, the one-minute time step size was selected.

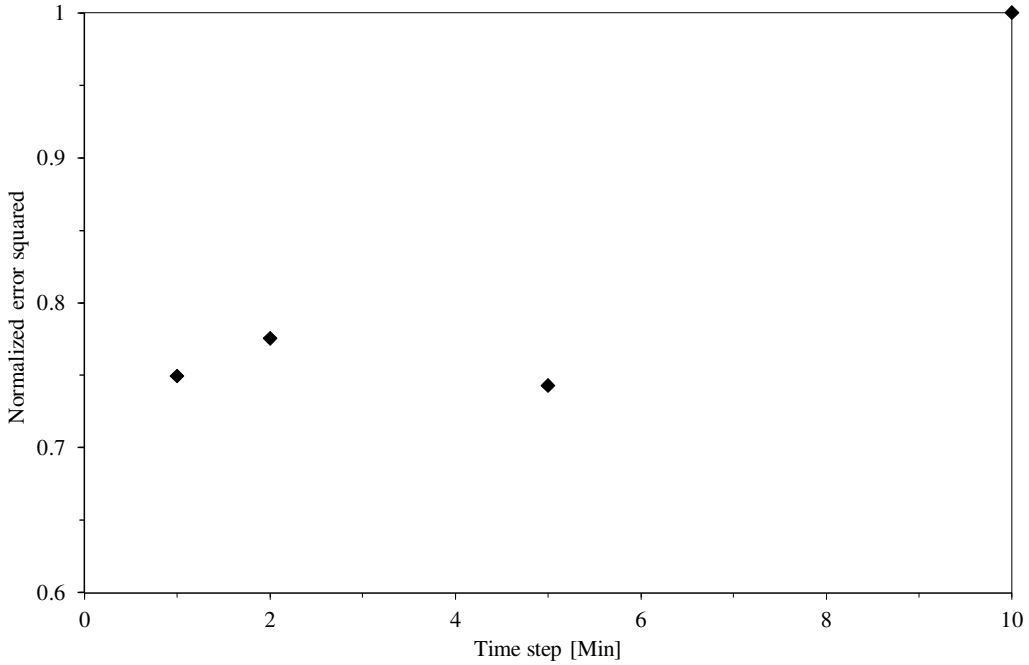

Figure 7-16:Normalized sum of error squared results from the transient model time step dependency analysis over the computational time domain.

Figure 7-17 presents steam temperature trends from the DCS as well as the discretized model. The inlet steam temperature trend illustrates a noticeable variation during the transient event between 22:40 and 23:30 and this was provided as an input to the model. A satisfactory comparison was achieved between the resultant outlet steam temperature from the model and the outlet steam temperature extracted from the DCS data. Overall the outlet steam temperature remains relatively constant regardless of the transient event. This conforms to the requirements of the operations as controlled by the operators using attemperators and other techniques during operations. The discretized model

predicted satisfactory results without any physical adjustments during the simulation of the transient event on the selected days. The results show that the model analysis provides an acceptable representation of the real-plant behaviour during transient events where there are complex interactions between various thermofluid processes while multiple parameters are changing at the same time. These parameters are the steam and flue gas flow rates, as well as the inlet steam and flue gas temperatures. The discretized model can therefore be used (after some calibration to account for the level of fouling) to study the impact of real-world operational scenarios in support of power plant flexibility and low load operation.

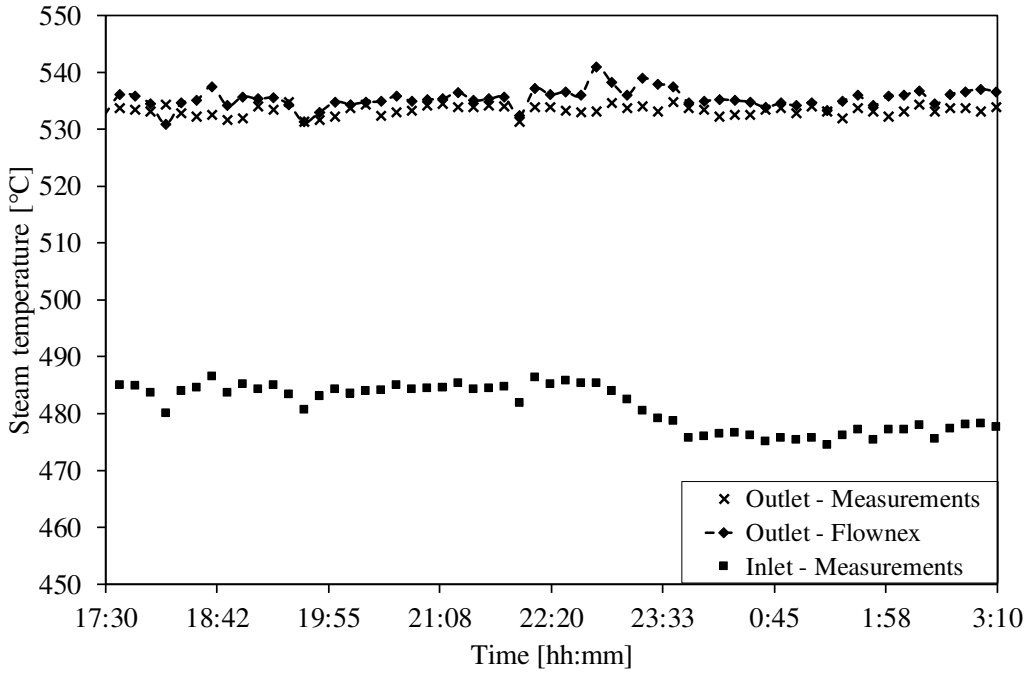

Figure 7-17: Inlet and outlet steam temperatures from both measurements and results from the Flownex model simulations for the selected days.

Figure 7-18 illustrates some of the potential advantages of having a discretised model since it shows some detail results of the metal temperatures on the outlet steam side as per the discretisation. It shows the temperature variation along the depth of the superheater highlighting the hottest building block rather than an average temperature as it would be in a lumped model. The variation of the metal temperatures at the outlet shows a difference of about 25°C between the hottest and the coldest bundle. This provides a better understanding of the phenomena taking place in the heat exchanger. Measurements to such details are usually not available in most coal-fired boilers, thus illustrating a potential benefit of the discretized model.

The insights from Figure 7-17 and Figure 7-18 illustrated that the model can be used to establish a better understanding of the relationship between the operational conditions and the metal temperatures in superheaters. In the case analysis, the model simulated the thermofluid processes of a final stage radiant superheater during steady state operations and a transient event. The detailed nature of the temperature results from the model can provide temperature inputs to FEM analyses to study the resulting thermal stresses during the operation. Thus, the model can used as a first step towards establishing a better understanding, predicting and managing how the operational conditions affect the life span of components such as the tubes, stub headers and main headers. Such integrated process models can therefore be employed to study complex thermofluid process phenomena that may occur during intermittent, transient and low load operation of power plants. In addition, such models could be useful for predictive and preventative maintenance as well as online condition monitoring.

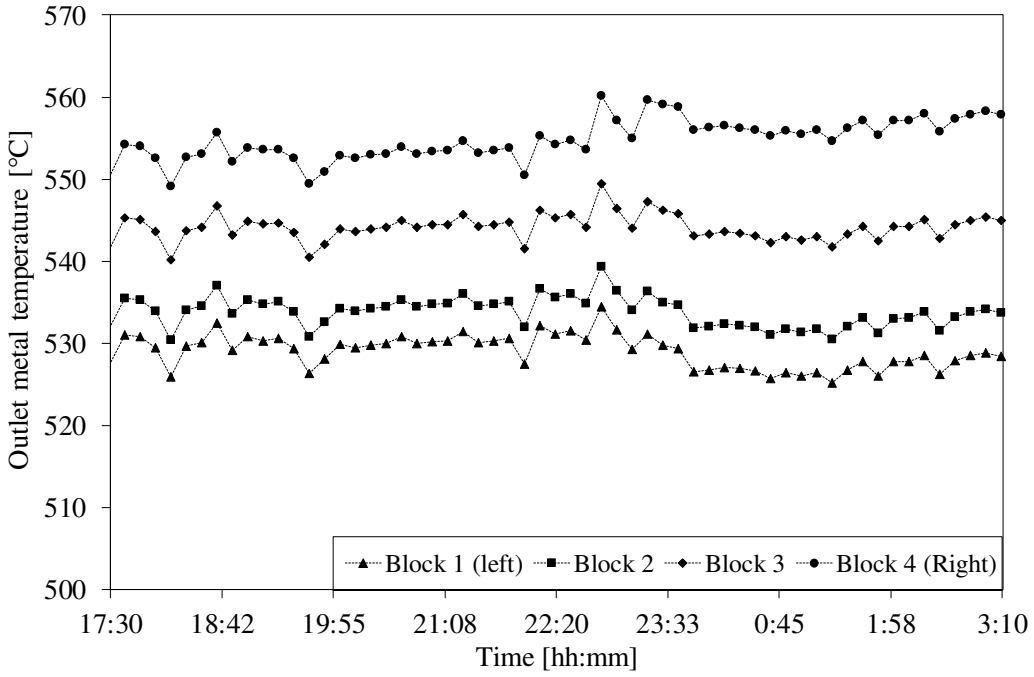

Figure 7-18: Outlet metal temperatures corresponding to the discretization of the Flownex model at the steam outlet side from the simulations of the events of the selected days.

It is important to note that in the transient analysis, the effect of different discretization of the heat exchangers were not looked at. The transient analysis was based on the least possible discretization that still captured the geometry effects correctly. However, increasing the number of building blocks, will increase the solvers' time to reach a solution.

7.5. Summary of the chapter

This chapter presented the application of the refined modelling methodology on a final stage radiant superheater heat exchanger in both steady state and transient regime. This refined modelling methodology and the model development of the final superheater were presented in the previous chapter. Since a radiant superheater was modelled, it meant that the direct radiation which is leaking both from the furnace and from the high temperature flue gas in the platen superheater region upstream had to be accounted for. Real plant data from the DCS was used as inputs to the steam side of the developed heat exchanger model as well as on the high-level models (boiler MEB and the Gurvich method) used to generate inputs on the flue gas side.

The model that was calibrated using the C-schedule data in the previous chapter was re-calibrated first before being used in the analyses of the behaviour of the heat exchanger. The rationale behind the re-calibration was that it was plausible that the UA value for the C-schedule cases and real plant cases would be different. This is because the operation environment and heat exchanger conditions for both cases were likely to be different. The heat exchanger would most likely have degraded from when the plant was commissioned.

The calibrated heat exchanger was then applied in steady state for two cases. In the first case, it was assumed that the inlet steam and flue gas conditions were uniform. From this study some insights were gained in cases where it would be difficult to install measuring instruments. 2-D temperature plots of the flue gas and the metal outer surface on a selected section of the heat exchanger were presented. Most important from the profiles was the illustration of the variation of the metal temperatures from the inlet to the outlet on the steam side. In addition, a variation was observed at the outlet where the inner tubes exhibited lower temperatures than the outer tubes which are slightly longer. A more detailed analyses of the temperature distribution in comparison with the modes of heat transfer present was also done corresponding to one discretisation channel on the flue gas side. It was insightful to note that due to the presence of the direct radiation that heats up the outer surface of the outer fouling layer, the temperature of this layer can be higher than that of the flue gas in the vicinity. Thus, this may result in gas radiation and convection to the flue gas in the region than into the steam from the flue gas. However, it is important to note that regardless of the possible reverse gas radiation and convection, the resultant heat transfer is conducted to the steam flow and this conducted heat is entirely due to the direct radiation.

The second case was slightly more complex with the acknowledgement that the input conditions are non-uniform as illustrated by plant measurements as well as CFD results. After adjusting for such conditions in the model and the UA value re-calibration across the width of the heat exchanger, the results were analysed. Notable the resulting temperatures compared well to the detailed temperature measurements from the custom installed thermocouples. Element 23 was also studied in detail, yielding successful and insightful results when compared to the detail plant data from measurements. Note that all along the discretized model allowed for the steam flows within the tubes to redistribute automatically based on the solution of the momentum conservation equations. This could unfortunately not be validated in detail since it is not practical to conduct measurements regarding this.

The model built using the refined modelling methodology was further employed to model a transient event that occurred during the operation of the plant. This was also aligned with illustrating the potential applicability of the model for online condition monitoring purposes. The transient event was sandwiched between two steady state cases: a full load and 65% full load. The developed high-level models were employed to obtain the flue gas side data for both these steady state cases, with linear distribution or averaging used to proportion the values during the transient event. The comparison of the resulting outlet steam temperature from the discretized model to that from the DCS was satisfactory and it conformed to expected operation norms. The discretised nature of the model also illuminated the capability of the model to determine more detailed results in the heat exchanger than measurements for most plants.

The detailed nature of the steam and metal temperature results that can be extracted from the discretized model illustrates the usefulness of such a model in providing boundary conditions for models that can be used to study the thermal stresses in tubes and header walls. The discretisation of the heat exchanger building block demonstrated the ability of the model to calculate metal temperatures radially along the thickness of the tube. The discretization of an element along the depth illustrated that detailed steam and metal temperatures can be obtained at the inlet and outlet. Also, the discretization of the element along the height provides access to tube metal temperatures that would not be easily accessible using conventional measuring techniques. In addition, the ability to discretise the heat exchanger across the width allows the model to be able to provide detailed outlet steam and metal temperatures along the main headers. The steady state and transient temperature results can provide useful input information for FEM analyses of the resultant thermal stresses in the tubes, stub headers and the main headers. This will in turn serve to better understand, predict and manage how

steady state and transient operational conditions affect the life span of these superheater heat exchanger components.

8. CONCLUSIONS AND FUTURE WORK

This chapter provides some conclusions based on the work presented in this report and highlights the need for further work to be done in future projects.

8.1. Conclusions

Failures of tubes and outlet headers in heat exchangers of coal-fired boilers are major contributors to unplanned capacity losses in the South African power generation sector. These failures are more prevalent in the critical components which operate at high pressures and temperatures such as final superheaters and reheaters. Various operational anomalies and operational procedures can contribute to these failures. The continued introduction of intermittent renewable energy power plants on the national electricity grid aggravates this situation. Coal-fired plants are now required to operate under varying and low load conditions rather than at the base load conditions for which they were originally designed. In order to mitigate the damage to critical components that may result from these changes in operational conditions, a better understanding of the relationship between the operational conditions and metal temperatures has to be established. Mathematical process models are invaluable to create such understanding

Hence, a methodology to model the thermofluid processes of a heat exchanger in the convective pass of a coal-fired boiler was developed. This methodology is based on the 1-D network approach encapsulated in the Flownex software. It entails the simultaneous solution of the transient 1-D forms of the conservation equations for mass, energy and momentum, combined with the applicable closure relations, boundary values and initial values. The modelling methodology was then applied to model two different superheater heat exchangers with complex geometries. On the tube side, the model traced the complex steam path layout as in the real plant, which becomes advantageous if detailed tube analysis is of importance. The sub-channel method was employed for the flue gas side. The heat exchanger geometry is discretized along the flue gas flow path as well as along the steam flow path. In order to limit the complexity, bundles of tubes can be grouped together and discretised along the height depending on the level of detail required. Each heat exchanger increment contains the appropriate geometrical information and thermal resistance characteristics. Empirical correlations were employed to model the inner and outer convective heat transfer. An effective heat transfer coefficient was used to account for radiation heat transfer on the flue gas side, accounting for radiation from both the gas and the ash particles. For the radiant superheater, the direct radiation was accounted

for as well. The methodology was applied on one tubesheet as well as connecting several tubesheets in parallel in order to capture flow maldistribution across the width of the heat exchanger.

The developed models struck an appropriate balance between simplicity and accuracy such that they were easily applied in a real-life cases to gain an understanding of operational flow and temperature distributions in the heat exchanger. The detailed nature of the steam and metal temperature results that can be extracted from the discretized model illustrated the usefulness of such a model in providing boundary conditions for models that can be used to study the resultant thermal stresses in tubes and header walls. The discretisation of the heat exchanger building block demonstrated the ability of the model to calculate metal temperatures radially along the thickness of the tube. The discretization of an element along the depth illustrated that detailed steam flow and temperatures as well as metal temperatures can be obtained at the inlet and outlet. Also, the discretization of the element along the height provides access to tube metal temperatures that would not be easily accessible using conventional measuring techniques. In addition, the ability to discretise the heat exchanger across the width allowed the model to be able to provide detailed outlet steam and metal temperatures as well as steam flows along the main headers. The steam flow results can be useful input values for CFD models for flow in the stub headers as well as the main headers. The steady state and transient temperature results can provide useful input information to sufficient details for FEM analyses of the resultant thermal stresses in the tubes, stub headers and the main headers.

Thus, the research has shown that a network approach can be employed to construct integrated thermofluid process models of radiant superheater heat exchangers that provide results of outlet steam flows and temperatures that can be used as boundary values for CFD and FEM analyses to determine the resultant thermal stresses in headers. This will in turn serve to better understand, predict and manage how steady state and transient operational conditions affect the life span of these components. Such integrated thermofluid process models could be used to gain insights on typical problems and to investigate the risks and impacts associated with intermittent operation, load following and variations in coal quality. This, together with appropriate and sufficiently accurate measurements of key parameters as well as the high-level models, could inform decision making for operating and maintenance strategies to improve component availability and reliability, and to reduce the cost of power produced.

Further insight that was gained is that the modelling methodology allows for a range of model discretisation. This is due to the ease of set-up a model provided by the developed heat exchanger

building blocks. Thus, the adopted level of discretisation depends on the complexity of the heat exchanger as well as the purpose of the developed model. It is important to mention that the level of discretization adopted in a specific model has an impact on the speed of developing the model especially the opening of the inputs and results grid. However, this might be dependent on the computer used. Thus, the use of a minimum number of heat exchanger building blocks for a particular purpose is advisable. The level of discretization along the width also influences how the calibration of the model is done. This is because different OFL thicknesses maybe employed at different width positions. This is case dependant as the operational conditions differ with time. In the model calibration, it is always important to observe if the inferred fouling thicknesses are reasonable.

8.2. Future work

Some insights were gained in the development and employment of the modelling methodology used in this work. Some of these insights shone some light on the limitations of the modelling approach with which further improvement could be done in order to fine tune the accuracy of the modelling and cater for more thermofluid phenomena taking place in the heat exchangers.

One particular limitation of the modelling approach was illuminated in chapter 5, where the flue gas side flow modelling was analysed. After the extensive analysis it was concluded that for the adopted 1-D network approach, the flue gas flow should be modelled using the subchannel approach. This basically meant that the flow was restricted to flow in channels without any mixing in between, which is not the case in a real plant. The major limitation was due to the solution technique adopted by the network approach. Due to the inherent assumption of one-dimensional flow in the network approach, the approach solves for total pressure as a non-directional parameter even at common nodes in cases of two-dimensional flows. This leads to the software being used outside its inherent computational domain characteristics which is flows in pipes. Thus, an extensive study can be introduced as future work where a 1-D approach that solves for static pressure other than total pressure at the nodes is used for comparison with the network approach. However, one of the advantages of the network approach is that it eliminates solving the convective term in the direction of the flow.

In the development of the refined methodology some further insight was gained when analysing the impact of accounting for the direct radiation originating from the flue gas in the final superheater region towards the downstream final reheater heat exchanger. The refined modelling methodology demonstrated some limitations in accounting for such a phenomenon. This was due to the number of non-linear connections that would be necessary hence hindering the speed of the solver. This analysis

illuminated that for better accounting of this direct radiation, refined models such as a zonal model should be used. Such is recommended as future work for further development of the modelling methodology. In this instance the convective pass will have to be modelled holistically accounting for all the radiation in the spaces between the tubesheets of the different heat exchangers.

9. References

[1] E. Z. Gwebu and P. G. Rousseau, “A network Approach Applied in Modelling the Heat Transfer and Fluid Flow in a Superheater Heat Exchanger,” in *Modelling, Simulation and Identification*, Calgary, Canada, 19 - 20 July 2017.

[2] P. G. Rousseau and E. Z. Gwebu, “Modelling of a Superheater Heat Exchanger with Complex Flow Arrangement Including Flow and Temperature Maldistribution,” *Heat Transfer Engineering,* vol. 0, no. 0, pp. 1-17, 2018.

[3] E. Z. Gwebu and P. G. Rousseau, “Development and Validation of a Process Model for a Superheater Heat Exchanger in a Coal-Fired Power Plant Boiler,” in *16th International Heat Transfer Conference, IHTC-16*, Beijing, China, 10 - 15 August 2018.

[4] D. Taler, M. Trojan and J. M. Taler, “Mathematical Modeling of Cross-Flow Tube Heat Exchangers with a Complex Flow Arrangement,” *Heat Transfer Engineering,* vol. 35, no. 14-15, pp. 1334-1343, 2014.

[5] Eskom, “Eskom Generation Division Plant Performance Report F2015,” in *Ops ManCom*, 2015.

[6] The Babcock & Wilcox Power Generation Group, “Boiler Tube Analyses,” The Babcock & Wilcox Company, Barberton, Ohio.

[7] G. J. Nakoneczny and C. C. Schultz, “Life Assessment of High Temperature Headers,” in *American Power Conference*, Chicago, Illinois, USA, 1995.

[8] S. J. Mills, “Integrating intermittent renewable energy technologies with coal-fired power plant,” IEA Clean Coal Centre, 2011.

[9] F. Alobaid, N. Mertens, R. Starkloff, T. Lanz, C. Heinze and B. Epple, “Progress in dynamic simulation of thermal power plants,” *Progress in Energy and Combustion Science,* vol. 59, pp. 79-162, 2016.

[10] J. P. King, “Condition Assessment of Boiler Piping and Header Components,” in *ASME Pressure Vessels and Piping Conference*, Seattle, Washington, 2000.

[11] W. O. Monnaemang, “A zonal model for radiation heat transfer in coal-fired boiler furnaces,” University of Cape Town, Cape Town, South Africa, 2015.

[12] The Babcock & Wilcox Company, Steam/its generation and use, Charlotte: The Babcock & Wilcox Company, 2015.

[13] J. P. Holman, Heat transfer, Boston: McGraw Hill, 2010.

[14] J. B. Kitto and S. C. Stultz, Steam: its Generation and Use, Ohio, United States of America: The Babcock & Wicox Company, 2005.

[15] W. M. Kays and A. L. London, Compact heat exchangers, New York: McGraw Hill, 1964.

[16] L. I. Dıez, C. Cortes and A. Campo, “Modelling of pulverized coal boilers: review and validation of on-line simulation techniques,” *Applied Thermal Engineering,* vol. 25, p. 1516–1533, 2005.

[17] C. Cantrell and S. Idem, “On-Line Performance Model of the Convection Passes of a Pulverized Coal Boiler,” *Heat Transfer Engineering,* vol. 31, no. 14, pp. 1173-1183, 2010.

[18] M. Trojan and D. Taler, “Thermal simulation of superheaters taking into account the processes occurring on the side of the steam and flue gas,” *Fuel,* vol. 150, pp. 75-87, 2015.

[19] D. Taler, M. Trojan and J. Taler, “Numerical Modeling of Cross-Flow Tube Heat Exchangers with Complex Flow Arrangements,” in *Evaporation, Condensation and Heat Transfer, Edited by Dr. Amimul Ahsan*, Rijeka, Croatia, InTech, 2011, pp. 261 - 278.

[20] D. Taler and J. Taler, “Simplified analysis of radiation heat exchange in boiler superheaters,” *Heat Transfer Engineering,* vol. 30, no. 8, pp. 661-669, 2009.

[21] J. Taler, M. Trojan and D. Taler, “Computer System for On-Line Monitering of Slagging and Fouling and Optimisation of Sootblowing in Steam Boilers,” in *2nd International Conference on Engineering Optimization*, Lisbon, Portugal, 2010.

[22] M. Trojan, D. Taler and J. Taler, “Analysis of the impact of ash and scale fouling on the superheater operation,” in *International Conference on Heat Exchanger Fouling and Cleaning*, Enfield, Ireland, 2015.

[23] M. Trojan, “Computer modeling of a convective steam superheater,” *archives of thermodynamics,* vol. 36, no. 1, pp. 125-137, 2015.

[24] D. Taler, M. Trojan, P. Dzierwa, K. Kaczmarski and J. Taler, “Numerical simulation of convective superheaters in steam boilers,” *International Journal of Thermal Sciences,* vol. 129, pp. 320-333, 2018.

[25] P. J. Coelho, “Mathematical modeling of the convection chamber of a utility boiler the theory,” *Numerical HeatTransfer, Part A: Applications: An International Journal of Computation and Methodology,* vol. 36, no. 4, pp. 429-447, 1999.

[26] A. Zukauskas, “Heat Transfer From Tubes in Cross Flow,” in *Advance in Heat Transfer*, New York, Academic Press, 1972, pp. 93-158.

[27] P. J. Coelho, “An engineering model for calculation of radiative heat transfer in the convection chamber of a utility boiler,” *Journal of the Institute of Energy,* vol. 72, pp. 117-126, 1999.

[28] P. J. Coelho, “Mathematical modeling of the convection chamber of a utility boiler an application,” *Numerical Heat Transfer, Part A: Applications: An International Journal of Computation and Methodology,* vol. 36, no. 4, pp. 411-428, 1999.

[29] H. Xu, B. Deng, D. Jiang, Y. Ni and N. Zhang, “The finite volume method for evaluating the wall temperature profiles of the superheater and reheater tubes in power plant,” *Applied Thermal Engineering,* vol. 112, p. 362–370, 2017.

[30] M. M. Prieto, I. Suarez, F. J. Fernandez, H. Sanchez and M. Mateos, “Theoretical development of a thermal model for the reheater of a power plant boiler,” *Applied Thermal Engineering,* vol. 27, pp. 619-626, 2007.

[31] M. Prieto, I. Suarez, F. Fernandez, H. Sanchez and C. Viescas, “Application of a thermal model to a power plant reheater with irregular tube temperatures,” *Applied Thermal Engineering,* vol. 27, p. 85–193, 2007.

[32] M. M. P. Gonzalez, F. J. F. Garcia, I. S. Ramon and H. S. Roces, “Experimental thermal behavior of a power plant reheater,” *Energy,* vol. 31, pp. 665-676, 2006.

[33] A. Gomez, N. Fueyo and L. I. Diez, “Modelling and simulation of fluid flow and heat transfer in the convective zone of a power-generation boiler,” *Applied Thermal Engineering,* vol. 28, pp. 532-546, 2008.

[34] S. V. Patankar and D. B. Spalding, “A calculation procedure for the transient and steady state behaviour of shell and tube heat exchangers,” in *Heat exchanger: Design and theory sourcebook*, McGraw - Hill, 1974, pp. 155-176.

[35] C. Cortés, L. I. Díez and A. Campo, “Modeling large-size boilers as a set of heat exchangers: Tips and Tricks,” *ASME HTD Combustion and Energy Systems,* vol. 369, pp. 41-48, 2001.

[36] L. I. Díez, C. Cortés, I. Arauzo and A. Valero, “Combustion and heat transfer monitoring in large utility boilers,” *International Journal of Thermal Science,* vol. 40, pp. 489-496, 2001.

[37] L. Xu, J. A. Khan and Z. Chen, “Thermal load deviation model for superheater and reheater of a utility boiler,” *Applied Thermal Engineering,* vol. 20, pp. 545-558, 2000.

[38] B. E. Tilton and U. Ratnam, “Integrated simulation of heat transfer and pressure drop in furnace convection sections,” *Industrial and Environmental Applications of Fluid Mechanics, ASME,* vol. 186, pp. 175-179, 1994.

[39] H. M. Paynter and Y. Takahashi, “A new method of evaluating dynamic response of counter-flow and parallel-flow heat exchangers,” in *ASME Diamond Jubilee Semi-Annual Meeting*, Boston, 19-23 June 1955.

[40] D. D. Gvozdenac, “Analytical solutions of the transient response of gas to gas cross flow heat exchanger with both fluids unmixed,” *ASME Journal of heat transfer,* vol. 108, no. 4, pp. 722-727, 1986.

[41] D. D. Gvozdenac, “Analytical Solution of Transient Response of Gas-to-Gas Parallel and Counterflow Heat Exchangers,” *ASME Journal of Heat Transfer,* vol. 109, no. 4, pp. 848-855, 1987.

[42] J. Yin and M. K. Jensen, “Analytical model for transient heat exchanger response,” *International journal of heat and mass transfer,* vol. 46, pp. 3255-3264, 2003.

[43] M. Enns, “Comparison of Dynamic Models of a Superheater,” *ASME Journal of Heat Transfer,* pp. 375-382, 1962.

[44] Y.-W. Kang, W. H. Yang Xue and Y.-F. Li, “A Nonlinear Lumped-Parameter Dynamic Model of Power Plant Boiler Superheater,” *Advanced Materials Research,* pp. 57-62, 2013.

[45] W. Zima, “Numerical modeling of dynamics of steam superheaters,” *Energy,* vol. 26, p. 1175–1184, 2001.

[46] W. Zima, “Mathematical model of transient processes in steam superheaters,” *Forschung im Ingenieurwesen,* vol. 68, p. 51 – 59, 2003.

[47] W. Zima, “Mathematical modelling of transient processes in convective heated surfaces of boilers,” *Forsch Ingenieurwes,* vol. 71, p. 113–123, 2007.

[48] W. Zima, “Mathematical Modelling of Dynamics of Boiler Surfaces Heated Convectively,” in *Heat Transfer - Engineering Applications*, Rijeka, INTECH, 2011, pp. 259-282.

[49] E. Z. Gwebu, “Transient boiler heat exchanger thermal behaviour analysis,” Master's Thesis, University of Cape Town, Cape Town, South Africa, 2014.

[50] E. Gwebu, L. Jestin, W. Fuls and P. Rousseau, “Transient boiler heat exchanger thermal behaviour analyses,” in *Second Eskom Power Plant Engineering Institute Student Workshop*, Midrand, 2015.

[51] A. K. Runchal, “Brian Spalding: CFD & Reality - A personal recollection,” *International Journal of Heat and Mass Transfer,* vol. 52, pp. 4063-4073, 2009.

[52] A. Gosman, W. Pun, A. Runchal, D. Spalding and M. Wolfshtein, Heat and Mass Transfer in Recirculating Flows, London: Academic Press, 1969.

[53] V. Artemov, S. Beale, G. d. V. Davis, M. Escudier, N. Fueyo, B. Launder, E. Leonardi, M. Malin, W. Minkowycz, S. Patankar, A. Pollard, W. Rodi, A. Runchal and S. Vanka, “A tribute to D.B. Spalding and his contributions in science and engineering,” *International Journal of Heat and Mass Transfer,* vol. 52, p. 3884–3905, 2009.

[54] A. K. Runchal and M. Wolfstein, “Numerical Integration Procedure for the Steady State Navier-Stokes Equations,” *Journal of Mechanical Engineering Science,* vol. 11, no. 5, pp. 445-453, 1969.

[55] H. Z. Barakat and J. A. Clark, “Analytical and Experimental Study Transient Laminar Natural Convection Flows in Partially Filled Containers,” in *International Heat Transfer Conference*, Chicago, 1966.

[56] R. A. Gentry, R. E. Martin and B. J. Daly, “An Eulerian differencing method for unsteady compressible flow problems,” *Journal of Computational Physics,* vol. 1, no. 1, pp. 87-118, 1966.

[57] R. Courant, E. Isaacson and M. Rees, "On the solution of nonlinear hyperbolic differential equations by finite differences," *Communications on Pure and Applied Mathematics,* vol. 5, no. 3, pp. 243-255, 1952.

[58] W. T. Sha, "A summary of methods used in rob-bundle thermal-hydraulic analysis," NATO Advanced Study Institute on Turbulent Forced Convection in Channels and Rod Bundles, Instanbul, Turkey, 1978.

[59] S. V. Patankar, "Numerical prediction of the shellside flow and heat transfer in heat exchangers," in *A reappraisal of shellside flow in heat exchnagers, 22nd Heat Transfer Conference and Exhibition*, Niagara Falls, New York, 1984.

[60] W. T. Sha, "An overview on rod-bundle thermal-hydraulic analysis," *Nuclear Engineering and Design,* vol. 62, pp. 1-24, 1980.

[61] D. S. Rowe, "COBRA III: A digital computer program for steady state and transient thermal-hydraulic analysis of rod bundle nuclear fuel elements," Battelle Pacific Northwest Laboratories, Richland, Washington, 1971.

[62] J. D. Macdougall and J. N. Lillington, "The SABRE code for fuel rod cluster thermohydraulics," *Nuclear Engineering and Design,* vol. 82, pp. 171-190, 1984.

[63] J. E. Cahalan and D. Hahn, "Passive Safety Optimization in Liquid Sodium-Cooled Reactors Final Report," Argonne National Laboratory, Chicago, 2005.

[64] S. V. Patankar and D. B. Spalding, "Computer analysis of the three-dimensional flow and heat transfer in a steam generator," *Forsch. Ing.-Wes,* vol. 44, no. 2, pp. 47-52, 1978.

[65] M. M. AbuRomia, B. C. Chan and S. M. Cho, "Flow distribution analysis in nuclear heat exchangers with application to CRBRP-IHX," in *Heat Transfer and Fluid Mechanics Institute*, California, 1976.

[66] D. Butterworth, "The development of a model for three-dimensional flow in tube bundles," *International Journal of Heat and Mass Transfer,* vol. 21, pp. 256-258, 1978.

[67] A. K. Singhal and D. B. Spalding, “Mathematical modelling of the mutli-phase and heat transfer in steam generators,” in *2nd Multi-Phase Flow and Heat Transfer Symposium Workshop*, Miami Beach, Florida, 1979.

[68] D. B. Spalding, “Numerical computation of multi-phase flow and heat transfer,” in *Recent Advances in Numerical Mechanics*, Pineridge Press, 1980.

[69] E. O. Marchand, A. K. Singhal and D. B. Spalding, “Predictions of Operation Transients for a Steam Generator of a PWR Nuclear Power System,” in *Century 2 Nuclear Engineering Conference*, San Francisco, 1980.

[70] A. K. Singhal, L. W. Keeton and D. B. Spalding, “Predictions of thermal hydraulics of a pwr steam generator by using the homogeneous, the two-fluid, and the algebraic-slip model,” in *American Institute of Chemical Engineers Symposium series*, New York, 1980.

[71] W. T. Sha, C. I. Yang, T. T. Kao and S. M. Cho, “Multidimensional numerical modeling of heat exchangers,” *Journal of Heat Transfer,* vol. 104, pp. 417-425, 1982.

[72] G. S. Srikantiah and A. K. Singhal, “Modeling and simulation of recirculating U-Tube nuclear steam generators,” in *10th IMACS World Congress on System Simulation and Scientific Computation*, Montreal, Canada, 1982.

[73] M. H. Hu, “Anisotropic modelling of tube bundle flow during steam generator wet layup,” *Nuclear Engineering and Design,* vol. 71, pp. 151-160, 1982.

[74] J. Bear, Dynamics of fluids in porous media, New York: American Elsevier Publishing Company, Inc., 1972.

[75] D. B. Rhodes and L. N. Carlucci, “Predicted and measured velocity distributions in a model heat exchanger,” in *CNS/ANS International Conference on Numerical Methods in Nuclear Engineering*, Montreal, 1983.

[76] V. M. Theodossiou, A. C. M. Soussa and L. N. Carlucci, “Flow field predictions in a model heat exchanger,” *Computational Mechanics,* vol. 3, pp. 419-428, 1988.

[77] A. N. Karayannis and N. C. G. Markatos, “Mathematical modelling of heat exchangers,” in *Tenth International Heat Transfer Conference*, Brighton, UK, 1994.

[78] M. Prithiviraj and M. J. Andrews, “Three-dimensional computer simulation of shell and tube heat exchangers,” *ASME IMECE, HTD,* vol. 318, pp. 119-127, 1995.

[79] B. E. Launder and D. B. Spalding, “The numerical computation of turbulent flows,” *Computer methods in applied mechanics and engineering,* vol. 3, pp. 269-289, 1974.

[80] K. Rehme, “Simple Method of Predicting Friction Factor of Turbulent Flow in Non-Circular Channels,” *International Journal of Heat and Mass Transfer,* vol. 16, pp. 933-950, 1973.

[81] M. Prithiviraj and M. J. Andrews, “Three-dimensional numerical simulation of shell and tube heat exchangers,” *Part I: Foundation and fluid mechanics, Numerical Heat Transfer, Part A: Applications: An International Journal of Computation and Methodology,* vol. 33, no. 8, pp. 799-816, 1998.

[82] M. Prithiviraj and M. J. Andrews, “Three dimensional numerical simulation of shell and tube heat exchangers,” *Part II: Heat Transfer, Numerical Heat Transfer, Part A: Applications: An International Journal of Computation and Methodology,* vol. 33, no. 8, pp. 817-828, 1998.

[83] L. Y. Huang, J. X. Wen, T. G. Karayiannis and R. D. Mathews, “CFD Modelling of Fluid Flow and Heat Transfer in a Shell and Tube Heat Exchanger,” *The Phoenics Journal of Computational Fluid Dynamics & its Applications,* vol. 9, no. 2, pp. 189-209, 1996.

[84] P. Mirzabeygi and C. Zhang, “Three-dimensional numerical model for the two-phase flow and heat transfer in condensers,” *International Journal of Heat and Mass Transfer,* vol. 81, pp. 618-637, 2015.

[85] G. P. Greyvenstein and P. G. Rousseau, “Design of a physical model of the PBMR with the aid of Flownet,” *Nuclear Engineering and Design,* vol. 222, pp. 203-213, 2003.

[86] C. G. du Toit and P. G. Rousseau, "Modeling the flow and heat transfer in a Packed Bed High Temperature Gas-Cooled Reactor in the context of a Systems CFD Approach," *Journal of Heat Transfer,* vol. 134, 2012.

[87] P. G. Rousseau and G. P. Greyvenstein, "One-Dimensional Reactor Model for the Integrated Simulation of the PBMR Power Plant," *SAIMecE R&D Journal,* vol. 19, pp. 25-30, 2003.

[88] S. Becker and E. Lauren, "Three-dimensional numerical simulation of the flow and heat transport in high-temperature nuclear reactors," *Nuclear Engineering and Design,* vol. 222, pp. 189-201, 2003.

[89] G. P. Greyvenstein and D. P. Laurie, "A segregated CFD Approach to Pipe Network Analysis," *International Journal of Numerical Methods in Engineering,* vol. 37, pp. 3685-3705, 1994.

[90] G. P. Greyvenstein, "An implicit method for the analysis of transient flows in pipe networks," *International Journal for Numerical Methods in Engineering,* vol. 53, pp. 1127-1143, 2002.

[91] C. G. du Toit, P. G. Rousseau, G. P. Greyvenstein and W. A. Landman, "A systems CFD model of a packed bed high temperature gas-cooled nuclear reactor," *International Journal of Thermal Sciences,* vol. 45, pp. 70-85, 2006.

[92] P. G. Rousseau, C. G. du Toit and W. A. Landman, "Validation of a transient thermal-fluid systems CFD model for a packed bed high temperature gas-cooled nuclear reactor," *Nuclear Engineering and Design,* vol. 236, pp. 555-564, 2006.

[93] C. G. du Toit, P. G. Rousseau and G. P. Greyvenstein, "Systems CFD analysis of complex thermal-fluid systems," in *13th International Heat Transfer Conference*, Sydney, 2006.

[94] C. G. du Toit and J. H. Kruger, "Integrated systems CFD analysis applied to boiler simulation," in *13th International Heat Transfer Conference*, Sydney, 2006.

[95] J. H. Kruger and C. G. du Toit, "The simulation of a thermal-fluid system using an integrated systems CFD approach," in *Fifth International Conference on CFD in the Process Industries*, Melbourne, 2006.

[96] M-Tech Industrial, Flownex Library Manual, Potchefstroom, North West Province, South Africa: M-Tech Industrial, 2013.

[97] M-Tech Industrial, "Flownex Simulation Environment [Computer software]," Version 8.3.5.2227, http://www.flownex.com/, August 2014.

[98] W. Fuls and P. Rousseau, "Progress on the development of high fidelity transient boiler model using a 1D thermal-hydraulic network solver," in *12th International Conference on Boiler Technology ICBT 2014*, Szczyrk, Poland, 2014.

[99] P. G. Rousseau, C. G. d. Toit, J. S. Jun and J. M. Noh, "Code-to-code comparison for analysing the steady-state heat transfer and natural circulation in an air-cooled RCCS using GAMMA+ and Flownex," *Nuclear Engineering and Design,* vol. 291, pp. 71-89, 2015.

[100] G. P. Greyvenstein, "An implicit method for the analysis of transient flows in pipe networks," *Int. Journal of Numerical Methods in Engineering,* vol. 53, pp. 1127-1143, 2002.

[101] P. Rousseau and W. Fuls, Power Plant Systems Analyses, Cape Town: University of Cape Town, 2017.

[102] M-Tech Industrial, "Flownex Library Manual," Flownex Simulation Environment, Potchefstroom, South Africa, December 2017.

[103] M. Trojan and J. Taler, "Effect of scale deposits on the internal surfaces of the tubes on the superheater operation," *Archives of Thermodynamics,* vol. 34, no. 4, pp. 73-91, 2013.

[104] V. Gnielinski, "Heat Transfer in Pipe Flow," in *VDI Heat Atlas*, Berlin, Heidelberg, Springer, 2010, pp. 693-699.

[105] M. Trojan and D. Taler, "Thermal simulation of superheaters taking into account the processes occuring on the side of the steam and flue gas," *Fuel,* vol. 150, pp. 75-87, 2015.

[106] V. Gnielinski, "Heat Transfer in Cross-flow Around Single Tubes, Wires, and Profiled Cylinders," in *VDI Heat Atlas*, Berlin, Heidelberg, Springer, 2010, pp. 723-724.

[107] D. Taler and J. Taler, “Simplified Analysis of Radiation Heat Exchange in Boiler Superheaters,” *Heat Transfer Engineering,* vol. 30, no. 8, pp. 661-669, 2009.

[108] H. R. N. Jones, Radiation Heat Transfer, Oxford: Oxford University Press, 2000.

[109] H. C. Hottel and A. F. Sarofim, Radiative Transfer, New York: MacGraw-Hill, Inc, 1967.

[110] T. F. Smith, Z. F. Shen and J. N. Friedman, “Evaluation of Coefficients for the Weighted Sum of Gray Gases Model,” *ASME,* vol. 104, pp. 602-608, 1982.

[111] P. K. Swamee and A. K. Jain, “Explicit equations for pipe flow problems,” *Journal of the Hydraulics Division,* vol. 102, no. 5, pp. 657-664, 1976.

[112] A. Zukauskas and R. Ulinaskas, “Banks of plain and finned tubes,” in *Heat Exchanger Design Handbook*, Washington, Hemisphere Publishing Corporation, 1983, pp. 2141-2157.

[113] M-tech Industrial, “Flownex Simulation Environment General User Manual,” Potchefstroom, South Africa, 2017.

[114] W. Fuls, “High level power plant analysis - Systems design course notes,” University of Cape Town, Cape Town, South Africa, 2013.

[115] F. Klepacki and S. Noworyta, “Superheater failures associated with present operation character of 200MW power units,” in *Pro Nocum 18th Informative & Training Symposium, Diagnostics as support of flexible and effective operation of power plants*, Katowice, Poland, 6 - 7 October 2016.

[116] W. J. Peet and T. K. P. Leung, “Development and Application of a Dynamic Simulation Model for a Drum Type Boiler with Turbine Bypass System,” in *International Power Engineering Conference*, Singapore, 27 February - 1 March 1995.

[117] J. D. Anderson, Computational Fluid Dynamics:The basics with applications, Singapore: McGraw-Hill, Inc, 1995.

[118] K. Bell, Cooperative Research Program on Shell and Tube Heat Exchangers, Newark, Delaware: University of Delaware, 1963.

[119] A. A. Zukauskas, "Heat transfer of banks of tubes in crossflow at high Reynolds numbers," in *Heat exchanger: Design and theory sourcebook*, McGraw-Hill, 1974, pp. 75-100.

[120] S. Oka, Z. Kostic and S. Sikmanovic, "Investigation of the heat transfer processes in tube-banks in cross-flow," in *Heat exchanger: Design and theory sourcebook*, McGraw-Hill, 1974, pp. 617-636.

[121] P. G. Rousseau and B. du Toit, Practical thermal-fluid system simulation; Short course, Potchefstroom: M-Tech Industrial, 2013.

[122] S. V. Patankar, Numerical heat transfer and fluid flow, New York, United States of America: Hemisphere Publishing Corporation, 1980.

[123] T. L. Bergman, A. S. Lavine, F. P. Incropera and D. P. Dewitt, Fundamentals of Heat and Mass Transfer, Hoboken NJ, USA: John Wiley & Sons, Inc., 2011.

[124] Y. A. Cengel, Heat and Mass Transfer - A Practical Approach, Singapore: McGraw-Hill, 2006.

[125] A. Zukauskas, "Heat Transfer from Tubes in Crossflow," *Advances in Heat Transfer,* vol. 8, pp. 93-160, 1972.

[126] K. H. Im and R. K. Ahluwalia, "Radiation properties of coal combustion products," *International Journal of Heat and Mass Transfer,* vol. 36, no. 2, pp. 293-302, 1993.

[127] Y. Zhang, Q. Li and H. Zhou, Theory and Calculation of Heat Transfer in Furnaces, Amsterdam: Academic Press, 2016.

[128] D. Vortmeyer and S. Kabelac, "Gas Radiation: Radiation from Gas Mixtures," in *VDI Heat Atlas*, Berlin Heidelberg, pringer-Verlag, 2010, pp. 979-988.

[129] H.-G. Brummel, “Thermal Radiation of Gas-Solids-Dispersions,” in *VDI Heat Atlas*, Berlin, Heidelberg, Springer, 2010, pp. 989-999.

[130] A. G. Blokh, Heat Transfer in Steam Boiler Furnaces, Washington: Hemisphere Publishing Corporation, 1988.

[131] N. E. Tootla, “Investigation into methods for the calculation and measurement of pulverised coal boiler flue gas furnace exit temperature,” University of Cape Town, Cape Town, South Africa, February 2016.

[132] E. P. P. B. Engineering, “Boiler Mass and Energy Balance's Guideline and user Manual-V1.15,” Eskom Gernation Business Engineering, Sunninghill, 2010.

[133] P. Basu, C. Kefa and L. Jestin, Boilers and Burners - Design and Theory, New York: Springer-Verlag, 2000.

[134] S. Kakac, Boiler, Evaporators & Condensers, New York: John Wiley & Sons, Inc, 1991.

[135] V. Ganapathy, Industrial Boilers and Heat Recovery Steam Generators - Design, Applications and Calculations, New York: Marcel Dekker, Inc., 2003.

[136] P. Rousseau, L. Vilakazi and A. Alugongo, “Analysis of measured process parameters and metal temperatures on a coal-fired boiler final superheater at different loads,” in *13th International conference on Boiler Technology*, Szczyrk, Poland, 2018.

[137] J.-P. du Preez, “Steam temperature and flow maldistribution in superheater headers,” To be published by the University of Cape Town, Cape Town, 2018.

[138] L. Vilakazi, “Indentification and analysis of steam temperature maldistribution in superheater tubes via measured and derived parameters,” To be published by Vaal University of Technology, Vanderbijlpark, South Africa, 2018.

[139] W. Le Grange, “Component development for a high fidelity transient simulation of a coal-fired power plant using Flownex SE,” University of Cape Town, Cape Town, South Africa, January 2018.

APPENDIX A. COMPARISON TO RESULTS FROM LUMPED PARAMETER MODELS – THE CALCULATIONS

A.1. Tube and shell geometrical information

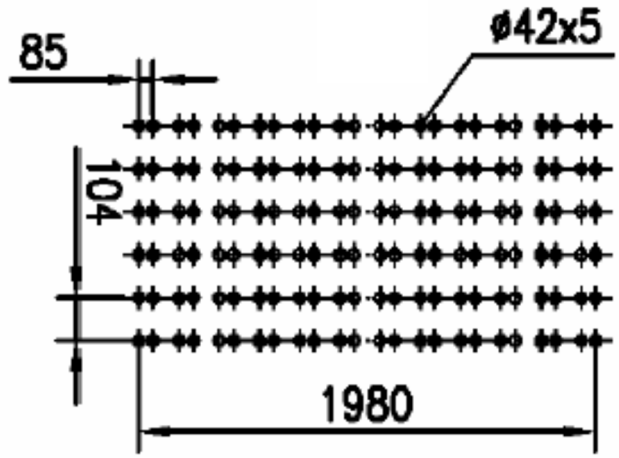

Fig. A-1: Geometrical information for the primary superheater heat exchanger [19].

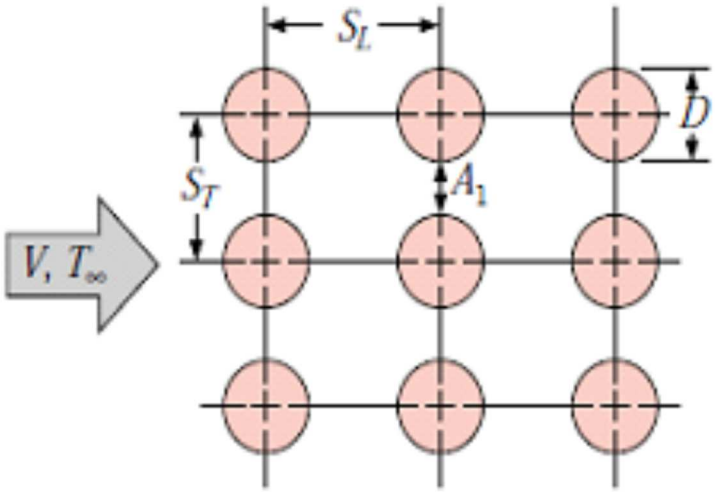

Fig. A-2: Aligned tube arrangements in a bank [123].

$D_i := 32mm$ $D_o := 42mm$

$t_w := \frac{(D_o - D_i)}{2} = 5 \cdot mm$ $D_{centre} := 0.5 \cdot (D_i + D_o) = 37 \cdot mm$

$S_T := 104mm$ $S_L := 85mm$

$t_{outerfoul} := 0.00102m$ $t_{innerfoul} := 0mm$

$L_{SH} := 24 \cdot S_L = 2040 \cdot mm$

$W_{Boiler} := 7920mm$

$N_{sheets} := \frac{148}{2} = 74$ Number of tube sheets in SH1

$W_{fgi} := N_{sheets} \cdot S_T = 7696 \cdot mm$ $W_{fge} := W_{fgi} = 7696 \cdot mm$

Inlet tube length: $L_{inlet} := 5.34m$

Outlet tube length: $L_{outlet} := 4.46m$

Number of passes: $N_{passes} := 12$

$$L_{tube} := \left| \begin{array}{l} \text{for} \quad i \in 1 .. 24 \\ \quad L_{tube_i} = L_{inlet} + (i - 1) \cdot \left(\frac{L_{outlet} - L_{inlet}}{2N_{passes} - 1} \right) \\ L_{tube} \end{array} \right.$$

$L_{tube.total} := 0.5 \sum L_{tube} = 58.8\,m$

$H_{fge} := 4.46m$

$\theta := atan\left(\frac{5.34m - 4.46m}{1.98m}\right) = 23.962 \cdot °$

$H_{fg_{24}} := H_{fge} = 4460 \cdot mm$

$N_{tubes} := 2 \cdot N_{sheets} = 148$ 2 tubes per pass

$Loop_{fg\_height} := \left| \begin{array}{l} \text{for} \quad i \in 23 .. 1 \\ \quad H_{fg_i} = H_{fg_{i+1}} + \tan(\theta) \cdot (S_L) \\ H_{fg} \end{array} \right.$

$H_{fgi} := H_{fg_1} = 5.329 \cdot m$

$A_{ffsi} := N_{tubes} \frac{\pi}{4} \cdot D_i^{\,2} = 0.119 \cdot m^2$

$A_{ffse} := N_{tubes} \frac{\pi}{4} \cdot D_i^{\,2} = 0.119 \cdot m^2$

$P_{wsi} := N_{tubes} \pi D_i = 14.879 \cdot m$

$P_{wse} := N_{tubes} \pi D_i = 14.879 \cdot m$

$A_{fffgi} := H_{fgi} \cdot (W_{fgi} - N_{sheets} \cdot D_o) = 24.449\,m^2$

$A_{fffge} := H_{fge} \cdot (W_{fge} - N_{sheets} \cdot D_o) = 20.462\,m^2$

$P_{wfgi} := \frac{4 \cdot A_{fffgi}}{D_o} = 2328.471\,m$

$P_{wfge} := \frac{4 \cdot A_{fffge}}{D_o} = 1948.808\,m$

$L_{fg} := \frac{Vol_{fg.total}}{0.5 \cdot (A_{fffgi} + A_{fffge})} = 2.886\,m$

$lengthratio_{fg} := \frac{L_{fg}}{L_{SH}} = 1.415$

Ratio of model length to actual length to ensure that volume of gas is calculated correctly within FNX.

$L_{fg} := L_{SH} \cdot lengthratio_{fg} = 2.886\,m$

A.2. Material characterisation

Pipe material characteristics

$\rho_{pipe} := 7832 \frac{kg}{m^3}$

$k_{pipe}(T) := \left[35.54 + 0.004084 \cdot (T/°C) - 2.0891 \cdot 10^{-5} \cdot (T/°C)^2\right] \frac{W}{m \cdot K}$

$T_{test} := 20\ °C$ $k_{pipe}(T_{test}) = 35.613 \cdot \frac{W}{m \cdot K}$

Inner fouling layer characteristics

$k_{innerfoul} := 0.07 \frac{W}{m \cdot K}$ $\rho_{innerfoul} := 1700 \frac{kg}{m^3}$ $cp_{innerfoul} := 1.085 \frac{kJ}{kg \cdot K}$

$D_{ii} := D_i - 2 \cdot t_{innerfoul} = 32 \cdot mm$

Outer fouling layer characteristics

$k_{outerfoul} := 0.07 \frac{W}{m \cdot K}$ $\rho_{outerfoul} := 1700 \frac{kg}{m^3}$ $cp_{outerfoul} := 1.085 \frac{kJ}{kg \cdot K}$

A.3. Steam conditions

$m_s := 46.2 \frac{kg}{s}$

$p_{si} := 9600kPa$ $T_{si} := 337.7\ °C$

$p_{se} := 9600kPa$ $T_{se} := 400.9\ °C$

$\rho_{si} := \frac{1}{v_{steam}(p_{si}, T_{si}, "", "", "")} = 44.378 \frac{kg}{m^3}$

$h_{si} := h_{steam}(p_{si}, T_{si}, "", "", "") = 2887.787 \cdot \frac{kJ}{kg}$

$cp_{si} := Cp_{steam}(p_{si}, T_{si}, "", "", "", "") = 4.27 \cdot \frac{kJ}{kg \cdot K}$

$$\rho_{se} := \frac{1}{v_{steam}(p_{se}, T_{se}, "", "", "")} = 35.934 \frac{kg}{m^3}$$

$$h_{se} := h_{steam}(p_{se}, T_{se}, "", "", "") = 3108.754 \cdot \frac{kJ}{kg}$$

$$cp_{se} := Cp_{steam}(p_{se}, T_{se}, "", "", "", "") = 3.024 \cdot \frac{kJ}{kg \cdot K}$$

$$Q_s := m_s \cdot (h_{se} - h_{si}) = 10208.655 \cdot kW$$

$$cp_s := \frac{(h_{se} - h_{si})}{(T_{se} - T_{si})} = 3.496 \cdot \frac{kJ}{kg \cdot K}$$

$$\mu_s := \mu_{steam}[0.5(p_{si} + p_{se}), 0.5 \cdot (T_{si} + T_{se}), "", "", "", ""] = 2.3 \times 10^{-5} \frac{kg}{m \cdot s}$$

$$k_s := \lambda_{steam}[0.5(p_{si} + p_{se}), 0.5(T_{si} + T_{se}), "", "", "", ""] = 0.065 \cdot \frac{W}{m \cdot K}$$

$$Pr_s := \frac{cp_s \cdot \mu_s}{k_s} = 1.238$$

$$v_{si} := \frac{m_s}{(\rho_{si} \cdot A_{ffsi})} = 8.746 \frac{m}{s} \qquad v_{se} := \frac{m_s}{(\rho_{se} \cdot A_{ffsi})} = 10.801 \frac{m}{s}$$

$$v_s := 0.5 \cdot (v_{si} + v_{se}) = 9.774 \frac{m}{s}$$

$$\rho_s := 0.5 \cdot (\rho_{si} + \rho_{se}) = 40.156 \frac{kg}{m^3}$$

$$Re_s := \frac{(\rho_s \cdot v_s \cdot D_i)}{\mu_s} = 5.4 \times 10^5$$

Gnielinski correlation

$$\xi_G := \left(1.8 \cdot log\left(Re_s\right) - 1.5\right)^{-2} = 0.013$$

$$Nu_{s.G} := \frac{\left(\frac{\xi_G}{8}\right) \cdot Re_s \cdot Pr_s}{1 + 12.7 \cdot \sqrt{\left(\frac{\xi_G}{8}\right)} \cdot \left(Pr_s^{\frac{2}{3}} - 1\right)} \cdot \left[1 + \left(\frac{D_{ii}}{L_{tube.total}}\right)^{\frac{2}{3}}\right] = 1009.622$$

$$h_{s.G} := Nu_{s.G} \cdot \frac{k_s}{D_{ii}} = 2057.445 \cdot \frac{W}{m^2 K}$$

$$h_i := h_{s.G}$$

A.4. Flue gas conditions

$$m_{fg} := 64.5 \frac{kg}{s}$$

$$p_{fgi} := 100kPa \qquad T_{fgi} := 632.6\ °C$$

$$p_{fge} := 100kPa \qquad T_{fge} := 558.6\ °C$$

$$cp_{fg} := \frac{-Q_s}{m_{fg} \cdot \left(T_{fge} - T_{fgi}\right)} = 2.139 \cdot \frac{kJ}{kg \cdot K}$$

$$R_{fg} := 0.250 \frac{kJ}{kg \cdot K}$$

$$\rho_{fgi} := \frac{p_{fgi}}{\left(R_{fg} \cdot T_{fgi}\right)} = 0.442 \frac{kg}{m^3}$$

$$\rho_{fge} := \frac{p_{fge}}{\left(R_{fg} \cdot T_{fge}\right)} = 0.481 \frac{kg}{m^3}$$

$$\mu_{fgi} := \frac{T_{fgi}}{1.2635 \times 10^{7} + \frac{1.2618 \cdot 10^{4}}{K} \cdot T_{fgi} - \frac{1.6929}{K^{2}} \cdot T_{fgi}^{2}} \cdot \frac{kg}{m \cdot s \cdot K} = 3.995 \times 10^{-5} \frac{kg}{m \cdot s}$$

$$\mu_{fge} := \frac{T_{fge}}{1.2635 \times 10^{7} + \frac{1.2618 \cdot 10^{4}}{K} \cdot T_{fge} - \frac{1.6929}{K^{2}} \cdot T_{fge}^{2}} \cdot \frac{kg}{m \cdot s \cdot K} = 3.788 \times 10^{-5} \frac{kg}{m \cdot s}$$

$$k_{fgi} := 9.1446 \cdot 10^{-5} \cdot 0.99958^{\frac{T_{fgi}}{K}} \cdot \frac{T_{fgi}^{1.0148}}{K^{1.0148}} \cdot \frac{W}{m \cdot K} = 0.063 \cdot \frac{W}{m \cdot K}$$

$$k_{fge} := 9.1446 \cdot 10^{-5} \cdot 0.99958^{\frac{T_{fge}}{K}} \cdot \frac{T_{fge}^{1.0148}}{K^{1.0148}} \cdot \frac{W}{m \cdot K} = 0.059 \cdot \frac{W}{m \cdot K}$$

$$v_{fgi} := \frac{m_{fg}}{\rho_{fgi} \cdot A_{fffgi}} = 5.974 \frac{m}{s}$$

$$v_{fge} := \frac{m_{fg}}{\rho_{fge} \cdot A_{fffge}} = 6.554 \frac{m}{s}$$

$$v_{fg} := 0.5 \cdot \left(v_{fgi} + v_{fge}\right) = 6.264 \frac{m}{s}$$

$$\rho_{fg} := 0.5 \cdot \left(\rho_{fgi} + \rho_{fge}\right) = 0.461 \frac{kg}{m^{3}}$$

$$\mu_{fg} := 0.5 \cdot \left(\mu_{fgi} + \mu_{fge}\right) = 3.891 \times 10^{-5} \frac{kg}{m \cdot s}$$

$$k_{fg} := 0.5 \cdot \left(k_{fgi} + k_{fge}\right) = 0.061 \cdot \frac{W}{m \cdot K}$$

$$Pr_{fg} := \frac{cp_{fg} \cdot \mu_{fg}}{k_{fg}} = 1.366$$

Gnielinski correlations

$$D_{oo} := D_o + 2 \cdot t_{outerfoul}$$

$$L_{stream} := \frac{\pi}{2} \cdot D_{oo} = 0.069\,m$$

$$Re_{fg.l} := \frac{\left(\rho_{fg} \cdot v_{fg} \cdot L_{stream}\right)}{\mu_{fg}} = 5136.921$$

$$Nu_{fg.G.laminar} := 0.664 \cdot \sqrt{Re_{fg.l}} \cdot Pr_{fg}^{\frac{1}{3}} = 52.803$$

$$Nu_{fg.G.turb} := \frac{0.037 \cdot Re_{fg.l}^{0.8} \cdot Pr_{fg}}{1 + 2.443 \cdot Re_{fg.l}^{-0.1} \cdot \left(Pr_{fg}^{\frac{2}{3}} - 1\right)} = 37.905$$

$$Nu_{fg.G} := 0.3 + \sqrt{Nu_{fg.G.laminar}^{2} + Nu_{fg.G.turb}^{2}} = 65.3$$

$$\xi_{fg.G} := \left(1.8 \cdot log\left(Re_{fg.l}\right) - 1.5\right)^{-2} = 0.037$$

$$h_{fg.G} := Nu_{fg.G} \cdot \frac{k_{fg}}{D_{Hfg}} = 90.342 \cdot \frac{W}{m^2 K}$$

$$h_{co} := h_{fg.G} = 90.342 \cdot \frac{W}{m^2 K}$$

A.5. Outside fouled wall temperature calculations

$$T_{s.av} := \frac{T_{si} + T_{se}}{2} = 369.3 \cdot °C$$

$$T_{fg.av} := \frac{T_{fgi} + T_{fge}}{2} = 595.6 \cdot °C$$

$$k_{fl} := 0.07 \frac{W}{m \cdot K}$$

$$k_{pipe} := k_{pipe}\left(T_{s.av}\right) = 34.199 \cdot \frac{W}{m \cdot K}$$

$$A_{i.tube} := \pi D_i \cdot L_{tube.total} = 5.911\, m^2$$

$$U_{i.tube} := \frac{1}{\frac{1}{h_{s.G}} + \frac{A_{i.tube} \cdot ln\left(\frac{D_o}{D_i}\right)}{2\pi \cdot k_{pipe} \cdot L_{tube.total}} + \frac{A_{i.tube} \cdot ln\left(\frac{D_{oo}}{D_o}\right)}{2\pi \cdot k_{fl} \cdot L_{tube.total}}} = 87.305 \cdot \frac{W}{m^2 \cdot K}$$

$$T_w := T_{s.av} + \frac{Q_s}{N_{tubes} \cdot U_{i.tube} \cdot A_{i.tube}} = 502.957 \cdot °C$$

A.6. Radiation heat transfer

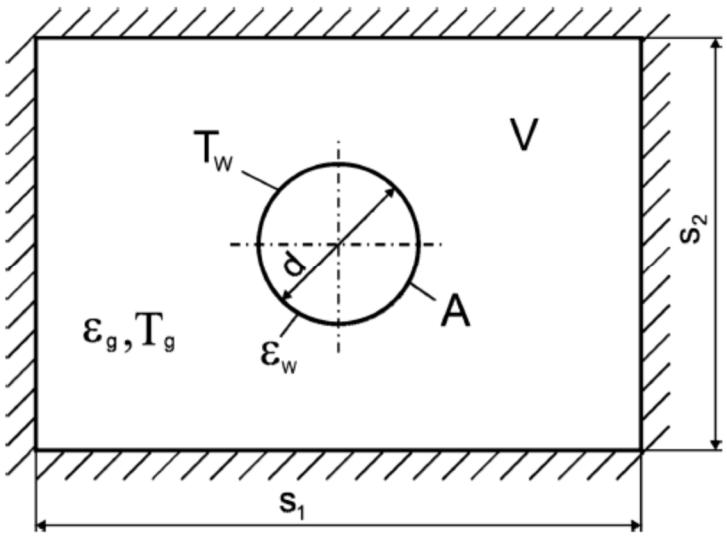

Fig. A.3: Control volume of a tube in a tube bank [20].

$\sigma := 5.67 \cdot 10^{-8} \frac{W}{m^2 \cdot K^4}$ Stefan Boltzman constant

$\varepsilon_w := 0.8$

$\varepsilon_{eq} := \frac{2 \cdot \varepsilon_w}{2 - \varepsilon_w} = 1.333$

$s_1 := S_L = 0.085\,m$ $s_2 := S_T = 0.104\,m$

$V_{permeter} := \left(s_1 \cdot s_2 - \frac{\pi}{4} \cdot D_o^{\,2} \right) = 0.007\,m^2$

$A_{permeter} := \pi \cdot D_o = 0.132\,m$

$C := 3.6$

$s := C \frac{V_{permeter}}{A_{permeter}} = 0.203\,m$ Geometric mean beam length

$s_{check} := C \cdot \frac{D_o}{4} \cdot \left(\frac{4}{\pi} \cdot \frac{s_1 \cdot s_2}{D_o^{\,2}} - 1 \right) = 0.203\,m$

Weighted sum of grey gasses (Smith et al 1982)

$atm := 101.325kPa$

$$\kappa := \begin{pmatrix} 0 \\ 0.4201 \\ 6.516 \\ 131.9 \end{pmatrix} \frac{1}{atm} \qquad b := \begin{pmatrix} 0 & 0 & 0 & 0 & 0 \\ 0 & 6.508 \cdot 10^{-1} & -5.551 \cdot 10^{-4} & 3.029 \cdot 10^{-7} & -5.353 \cdot 10^{-11} \\ 0 & -0.2504 \cdot 10^{-1} & 6.112 \cdot 10^{-4} & -3.882 \cdot 10^{-7} & 6.528 \cdot 10^{-11} \\ 0 & 2.718 \cdot 10^{-1} & -3.118 \cdot 10^{-4} & 1.221 \cdot 10^{-7} & -1.612 \cdot 10^{-11} \end{pmatrix}$$

$$a_1 := \sum_{j=1}^{3} \left[b_{1,j} \cdot \left(\frac{T_g}{K} \right)^{(j-1)} \right] = 0.397$$

$$a_2 := \sum_{j=1}^{3} \left[b_{2,j} \cdot \left(\frac{T_g}{K} \right)^{(j-1)} \right] = 0.213$$

$$a_3 := \sum_{j=1}^{3} \left[b_{3,j} \cdot \left(\frac{T_g}{K} \right)^{(j-1)} \right] = 0.093$$

$$a_0 := 1 - a_1 - a_2 - a_3 = 0.297$$

$$\varepsilon g_1 := 1 - e^{-\kappa_1 \cdot p_g \cdot \frac{s}{m}} = 0.081$$

$$\varepsilon g_2 := 1 - e^{-\kappa_2 \cdot p_g \cdot \frac{s}{m}} = 0.73$$

$$\varepsilon g_3 := 1 - e^{-\kappa_3 \cdot p_g \cdot \frac{s}{m}} = 1$$

$$\varepsilon_g := \sum_{i=0}^{3} \left[a_i \left(1 - e^{-\kappa_i \cdot p_g \cdot \frac{s}{m}} \right) \right] = 0.281$$

$$a := \frac{-ln(1 - \varepsilon_g)}{s} = 1.619 \frac{1}{m}$$

$$a \cdot s = 0.329$$

$$h_{ro} := \frac{\sigma \cdot \varepsilon_{eq} \cdot a \cdot s}{a \cdot s + \varepsilon_{eq}} \cdot \frac{\left(T_g^{\,4} - T_w^{\,4} \right)}{\left(T_g - T_w \right)} = 33.423 \cdot \frac{W}{m^2 K}$$

$$F_{wg} := \frac{\sigma \cdot \varepsilon_{eq} \cdot a \cdot s}{a \cdot s + \varepsilon_{eq}} \cdot \sigma^{-1} = 0.264$$

$$h_o := h_{co} + h_{ro} = 123.765 \cdot \frac{W}{m^2 K}$$

A.7. Overall heat transfer coefficient (UA)

$$A_{o.tube} := \pi D_{oo} \cdot L_{tube.total} = 8.135\,m^2$$

$$U_{i.tube.total} := \frac{1}{\frac{1}{h_i} + \frac{A_{i.tube} \cdot ln\left(\frac{D_o}{D_i}\right)}{2\pi \cdot k_{pipe} \cdot L_{tube.total}} + \frac{A_{i.tube} \cdot ln\left(\frac{D_{oo}}{D_o}\right)}{2\pi \cdot k_{fl} \cdot L_{tube.total}} + \frac{A_{i.tube}}{A_{o.tube}} \cdot \frac{1}{h_o}} = 57.72 \frac{kg}{s^3 \cdot K}$$

$$UA_{Tubesheet} := U_{i.tube.total} \cdot A_{i.tube} \cdot \frac{N_{tubes}}{N_{sheets}} = 0.682 \cdot \frac{kW}{K}$$

$$UA_{HX} := U_{i.tube.total} \cdot A_{i.tube} \cdot N_{tubes} = 50.497 \cdot \frac{kW}{K}$$

A.8. Effectiveness NTU method – Part 1

$$C_{fg} := cp_{fg} \cdot \frac{m_{fg}}{N_{sheets}} = 1864.254 \cdot \frac{W}{K}$$

$$C_s := cp_s \cdot \frac{m_s}{N_{sheets}} = 2182.829 \cdot \frac{W}{K}$$

$$C_c := \frac{min\left(C_{fg}, C_s\right)}{max\left(C_{fg}, C_s\right)} = 0.854$$

$$UA_{Tubesheet} = 0.682 \frac{kW}{K}$$

$$NTU := \frac{UA_{Tubesheet}}{min\left(C_{fg}, C_s\right)} = 0.366$$

$$q_{HX} := \frac{Q_s}{N_{sheets}} = 137.955\,kW$$

Calculated using given steam conditions

A.8.1. Assume a counterflow heat exchanger

$$\varepsilon_{cf} := \frac{1 - exp\left[-NTU \cdot \left(1 - C_c\right)\right]}{1 - C_c \cdot exp\left[-NTU \cdot \left(1 - C_c\right)\right]} = 0.273$$

Effectiveness: Counterflow HX

$$\Delta T_{fg.cf} := \varepsilon_{cf} \cdot \left(T_{fgi} - T_{si}\right) = 80.582 \cdot \Delta°C$$

$$\Delta T_{fg.given} := T_{fgi} - T_{fge} = 74 \cdot \Delta°C$$

$$T_{fge.resultant.cf} := T_{fgi} - \Delta T_{fg.cf} = 552.018 \cdot °C$$

$$T_{fge.given} := T_{fge} = 558.6 \cdot °C$$

$$q_{cf} := \frac{m_{fg}}{N_{sheets}} \cdot cp_{fg} \cdot \Delta T_{fg.cf} = 150.226 \cdot kW$$

$$\%Error_{cf} := \frac{q_{cf} - q_{HX}}{q_{HX}} = 8.9 \cdot \%$$

$$T_{se.resultant.cf} := T_{si} + \frac{q_{cf}}{\frac{m_s}{N_{sheets}} \cdot cp_s} = 406.522 \cdot °C$$

$$T_{se.given} := T_{se} = 400.9 \cdot °C$$

A.8.2. Assume a parallel flow heat exchanger

$$\varepsilon_{pf} := \frac{1 - exp\left[-NTU \cdot \left(1 + C_c\right)\right]}{1 + C_c} = 0.266$$

Effectiveness: parallel flow HX

$$\Delta T_{fg.pf} := \varepsilon_{pf} \cdot \left(T_{fgi} - T_{si}\right) = 78.368 \cdot \Delta°C$$

$$\Delta T_{fg.given} = 74 \cdot \Delta°C$$

$$T_{fge.resultant.pf} := T_{fgi} - \Delta T_{fg.pf} = 554.232 \cdot °C$$

$$T_{fge.given} = 558.6 \cdot °C$$

$$q_{pf} := \frac{m_{fg}}{N_{sheets}} \cdot cp_{fg} \cdot \Delta T_{fg.pf} = 146.097 \cdot kW$$

$$\%Error_{pf} := \frac{q_{pf} - q_{HX}}{q_{HX}} = 5.9 \cdot \%$$

$$T_{se.resultant.pf} := T_{si} + \frac{q_{pf}}{\frac{m_s}{N_{sheets}} \cdot cp_s} = 404.63 \cdot °C$$

$$T_{se.given} = 400.9 \cdot °C$$

A.8.3. Assume a cross flow heat exchanger

Cmax mixed, Cmin unmixed

$$\varepsilon_{crossf.m.u} := \left(\frac{1}{C_c}\right)\cdot\left[1 - exp\left[-C_c\cdot(1 - exp(-NTU))\right]\right] = 0.27$$

Effectiveness: Cross flow HX
C max mixed and C min unmixed

$$\Delta T_{fg.crossf.m.u} := \varepsilon_{crossf.m.u}\cdot\left(T_{fgi} - T_{si}\right) = 79.53\cdot\Delta°C \qquad \Delta T_{fg.given} = 74\cdot\Delta°C$$

$$T_{fge.resultant.crossf.m.u} := T_{fgi} - \Delta T_{fg.crossf.m.u} = 553.07\cdot°C \qquad T_{fge.given} = 558.6\cdot°C$$

$$q_{crossf.m.u} := \frac{m_{fg}}{N_{sheets}}\cdot cp_{fg}\cdot\Delta T_{fg.crossf.m.u} = 148.265\cdot kW \qquad \%Error_{crossf.m.u} := \frac{q_{crossf.m.u} - q_{HX}}{q_{HX}} = 7.5\cdot\%$$

$$T_{se.resultant.crossf.m.u} := T_{si} + \frac{q_{crossf.m.u}}{\frac{m_s}{N_{sheets}}\cdot cp_s} = 405.623\cdot°C \qquad T_{se.given} = 400.9\cdot°C$$

Both fluids unmixed

$$n := NTU^{-0.22}$$

$$\varepsilon_{crossf.u} := 1 - exp\left(\frac{exp\left(-NTU\cdot C_c\cdot n\right) - 1}{C_c\cdot n}\right) = 0.261$$

Effectiveness: Cross flow HX
Both fluids unmixed

$$\Delta T_{fg.crossf.u} := \varepsilon_{crossf.u}\cdot\left(T_{fgi} - T_{si}\right) = 77.11\cdot\Delta°C \qquad \Delta T_{fg.given} = 74\cdot\Delta°C$$

$$T_{fge.resultant.crossf.u} := T_{fgi} - \Delta T_{fg.crossf.u} = 555.49\cdot°C \qquad T_{fge.given} = 558.6\cdot°C$$

$$q_{crossf.u} := \frac{m_{fg}}{N_{sheets}}\cdot cp_{fg}\cdot\Delta T_{fg.crossf.u} = 143.753\cdot kW \qquad \%Error_{crossf.u} := \frac{q_{crossf.u} - q_{HX}}{q_{HX}} = 4.2\cdot\%$$

$$T_{se.resultant.crossf.u} := T_{si} + \frac{q_{crossf.u}}{\frac{m_s}{N_{sheets}}\cdot cp_s} = 403.556\cdot°C \qquad T_{se.given} = 400.9\cdot°C$$

A.9. Flownex

Steam and flue gas temperature results that were extracted from the Flownex model with no discretisation are shown below together with the resultant heat transfer for each tube in a pass.

$$T_{steam.Flownex} := \begin{pmatrix} 397.393797 \\ 397.4361909 \\ 390.8831236 \\ 390.8371868 \\ 384.5447741 \\ 384.5870671 \\ 378.556493 \\ 378.5109802 \\ 372.7408073 \\ 372.782771 \\ 367.2767574 \\ 367.2319059 \\ 361.9832094 \\ 362.0237995 \\ 339.9906161 \\ 339.9412232 \\ 344.470647 \\ 344.5228099 \\ 357.2415061 \\ 357.1931208 \\ 352.8534389 \\ 352.8988971 \\ 348.7718925 \\ 348.7246077 \end{pmatrix} °C \quad T_{fluegas.Flownex} := \begin{pmatrix} 630.854414 \\ 627.4197773 \\ 624.0145121 \\ 620.6369988 \\ 617.2886246 \\ 613.9690613 \\ 610.6799903 \\ 607.419829 \\ 604.189837 \\ 600.9896815 \\ 597.8209975 \\ 594.6822455 \\ 591.5744964 \\ 588.4974044 \\ 585.3388193 \\ 582.099753 \\ 578.958217 \\ 575.9125004 \\ 573.0127995 \\ 570.2550907 \\ 567.5261851 \\ 564.8258984 \\ 562.1554136 \\ 559.5133685 \end{pmatrix} °C \quad Q_{Flownex} := \begin{pmatrix} 6.475734094 \\ 6.330787975 \\ 6.366197743 \\ 6.227315389 \\ 6.257540238 \\ 6.119881041 \\ 6.143823505 \\ 6.012090991 \\ 6.031323777 \\ 5.900831498 \\ 5.913953841 \\ 5.789229733 \\ 5.798344595 \\ 5.674909837 \\ 6.102194089 \\ 5.975015747 \\ 5.738517083 \\ 5.617718387 \\ 5.19403048 \\ 5.088267188 \\ 5.086621233 \\ 4.981544194 \\ 4.975468861 \\ 4.875506116 \end{pmatrix} kW$$

For each tube, the overall heat transfer coefficient (UA) was calculated as follows:

$$UA_{Flownex} := \frac{Q_{Flownex}}{T_{fluegas.Flownex} - T_{steam.Flownex}}$$

Some of the results are shown below.

$UA_{Flownex} =$

	0
0	0.028
1	0.028
2	0.027
3	0.027
4	0.027
5	0.027
6	0.026
7	0.026
8	0.026
9	0.026
10	0.026
11	0.025
12	0.025
13	0.025
14	0.025
15	...

$\cdot \frac{kW}{K}$

$UA_{Flownex} =$

	0
8	0.026
9	0.026
10	0.026
11	0.025
12	0.025
13	0.025
14	0.025
15	0.025
16	0.024
17	0.024
18	0.024
19	0.024
20	0.024
21	0.024
22	0.023
23	...

$\cdot \frac{kW}{K}$

Thus, the resultant average overall heat transfer coefficient (UA) from the Flownex model is

$$UA_{av.Flownex} := \sum UA_{Flownex} = 0.609 \cdot \frac{kW}{K}$$

A.10. Effectiveness NTU method – Part 2

Using the overall heat transfer coefficient (UA) calculated from the Flownex model results, the process of using different lumped heat exchanger arrangements assumptions in conjunction with the effectiveness NTU method was repeated.

The Number of Transfer Units (NTU) were re-calculated as shown below.

$$NTU_r := \frac{UA_{av.Flownex}}{min(C_{fg}, C_s)} = 0.327$$

$$\Delta T_{max} := T_{fgi} - T_{si}$$

$$q_{max} := min(C_{fg}, C_s) \cdot \Delta T_{max} = 549.769 \cdot kW$$

A.10.1. Assume a counterflow heat exchanger

$$\varepsilon_{cf.new} := \frac{1 - exp\left[-NTU_r \cdot \left(1 - C_c\right)\right]}{1 - C_c \cdot exp\left[-NTU_r \cdot \left(1 - C_c\right)\right]} = 0.251$$

Effectiveness: Counterflow HX

$$q_{cf.new} := \varepsilon_{cf.new} \cdot q_{max} = 137.864 \cdot kW$$

$$\%Error_{cf.new} := \frac{q_{cf.new} - q_{HX}}{q_{HX}} = -0.07 \cdot \%$$

A.10.2. Assume a parallel flow heat exchanger

$$\varepsilon_{pf.new} := \frac{1 - exp\left[-NTU_r \cdot \left(1 + C_c\right)\right]}{1 + C_c} = 0.245$$

Effectiveness: parallel flow HX

$$q_{pf.new} := \varepsilon_{pf.new} \cdot q_{max} = 134.739 \cdot kW$$

$$\%Error_{pf.new} := \frac{q_{pf.new} - q_{HX}}{q_{HX}} = -2.3 \cdot \%$$

A.10.3. Assume a cross flow heat exchanger

<u>Cmax mixed, Cmin unmixed</u>

$$\varepsilon_{crossf.m.u.new} := \left(\frac{1}{C_c}\right) \cdot \left[1 - exp\left[-C_c \cdot \left(1 - exp\left(-NTU_r\right)\right)\right]\right] = 0.248$$

Effectiveness: Cross flow HX
C max mixed and C min unmixed

$$q_{crossf.m.u.new} := \varepsilon_{crossf.m.u.new} \cdot q_{max} = 136.375 \cdot kW$$

$$\%Error_{crossf.m.u.new} := \frac{q_{crossf.m.u.new} - q_{HX}}{q_{HX}} = -1.1 \cdot \%$$

Both fluids unmixed

$$n_r := NTU_r^{-0.22}$$

$$\varepsilon_{crossf.u.new} := 1 - exp\left(\frac{exp\left(-NTU_r \cdot C_c \cdot n_r\right) - 1}{C_c \cdot n_r}\right) = 0.24$$

Effectiveness: Cross flow HX

Both fluids unmixed

$$q_{crossf.u.new} := \varepsilon_{crossf.u.new} \cdot q_{max} = 132.104 \cdot kW$$

$$\%Error_{crossf.u.new} := \frac{q_{crossf.u.new} - q_{HX}}{q_{HX}} = -4.2 \cdot \%$$

APPENDIX B. FLUE GAS SIDE MODELLING

B.1. Inviscid flow: Network approach

Consider the case shown in Fig. B.1, with the known inputs as follows;

$$u_W = 5\frac{\text{m}}{\text{s}} \quad p_E = 0\text{Pa}$$

$$v_S = 1\frac{\text{m}}{\text{s}} \quad p_N = 0\text{Pa}$$

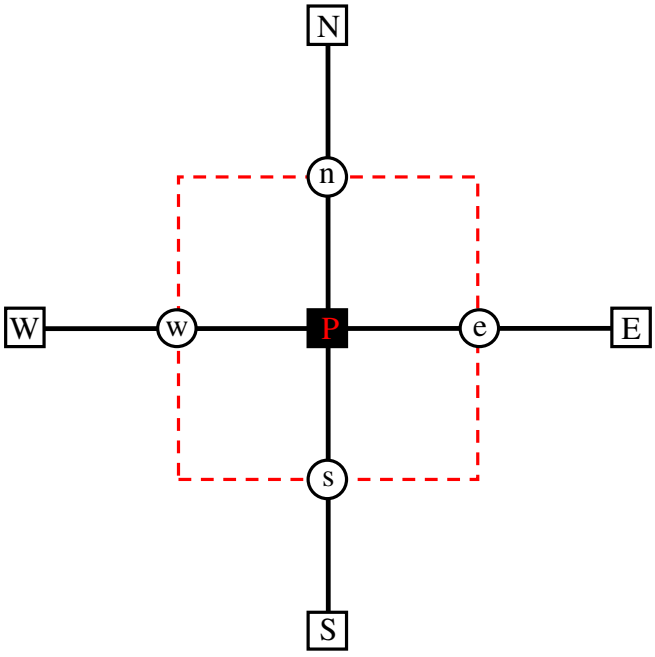

Fig. B.1: Set-up for a 2-D technique that solves for total pressure (1-D network approach).

The total pressure at the outlet nodes is given by

$$p_{0E} = p_E + \frac{1}{2}\rho u_E^2 = 0.5u_E^2$$

$$p_{0N} = p_N + \frac{1}{2}\rho v_N^2 = 0.5v_N^2$$

Solving for total pressure on the common node **P** for this case which has no resistance to flow implies that

$$p_{0P} = p_{0E} = p_{0N}$$

Combining the two equations, it can be concluded that

$$u_E = v_N = 3\frac{\text{m}}{\text{s}}$$

Thus, with the technique that solves for total pressure, the flow equally splits between the two legs. A summary of the results from the basic fluid mechanics calculations are as follows;

$$u_w = 5\frac{\text{m}}{\text{s}} \quad u_e = 3\frac{\text{m}}{\text{s}} \quad v_s = 1\frac{\text{m}}{\text{s}} \quad u_n = 3\frac{\text{m}}{\text{s}}$$

$$p_{0W} = 4.5\text{Pa} \quad p_{0S} = 4.5\text{Pa} \quad p_{0P} = 4.5\text{Pa} \quad p_{0E} = 4.5\text{Pa} \quad p_{0N} = 4.5\text{Pa}$$

$$u_P = \frac{5}{12}\times 5 + \frac{1}{12}\times 1 + \frac{3}{12}\times 3 + \frac{3}{12}\times 3 = 3.667\frac{\text{m}}{\text{s}}$$

$$u_W = 5\frac{\text{m}}{\text{s}} \quad v_S = 1\frac{\text{m}}{\text{s}} \quad u_P = 3.667\frac{\text{m}}{\text{s}} \quad u_E = 3\frac{\text{m}}{\text{s}} \quad v_N = 3\frac{\text{m}}{\text{s}}$$

$$p_W = -8\text{Pa} \quad p_S = 4\text{Pa} \quad p_P = -2.22\text{Pa} \quad p_E = 0\text{Pa} \quad p_N = 0\text{Pa}$$

These results are summarised in Table B.1.

Table B.1: A summary results from the network approach for a steady state case with inviscid flow.

Details	**Symbols**	**Units**	**Values**
x outlet velocity	u_e	m/s	3
y outlet velocity	v_n	m/s	3
Internal static pressure	p_P	Pa	-2.22
Inlet x static pressure	p_W	Pa	-8
Inlet y static pressure	p_S	Pa	4

APPENDIX C. RADIATION MODEL – VDI HEAT ATLAS

General inputs

Emissivity of the tube wall: $\varepsilon_w := 0.7$

Stefan Boltzman constant: $\sigma := 5.67 \cdot 10^{-8} \cdot \frac{W}{m^2 \cdot K^4}$

Inlet flue gas temperature: $T_{g.FSH.in} := 1059.07\,°C$

Outlet flue gas temperature: $T_{g.FSH.out} := 942.608\,°C$

Average flue gas temperature: $T_g := \frac{T_{g.FSH.in} + T_{g.FSH.out}}{2} = 1273.989\,K$

Average wall temperature of the outer fouling layer: $T_w := 790.826\,K$

Mean beam length

Outer tube diameter: $D_o := 0.0445m$

Transverse pitch: $s_1 := 0.0455m$

Longitudinal pitch: $s_2 := 0.8571m$

Radiation constant: $C_{rad} := 3.6$

Mean beam length: $L_{mb} := C_{rad} \cdot \frac{D_o}{4} \cdot \left(\frac{4}{\pi} \cdot \frac{s_1 \cdot s_2}{D_o^2} - 1 \right) = 0.964\,m$

Gas specification

Total pressure of the system: $p_t := 1bar$

Fraction of CO2 in flue gas: $\chi_{CO2} := 21.424\%$

Partial pressure of CO2: $p_{CO2} := \chi_{CO2} \cdot p_t = 0.214 \cdot bar$

Fraction of H2O in flue gas: $\chi_{H2O} := 4.545\%$

Partial pressure of H2O: $p_{H2O} := \chi_{H2O} \cdot p_t = 0.045 \cdot bar$

Emissivity of gases and particles

Emissivity of gases

Carbon dioxide: $p_{CO2} \cdot L_{mb} = 0.207 \cdot bar \cdot m$

Gas temperature: $T_g = 1274\,K$

Emissivity of Carbon dioxide: $\varepsilon_{CO2} := 0.13$

Water vapour: $p_{H2O} \cdot L_{mb} = 0.044 \cdot bar \cdot m$

Gas temperature: $T_g = 1274\,K$

Emissivity of Water Vapour uncorrected: $\varepsilon_{H2O.uncorrected} := 6 \cdot 10^{-2}$

Pressure for correction: $p_{f.H2O} := \frac{p_{H2O} + p_t}{2} = 0.523 \cdot bar$

Correction factor f: $f_{H2O} := 1.0$

Emissivity of Water Vapour: $\varepsilon_{H2O} := f_{H2O} \cdot \varepsilon_{H2O.uncorrected} = 0.06$

Pressure for interphase: $p_{interphase} := \frac{p_{H2O}}{p_{CO2} + p_{H2O}} = 0.175$

Combined : $pL_{comb} := \left(p_{CO2} + p_{H2O}\right) \cdot L_{mb} = 0.25 \cdot bar \cdot m$

Gas mixtures interphase $\Delta\varepsilon_g := 0.0125$

Emissivity of the gas mixture: $\varepsilon_g := \varepsilon_{H2O} + \varepsilon_{CO2} - \Delta\varepsilon_g$

Emission coefficient for the gas phase: $K_{emi.g} := \frac{-\ln\left(1 - \varepsilon_g\right)}{L_{mb}} = 0.203 \frac{1}{m}$

Emissivity of particles

Density of the fly ash material: $\rho_p := 2963 \cdot \frac{kg}{m^3}$

Diameter of the particle: $d_p := 16 \cdot 10^{-6} m$

Mean relative absorption efficiency: $Q_{abs} := 0.32$

Particle load: $L_p := 0.046 \cdot \frac{kg}{m^3}$

Specific projection area for the particle: $A_p := \frac{3}{2 \cdot \rho_p \cdot d_p} = 31.64 \frac{m^2}{kg}$

Mean relative backscattering efficiency: $Q_{bsc} := 0.75$

Auxiliary term: $\gamma_p := \sqrt{1 + \frac{2 \cdot Q_{bsc}}{Q_{abs}}} = 2.385$

Auxiliary term: $\beta_p := \frac{\gamma_p - 1}{\gamma_p + 1} = 0.409$

Optical thickness for emission for particles: $\Phi_p := Q_{abs} \cdot A_p \cdot L_p \cdot L_{mb} \cdot \gamma_p$

Emissivity of particles: $\varepsilon_p := \left(1 - \beta_p\right) \cdot \left(\frac{1 - \exp\left(-\Phi_p\right)}{1 + \beta_p \cdot \exp\left(-\Phi_p\right)} \right)$

Optical thickness for emission for the gas solid mixture: $\Phi_{emi.gp} := \left(Q_{abs} \cdot A_p \cdot L_p + K_{emi.g}\right) \cdot L_{mb} \cdot \gamma_p$

Emissivity of gas + particle mixture: $\varepsilon_{gp} := \left(1 - \beta_p\right) \cdot \left(\frac{1 - \exp\left(-\Phi_{emi.gp}\right)}{1 + \beta_p \cdot \exp\left(-\Phi_{emi.gp}\right)} \right)$

Absorptivity of gases and particles

Carbon dioxide: $p_{CO2} \cdot L_{mb} = 0.207 \cdot bar \cdot m$

Wall temperature: $T_w = 791\,K$

Emissivity of Carbon dioxide: $\varepsilon_{CO2.w} := 0.125$

Correction factor $f_{CO2.w} := 1$

Absorptivity of Carbon dioxide: $\alpha_{CO2} := f_{CO2.w} \cdot \left(\frac{T_g}{T_w} \right)^{0.65} \cdot \varepsilon_{CO2.w}$

Water vapour: $p_{H2O} \cdot L_{mb} = 0.044 \cdot bar \cdot m$

Wall temperature: $T_w = 791\,K$

Emissivity of Water Vapour uncorrected: $\varepsilon_{H2O.uncorrected.w} := 9 \cdot 10^{-2}$

Pressure for correction: $p_{f.H2O} = 0.523 \cdot bar$

Correction factor f: $f_{H2O} = 1$

Emissivity of Water Vapour: $\varepsilon_{H2O.w} := f_{H2O} \cdot \varepsilon_{H2O.uncorrected.w} = 0.09$

Absorptivity of Water vapour: $\alpha_{H2O} := \left(\frac{T_g}{T_w} \right)^{0.45} \cdot \varepsilon_{H2O.w}$

Pressure for interphase: $p_{interphase} = 0.175$

Combined : $pL_{comb} = 0.25 \cdot bar \cdot m$

Gas mixtures emissivity interphase at wall: $\Delta\varepsilon_w := 0.007$

Absorption of the gas: $\alpha_g := \alpha_{H2O} + \alpha_{CO2} - \Delta\varepsilon_w$

Absorption coefficient for the gas phase: $K_{abs.g} := \frac{-\ln(1-\alpha_g)}{L_{mb}} = 0.333 \frac{1}{m}$

Optical thickness for emission for the gas solid mixture: $\Phi_{abs.gp} := (Q_{abs} \cdot A_p \cdot L_p + K_{abs.g}) \cdot L_{mb} \cdot \gamma_p$

Absorptivity of the gas + particle mixture: $\alpha_{gp} := (1-\beta_p) \cdot \left(\frac{1 - \exp(-\Phi_{abs.gp})}{1 + \beta_p \cdot \exp(-\Phi_{abs.gp})} \right)$

Heat transfer coefficient

$$h_{rad} := \frac{\varepsilon_w}{\alpha_{gp} + \varepsilon_w - \alpha_{gp} \cdot \varepsilon_w} \cdot \sigma \cdot \left(\frac{\varepsilon_{gp} \cdot T_g^4 - \alpha_{gp} \cdot T_w^4}{T_g - T_w} \right) = 91.989 \frac{W}{m^2 \cdot K}$$

APPENDIX D. MASS AND ENERGY BALANCE

D.1. Coal composition

NOx fraction during combustion: $f_{NOx} := 70\%$

	Mass fraction	Calorific value:	Stoichiometric coefficient
Carbon:	$mf_C := 43.94\%$	$CV_C := 32778.15\frac{kJ}{kg}$	$St_C := 1$
Hydrogen:	$mf_H := 2.5\%$	$CV_H := 119931.72\frac{kJ}{kg}$	$St_H := \frac{1}{4}$
Oxygen:	$mf_O := 9.61\%$	$CV_O := 0\frac{kJ}{kg}$	$St_O := -\frac{1}{2}$
Nitrogen:	$mf_N := 1.11\%$	$CV_N := 0\frac{kJ}{kg}$	$St_N := f_{NOx}\cdot\frac{1}{2}$
Sulphur:	$mf_S := 1\%$	$CV_S := 9257.524\frac{kJ}{kg}$	$St_S := 1.0$
Water:	$mf_{H2O} := 10.51\%$	$CV_{H2O} := 0\frac{kJ}{kg}$	$St_{H2O} := 0$
Ash:	$mf_{ash} := 31.33\%$	$CV_{ash} := 0\frac{kJ}{kg}$	$St_{ash} := 0$

Confirming mass fractions

$$mf_{tot} := mf_C + mf_O + mf_H + mf_N + mf_S + mf_{H2O} + mf_{ash} = 1$$

D.2. Mass balance and flue gas composition

Unburnt carbon

Mass of Unburnt Carbon per kg of Coal: $C' := mf_{ash}\cdot\left[\left(\%C_{fa}\cdot\%FA\right) + \left(\%C_{ba}\cdot\%BA\right)\right] = 0.313\cdot\%$

Mass of Unburnt Carbon per kg of Cabon: $C'' := \frac{C'}{mf_C} = 0.713\cdot\%$

Energy loss of Unburnt Carbon per kJ of Energy input: $C''' := \frac{CV_C\cdot C'}{CV_{coal}} = 0.626\cdot\%$

Air Ratios

Theoretical Air/Fuel Ratio:

$$TAR := \frac{M_{air}}{\%O_{2.air}} \cdot \left[St_C \cdot \frac{\left(mf_C - C'\right)}{M_C} + St_O \cdot \frac{mf_O}{M_O} + St_H \cdot \frac{mf_H}{M_H} + \frac{1}{2} St_N \cdot \frac{mf_N}{M_N} + St_S \cdot \frac{mf_S}{M_S} \right]$$

$TAR = 5.523$

Dry Air Required at Furnace: $DAR := TAR \cdot \left(1 + EA_{AH.fg.inlet}\right) = 6.481$

Humid Air Ratio: $HAR := (1 + \omega) \cdot DAR = 6.492$

Mole Fractions

New Carbon Mass Fraction: $mf_{C'} := mf_C - C' = 43.627 \cdot \%$

Moles of Carbon: $n_C := \frac{mf_{C'}}{M_C} \cdot \frac{M_C}{mf_{C'}} = 1$

Moles of Hydrogen: $n_H := \frac{mf_H}{M_H} \cdot \frac{M_C}{mf_{C'}} = 0.683$

Moles of Oxygen: $n_O := \frac{mf_O}{M_O} \cdot \frac{M_C}{mf_{C'}} = 0.165$

Moles of Nitrogen $n_N := \frac{mf_N}{M_N} \cdot \frac{M_C}{mf_{C'}} = 0.022$

Moles of Sulphur: $n_S := \frac{mf_S}{M_S} \cdot \frac{M_C}{mf_{C'}} = 0.009$

Flue gas constituents per kg Coal (FRconst)

Mass Flow Rate of CO_2 per kg Coal:

$$FR_{CO2} := n_C \cdot \frac{M_{CO2}}{M_C} \cdot mf_{C'} = 1.599$$

Mass Flow Rate of H_2O per kg Coal:

$$FR_{H2O} := \frac{1}{2} \cdot n_H \cdot \frac{M_{H2O}}{M_C} \cdot mf_{C'} + DAR \cdot \omega + mf_{H2O} = 0.339$$

Mass Flow Rate of O_2 per kg Coal:

$$FR_{O2} := EA_{AH.fg.inlet} \cdot TAR \cdot \%O_{2.air} \cdot \frac{M_{O2}}{M_{air}} = 0.222$$

Mass Flow Rate of N_2 per kg Coal:

$$FR_{N2} := \frac{1}{2} \cdot \left(1 - f_{NOx}\right) \cdot n_N \cdot \frac{M_{N2}}{M_C} \cdot mf_{C'} + DAR \cdot \%N_{2.air} \cdot \frac{M_{N2}}{M_{air}} = 4.901$$

Mass Flow Rate of NO per kg Coal:

$$FR_{NO} := f_{NOx} \cdot n_N \cdot \frac{M_{NO}}{M_C} \cdot mf_{C'} = 0.017$$

Mass Flow Rate of SO_2 per kg Coal:

$$FR_{SO2} := n_S \cdot \frac{M_{SO2}}{M_C} \cdot mf_{C'} = 0.02$$

Mass Flow Rate of Argon per kg Coal:

$$FR_{Ar} := DAR \cdot \%Ar_{air} \cdot \frac{M_{Ar}}{M_{air}} = 0.082$$

Mass Flow Rate of Fly Ash per kg Coal:

$$FR_{FA} := mf_{ash} \cdot \%FA \cdot \left(1 - \%C_{fa}\right) = 0.279$$

Mass Flow Rate of Unburnt Carbon in Coal:

$$FR_{UBC} := mf_{ash} \cdot \left(\%C_{fa} \cdot \%FA\right) = 0.003$$

Mass Flow Rate of Flue Gas per kg Coal:

$$FGR := FR_{CO2} + FR_{H2O} + FR_{O2} + FR_{N2} + FR_{NO} \ldots + FR_{SO2} + FR_{Ar} + FR_{FA} + FR_{UBC} = 7.462$$

Checking if flue gas mole fractions are calculated properly:

$$FGR_{check} := HAR + 1 - mf_{ash} \cdot \%BA = 7.461$$

Flue gas constituents per kg Flue Gas (mfconst.fg)

Mass fraction of CO2: $mf_{CO2.fg} := \frac{FR_{CO2}}{FGR} = 21.424 \cdot \%$

Mass fraction of H2O: $mf_{H2O.fg} := \frac{FR_{H2O}}{FGR} = 4.545 \cdot \%$

Mass fraction of O2: $mf_{O2.fg} := \frac{FR_{O2}}{FGR} = 2.976 \cdot \%$

Mass fraction of N2: $mf_{N2.fg} := \frac{FR_{N2}}{FGR} = 65.684 \cdot \%$

Mass fraction of NO: $mf_{NO.fg} := \frac{FR_{NO}}{FGR} = 0.223 \cdot \%$

Mass fraction of SO2: $mf_{SO2.fg} := \frac{FR_{SO2}}{FGR} = 0.268 \cdot \%$

Mass fraction of Argon: $mf_{Ar.fg} := \frac{FR_{Ar}}{FGR} = 1.102 \cdot \%$

Mass fraction of Fly Ash: $mf_{FA.fg} := \frac{FR_{FA}}{FGR} = 3.741 \cdot \%$

Mass fraction of UBC: $mf_{UBC.fg} := \frac{FR_{UBC}}{FGR} = 0.038 \cdot \%$

Flue Gas molar mass

$$M_{FG} := mf_{O2.fg} \cdot M_{O2} + mf_{CO2.fg} \cdot M_{CO2} + mf_{N2.fg} \cdot M_{N2} \ldots + mf_{SO2.fg} \cdot M_{SO2} + mf_{H2O.fg} \cdot M_{H2O} + mf_{NO.fg} \cdot M_{NO} + mf_{UBC.fg} \cdot M_{C} = 29.842 \cdot \frac{kg}{kmol}$$

D.3. Energy balance

Enthalpy of flue gas using NIST Data:

$$h_{fg}(T) := mf_{O2.fg} \cdot h\left(Constants_h, O_2, T\right) + mf_{CO2.fg} \cdot h\left(Constants_h, CO_2, T\right) \ldots + mf_{N2.fg} \cdot h\left(Constants_h, N_2, T\right) + mf_{SO2.fg} \cdot h\left(Constants_h, SO_2, T\right) \ldots + mf_{H2O.fg} \cdot h_{water}(T) + mf_{UBC.fg} \cdot h_{UBC}(T) + mf_{FA.fg} \cdot h_{FlyAsh}(T) \ldots + h\left(Constants_h, NO, T\right) \cdot mf_{NO.fg}$$

Moist Air Enthalpy:

$$h_{ASHRAE}(T,\omega) := \left[1.006\cdot\left(\frac{T-0\,°C}{K}\right)+\omega\cdot\left[2501+1.86\left(\frac{T-0\,°C}{K}\right)\right]\right]\cdot\frac{kJ}{kg}$$

$$h_{moist.air}(T,\omega) := h_{ASHRAE}(T,\omega)$$

Net Energy recieved by Steam:

$$E_{s.in} := m'_{s.PrimRH}\cdot h_{s.PrimRH.in} + m'_{s.econ}\cdot h_{s.econ.in} \cdots + m'_{s.ATT1}\cdot h_{s.ATT1} + m'_{s.ATT2}\cdot h_{s.ATT2} + m'_{s.ATT3}\cdot h_{s.ATT3}$$

$$E_{s.out} := m'_{s.FSH}\cdot h_{s.FSH.out} + m'_{s.FRH}\cdot h_{s.FRH.out} = 3424.97\cdot MW$$

$$\Delta Q_{steam} := E_{s.out} - E_{s.in} = 1445.628\cdot MW$$

Mass flow rate of coal

$$m'_{coal} := \frac{\Delta Q_{steam} - Q_{credits} + \left(h_{moist.air}\left(T_{air.A/H.out},\omega\right) - h_{moist.air}\left(T_{amb},\omega\right)\right)\cdot m'_{seal.air}}{\left(1-q_{rad.loss}\right)\cdot CV_{coal} \cdots + h_{coal}\left(T_{amb}\right) \cdots + HAR\cdot\%Air_{ing}\cdot h_{moist.air}\left(T_{amb},\omega\right) \cdots + HAR\cdot\left(1-\%Air_{ing}\right)\cdot h_{moist.air}\left(T_{air.A/H.out},\omega\right) \cdots + -FGR\cdot h_{fg}\left(T_{fg.A/H.in}\right) \cdots + -mf_{ash}\cdot\%BA\cdot h_{FlyAsh}\left(T_{ba.exit}\right)} = 97.616\,\frac{kg}{s}$$

D.4. Mass flow calculations

Mass flow rate of total humid air into the boiler

Including ingress air

$$m'_{ha} := HAR\cdot m'_{coal} = 633.723\,\frac{kg}{s}$$

Mass flow rate of humid air into the furnace

$$m'_{ha.furnace} := HAR\cdot\left(1-\%Air_{ing}\right)\cdot m'_{coal} = 621.936\,\frac{kg}{s}$$

Mass flow rate of ingress air

$$m'_{air.ing} := HAR\cdot\%Air_{ing}\cdot m'_{coal} = 11.787\,\frac{kg}{s}$$

Mass flow rate of flue gas at the economizer exit

$$m'_{fg} := FGR\cdot m'_{coal} = 728.415\,\frac{kg}{s}$$

APPENDIX E. GURVICH THERMAL MODEL

E.1. Flame temperature calculation

Calorific value (HHV): $CV_{coal} = 16.41 \cdot \frac{MJ}{kg}$

Mass flow rate of coal: $m'_{coal} = 97.616 \frac{kg}{s}$

Enthalpy of coal: $h_{coal} := h_{coal}(T_{amb}) = 60.706 \cdot \frac{kJ}{kg}$

Humid air ratio: $HAR = 6.492$

Mass flow rate of hot air into the furnace: $m'_{ha.furnace} = 621.936 \frac{kg}{s}$

Mass flow rate of flue gas: $m'_{fg.furnace} = 716.628 \frac{kg}{s}$

Enthaply of hot air: $h_{ha.furnace} := h_{moist.air}(T_{air.A/H.out}, \omega)$

$$h_{ha.furnace} = 294.705 \cdot \frac{kJ}{kg}$$

Flame enthalpy:

$$h_{flame} := \frac{m'_{ha.furnace} \cdot h_{ha.furnace} + m'_{coal} \cdot (h_{coal} + CV_{coal})}{m'_{ha.furnace} + m'_{coal}}$$

$$h_{flame} = 2489.18 \cdot \frac{kJ}{kg}$$

Calculation of Flame Temperature:

Initial Guess Value: $T_{flame.num} := 1800\,°C$ Assumed only for this short calculation. No need to update.

$f(T) := h_{fg}(T) - h_{flame}$

$T_{flame} := root(f(T_{flame.num}), T_{flame.num})$

$T_{flame} = 1983.55 \cdot °C$

E.2. Furnace geometry

Width of the furnace (at burner level): $W_{furnace} := 24.003m$

Depth of the furnace (at burner level) $b_{furnace} := 13.716m$

Height at the middle of the hopper: $h_{hopper} := 11084mm$

Height of the burner rows:

Row 1: $h_{row1} := 19360mm$

Row 2: $h_{row2} := 26675mm$

Row 3: $h_{row3} := 33390mm$

Burner height: $h_b := \frac{h_{row1} + h_{row2} + h_{row3}}{3} - h_{hopper}$

$h_b = 15.391\,m$

Height at the bottom of the platen superhater: $h_{plat.bot} := 53400mm$

Height at the roof: $h_{roof} := 71385mm$

Height at the middle of the platen superheter; $h_{plat.mid} := \frac{h_{plat.bot} + h_{roof}}{2}$

Height from dry hopper to center of furnace exit: $h_{hp} := h_{plat.mid} - h_{hopper}$

$h_{hp} = 51.308\,m$

Burner relative height: $x_b := \frac{h_b}{h_{hp}} = 0.3$

Parameter: $\Delta x := 0.05$

Relative height of flame center: $x_{flame} := x_b + \Delta x = 0.35$

Area of the furnace: $A_{furnace} := 4281m^2$

Volume of the furnace: $V_{furnace} := 15794m^3$

E.3. Furnace Exit Gas Temperature and Flame radiation

Calculation of Furnace Exit Temperature:

Furnace exit temperature: $T_{FE} := 1270.52\,°C$ Trial and error

Furnace exit enthalpy: $h_{FE} := h_{fg}(T_{FE}) = 1573.32 \cdot \frac{kJ}{kg}$

$f(T) := h_{fg}(T) - h_{FE}$

$T_{FE} := \text{root}(f(T_{FE}), T_{FE}) = 1270.52 \cdot °C$

Theoretical combustion temperature: $T_{flame} = 1983.55 \cdot °C$

Furnace outlet gas temperature: $T_{FE} = 1270.52 \cdot °C$

Mean overall heat capacity of the combustion products: $Cp_{furnace} := \frac{h_{flame} - h_{FE}}{T_{flame} - T_{FE}} \cdot \left(\frac{m'_{fg.furnace}}{m'_{coal}} \right)$

$Cp_{furnace} = 9.43 \cdot \frac{kJ}{kg \cdot K}$

Excess air in the furnace: $EA_{furnace} := 15.0\%$

Coal ash (as-received basis) $x_{ash} := 31.33\%$

Fly ash ratio: $\%FA = 90 \cdot \%$

Flue gas pressure: $p_{furnace} := 10^5 Pa$

Reference pressure: $p_0 := 9.81 \cdot 10^4 Pa$

Diameter of ash particles: $d_{fa} := 16 \mu m$

Calculations

Excess air coefficient: $EA_{coef.furnace} := 1 + EA_{furnace} = 1.15$

Water vapor volume (normal state):

$$V_{H2O.furnace} := V_{0.H2O} + 0.0161 \cdot \left(EA_{coef.furnace} - 1\right) \cdot V_0$$

$$V_{H2O.furnace} = 0.541 \frac{m^3}{kg}$$

Flue gas volume (normal state):

$$V_{g.furnace} := V_{0.g} + \left(EA_{coef.furnace} - 1\right) \cdot V_0 + 0.0161 \cdot \left(EA_{coef.furnace} - 1\right) \cdot V_0$$

$$V_{g.furnace} = 5.951 \frac{m^3}{kg}$$

$$r_{RO2.furnace} := \frac{V_{RO2}}{V_{g.furnace}} = 0.148$$

Volume fraction of water vapor: $r_{H2O.furnace} := \frac{V_{H2O.furnace}}{V_{g.furnace}} = 0.091$

Volume fraction of triatomic gas: $r_{n.furnace} := r_{H2O.furnace} + r_{RO2.furnace} = 0.239$

Partial pressure of triatomic gas: $p_{n.furnace} := r_{n.furnace} \cdot p_{furnace} = 23.905 \cdot kPa$

Flue gas mass excluding the fly ash:

$$G_{g.furnace} := 1 - x_{ash} + 1.306 \cdot EA_{coef.furnace} \cdot V_0 \cdot \frac{kg}{m^3}$$

$$G_{g.furnace} = 7.911$$

Flue gas density:

$$\rho_{g.furnace} := \frac{G_{g.furnace}}{V_{g.furnace}} = 1.329 \frac{kg}{m^3}$$

Effective radiation layer thickness (Mean beam length):

$$L_{mb.furnace} := 3.6 \cdot \frac{V_{furnace}}{A_{furnace}}$$

$$L_{mb.furnace} = 13.282\,m$$

Gas coefficient:

$$k_{g.furnace} := \left(\frac{0.78 + 1.6 \cdot r_{H2O.furnace}}{\sqrt{\frac{p_{n.furnace}}{p_0} \cdot \frac{L_{mb.furnace}}{m}}} - 0.1 \right) \cdot \left(1 - 0.37 \cdot \frac{T_{flame}}{1000 \cdot K} \right) \cdot 10^{-5} \cdot \frac{1}{m \cdot Pa}$$

$$k_{g.furnace} = 6.838 \times 10^{-7} \cdot \frac{1}{m \cdot Pa}$$

Extinction coefficient of the gas:

$$K_{g.furnace} := k_{g.furnace} \cdot r_{n.furnace} \cdot p_{furnace} = 0.016 \frac{1}{m}$$

Fly ash concentration:

$$\mu_{fa.furnace} := \frac{\%FA \cdot x_{ash}}{G_{g.furnace}} = 0.0356$$

Fly ash coefficient:

$$k_{fa.furnace} := \frac{4300 \cdot \left(\rho_{g.furnace} \cdot \frac{m^3}{kg} \right)^{\frac{1}{3}}}{\left[\left(\frac{T_{flame}}{K} \right)^2 \cdot \left(\frac{d_{fa}}{\mu m} \right)^2 \right]} \cdot 10^{-5} \cdot \frac{1}{m \cdot Pa}$$

$$k_{fa.furnace} = 5.232 \times 10^{-5} \cdot \frac{1}{m \cdot Pa}$$

Extinction coefficient for fly ash:

$$K_{fa.furnace} := k_{fa.furnace} \cdot \mu_{fa.furnace} \cdot p_{furnace} = 0.186 \frac{1}{m}$$

$$k_{co} := 10^{-5} \cdot \frac{1}{m \cdot Pa}$$

Dimensionless number for bitumite coal: $x_1 := 0.5$

Dimensionless number for pulverized coal furnace combustion: $x_2 := 0.1$

Extinction coefficient of the coal flame: $K_{co} := x_1 \cdot x_2 \cdot k_{co} \cdot p_{furnace}$

$$K_{co} = 0.05 \frac{1}{m}$$

Extinction coefficient of the coal flame: $K_{flame} := K_{g.furnace} + K_{fa.furnace} + K_{co} = 0.253 \frac{1}{m}$

Coal flame emissivity: $\varepsilon_{flame} := 1 - \exp\left(-K_{flame} \cdot L_{mb.furnace}\right)$

$$\varepsilon_{flame} = 0.965$$

Furnace configuartion factor: $X_{furnace} := 1$

Water wall fouling factor: $\zeta_{slag} := 0.45$

Average thermal efficiency coefficient: $\psi_{ave} := \zeta_{slag} \cdot X_{furnace} = 0.45$

Average thermal efficiency coefficent: $\varepsilon_{furnace} := \frac{\varepsilon_{flame}}{\psi_{ave} \cdot \left(1 - \varepsilon_{flame}\right) + \varepsilon_{flame}}$

$$\varepsilon_{furnace} = 0.984$$

Flame center modification factor: $B := 0.56 \qquad C := 0.5$

$$M := B - C \cdot x_{flame} = 0.385$$

Heat loss due to furnace wall radiation and convection: $q_{rad.loss} = 0.9 \cdot \%$

Heat preservation coefficent: $\varphi_{furnace} := 1 - q_{rad.loss} = 0.991$

Stefan boltzmann constant:

$$\sigma_0 := 5.67 \cdot 10^{-8} \cdot \frac{W}{m^2 \cdot K^4}$$

Furnace exit gas temperature:

$$T_{FE.calc} := \frac{T_{flame}}{\left[M \cdot \left[\frac{\left(\sigma_0 \cdot T_{flame}^{\ 3} \cdot \varepsilon_{furnace} \cdot A_{furnace} \cdot \psi_{ave} \right)}{\varphi_{furnace} \cdot m'_{coal} \cdot Cp_{furnace}} \right]^{0.6} + 1 \right]}$$

$$T_{FE.calc} = 1270.59 \cdot °C$$

Remember to update initial guess value

Furnace outlet gas temperature error:

$$Error_{T.FE} := T_{FE} - T_{FE.calc}$$

$$Error_{T.FE} = -0.072 \cdot \Delta °C$$

Furnace outlet enthalpy:

$$h_{FE.calc} := h_{fg}\left(T_{FE.calc}\right)$$

$$h_{FE.calc} = 1573.41 \cdot \frac{kJ}{kg}$$

Furnace outlet gas enthalpy error:

$$Error_{h.FE} := h_{FE} - h_{FE.calc}$$

$$Error_{h.FE} = -0.091 \cdot \frac{kJ}{kg}$$

Radiative absorbed heat of furnace:

$$q_{r.furnace} := \varphi_{furnace} \cdot \left(h_{flame} - h_{FE.calc}\right) \cdot \left(\frac{m'_{fg.furnace}}{m'_{coal}} \right)$$

$$q_{r.furnace} = 6662.4 \cdot \frac{kJ}{kg}$$

Thermal load of radiation heating surface:

Calculated value:

$$Q_{r.furnace} := \frac{m'_{coal} \cdot q_{r.furnace}}{A_{furnace}}$$

$$Q_{r.furnace} = 151.917 \cdot \frac{kW}{m^2}$$

E.4. Platen superheater geometry

Platen superheater height:

$$h_{plat} := h_{roof} - h_{plat.bot} = 17.985\,m$$

Platen superheater depth:

$$b_{plat} := 1053mm + 914mm + 2145mm + 914mm + 1053mm$$

$$b_{plat} = 6.079\,m$$

Platen superheater avarage transverse spacing: $S_{T.plat} := 1143mm$

Platen superheater average longitudinal spacing: $S_L := 39mm$

Outer diameter of the tubes: $OD_{plat} := 38mm$

Average thickness of the tubes: $t_{plat} := \frac{3.6mm + 5.6mm + 8.8mm}{3}$

$t_{plat} = 6 \cdot mm$

Inner diameter of the tubes: $ID_{plat} := OD_{plat} - 2 \cdot t_{plat} = 26 \cdot mm$

Number of rows: $N_{rows.plat} := 28 \cdot 2 \cdot 2 = 112$

Average spacing in the longitudinal direction: $S_{L.plat} := \frac{b_{plat}}{N_{rows.plat} - 1} = 54.766 \cdot mm$

Number of tubesheets/elements in parallel: $N_{tubesheets.plat} := \frac{W_{furnace}}{S_{T.plat}} - 1 = 20$

Number of tubes per tubesheet: $N_{tubes.tubesheet.plat} := 28 \cdot 2 = 56$

Inlet radiation area: $A_{rad.plat.in} := \left(h_{plat} + b_{plat}\right) \cdot S_{T.plat} \cdot N_{tubesheets.plat}$

$A_{rad.plat.in} = 550.103\,m^2$

Outlet radiation area: $A_{rad.plat.out} := h_{plat} \cdot S_{T.plat} \cdot N_{tubesheets.plat}$

$A_{rad.plat.out} = 411.137\,m^2$

Configuration factor from inlet to outlet: $\varphi_{plat} := \sqrt{\left(\frac{b_{plat}}{S_{T.plat}}\right)^2 + 1} - \frac{b_{plat}}{S_{T.plat}}$

$\varphi_{plat} = 0.093$

Superheater area exposed to radiation: $A_{plat} := 3156m^2$

E.5. Platen superheater thermal calculations

Furnace exit temperature: $T_{FE} = 1270.52 \cdot °C$

Furnace exit enthalpy: $h_{FE.plat} := h_{FE} \cdot \frac{m'_{fg.furnace}}{m'_{coal}} = 11550.22 \cdot \frac{kJ}{kg}$

Absorbed convection heat of furnace roof at panel zone: $Q_{roof.plat} := 9.754MW$ Trial and error

Absorbed convection heat of furnace roof at panel zone: $Q_{ww.plat} := 14.178MW$ Trial and error

Platen superheater exit temperature: $T_{g.plat.out} := 1059.07\,°C$ Trial and error

Average platen superheater flue gas temperature: $T_{g.plat.ave} := \frac{T_{FE} + T_{g.plat.out}}{2}$

$T_{g.plat.ave} = 1164.8 \cdot °C$

Mean beam length for the platen superheater: $L_{mb.plat} := \frac{1.8}{\left(\frac{1}{b_{plat}} + \frac{1}{h_{plat}} + \frac{1}{S_{T.plat}}\right)}$

$L_{mb.plat} = 1.644\,m$

Excess air coefficient: $EA_{coef.conv.pass} := 1 + EA_{AH.fg.inlet} = 1.174$

Water vapor volume (normal state):

$V_{H2O.conv.pass} := V_{0.H2O} + 0.0161 \cdot \left(EA_{coef.conv.pass} - 1\right) \cdot V_0$

$V_{H2O.conv.pass} = 0.542 \frac{m^3}{kg}$

Flue gas volume (normal state):

$V_{g.conv.pass} := V_{0.g} + \left(EA_{coef.conv.pass} - 1\right) \cdot V_0 + 0.0161 \cdot \left(EA_{coef.conv.pass} - 1\right) \cdot V_0$

$V_{g.conv.pass} = 6.066 \frac{m^3}{kg}$

$r_{RO2.conv.pass} := \frac{V_{RO2}}{V_{g.conv.pass}} = 0.145$

Volume fraction of water vapor: $r_{H2O.conv.pass} := \frac{V_{H2O.conv.pass}}{V_{g.conv.pass}} = 0.089$

Volume fraction of triatomic gas:

$r_{n.conv.pass} := r_{H2O.conv.pass} + r_{RO2.conv.pass} = 0.235$

Partial pressure of triatomic gas:

$$p_{n.conv.pass} := r_{n.conv.pass} \cdot p_{conv.pass} = 23.481 \cdot kPa$$

Flue gas mass excluding the fly ash:

$$G_{g.conv.pass} := 1 - x_{ash} + 1.306 \cdot EA_{coef.conv.pass} \cdot V_0 \cdot \frac{kg}{m^3}$$

$$G_{g.conv.pass} = 8.059$$

Flue gas density:

$$\rho_{g.conv.pass} := \frac{G_{g.conv.pass}}{V_{g.conv.pass}} = 1.328 \frac{kg}{m^3}$$

Gas coefficient:

$$k_{g.plat} := \left(\frac{0.78 + 1.6 \cdot r_{H2O.conv.pass}}{\sqrt{\frac{p_{n.conv.pass}}{p_0} \cdot \frac{L_{mb.plat}}{m}}} - 0.1 \right) \cdot \left(1 - 0.37 \cdot \frac{T_{g.plat.ave}}{1000 \cdot K} \right) \cdot 10^{-5} \cdot \frac{1}{m \cdot Pa}$$

$$k_{g.plat} = 6.418 \times 10^{-6} \cdot \frac{1}{m \cdot Pa}$$

Extinction coefficient of the gas:

$$K_{g.plat} := k_{g.plat} \cdot r_{n.conv.pass} \cdot p_{conv.pass} = 0.151 \frac{1}{m}$$

Fly ash concentration:

$$\mu_{fa.conv.pass} := \frac{\%FA \cdot x_{ash}}{G_{g.conv.pass}} = 0.035$$

Fly ash coefficient:

$$k_{fa.plat} := \frac{4300 \cdot \left(\rho_{g.conv.pass} \cdot \frac{m^3}{kg} \right)^{\frac{1}{3}}}{\left[\left(\frac{T_{g.plat.ave}}{K} \right)^2 \cdot \left(\frac{d_{fa}}{\mu m} \right)^2 \right]} \cdot 10^{-5} \cdot \frac{1}{m \cdot Pa}$$

$$k_{fa.plat} = 7.062 \times 10^{-5} \cdot \frac{1}{m \cdot Pa}$$

Extinction coefficient for fly ash:

$$K_{fa.plat} := k_{fa.plat} \cdot \mu_{fa.conv.pass} \cdot p_{conv.pass} = 0.247 \frac{1}{m}$$

Radiant absorption coefficient of flue gas radiation:

$$K_{plat} := \left(k_{g.plat} \cdot r_{n.conv.pass} + k_{fa.plat} \cdot \mu_{fa.conv.pass} \right)$$

$$K_{plat} = 3.978 \cdot \frac{1}{m \cdot MPa}$$

Flue gas emissivity:

$$\varepsilon_{g.plat} := 1 - \exp\left(-K_{plat} \cdot p_{conv.pass} \cdot L_{mb.plat} \right)$$

$$\varepsilon_{g.plat} = 0.48$$

Coefficient considering reradiation: $\beta_{plat} := 0.92$ from figure D6

Relative height of window: $x_{plat} := \frac{(h_{roof} - h_{hopper}) - 0.5 \cdot h_{plat}}{h_{roof} - h_{hopper}}$

$x_{plat} = 0.851$

Thermal load distribution coefficient: $\eta_{plat} := 0.78$

Radiation heat flow of panel zone: $q_{r.plat.in} := \frac{\eta_{plat} \cdot q_{r.furnace} \cdot m'_{coal}}{A_{furnace}}$

$q_{r.plat.in} = 118.495 \cdot \frac{kW}{m^2}$

Corrected radiative intensity of panel zone: $q_{r.plat.in.cor} := \beta_{plat} \cdot q_{r.plat.in} = 109.016 \cdot \frac{kW}{m^2}$

Radiation heat absorbed by panel directly from furnace: $q'_{r.plat.in} := \frac{q_{r.plat.in.cor} \cdot A_{rad.plat.in}}{m'_{coal}}$

$q'_{r.plat.in} = 614.344 \cdot \frac{kJ}{kg}$

Furnace radiation heat leaked out of panel: $q'_{r.plat.out} := \frac{q'_{r.plat.in} \cdot (1 - \varepsilon_{g.plat}) \cdot \varphi_{plat}}{\beta_{plat}}$

$q'_{r.plat.out} = 32.362 \cdot \frac{kJ}{kg}$

Direct heat transfer from the furnace - photons

Radiation heat absorbed by panel: $q'_{r.plat} := q'_{r.plat.in} - q'_{r.plat.out}$

$q'_{r.plat} = 581.982 \cdot \frac{kJ}{kg}$

$Q_{r.plat} := q'_{r.plat} \cdot m'_{coal}$

$Q_{r.plat} = 56.811 \cdot MW$

Direct heat transfer from the flue gas in the platen superheater into the final superhater:

Inlet area of heating surface behind the platen superheater: $A_{rad.FSH.in} := A_{rad.plat.out} = 411.137 m^2$

Flue gas absorptivity in the platen: $\alpha_{g.plat} := \varepsilon_{g.plat} = 0.48$

Correction factor of fuel: $\zeta_r := 0.5$

Platen gas direct radiation into FSH: $q_{rl} := \frac{\sigma_0 \cdot \alpha_{g.plat} \cdot A_{rad.FSH.in} \cdot T_{g.plat.ave}^4 \cdot \zeta_r}{m'_{coal}}$

$q_{rl} = 245.027 \cdot \frac{kJ}{kg}$

Total direct radiation into the final superheater

Direct heat to the FSH from flue gas in platen:

$$Q_{g.direct.FSH} := q_{rl} \cdot m'_{coal}$$

$$Q_{g.direct.FSH} = 23.919 \cdot MW$$

Direct heat to the FSH from photons from the furnace leaking out of the platen:

$$Q_{phot.direct.FSH} := q'_{r.plat.out} \cdot m'_{coal}$$

$$Q_{phot.direct.FSH} = 3.159 \cdot MW$$

Total direct radiation into FSH

$$Q_{rad.direct.FSH} := Q_{g.direct.FSH} + Q_{phot.direct.FSH}$$

Value

$$Q_{rad.direct.FSH} = 27.078 \cdot MW$$

From energy balance

Inlet steam conditions

Temperature:

$$T_{s.plat.in} := 386\,°C$$

Pressure:

$$p_{s.plat.in} := 18.02MPa$$

Enthalpy:

$$h_{s.plat.in} := h_{steam}\left(p_{s.plat.in}, T_{s.plat.in}, "", "", ""\right)$$

$$h_{s.plat.in} = 2804.66 \cdot \frac{kJ}{kg}$$

Outlet steam conditions

Temperature:

$$T_{s.plat.out} := 480\,°C$$

Pressure:

$$p_{s.plat.out} := 18.02MPa$$

Enthalpy:

$$h_{s.plat.out} := h_{steam}\left(p_{s.plat.out}, T_{s.plat.out}, "", "", ""\right)$$

$$h_{s.plat.out} = 3205.37 \cdot \frac{kJ}{kg}$$

Energy absorbed by the platen:

$$q_{plat} := h_{s.plat.out} - h_{s.plat.in}$$

$$q_{plat} = 400.715 \cdot \frac{kJ}{kg}$$

Mass flow rate of steam:

$$m'_{s.plat} := 504.667 \frac{kg}{s}$$

Total heat absorbed the platen

$$Q_{plat.tot} := m'_{s.plat} \cdot q_{plat} = 202.228 \cdot MW$$

Convection + gas radiation in the platen:

$$Q_{c.plat} := Q_{plat.tot} - Q_{r.plat}$$

$$Q_{c.plat} = 145.417 \cdot MW$$

If steam conditions are not known, this value is assumed then adjusted via trial and error

Flue gas exit temperature for the platen superheater

Energy balance:

$$h_{g.plat.out.calc} := \frac{m'_{fg} \cdot h_{FE.calc} + m'_{air.ing} \cdot h_{moist.air}(T_{amb}, \omega) - Q_{c.plat} - Q_{ww.plat} - Q_{roof.plat} - Q_{g.direct.FSH}}{m'_{fg}}$$

$$h_{g.plat.out.calc} = 1308.87 \cdot \frac{kJ}{kg}$$

Initial Guess Value $T_{g.plat.out} = 1059.07 \cdot °C$

$$f(T) := h_{fg}(T) - h_{g.plat.out.calc}$$

$$T_{g.plat.out.calc} := root\left(f\left(T_{g.plat.out}\right), T_{g.plat.out}\right) = 1058.473 \cdot °C$$

Check the temperature: $Error_{T.g.plat.out} := T_{g.plat.out} - T_{g.plat.out.calc}$

$Error_{T.g.plat.out} = 0.597 \cdot \Delta°C$ Remember to update initial guess value

Heat transfer to the roof zone above the platen superheater

Ash deposit layer thickness: $t_{ofl.plat} := 0.8mm$ assumed and adjusted

Ash deposit layer thermal conductivity: $\lambda_{ofl.plat} := 0.07 \frac{W}{m \cdot K}$

Ash deposit coefficient: $E_{ash.plat} := \frac{t_{ofl.plat}}{\lambda_{ofl.plat}} = 0.011 \cdot \frac{m^2 K}{W}$

Outer diameter of the tubes in the platen superheater: $OD_{plat} = 38 \cdot mm$

Average longitudinal spacing: $S_{L.plat} = 54.766 \cdot mm$

Density of the platen superheater: $\rho_{g.plat} := \rho_{g.conv.pass}$

Inlet flow area: $A_{flow.plat.in} := N_{tubesheets.plat} \cdot S_{T.plat} \cdot (h_{plat} + b_{plat})$

$A_{flow.plat.in} = 550.103\,m^2$

Outlet flow area $A_{flow.plat.out} := N_{tubesheets.plat} \cdot S_{T.plat} \cdot h_{plat}$

$A_{flow.plat.out} = 411.137\,m^2$

Velocity of the flue gas at the inlet of the platen: $v_{g.plat.in} := \frac{m'_{fg}}{\rho_{g.plat} \cdot A_{flow.plat.in}} = 0.997 \frac{m}{s}$

Velocity of the flue gas at the outlet of the platen: $v_{g.plat.out} := \frac{m'_{fg}}{\rho_{g.plat} \cdot A_{flow.plat.out}} = 1.334 \frac{m}{s}$

Average flue gas velocity in the platen: $v_{g.plat} := \frac{v_{g.plat.in} + v_{g.plat.out}}{2} = 1.165 \frac{m}{s}$

Thermal conductivity of the flue gas:

Interpolation values:

$$T_1 := 1100\,°C \qquad \lambda_1 := 11.7$$
$$T_2 := 1200\,°C \qquad \lambda_2 := 12.6$$

$$\lambda_{g.plat} := \left[\lambda_1 + \left(\frac{T_{g.plat.ave} - T_1}{T_2 - T_1}\right)\cdot(\lambda_2 - \lambda_1)\right]\cdot 10^{-2}\cdot\frac{W}{m\cdot K}$$

$$\lambda_{g.plat} = 0.12\cdot\frac{W}{m\cdot K}$$

Kinematic viscosity:

Interpolation values:

$$\nu_1 := 180\cdot 10^{-5}\,\frac{m^2}{s} \qquad \nu_2 := 211\cdot 10^{-5}\,\frac{m^2}{s}$$

$$\nu_{g.plat} := \left[\nu_1 + \left(\frac{T_{g.plat.ave} - T_1}{T_2 - T_1}\right)\cdot(\nu_2 - \nu_1)\right]$$

$$\nu_{g.plat} = 2\times 10^{-3}\,\frac{m^2}{s}$$

Prandt number

$$Pr_1 := 0.57 \qquad Pr_2 := 0.56$$

$$Pr_{g.plat.ave} := \left[Pr_1 + \left(\frac{T_{g.plat.ave} - T_1}{T_2 - T_1}\right)\cdot(Pr_2 - Pr_1)\right]$$

$$Pr_{g.plat.ave} = 0.56$$

Flue gas prandtl number: $Pr_{g.plat} := \left(0.94 + 0.56\cdot r_{H2O.conv.pass}\right)\cdot Pr_{g.plat.ave} = 0.558$

Correction factor of tube rows: $C_{z.plat} := 0.91 + 0.0125\cdot\left(N_{rows.plat} - 2\right) = 2.285$

Relative transverse pitch: $\sigma_1 := \frac{S_{T.plat}}{OD_{plat}} = 30.079$

Relative vertical pitch: $\sigma_2 := \frac{S_{L.plat}}{OD_{plat}} = 1.441$

Correction factor for geometric arrangement:

$$C_{s.plat} := \left[1 + \left(2\cdot\sigma_1 - 3\right)\cdot\left(1 - \frac{\sigma_2}{2}\right)^3\right]^{-2} = 0.198$$

Flue gas composition and temperature correction coefficient: $C_{w.plat} := 0.92 + 0.726\cdot r_{H2O.conv.pass} = 0.985$

The flue gas side Reynolds number: $Re_{g.plat} := \frac{v_{g.plat}\cdot OD_{plat}}{\nu_{g.plat}} = 22.129$

Flue gas Nusselt number:

$$Nu_{g.plat} := 0.2 \cdot \left(Re_{g.plat}\right)^{0.65} \cdot Pr_{g.plat}^{0.33} \cdot C_{z.plat} \cdot C_{s.plat} \cdot C_{w.plat}$$

Flue gas convection side coefficient: $h_{g.conv.plat} := \frac{\lambda_{g.plat}}{OD_{plat}} \cdot Nu_{g.plat} = 1.78 \frac{W}{m^2 \cdot K}$

Tube wall fouling emissivity: $\varepsilon_w := 0.7$

Average steam temperature: $T_{s.plat} := \frac{T_{s.plat.in} + T_{s.plat.out}}{2}$

$T_{s.plat} = 433 \cdot °C$

Correction coefficient of tube diamter: $C_{d.plat} := 1.04$ Figure D8

Average free flow area on the steam side:

$$A_{ff.s.plat} := \frac{\pi}{4} \cdot ID_{plat}^2 \cdot N_{tubes.tubesheet.plat} \cdot N_{tubesheets.plat}$$

$A_{ff.s.plat} = 0.595 m^2$

Steam conditions for steam heat transfer coefficient

Density of the steam in the platen superheater:

Inlet density: $\rho_{s.plat.in} := \frac{1}{v_{steam}\left(p_{s.plat.in}, T_{s.plat.in}, "", "", ""\right)}$

Outlet density: $\rho_{s.plat.out} := \frac{1}{v_{steam}\left(p_{s.plat.out}, T_{s.plat.out}, "", "", ""\right)}$

Average density: $\rho_{s.plat} := \frac{\rho_{s.plat.in} + \rho_{s.plat.out}}{2} = 77.223 \frac{kg}{m^3}$

Dynamic viscosity of the steam in the platen superheater:

Inlet dynamic viscosity: $\mu_{s.plat.in} := \mu_{steam}\left(p_{s.plat.in}, T_{s.plat.in}, "", "", "", ""\right)$

Outlet dynamic viscosity: $\mu_{s.plat.out} := \mu_{steam}\left(p_{s.plat.out}, T_{s.plat.out}, "", "", "", ""\right)$

Average dynamic viscosity: $\mu_{s.plat} := \frac{\mu_{s.plat.in} + \mu_{s.plat.out}}{2} = 2.697 \times 10^{-5} \frac{kg}{s \cdot m}$

Thermal conductivity of the steam in the platen superheater:

Inlet thermal conductivity: $\lambda_{s.plat.in} := \lambda_{steam}\left(p_{s.plat.in}, T_{s.plat.in}, "", "", "", ""\right)$

Outlet thermal conductivity: $\lambda_{s.plat.out} := \lambda_{steam}\left(p_{s.plat.out}, T_{s.plat.out}, "", "", "", ""\right)$

Average thermal conductivity: $\lambda_{s.plat} := \frac{\lambda_{s.plat.in} + \lambda_{s.plat.out}}{2} = 0.089 \cdot \frac{W}{m \cdot K}$

Specific heat of the steam in the platen superheater:

Inlet specific heat: $Cp_{s.plat.in} := Cp_{steam}(p_{s.plat.in}, T_{s.plat.in}, "", "", "", "")$

Outlet specific heat: $Cp_{s.plat.out} := Cp_{steam}(p_{s.plat.out}, T_{s.plat.out}, "", "", "", "")$

Average specific heat: $Cp_{s.plat} := \frac{Cp_{s.plat.in} + Cp_{s.plat.out}}{2} = 4.852 \cdot \frac{kJ}{kg \cdot K}$

Steam velocity in the steam: $v_{s.plat} := \frac{m'_{s.plat}}{A_{ff.s.plat} \cdot \rho_{s.plat}} = 10.99 \frac{m}{s}$

Reynolds number of the steam: $Re_{s.plat} := \frac{\rho_{s.plat} \cdot v_{s.plat} \cdot ID_{plat}}{\mu_{s.plat}} = 8.181 \times 10^5$

Prandtl number of the steam: $Pr_{s.plat} := \frac{Cp_{s.plat} \cdot \mu_{s.plat}}{\lambda_{s.plat}} = 1.464$

Heat transfer coefficient from tube wall to steam:

Nusselt number on the steam side: $Nu_{s.plat} := 0.023 \cdot C_{d.plat} \cdot Re_{s.plat}^{0.8} \cdot Pr_{s.plat}^{0.4}$

Heat transfer coefficient on the steam side: $h_{s.plat} := Nu_{s.plat} \cdot \frac{\lambda_{s.plat}}{ID_{plat}} = 5148 \cdot \frac{W}{m^2 \cdot K}$

Platen superheater configuration factor:

$\frac{S_{L.plat}}{OD_{plat}} = 1.441$ $e_{plat} := \frac{S_{T.plat}}{2} = 571.5 \cdot mm$ Figure D5

$x_{plat.conf} := 1$

Platen superheater total heating area:

$A_{g.plat.conv} := x_{plat.conf} \cdot h_{plat} \cdot b_{plat} \cdot N_{tubesheets.plat} \cdot 2$

Fouling layer temperature of tube:

$T_{w.plat} := T_{s.plat} + \left(E_{ash.plat} + \frac{1}{h_{s.plat}}\right) \cdot \frac{(Q_{r.plat} + Q_{c.plat})}{A_{g.plat.conv}}$

$T_{w.plat} = 970.465 \cdot °C$

Radiation heat transfer coefficient:

$$h_{g.rad.plat} := \sigma_0 \cdot \frac{(\varepsilon_w + 1)}{2} \cdot \left[\varepsilon_{g.plat} \cdot T_{g.plat.ave}^3 \cdot \left[\frac{1 - \left(\frac{T_{w.plat}}{T_{g.plat.ave}}\right)^4}{1 - \left(\frac{T_{w.plat}}{T_{g.plat.ave}}\right)} \right] \right] = 224.2 \frac{W}{m^2 \cdot K}$$

Utilization coefficient of the panel: $\zeta_{g.plat} := 0.85$

Flue gas side heat transfer coefficient:

$$h_{g.plat} := \zeta_{g.plat}\cdot\left(\frac{\pi\cdot OD_{plat}}{2\cdot S_{L.plat}}\cdot h_{g.conv.plat} + h_{g.rad.plat}\right) = 192.219\,\frac{W}{m^2\cdot K}$$

Overall heat transfer coeffiecient for the platen superheater:

$$U_{plat} := \frac{h_{g.plat}}{1+\left(1+\frac{Q_{r.plat}}{Q_{c.plat}}\right)\cdot\left(E_{ash.plat}+\frac{1}{h_{s.plat}}\right)\cdot h_{g.plat}}$$

$$U_{plat} = 46.803\cdot\frac{W}{m^2\cdot K}$$

Maximum temperature difference: $\Delta T_{max.plat} := T_{FE} - T_{s.plat.in} = 884.52\cdot\Delta°C$

Minimum temperature difference: $\Delta T_{min.plat} := T_{g.plat.out} - T_{s.plat.out} = 579.07\cdot\Delta°C$

Logarithmic mean temperature difference:

$$\Delta T_{LMTD.plat} := \frac{\Delta T_{max.plat} - \Delta T_{min.plat}}{\ln\left(\frac{\Delta T_{max.plat}}{\Delta T_{min.plat}}\right)}$$

$$\Delta T_{LMTD.plat} = 721.044\,K$$

Convective heat transferred by the panel:

$$Q_{c.plat.calc} := U_{plat}\cdot A_{g.plat.conv}\cdot\Delta T_{LMTD.plat}$$

$$Q_{c.plat.calc} = 147.585\cdot MW$$

Error:

$$Error_{Q.c.plat} := Q_{c.plat} - Q_{c.plat.calc}$$

$$Error_{Q.c.plat} = -2.168\cdot MW$$

In this case since the heat transferred into the steam is known from the given conditions in the C-schedule then it is not assumed first and then corrected by iteration. Some terms still need to be adjusted on the calculated values of convection and radiation heat transfer to reduce the error

Heat absorbed by the waterwalls around the platen superheater

Diameter of tubes in the water wall: $OD_{ww} := 63.5mm$

Spacing of the waterwalls: $S_{ww} := 72.6mm$

Distance from the platen superheater backside to furnace nose: $\delta_{nose.plat} := 914mm$

Side water wall heating around the platen:

$$A_{ww.plat} := \frac{0.5\pi\cdot OD_{ww} + \left(S_{ww} - OD_{ww}\right)}{S_{ww}}\cdot\left[h_{plat}\cdot\left(b_{plat} + \delta_{nose.plat}\right)\right]\cdot 2 = 377.119\,m^2$$

Steam conditions

Pressure: $p_{ww.out} := 19.01MPa$

Water temperature of water wall at palten side: $T_{s.ww.plat} := T_{steam}(p_{ww.out}, "", "", "")$

$T_{s.ww.plat} = 361.51 \cdot °C$

Average temperature difference of heat transfer: $\Delta T_{s.plat} := T_{g.plat.ave} - T_{s.ww.plat}$

$\Delta T_{s.plat} = 803.28\,K$

Heat transferred by the water walls: $Q_{ww.plat.calc} := U_{plat} \cdot A_{ww.plat} \cdot \Delta T_{s.plat}$

$Q_{ww.plat.calc} = 14.178 \cdot MW$ Remember to update initial guess value

Error on heat transferred by water wall: $Error_{Q.ww.plat} := Q_{ww.plat} - Q_{ww.plat.calc}$

$Error_{Q.ww.plat} = -251.11\,W$

Roof infront of the platen superheater

Length of the roof in the furnace: $L_{roof.furnace} := 2056mm$

Area of roof in furnace $A_{roof.furnace} := W_{furnace} \cdot L_{roof.furnace}$

$A_{roof.furnace} = 49.35\,m^2$

Relative height of furnace roof cover: $x := 1$

Thermal load distribution coefficient: $\eta_{roof.furnace} := 0.633$

Furnace radiation heat flux absorbed by furnace roof cover: $Q_{roof.furnace} := \frac{\eta_{roof.furnace} \cdot q_{r.furnace} \cdot m'_{coal}}{A_{furnace}}$

$Q_{roof.furnace} = 96.163 \cdot \frac{kW}{m^2}$

Furnace radiation heat absorbed by the furnace roof cover: $q_{roof.furnace} := \frac{\beta_{plat} \cdot Q_{roof.furnace} \cdot A_{roof.furnace}}{m'_{coal}}$

$q_{roof.furnace} = 44.727 \cdot \frac{kJ}{kg}$

Mass flow rate of water/steam in the water walls: $m'_{s.ww} := 487.841 \frac{kg}{s}$

Primary desuperheating water flow rate: $m'_{s.ds} := 0 \frac{kg}{s}$

Mass flow are of water/steam in the roof cover above the furnace: $m'_{s.roof.furnace} := m'_{s.ww} - m'_{s.ds}$

Steam enthalpy increment of furnace roof cover: $\Delta h_{s.roof.furnace} := \frac{m'_{coal} \cdot q_{roof.furnace}}{m'_{s.roof.furnace}}$

$$\Delta h_{s.roof.furnace} = 8.95 \cdot \frac{kJ}{kg}$$

Saturated steam temperature of the drum outlet: $T_{s.roof.furnace.in} := 361\,°C$

Quality of the steam out of the drum: $x_{drum.out} := 0.96$

Dry saturated steam enthalpy of drum outlet:

$$h_{s.roof.furnace.in} := h_{steam}("", T_{s.roof.furnace.in}, "", x_{drum.out}, "")$$

$$h_{s.roof.furnace.in} = 2442.58 \cdot \frac{kJ}{kg}$$

Furnace roof steam pressure: $p_{drum} := 19.01MPa$

Steam enthalpy of furnace roof inlet to the roof of the platen superheater:

$$h_{s.roof.furnace.out} := h_{s.roof.furnace.in} + \Delta h_{s.roof.furnace}$$

$$h_{s.roof.furnace.out} = 2451.53 \cdot \frac{kJ}{kg}$$

Heat absorbed by the roof around the platen superheater

Steam temperature of roof inlet into the roof of the platen superheater: $T_{s.roof.plat.in} := T_{steam}(p_{drum}, "", h_{s.roof.furnace.out}, "")$

$$T_{s.roof.plat.in} = 361.515 \cdot °C$$

Steam enthalpy increment of platen superheater roof: $\Delta h_{s.roof.plat} := \frac{Q_{roof.plat}}{m'_{s.roof.furnace}} = 19.994 \cdot \frac{kJ}{kg}$

Steam enthalpy at the outlet of platen superheater roof: $h_{s.roof.plat.out} := h_{s.roof.furnace.out} + \Delta h_{s.roof.plat}$

$$h_{s.roof.plat.out} = 2471.53 \cdot \frac{kJ}{kg}$$

Steam temperature at the outlet of platen superheater roof: $T_{s.roof.plat.out} := T_{steam}(p_{s.PrimSH.in}, "", h_{s.roof.plat.out}, "")$

$$T_{s.roof.plat.out} = 361.556 \cdot °C$$

Average steam temperature at the roof of the platen:

$$T_{s.roof.plat.ave} := \frac{T_{s.roof.plat.in} + T_{s.roof.plat.out}}{2}$$

$$T_{s.roof.plat.ave} = 361.535 \cdot °C$$

Average temperature difference of heat transfer on the roof of the platen superheater:

$$\Delta T_{roof.plat} := T_{g.plat.ave} - T_{s.roof.plat.ave}$$

$$\Delta T_{roof.plat} = 803.26 \cdot \Delta °C$$

Geometry for heat transfer area calculation

Roof tube spacing:

$$S_{roof} := 73mm$$

Outer diameter of the tubes in the roof:

$$OD_{roof} := 70mm$$

Roof tube length within the platen superehater zone:

$$L_{roof.plat} := b_{plat} + \delta_{nose.plat} = 6.993\,m$$

Width of the furnace:

$$W_{furnace} = 24.003\,m$$

Heating area of the roof tubes above the platen superheater:

$$A_{roof.plat} := \frac{0.5\pi \cdot OD_{roof} + \left(S_{roof} - OD_{roof}\right)}{S_{roof}} \cdot \left(W_{furnace} \cdot L_{roof.plat}\right) = 259.725\,m^2$$

Absorbed heat on the roof of the platen superheater:

$$Q_{roof.plat.calc} := U_{plat} \cdot A_{roof.plat} \cdot \Delta T_{roof.plat}$$

$$Q_{roof.plat.calc} = 9.764 \cdot MW$$

Remember to update initial guess value

Error of the heat transferred into the roof of the platen superheater:

$$Error_{Q.roof.plat} := Q_{roof.plat} - Q_{roof.plat.calc}$$

$$Error_{Q.roof.plat} = -1.046 \times 10^4\,W$$

Parameters that were assumed which should be updated

Absorbed convection heat of furnace roof at panel zone:

$$Q_{ww.plat.calc} = 14.178 \cdot MW$$

$$Error_{Q.ww.plat} = -0.25 \cdot kW$$

Absorbed convection heat of furnace roof at panel zone:

$$Q_{roof.plat.calc} = 9.764 \cdot MW$$

$$Error_{Q.roof.plat} = -10.46 \cdot kW$$

Platen superheater gas exit temperature:

$$T_{g.plat.out.calc} = 1058.47 \cdot °C$$

$$Error_{T.g.plat.out} = 0.597 \cdot \Delta °C$$

E.6. Cascading direct radiation through the Final superheater

Direct radiation into the final superheater: $Q_{rad.direct.FSH} = 27.078 \cdot MW$

Cascading the energy over the superheater rows:

$$a(OD, S_T) := 3.14 \cdot \frac{OD}{2 \cdot S_T} - \frac{OD}{S_T} \cdot \left[\operatorname{asin}\left(\frac{OD}{S_T}\right) + \sqrt{\left(\frac{S_T}{OD}\right)^2 - 1} - \frac{S_T}{OD} \right]$$

Outer diamter of the tubes: $OD_{FSH} := 44.5mm$

Pitch across depth: $S_{T.FSH} := 0.8571m$

Fraction of energy from the first row: $a_{FSH} := a(OD_{FSH}, S_{T.FSH}) = 0.08$

Number of rows: $N_{rows.FSH} := 2 \cdot 34$

Direct radiation energy consumed per row:

$$Q_{rad.direct.FSH.casc} := \left| \begin{array}{l} \text{for } i \in 0 .. N_{rows.FSH} - 1 \\ \quad \left| \begin{array}{l} a_{f_0} \leftarrow a_{FSH} \\ a_{f_i} \leftarrow \left[1 - \left(\sum_{i=0}^{i-1} a_{f_i} \right) \right] \cdot a_{FSH} \text{ if } i > 0 \end{array} \right. \\ Q_{rad.direct.FSH} \cdot a_f \end{array} \right.$$

Rows 1-8: $Q_{rad.direct.FSH.1to8} := \sum_{i=0}^{7} Q_{rad.direct.FSH.casc_i} = 13200.81 \cdot kW$

Rows 9-16: $Q_{rad.direct.FSH.9to16} := \sum_{i=8}^{15} Q_{rad.direct.FSH.casc_i} = 6765.18 \cdot kW$

Rows 17-25: $Q_{rad.direct.FSH.17to25} := \sum_{i=16}^{24} Q_{rad.direct.FSH.casc_i} = 3759.21 \cdot kW$

Rows 26-34: $Q_{rad.direct.FSH.26to34} := \sum_{i=25}^{33} Q_{rad.direct.FSH.casc_i} = 1772.09 \cdot kW$

Rows 35-43: $Q_{rad.direct.FSH.35to43} := \sum_{i=35-1}^{43-1} Q_{rad.direct.FSH.casc_i} = 835.36 \cdot kW$

Rows 44-52: $Q_{rad.direct.FSH.44to52} := \sum_{i=44-1}^{52-1} Q_{rad.direct.FSH.casc_i} = 393.79 \cdot kW$

Rows 53-60: $Q_{rad.direct.FSH.53to60} := \sum_{i=53-1}^{60-1} Q_{rad.direct.FSH.casc_i} = 171.2 \cdot kW$

Rows 61-68: $Q_{rad.direct.FSH.61to68} := \sum_{i=61-1}^{68-1} Q_{rad.direct.FSH.casc_i} = 87.74 \cdot kW$

E.7. Final superheater geometry

Area of heating surfaces: $A_{FSH} := 3660m^2$

Outer tube diameter: $OD_{FSH} = 44.5 \cdot mm$

Transverse pitch: $S_{L.FSH} := 45.5mm$

Longitudinal pitch: $S_{T.FSH} = 0.857m$

Thickness of the outer fouling layer: $t_{ofl.FSH} := 0.9mm$

Number of tubes per tubesheet: $N_{tubes.tubesheet.FSH} := 34$

Number of tubesheets: $N_{tubesheets.FSH} := 28$

Height at the inlet of the FSH: $h_{FSH.in} := 71305mm - 54697mm$

Height at the outlet of the FSH: $h_{FSH.out} := 71305mm - 57018mm$

Final superheater depth: $b_{FSH} := 1958.5mm + 1962mm$

E.8. Final superheater thermal calculations

Inlet flue gas temperature: $T_{g.FSH.in} := T_{g.plat.out} = 1059.07 \cdot °C$

Outlet flue gas temperature: $T_{g.FSH.out} := 942.608\ °C$

Inlet steam temperature: $T_{s.FSH.in} = 473.581 \cdot °C$

Inlet steam pressure: $p_{s.FSH.in} = 17.88 \cdot MPa$

Outlet steam temperature: $T_{s.FSH.out} = 540 \cdot °C$

Outlet steam pressure: $p_{s.FSH.out} = 17.35 \cdot MPa$

Steam mass flow rate: $m'_{s.FSH} = 509.763 \frac{kg}{s}$

Heat transfer to the surroundings walls $Q_{ww.FSH} := 23.234MW$ trial and error

Exit enthalpy of the final superheater:

$$h_{g.FSH.out} := \frac{\left(m'_{fg} \cdot h_{g.plat.out.calc} + Q_{rad.direct.FSH} - Q_{FSH} - Q_{ww.FSH}\right)}{m'_{fg}}$$

$$h_{g.FSH.out} = 1166.76 \cdot \frac{kJ}{kg}$$

Flue gas exit temperature calculation

Initial guess value: $T_{g.plat.out} = 1059.07 \cdot °C$

$f(T) := h_{fg}(T) - h_{g.FSH.out}$

$T_{g.FSH.out.calc} := root\left(f\left(T_{g.plat.out}\right), T_{g.plat.out}\right) = 942.515 \cdot °C$

$Error_{T.g.FSH.out} := T_{g.FSH.out} - T_{g.FSH.out.calc} = 0.093 \cdot \Delta°C$

Constants

Emissivity of fouling on the tube wall: $\varepsilon_{ofl.FSH} := 0.7$

Thermal condutivity of the outer fouling layer: $\lambda_{ofl.FSH} := 007 \frac{W}{m \cdot K}$

Stefan- Boltzmann constant: $\sigma_0 = 5.67 \times 10^{-8} \cdot \frac{W}{m^2 \cdot K^4}$

Radiation constant: $C_{rad} := 3.6$

Calculations

Flue gas pressure: $p_{conv.pass} = 100 \cdot kPa$

Flue gas density: $\rho_{g.conv.pass} = 1.328 \frac{kg}{m^3}$

Average flue gas temperature: $T_{g.FSH.ave} := \frac{T_{g.FSH.in} + T_{g.FSH.out}}{2}$

$T_{g.FSH.ave} = 1273.99\,K$

Average temperature difference of the working fluid: $T_{s.FSH.ave} := \frac{T_{s.FSH.in} + T_{s.FSH.out}}{2}$

$T_{s.FSH.ave} = 506.79 \cdot °C$

Ash deposition coefficient of the heating surface: $E_{ash.FSH} := \frac{t_{ofl.FSH}}{\lambda_{ofl.FSH}}$

$E_{ash.FSH} = 1.286 \times 10^{-4} \cdot \frac{m^2 \cdot K}{W}$

Outer diameter of the fouled layer: $OD_{ofl.FSH} := OD_{FSH} + 2 \cdot t_{ofl.FSH}$

$OD_{ofl.FSH} = 0.046\,m$

Effective radiation layer thickness (Mean beam length): $L_{mb.FSH} := C_{rad} \cdot \frac{OD_{ofl.FSH}}{4} \cdot \left(\frac{4}{\pi} \cdot \frac{S_{T.FSH} \cdot S_{L.FSH}}{OD_{ofl.FSH}^2} - 1 \right)$

$L_{mb.FSH} = 0.924\,m$

Gas coefficient:

$$k_{g.FSH} := \left(\frac{0.78 + 1.6 \cdot r_{H2O.conv.pass}}{\sqrt{r_{n.conv.pass} \cdot \frac{L_{mb.FSH}}{m}}} - 0.1 \right) \cdot \left(1 - 0.37 \cdot \frac{T_{g.FSH.ave}}{1000 \cdot K} \right) \cdot 10^{-5} \cdot \frac{1}{m \cdot Pa}$$

$k_{g.FSH} = 9.95 \times 10^{-6} \cdot \frac{1}{m \cdot Pa}$

$K_{g.FSH} := k_{g.FSH} \cdot r_{n.conv.pass} \cdot p_{conv.pass} = 0.234 \frac{1}{m}$

Fly ash coefficient:

$$k_{fa.FSH} := \frac{4300 \cdot \left(\rho_{g.conv.pass} \cdot \frac{m^3}{kg} \right)^{\frac{1}{3}}}{\left[\left(\frac{T_{g.FSH.ave}}{K} \right)^2 \cdot \left(\frac{d_{fa}}{\mu m} \right)^2 \right]^{\frac{1}{3}}} \cdot 10^{-5} \cdot \frac{1}{m \cdot Pa}$$

$k_{fa.FSH} = 7.655 \times 10^{-5} \cdot \frac{1}{m \cdot Pa}$

$K_{fa.FSH} := k_{fa.FSH} \cdot \mu_{fa.conv.pass} \cdot p_{conv.pass} = 0.268 \frac{1}{m}$

Extinction coefficient of the flue gas: $K_{FSH} := K_{g.FSH} + K_{fa.FSH} = 0.501 \frac{1}{m}$

Flue gas emissivity: $\varepsilon_{g.FSH} := 1 - \exp(-K_{FSH} \cdot L_{mb.FSH})$

$\varepsilon_{g.FSH} = 0.371$

View factor for flownex: $F_{rad.FSH.Flownex} := \left(\frac{\varepsilon_{ofl.FSH} + 1}{2}\right) \cdot \varepsilon_{g.FSH} = 0.315$

Outside radiation heat transfer coefficient

Average thickness of the tube: $t_{FSH.ave} := \frac{6.3mm + 8.8mm + 11mm}{3}$

Average inner diameter: $ID_{FSH} := OD_{FSH} - 2 \cdot t_{FSH.ave} = 27.1 \cdot mm$

Average free flow area on the steam side:

$$A_{ff.s.FSH} := \frac{\pi}{4} \cdot ID_{FSH}^{2} \cdot N_{tubes.tubesheet.FSH} \cdot N_{tubesheets.FSH}$$

$$A_{ff.s.FSH} = 0.549 m^{2}$$

Steam conditions for steam heat transfer coefficient

Thermal condictivity of the steam in the final superheater:

Inlet steam thermal conductivity: $\lambda_{s.FSH.in} := \lambda_{steam}(p_{s.FSH.in}, T_{s.FSH.in}, "", "", "", "")$

$$\lambda_{s.FSH.in} = 0.084 \cdot \frac{W}{m \cdot K}$$

Outlet steam thermal conductivity: $\lambda_{s.FSH.out} := \lambda_{steam}(p_{s.FSH.out}, T_{s.FSH.out}, "", "", "", "")$

$$\lambda_{s.FSH.out} = 0.087 \cdot \frac{W}{m \cdot K}$$

Average steam thermal conductivity: $\lambda_{s.FSH.ave} := \frac{\lambda_{s.FSH.in} + \lambda_{s.FSH.out}}{2} = 0.086 \frac{W}{m \cdot K}$

Density of the steam in the final superheater:

Inlet density: $\rho_{s.FSH.in} := \frac{1}{v_{steam}(p_{s.FSH.in}, T_{s.FSH.in}, "", "", "")}$

Outlet density: $\rho_{s.FSH.out} := \frac{1}{v_{steam}(p_{s.FSH.out}, T_{s.FSH.out}, "", "", "")}$

Average density: $\rho_{s.FSH.ave} := \frac{\rho_{s.FSH.in} + \rho_{s.FSH.out}}{2} = 57.697 \frac{kg}{m^{3}}$

Dynamic viscosity of the steam in the final superheater:

Inlet dynamic viscosity: $\mu_{s.FSH.in} := \mu_{steam}(p_{s.FSH.in}, T_{s.FSH.in}, "", "", "", "")$

Outlet dynamic viscosity: $\mu_{s.FSH.out} := \mu_{steam}(p_{s.FSH.out}, T_{s.FSH.out}, "", "", "", "")$

Average dynamic viscosity: $\mu_{s.FSH.ave} := \frac{\mu_{s.FSH.in} + \mu_{s.FSH.out}}{2} = 2.994 \times 10^{-5} \frac{kg}{s \cdot m}$

Specific heat of the steam in the final superheater:

Inlet specific heat: $p_{s.FSH.in} := Cp_{steam}(p_{s.FSH.in}, T_{s.FSH.in}, "", "", "", "")$

Outlet specific heat: $Cp_{s.FSH.out} := Cp_{steam}(p_{s.FSH.out}, T_{s.FSH.out}, "", "", "", "")$

Average specific heat: $Cp_{s.FSH.ave} := \frac{Cp_{s.FSH.in} + Cp_{s.FSH.out}}{2} = 3.102 \cdot \frac{kJ}{kg \cdot K}$

Steam velocity in the steam: $v_{s.FSH.ave} := \frac{m'_{s.FSH}}{A_{ff.s.FSH} \cdot \rho_{s.FSH.ave}} = 16.09 \frac{m}{s}$

Reynolds number of the steam: $Re_{s.FSH} := \frac{\rho_{s.FSH.ave} \cdot v_{s.FSH.ave} \cdot ID_{FSH}}{\mu_{s.FSH.ave}}$

$Re_{s.FSH} = 8.403 \times 10^5$

Prandtl number of the steam: $Pr_{s.FSH} := \frac{Cp_{s.FSH.ave} \cdot \mu_{s.FSH.ave}}{\lambda_{s.FSH.ave}} = 1.083$

Steam side Reynolds number: $Nu_{s.FSH} := 0.023 \cdot Re_{s.FSH}^{0.8} \cdot Pr_{s.FSH}^{0.4}$

Convective heat transfer coefficient on the steam side: $h_{s.FSH} := \frac{\lambda_{s.FSH.ave} \cdot Nu_{s.FSH}}{ID_{FSH}}$

$h_{s.FSH} = 4.123 \times 10^3 \cdot \frac{W}{m^2 \cdot K}$

Duty of the final superheater: $Q_{FSH} = 107.358 \cdot MW$

Temperature of the outer fouling layer:

$$T_{ofl.FSH} := T_{s.FSH.ave} + \left(E_{ash.FSH} + \frac{1}{h_{s.FSH}}\right) \cdot \left(\frac{Q_{FSH}}{A_{FSH}}\right) = 790.826\,K$$

Radition heat transfer coeffiecient:

$$h_{g.rad.FSH} := \sigma_0 \cdot \left(\frac{\varepsilon_{ofl.FSH} + 1}{2} \right) \cdot \varepsilon_{g.FSH} \cdot \left(\frac{T_{g.FSH.ave}^{4} - T_{ofl.FSH}^{4}}{T_{g.FSH.ave} - T_{ofl.FSH}} \right)$$

$$h_{g.rad.FSH} = 82.941 \cdot \frac{W}{m^2 \cdot K}$$

APPENDIX F. INPUTS FOR THE REAL PLANT DATA CASES

F.1. Inputs for the full load case

Parameter	Units	Full load
Excess air	%	20
Ingress air	%	7
Unburnt carbon per kg of coal	%	0.8
Coal CV (HHV)	MJ/kg	15.07
Feedwater flow rate	kg/s	428.6
Cold reheat flow rate	kg/s	411.2
EC water inlet temperature	°C	247.5
EC water outlet temperature	°C	293.1
Drum outlet temperature	°C	352
RH 1 steam inlet temperature	°C	334.1
RH 2 steam outlet temperature	°C	534.9
ATT 1 spray water temperature	°C	247.5
ATT 2 spray water temperature	°C	247.5
ATT 3 spray water temperature	°C	148.6
EC flue gas outlet temperature	°C	397.9
Ambient air temperature	°C	44
AH air outlet temperature	°C	284.4
FW inlet pressure	MPa	16.9
Drum pressure	MPa	16.9
SH 2 steam inlet pressure	MPa	16.45
SH 3 steam inlet pressure	MPa	16.3
SH 3 outlet pressure	MPa	16.2
RH 1 inlet pressure	MPa	3.7
RH 2 outlet pressure	MPa	3.7

F.2. Inputs for the 65% full load case

Parameter	Units	65% full load
Excess air	%	20
Ingress air	%	7
Unburnt carbon per kg of coal	%	0.8
Coal CV (HHV)	MJ/kg	15.07
Feedwater flow rate	kg/s	262.4
Cold reheat flow rate	kg/s	251.7
EC water inlet temperature	°C	247.5
EC water outlet temperature	°C	273.3
Drum outlet temperature	°C	413.4
RH 1 steam inlet temperature	°C	323.1
RH 2 steam outlet temperature	°C	531.8
ATT 1 spray water temperature	°C	247.5
ATT 2 spray water temperature	°C	247.5
ATT 3 spray water temperature	°C	148.5
EC flue gas outlet temperature	°C	369.7
Ambient air temperature	°C	44
AH air outlet temperature	°C	268.2
FW inlet pressure	MPa	16.1
Drum pressure	MPa	15.9
SH 2 steam inlet pressure	MPa	15.9
SH 3 steam inlet pressure	MPa	15.9
SH 3 outlet pressure	MPa	15.9
RH 1 inlet pressure	MPa	2.4
RH 2 outlet pressure	MPa	2.4